PhD School of Physics, The University of Milan

Department of Physics

Corso di Dottorato in Fisica

Ciclo XXX

Modelling Superfluid Neutron Stars Applications to Pulsar Glitches

Settore Scientifico Disciplinare FIS/05

Supervisore: Professor Pierre M. PIZZOCHERO

Tesi di Dottorato di:

Marco ANTONELLI

Anno Accademico 2017-2018

Final examination committee:

External Referee: Professor Mehmet Ali Alpar, Sabancı Üniversitesi, Mühendislik ve Doğa Bilimleri Fakültesi

External referee: Professor Jérôme Novak, LUTH, Observatoire de Paris, PSL Research University, CNRS

External Member: Professor Roberto Turolla, Università di Padova, Dipartimento di Fisica e Astronomia Galileo Galilei

External Member: Professor Nicolas Chamel, Université Libre de Bruxelles, Institute of Astronomy and Astrophysics

External Member: Professor Ian Jones, University of Southampton, Mathematical Sciences

Final examination:

January, 2017

Dipartimento di Fisica dell'Università degli Studi di Milano
Via Celoria 16 - Milano

Contents

Introduction

Gravity pushes matter in neutron stars up to densities at which long lasting unusual degrees of freedom and exotic phases of matter appear: nuclear superfluids and strange matter such as hyperons, different deconfined quarks states and possibly also colour superconducting phases. Therefore neutron stars, and the still hypothetical quark stars (Itoh, 1970), are probes of the high density and low temperature zone of the QCD phase diagram, as shown in Fig (0.1).

The most common astronomical manifestation of neutron stars are *radio pulsars*, intermittent and precise radio signals from a point-like source in the sky. This phenomenon is firmly interpreted as the beamed emission from a magnetized and rotating neutron star. The precise timing of such rotation-powered neutron stars reveals a steady and extremely slow increase of the pulse period, indicating that these objects loose angular momentum and kinetic energy due to the emission mechanism. Even if pulsars are known to be very stable clocks, many of them show sudden and random increases in their spin frequency, dubbed *glitches*, that are instantaneous to the accuracy of the data.

Anderson and Itoh (1975) proposed a natural and elegant interpretation of the glitch phenomenon, based on the intermittent motion of a myriad of quantized vortices[1] that permeate the solid inner crust of the neutron star. Complex interaction of vortices with the crystalline solid present in a neutron star's crust can pin the vortex in place (or, more generally, hinder the natural outward creep motion of vortices). Pinning freezes the superfluid vorticity in its configuration, so that the superfluid cannot spin down together with the observable component. As a consequence a superfluid current of neutrons develops in the inner crust: in the frame of reference of the solid medium, the neutron fluid is seen to flow in a definite direction. This current provides the extra angular momentum that can eventually be released in a glitch.

While the exact nature of the trigger mechanism for glitches is still debated, with crustquakes, vortex avalanches and fluid instabilities likely contenders (Haskell and Melatos, 2015), the multifluid framework for describing the hydrodynamics of superfluid neutrons

---

[1] In this work some basic knowledge about the description of superfluids and condensates is assumed: basic notions can be found in the seminal paper of Anderson on the flow of superfluid ^{4}He (Anderson, 1966). Some of his considerations, like the role of the quantum phase as a dynamical variable, and the way they have evolved over the past half century are recounted by Varoquaux (2015). An introduction to the theoretical description and properties of quantum fluids (more focused on gaseous atomic BEC) is given by Barenghi and Parker (2016).

Figure 0.1: The conjectured phase diagram of QCD [see e.g. Stephanov (2004) for a review]. At low temperatures (below 1 MeV) and for intermediate densities hadronic matter develops nuclear superfluidity comprising condensates of paired nucleons. At even higher densities colour-superconducting and superfluid phase known as color-flavor-locked is expected. The non-color-flavor-locked region is actually unknown but may comprise two-colour-superconducting phases, pion and kaon condensates or crystalline phases, among other possibilities. Relativistic heavy-ion collider experiments explore a region of the phase diagram that is complementary to the cold region of neutron stars.

in NSs is quite established (Hall and Vinen, 1956; Mendell, 1991; Carter, 1989; Prix, 2004) and enables us to model the glitch itself and the subsequent relaxation (Peralta et al., 2006; Haskell et al., 2013; Howitt et al., 2016; Sourie et al., 2016). Moreover, as early proposed by Datta and Alpar (1993), recent calculations have shown that combining the measured *average* glitch activity of the Vela pulsar with state of the art nuclear physics models of the effective mass of superfluid neutrons, can lead to constraints on the mass of the star and on the equation of state of dense matter (Datta and Alpar, 1993; Link et al., 1999; Andersson et al., 2012; Chamel, 2013; Ho et al., 2015; Delsate et al., 2016).

In this dissertation I discuss how observations of the *maximum* glitch occurred in a certain pulsar provides a test for the microscopic physics of neutron star interiors, in particular the pinning forces (a parameter which effectively describes the strength of the vortex-lattice interaction at the mesoscopic scale). Conversely, by fixing the input parameters by taking estimates from recent literature, it is possible to estimate the mass of a glitching pulsar. A proof of concept of this thesis is given by constructing a quantitative model for pulsar rotational dynamics that can consistently encode state of the art models of the pinning force between vortices and ions in the crust, as well as the stratified structure of a neutron star. This point is far from being secondary as most studies on pulsar glitches are based on body-averaged models or differential models that tacitly assume a cylindrical symmetry, not consistent with the spherically layered structure.

The procedure used to estimate pulsar masses can be adapted to more refined dynami-

cal modellization of pulsar rotation, in the hope that current and future observations of glitching pulsars will help astrophysicists to pin down an accepted description of the glitch mechanism itself and the related superfluid properties of dense matter.

The picture outlined indicates a particular aspect of the problem, common to many astrophysical models which aim to be "realistic" or "consistent": the microscopic properties of matter determine the input needed to describe the global dynamics of the whole system (in this case the superfluid neutron star). However, due to the presence of quantized vortex lines, we have to face an additional difficulty: there is also an intermediate scale (the so-called *mesoscopic scale*, in between the microscopic fermi-scale and the centimeter-scale) which is defined by the coherence length of the superfluid. Therefore, the mesoscopic scale ranges from the radius of a vortex core (for which the coherence length provides an estimate) to the typical distance between two vortices l_v, defined as the Wigner-Seitz radius of a two-dimensional array of density $n_v = 4\pi/(\kappa P)$:

$$\pi \, l_v^2 \, = \, n_v^{-1} \qquad \Rightarrow \qquad l_v \, = \, \frac{\sqrt{\kappa \, P}}{2\pi} \, \approx \, 7 \times 10^{-3} \, \sqrt{P} \text{ cm.}$$

In this equation P is the rotational period of the pulsar, measured in seconds, and κ the circulation of a single quantized vortex which permeates the neutron superfluid. Pulsar magneto-rotational dynamics is typically modeled by means of an hydrodynamical approach, well defined only after an average over regions that encompass many inter-vortex spacings l_v is considered (Glampedakis et al., 2011).

After the introductory material, where some background concepts about neutron stars are recalled, contents are divided into three main parts:

Chapter (2) A three-dimensional hydrodynamical simulation of a neutron star interior it is not simple to take into account consistently for stratification, pinning forces and entrainment. Therefore, we show how to implement these fundamental ingredients within a simplified geometry (axially symmetric), as a first natural approximation to the full problem. This part is based on a revised and extended version of the work already published in (Antonelli and Pizzochero, 2017).

Chapter (3) We apply the new simplified (but consistent) model to estimate the maximum angular momentum which can be stored into the region of pinned vorticity. Using state of the art pinning forces of vortex lines in the inner crust we can estimate the theoretical maximum glitch for a pulsar of given mass: comparison with observational data provides a constraint on the pulsar mass, or in a more conservative interpretation, a test for the microscopic inputs. This part consists of a personal presentation of the work already published in (Antonelli and Pizzochero, 2017) and (Pizzochero et al., 2017).

Chapter (4) After a brief review of some basic concepts of relativistic hydrodynamics, the study of the angular momentum reservoir is extended to a general relativistic context. We see that, even though curved spacetime can cause corrections to the moments of inertia from 20% for low mass stars to 50% for high mass stars, the maximum glitch sizes are affected by corrections of the order of $\sim 10\%$, implying that the Newtonian mass constraint are be raised by only few percents. A critical and quantitative revision of the previous Newtonian model is then presented. This part extends the results of Antonelli et al. (2017).

Finally we draw some general conclusion on the work presented: the procedure used to estimate the masses must be refined in order to account for a better dynamical modellization of pulsar rotation: the major unknown is the behavior of vortices (in particular pinning) at the mesoscopic scale. On the other hand, one can always assume microscopic inputs and an hydrodynamical model: in this case the ability to reproduce a broad distribution of pulsar masses that fall in the expected range of 1-2 $M_\odot$ provides a quantitative test for the model itself. The problems underlying the glitch phenomenon are then briefly reviewed and the future directions (like the systematic use of dynamical simulations based on more refined models) are summarized.

Neutron stars: astrophysical background

Neutron stars are classified as compact objects for their exceptional density, responsible for many high-energy phenomena, like glitches, gamma ray bursts but also emission of gravitational waves (by binaries, persistent mountains or oscillation modes of their surface).

The macroscopic characteristics of neutron stars immediately show how much these objects are extreme: measured masses fall around $\sim 1.5\,M_\odot$, but their radius is only $\sim 10^{-5}$ times the Sun's radius. This results in a very high central density which can overcome (up tp ten times) that of nuclear matter at saturation[1], making the inner core of a neutron star the densest object "this side" of an event horizon.

The stabilization of these compact objects due to strong gravity. This allows for long-timescale weak interactions in their interiors (like electron capture): along the path toward thermodynamic equilibrium this generates neutron-rich matter which may have net strangeness[2]. For these hands-off laboratories of extreme physics progress is made by matching observational data to quantitative theory-based models.

Although *pulsars* (PSRs), so named because they are sources of periodic signals of great timing stability, are assumed to comprise the most populous class of neutron stars (NSs), these two terms are *not* equivalent: pulsars are thought [for very good and accepted reasons, as reviewed e.g. by Glendenning (2000)] to be the astronomical manifestations of neutron stars. On the other hand, a neutron star is a successful theoretical model by which we can explain many astronomical phenomena. The current explanation for the pulsar phenomenon is that of a rotating and magnetized neutron star emitting beamed radiation, a cosmic lighthouse which can be observed from Earth only in the fortunate

---

[1] Nuclear matter is said to be at saturation when the minimum of the energy per nucleon is achieved: this can be done for nuclei (where the nuclear force between nucleons saturates very quickly due to its short range) as well as for a bulk of nearly symmetric nuclear matter. In the latter case, saturation is reached for $\rho_0 \approx 2.8 \times 10^{14}\,\mathrm{g/cm^3}$. The corresponding baryon density is $n_0 = \rho_0/m_n \approx 0.0167\,\mathrm{fm^3}$.

[2] The s quark is the second-generation lightest one, after the u and the d: since the nuclear force affects quarks in the same way (regardless of their flavor), replacing one u or d with s in a hadron should not alter its mass (that is almost completely due to gluons) very much. Therefore, when usual nuclear matter is compressed beyond a critical density, baryons can dissociate into quarks, yielding quark matter and strange matter. There is however narrower meaning of the so-called "strange matter hypothesis": quark matter could be more stable than nuclear matter (Witten, 1984), implying that the aforementioned critical density is zero. Following this hypothesis, nuclei (droplets of nuclear matter) are only metastable stares: given enough time, or an opportune external trigger, they would decay into strangelets (droplets of strange matter).

case that the rotating beam sweeps our line of sight. Not all the neutron stars that we know are pulsars[3] (or are detected as pulsars): a famous example is the companion of the Hulse-Taylor pulsar, which pulsation is unobserved. However, from careful study of the orbital motion (thanks to the Doppler shift on timing of pulses from the main star) we know that this invisible partner is required to be very compact, so that it must be a neutron star. Clearly it is still possible that the Earth is not on the cone swept out by the rotation of this claimed neutron star, so that we do not have any chance to observe it as a pulsed source.

It is unlikely that all neutron stars can power such a beamed emission, as it seems both by theoretical reasons and by the fact that we also observe compact objects at the center of a supernova remnant that do not show any of the features of pulsars. Therefore, while pulsars can be considered to be the most evident observational basis of neutron stars, new discoveries tell us that neutron stars can come in many guises, populating the so called *neutron star zoo*.

Given the fact that NSs are observed under such a variety of circumstances, our current understanding of these objects is limited by small-number statistics and uncertain systematics. Nonetheless observational breakthroughs are expected in the next decade as a new generation of facilities (e.g. Advanced LIGO and Virgo for the detection of gravitational waves and the SKA[4] for radio timing surveys) comes into operation and will reach the design sensitivity.

This dissertation is about recent advances in models of *pulsar glitches*, sudden irregularities detected in the precise timing of radio pulsars. The main motivation is that, within the current interpretation, glitches provide us the astronomical clue that rotating and magnetized neutron stars can also develop extended internal regions that are *superfluid*. Few glitches have been discovered also in classes other that radio pulsars, noteworthy an *anti-glitch* in a magnetar, the extremely magnetized version of a pulsar (Archibald et al., 2013). However, due to the fact that full explanation of this phenomenon is still elusive, we will concentrate mainly on the most common realizations of glitches, that are found in the timing of pulses coming from isolated objects, typically detected in the radio band. Unfortunately no glitches have been so far detected in pulsars belonging to a binary system, except for a unique and very small-amplitude event in the accretion-powered pulsar SXP 1062, a high-mass X-ray binary system that consist of a Be star and a NS (Serim et al., 2017).

The scientific knowledge about neutron stars is so vast that is impossible to summarize, as it lies at the intersection of many fields that usually do not touch: nuclear and sub-nuclear physics, plasma physics, strongly-correlated fermion systems and general relativity, not to cite the technical advances that recently pushed astronomy into the new era of multimessenger astronomy[5]. In this chapter, without any purpose of completeness, the main properties of NSs are reviewed.

---

[3] Astrophysical manifestations of neutron stars which are not PSRs are broadly classified by using the acronyms HMXBs, LMXBs, AXPs, SGRs, XDINs and CCOs. A brief description of these phenomena will be given in section (1.4).

[4] The acronyms stand for "Laser Interferometer Gravitational-Wave Observatory" and "Square Kilometer Array". The latter is a large multi radio telescope project aimed to be built in Australia, New Zealand, and South Africa. Its total collecting area of $\sim 1\,\mathrm{km}^2$ will make it ~ 50 times more sensitive than any other operating radio telescope.

[5] Traditionally the telescope is a device that increases the sensitivity of human eye (and thus works in the optical). Today we can consider "telescopes" also radio antennas, X-ray and γ-ray cameras on

1.1 Historical overview: compact stars

Neutron stars existed for a long time only in the form of theoretical speculation. The discovery of the neutron (Chadwick, 1932b) prompted physicists to seriously take into account for the possible existence of a dense stellar object comprised of neutrons[6]. The theoretical concept of compact stars (white dwarfs and neutron stars) is quite recent since quantum mechanics is mandatory. However the first observation of a degenerate object dates back to the 1783, when Herschel discovered two companions of a main sequence star. Today this triple system is known as 40 Eridani (or Keid) and the main sequence star is visible to the naked eye. Only in 1910 it was discovered that 40 Eridani B was of spectral type A (white) despite being a faint star. As reported in the famous book of Shapiro and Teukolsky (1983), the same was found also for Sirius B few years later: the radius of Sirius B (inferred from its luminosity) and its mass (derived from the binary dynamics), suggested its density to be $\sim 10^5$ times higher than that of Sirius A. Confirmation arrived in 1925 thanks to the measurement of the gravitational redshift of Sirius B. Today it is known that like all white dwarfs[7] (WD), Sirius B's low luminosity and high temperature imply a radius that is slightly less than that of the Earth.

In 1926 Fowler used the newly-born theory of quantum mechanics to show that WDs are supported primarily by electron degeneracy pressure [see Chandrasekhar (1984) and references therein]. The Fermi gas model was then used by Stoner (1930) to calculate the relationship among the mass, radius, and density of WDs, assuming them to be homogeneous spheres. Important breakthrough came with a series of works between 1931 and 1935, where the young Chandrasekhar solved the hydrostatic equation together with both non-relativistic and relativistic Fermi gas equation of state. The result was the existence of a maximum mass of $\sim 1.4\,M_\odot$ for stable WDs, the exact value depending on composition of matter. However a rigorous derivation of the early Chandrasekhar semiclassical mass limit is much more recent: starting from the relativistic many-particle Schrödinger equation, Lieb and Yau (1987) have given a method to estimate a mass limit that accounts also for the electrostatic interactions between the electrons and nuclei. A further step in the understanding of WDs occurred when Mestel (1952) showed that the energy radiated is the surviving heat from a prior period of nuclear burning; thus white dwarfs were recognized to be the degenerate remnants of a main sequence star's core, that become exposed during the planetary nebula phase.

On the other hand, the early development of the neutron star theory is generally attributed to Landau: according to Yakovlev et al. (2013) we know that during February 1931 in Copenhagen, Landau, Bohr and Rosenfeld discussed the possible existence of extremely dense stars "similar to a giant nucleus"[8]. In particular Landau (1932) presented a simple explanation of the Chandrasekhar limit and immediately applied his argument to

---

spacecrafts, and interferometers for gravitational waves: on August 17, 2017 astronomers were alerted to the observation of a binary neutron star coalescence candidate (GW170817). It was detected by LIGO and Virgo through gravitational waves less than two seconds before a short gamma-ray burst (GRB170817A) had been reported by the Fermi Space Telescope. For the first time gravitational waves and electromagnetic counterpart (over a wide region of the spectrum) from a single source have been observed. On the other hand, the difficult field of neutrino astronomy is still in its infancy since the only confirmed extraterrestrial sources so far are the Sun and supernova SN 1987A, plus ~ 30 neutrinos that likely originated outside of the Solar System (detected by IceCube).

[6] By 1932 it was not definitively established whether the newly discovered neutron was a new fundamental particle or a proton and an electron bound together (as Rutherford originally suggested).

[7] It seems that the term was coined in the '20s by the dutch-american astronomer Luyten that discovered and cataloged an incredible amount of white dwarfs.

[8]The analogy is imperfect: nuclei are bound thanks to the attractive component of the nuclear force,

NSs as he learned of the discovery of the neutron (Chadwick, 1932a). In the same years
Baade and Zwicky (1934) proposed that in supernova explosions ordinary stars are turned
into dense stars made of neutrons and argued that the release of the gravitational binding
energy of the NS powers the supernova:

> "With all reserve we advance that supernovae represent the transition from ordinary stars
> into neutron stars, which in their final states consist of extremely packed neutrons."

The first correct model of a star formed by free degenerate neutrons in general relativity
(GR) was put forward by Tolman (1939) and Oppenheimer and Volkoff (1939), TOV in
short. Studying the hydrostatic equilibrium of a noninteracting and strongly degenerate
relativistic gas of neutrons (sustained only by degeneracy pressure), TOV estimated the
maximum mass for neutron stars, which was found to be nearly half the $\sim 1.4 M_\odot$ limit
for white dwarfs. It was therefore thought that NSs could not originate from collapsing
WDs, their maximum mass being smaller; this resulted in a puzzling gap in the theory of
stellar evolution. This consideration, together with the small predicted radii (making NS
virtually undetectable) produced a stalemate in the NS theoretical modelling[9].

Little happened till Cameron (1959) recognized that matter in a neutron star was too
compressed to neglect the strong interaction between nucleons: the models based on the
free fermion gas did not seem to be viable anymore. New refined models were computed,
resulting in a maximum mass higher than the Chandrasekhar limit for white dwarfs as
reported by Wheeler (1966) and shown in Fig (1.1).

However, there was still the problem of how to detect neutron stars. The first cooling
calculations predicted surface temperatures $T \sim 10^6$ K for young neutron stars $\sim 10^3$ year
old [see e.g. the photon luminosities associated to the cooling times estimated by Chiu
and Salpeter (1964)]. Therefore the Stefan-Boltzmann law gives that the luminosity L of
a NS of radius $R \sim 10$ km is comparable to that of the Sun[10] $L = 4\pi R^2 \sigma T^4 \sim 10^{33}$ erg/s.
According to Wien's displacement law, emission intensity is peaked at the wavelength
$\lambda = 0.289$ cm K$/T \approx 3$ nm so that thermal emission of a neutron star was expected to be
mainly in the soft X-rays[11]: NSs were not expected to be seen with ground-based facilities
since X-rays cannot penetrate the atmosphere. The first X-ray detectors were launched on
rockets and balloons in the early Sixties but attempts failed to prove the relation between
NSs and newly discovered compact X-ray sources like Sco X-1 (Giacconi et al., 1962).
Now we know that Sco X-1 is an X-ray binary containing an accreting neutron star, as
anticipated by Shklovsky (1967), which argument was nearly ignored at that time:

> "If the identification of the optical object similar to an old nova with the X-ray source
> is correct, then the natural and very efficient supply of gas for such accretion is a
> stream of gas, which flows from a secondary component of a close binary system
> toward the primary component which is a neutron star."

NS are bound because of strong gravity while the short-range repulsion between nucleons supports them.

[9] As discussed by Haensel et al. (2007), Gamow and Landau proposed independently in 1937 that a
possible stellar energy source could be the slow contraction of the outer layers onto a dense neutron core.
However it was shown very soon that stars are powered by thermonuclear reactions, as suggested in the
'20s by Eddington and others. This probably also contributed to the fading interest in neutron stars.

[10] The luminosity of the Sun is $L_\odot = 3.839 \times 10^{33}$ erg/s. We also recall that the mass of the Sun is
$M_\odot = 1.989 \times 10^{33}$ g. In the formula σ is the Stefan-Boltzmann constant $\sigma = \pi^2 k_B^4/(60\hbar^3 c^2)$.

[11] Actually the Magnificent Seven were discovered in the soft X-rays through their purely thermal
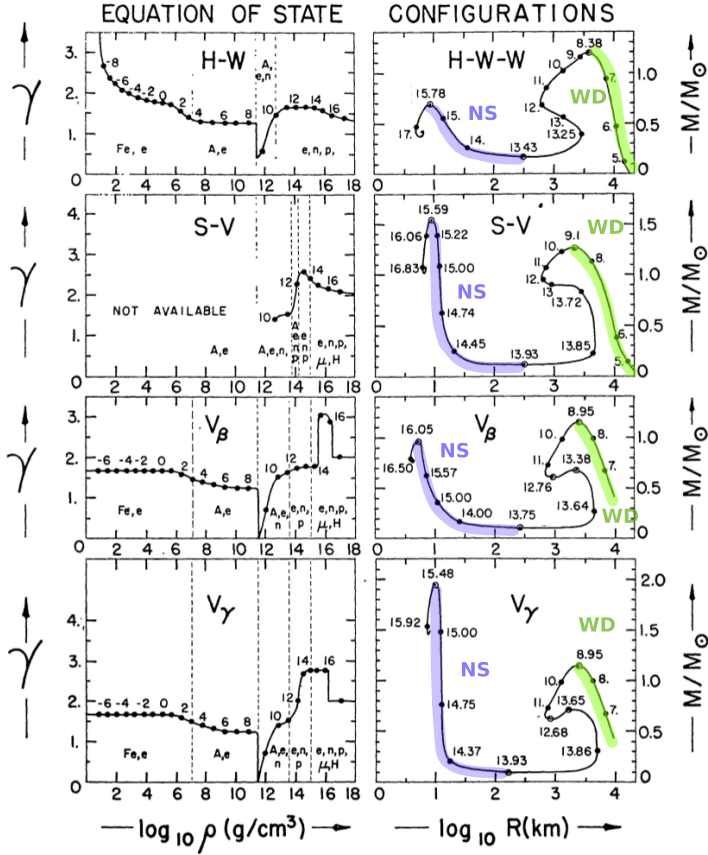surface emission. All seven sources were discovered by the ROSAT satellite (see also Appendix (B)).

Figure 1.1: Equilibrium configurations of compact stars for different early EOSs of the form $P(\rho)$, where ρ is the gravitational mass density (i.e. the total energy density including the rest mass) and P the pressure. Properties have been evaluated under the idealizations of cold and catalyzed matter (i.e. matter at the end point of thermonuclear evolution with $T < 10^8$ ms) that is non-magnetized (the magnetic field is much less than the quantum critical field of 4.4×10^{13} G) and non-rotating. Adapted from the review of Wheeler (1966). *Left* - The relativistic the adiabatic index as a function of density. The curves are parametrized by the values of $\log_{10}(P/c^2)$, where P and c are expressed in cgs units. *Right* - The total gravitational mass (M) versus radius (the Schwarzschild coordinate of surface R) relation given by the TOV equations. Each curve ends up in the left extremity into a spiral that converges to an unphysical configuration of finite M and R but infinite central pressure. The two regions where the configuration is stable against all modes small vibration are colored.
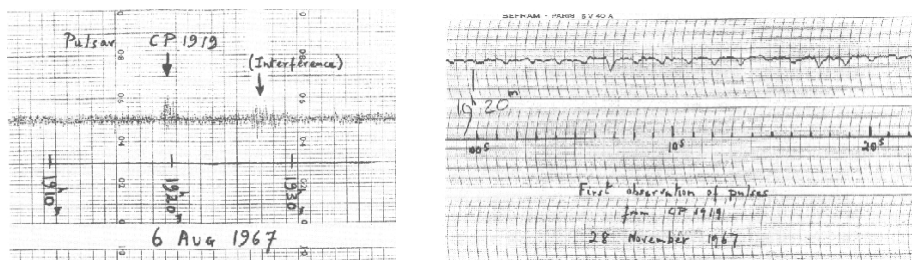
Figure 1.2: The radio signals detected with the Interplanetary Scintillation Array of the Mullard Radio Astronomy Observatory in 1967 that lead to the discovery of pulsars. *Left* - The pulsar CP1919 (today known as B1919+21 or J1921+2153) appeared on the chart record as barely distinguishable from typical interference. *Right* - A subsequent high-speed chart recording (dated 28 November 1967) showed that the scruff was a series of periodic pulses.
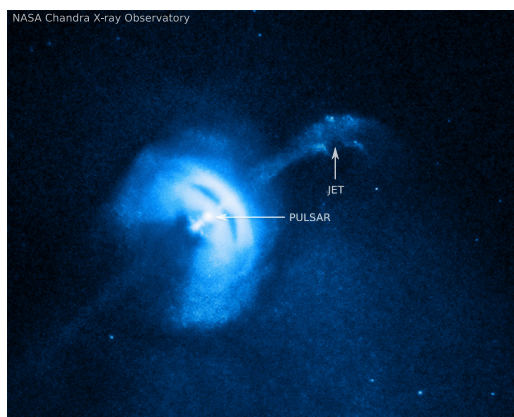

Figure 1.3: X-ray image of the wind nebula around the Vela pulsar (PSR J0835-4510 or B0833-45). Observations with the Chandra satellite led to the discovery of the Vela's outer jet (that extends in the direction of the proper motion of the pulsar). The Vela pulsar is also the brightest persistent object in the gamma-ray sky. Adapted from Durant et al. (2013).

Breakthrough came when Pacini (1967) and Gold (1968) pointed out independently that coherent emission is possible for spinning neutron stars that posses a strong dipolar component of the magnetic field.

Pulsars were discovered in 1967 on chart-records (Fig (1.2)) obtained during a low-frequency survey of extragalactic radio sources: little after the Pacini's article, Jocelyn Bell Burnell observed pulses that originated from a point-like location on the sky (Hewish et al., 1968): the signal in Fig (1.2) was detected at 81.5 MHz (thus in the radio interval of the spectrum), at periodic intervals of 1.337 s and with the average on-state of the pulse lasting ~ 0.3 s. Later it became evident that pulsars were also recorded (but not recognized) few years earlier with the Jodrell Bank telescope: most pulses seen by radio astronomers are artificial interferences, however Bell noticed signals in her scintillation surveys that appeared earlier by about 4 minutes every solar day (i.e. once per sidereal day), thus coming from outside the solar system.

Several explanations were put forward, including that the signals might be generated by another civilization. The short period of these radio emissions eliminated most astrophysical

sources of radiation: accretion on black holes is unlikely to give precise intermittent signals, vibrations of WDs were excluded because of the small period observed[12]. Also the scenario of a vibrating NS was dropped after it was realized that the period was steadily increasing with time (on the contrary normal modes of vibration have definite frequencies).

The decisive piece of evidence for the rotating neutron star model were the discoveries of two higher frequency pulsars; the 89 ms Vela pulsar (Large et al., 1968) and the pulsar at the center of the Crab nebula[13]. Both associated with supernova remnants (Figs (1.3) and (1.4)), they rotate too fast to be binaries or radial pulsations analogous to those in classical Cepheids. In particular the pulsation (or "spin") period P of the Crab was measured by Comella et al. (1969) and appeared to be very short[14], $P = 33.08$ ms: WDs could not sustain such a rapid rotation as they would be dispersed by centrifugal forces[15].

Therefore all the possibilities among observed and hypothetical celestial objects were dropped, except that of a rotating neutron star: in this sense this first detection of a pulsar is widely accepted also to be the first observational confirmation of the existence of neutron stars.

After exactly 50 years from the discovery of Bell and Hewish more than two thousand NSs have been discovered, the vast majority of which are pulsars. Other classes are also present with tens of members, including magnetars (NSs with strong magnetic field whose emission is likely powered by the magnetic field decay), and thermal isolated neutron stars (NS with a weak magnetic field and purely thermal spectrum). All these classes populate different regions of the so-called $P - \dot{P}$ diagram, shown in the left panel of Fig (1.5).

Thanks to Chandra and XMM-Newton satellites several sub-classes of isolated neutron stars were discovered during the last decades: Anomalous X-ray Pulsars (AXPs), Soft Gamma Repeaters (SGRs), Rotating Radio Transients (RRATs), X-ray Dim Isolated Neutron stars (XDINSs, also known as the Magnificent Seven), and Central Compact Objects (CCOs) like the famous Cassiopeia A (Fig (1.6)). One of the aims of on-going astrophysical research is to unify all the astronomical classes of sources by considering them as manifestations of neutron stars at different evolutionary stages. Hypothesis for a unification picture have been proposed; for instance a refined modellization of magneto-thermal evolution (in which spin evolution, cooling and magnetic field decay are intimately linked) may establish the evolutionary links between these families, as show in the right panel of Fig (1.5).

---

[12] The period of gravity-modes should be of the order of the free-fall timescale $\sim (G\rho)^{-1/2}$ for an object with typical density ρ.

[13] The discovery of the Crab pulsar in the remnant of SN-1054 (observed by the chinese in 1054 A.D. and distant 6500 light-years from Earth) also confirmed the link to supernovae. Early X-ray observations aimed also to detect the activity of a possible remnant of this supernova. X-ray activity was measured but not directly from the central NS that is hidden within the very luminous plerion nebula, powered by pulsar wind: the decrease in rotational kinetic energy of the Crab $4\pi^2 I_{\mathrm{Crab}} P^{-3} \dot{P}$ matches the measured luminosity of the nebula $L_{\mathrm{Crab}} \approx 5 \times 10^{38}$erg/s if the moment of inertia of the pulsar is of the order $I_{\mathrm{Crab}} \sim 10^{45}$ g cm^2, which is indeed the case for a typical NS.

[14] According to the ATNF pulsar catalogue, the Crab pulsar (known also as B0531+21 or J0534+2200) has a rotational period of $P = 0.0333924123$ s and a spin down rate $\dot{P} = 4.20972 \times 10^{-13}$ s/s.

[15] A crude estimate of the maximum allowed angular velocity for neutron stars Ω_{max} (above which the star sheds mass at the equator) is given by considering the angular velocity Ω_K of a particle in a circular Keplerian orbit at the equator, i.e. $\Omega_K = (GM/R^3)^{1/2}$. With an accuracy of 7% we have that $\Omega_{max} \approx 0.67 \Omega_K$, where the Keplerian angular velocity is calculated by considering $M = M_{max}$ and $R = R_{max}$, the mass and radius of the most massive non-rotating relativistic configuration (Friedman, 1990). The Keplerian velocity for a NS with $M = M_\odot$ and $R = 10^6$ cm turns out to be $\Omega_K \approx 10^4$ rad/s and the corresponding equatorial velocity is $\Omega_K R \approx 0.38 c$. A WD with the same mass and $R = 6 \times 10^8$ cm gives $\Omega_K \approx 0.8$ rad/s and $\Omega_K R \approx 0.02 c$.
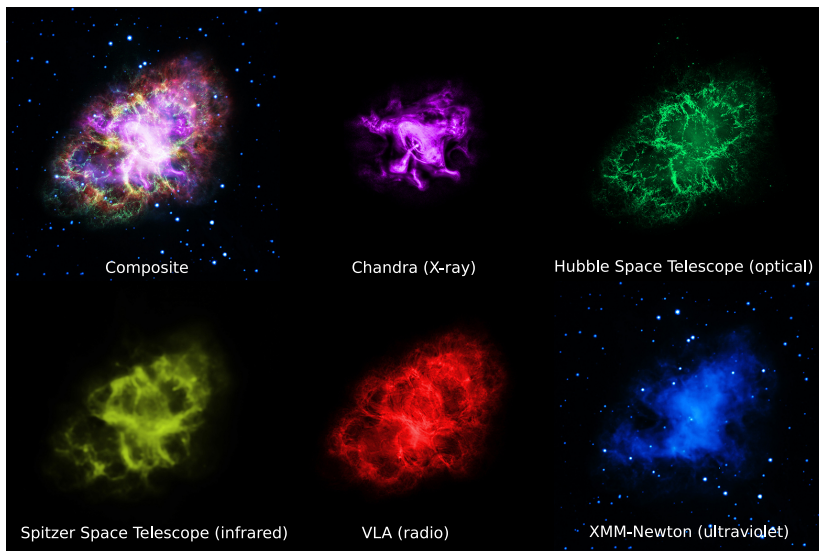
Figure 1.4: The Crab Nebula as seen by combining data from five different telescopes that span nearly the entire breadth of the spectrum. X-ray image gives a clear view of the pulsar wind nebula powered by the neutron star (white dot near the center). Jets moving away from the north and south poles of the pulsar are clearly visible. Intense wind is flowing out in the equatorial direction: the inner ring is a shock wave that marks the boundary between the surrounding nebula and the flow from the pulsar. Energetic electrons and positrons move outward from this ring to brighten the outer ring and produce extended X-ray glow. The same can be seen, less clearly, in the ultraviolet. Adapted from Dubner et al. (2017).

Starting from the Seventies NS gained importance also as test-beds of gravitation[16]. Hulse and Taylor (1975) discovered PSR B1913+16 at Arecibo, the first binary system consisting of two neutron stars (one seen as a pulsar) orbiting around their center of mass. Thirty years of subsequent observations have enabled to measure numerous relativistic phenomena: massive objects in short binary orbits emit gravitational waves, implying that their orbit shrinks with time. This was indeed observed in precise agreement with GR, thus providing the first indirect observation of gravitational waves [see e.g. Taylor and Weisberg (1982)].

The only double pulsar, a NS-NS system where both components are detectable as pulsars, known to date is PSR J0737-3039 (Burgay et al., 2003). The 2.5 hours orbital period of J0737-3039[17] is the shortest yet known for such an object, only one-third that of the Taylor-Hulse one. This enabled Kramer et al. (2006) to measure six post-Keplerian parameters and to perform five different tests of general relativity, some of these with the unprecedented precision of 0.05%.

As said, the rotation period of neutron stars is incredibly stable; in particular millisecond pulsars (MSPs, that are thought to comprise the $\sim 15\%$ of the entire pulsar population)

---

[16] To give a feeling of how much relativistic effects can be pronounced in compact binaries, it is worth to mention that the pulsar's periastron in PSR 1913+16 advances every day by the same amount as Mercury's perihelion advances in a century.

[17] It seems that the double pulsar evolved from a system where the older NS was spun up to its current period of 23 ms by accretion from its binary companion. The companion imploded, leaving a 2.8 s pulsar as remnant [see (Piran and Shaviv, 2005) for further discussion of this scenario].

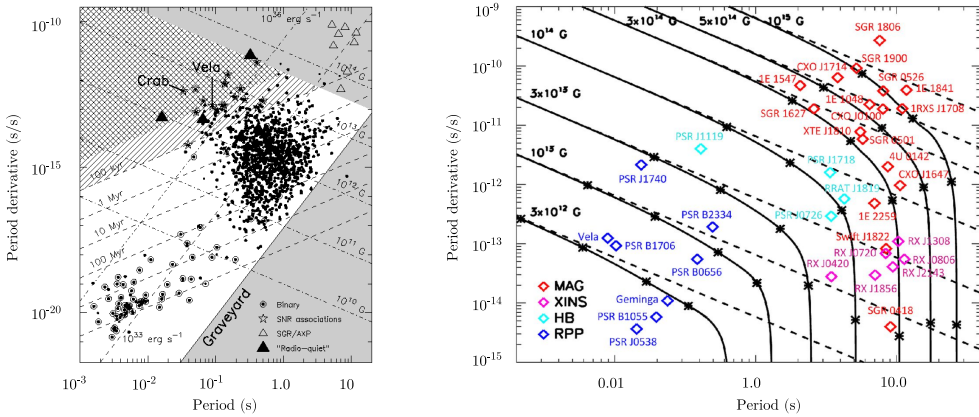**Figure 1.5:** The P-$\dot{P}$ diagram plays a role similar to the Hertzsprung-Russell diagram for classical stars; it encodes important information (like the pulsar age, magnetic field strength, and spin-down power) about the pulsar population. *Left* - The famous diagram adapted from Lorimer and Kramer (2004). The death-line corresponds to neutron stars with sufficiently low magnetic field and high period that the curvature radiation near the polar surface is no longer capable of generating particle cascades: neutron stars can thus exist in this part of the diagram, but a re unlikely to be detected. *Right* - Evolutionary tracks in the diagram with mass for different magnetic fields. Asterisks mark the real ages of 10^3, 10^4, 10^5, 5×10^5 yr, while dashed lines show the tracks followed in absence of magnetic field decay. As a pulsar ages, it moves from left to the right on the diagram. At, a certain point in its evolution, the pulsar can cross the line into the graveyard. Adapted from Viganò et al. (2013).
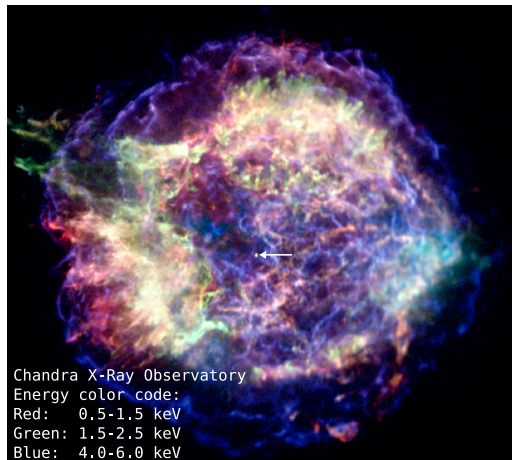

Figure 1.6: X-ray image of the Cassiopeia nebula taken with the Chandra X-Ray Observatory satellite, one of the most detailed image ever made of an exploded star. The CCO, known as Cassiopeia A, is the white dot in the center indicated by the arrow. Unlike the Crab and the Vela that are surrounded by pulsar wind nebulae, Cas-A is faint and shows no pulsed radiation. The image is color coded for energy. The outer ring (blue) is ten light years in diameter and marks the location of a shock wave generated by the supernova. A jet-like structure that extends beyond the shock can be seen in the upper left. Adapted from `chandra.harvard.edu`.
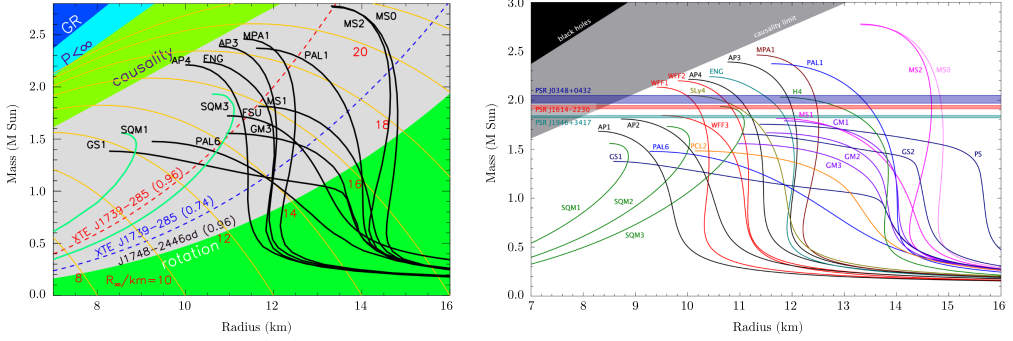
Figure 1.7: Two examples of the mass radius diagram for NSs, i.e. the recent version of Fig (1.1) made with more realistic EOSs. *Left* - Green curves: self-bound quark stars. Orange lines: contours of constant radiation radius $R_\infty = R(1 - 2GM/Rc^2)^{-1/2}$. The region $R < 2GM/c^2$ is excluded by the GR constraint, $R < 9GM/(4c^2)$ by the finite pressure constraint and $R < 2.9\,GM/c^2$ is excluded by the causality limit (the sound speed at large densities in quark matter tends to $c_s^2 = 1/3$ because of asymptotic freedom and, in general, is always less than c in an interacting gas). The lower green region is bounded by the realistic mass-shedding limit for J1748-2446ad. Adapted from (Lattimer and Prakash, 2007). *Right* - The horizontal bands show the observational constraint from the mass measurement of J1614-2230 and from similar measurements for two other millisecond pulsar. Most EOS curves involving exotic matter do not intersect the J1614-2230 band and are therefore ruled out. Adapted from (Demorest et al., 2010).

provide us a stability comparable to that of the best atomic clocks (Hobbs et al., 2012): since the level of intrinsic period irregularities is related to the spin-down rate and MSPs have $\dot{P}$ values about five orders of magnitude less than normal pulsars, these objects are perfect clocks and suitable tools for detecting the stochastic gravitational waves background by using a Pulsar Timing Array[18]. Moreover tiny perturbations to their period resulting from relativistic effects in a binary orbit, can be detected. Many theories other than GR are effectively ruled out or at least severely constrained by these results [see Manchester (2015) for a review]. Backer et al. (1982) detected the first millisecond pulsar PSR B1937+21. This object spins 642 times per second, a value that placed fundamental constraints on the mass and radius of neutron stars, as shown in Fig (1.7).

Two hundred millisecond pulsars have been cataloged to date, but PSR B1937+21 remained the fastest-spinning known pulsar for 24 years, until PSR J1748-2446ad (which spins at 716 Hz, implying an equatorial velocity of about $\lesssim 0.25\,c$) was discovered (Hessels et al., 2006).

If pulsar timing can be used to test general relativity and possibly to detect the stochastic gravitational wave background, mass measurements of neutron stars can severely constrain microscopic modellization of dense matter. Demorest et al. (2010) measured the mass of the millisecond pulsar J1614-2230 to be $1.97 \pm 0.04\,M_\odot$ by using Shapiro delay, Fig. (1.8). This value is substantially higher than any previously measured neutron star mass, namely the $1.67\,M_\odot$ of PSR J1903+0327, and places strong constraints on the

---

[18] The main target of the PTA experiment is the detection of the stochastic and isotropic gravitational wave background. Such a signal induces low frequency noise in the pulse time-of-arrival (TOA) of a pulsar, that is correlated between pulsars pairs on the basis of a theoretically derived function. The detection will thus be achieved by searching for this particular signature in the correlation of the TOAs between pairs of pulsars
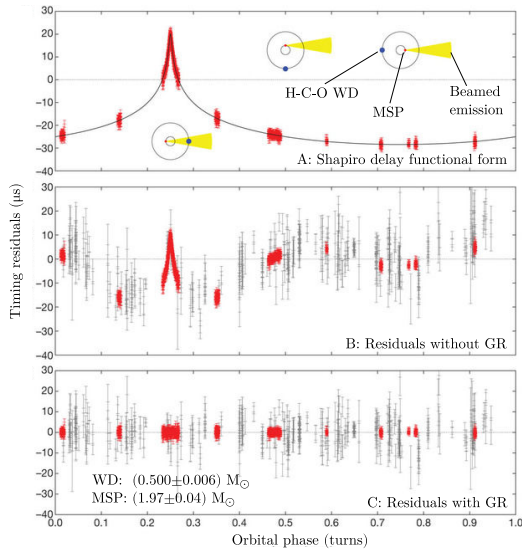
Figure 1.8: The Shapiro delay measurement for J1614-2230. For highly inclined (nearly edge-on) binary systems containing a millisecond radio pulsar, Shapiro delay allows to infer the masses of both the NS and its companion. Each panel shows timing residuals as a function of the pulsar orbital phase. *A* - Excess delay not accounted for by the timing model, the solid line shows the Shapiro delay functional form. The maximum delay of the time of arrival of the pulses corresponds to the peak, occurring when the pulsar is hidden behind the companion (as can be seen in the inserted top-down view of the binary system). *B* - Best-fit residuals obtained using an orbital model that does not account for GR: significant deviation from a Gaussian distribution of zero mean indicates that the Shapiro delay must be included to model the pulse arrival. *C* - The post-fit residuals for the fully relativistic timing model (including Shapiro delay). Adapted from Demorest et al. (2010).

interior composition of neutron stars.

Another striking mass measurement was made by Antoniadis et al. (2013): phase-resolved optical spectroscopy of its WD companion allowed to extract the orbital parameters of the binary system and the mass of PSR J0348+0432 turned out to be $2.01 \pm 0.04 \, M_\odot$. This confirmed (using a different technique) the existence of very massive NSs.

In this brief survey some important aspects were skipped: in particular the claimed observation of fast cooling of Cassiopeia A that, together with pulsar glitches, is one of the probes of nuclear superfluidity, theoretically anticipated by Migdal (1959). These concepts will be recalled when needed. Much more information about the historical development of the theoretical understanding and astronomical observations of neutron stars can be found in Haensel et al. (2007), Glendenning (2000) and Yakovlev et al. (2013).

1.2 Neutron stars formation

Compact objects are the ashes of stellar cores after a lifetime of nuclear burning that can last 10^6-10^{12} yr, depending on mass and composition. During the main sequence part of their lives, stars evolve trough a continuum of quasi-equilibrium phases, driven by the competition between gravity and the pressure of matter. Compression induced by gravity
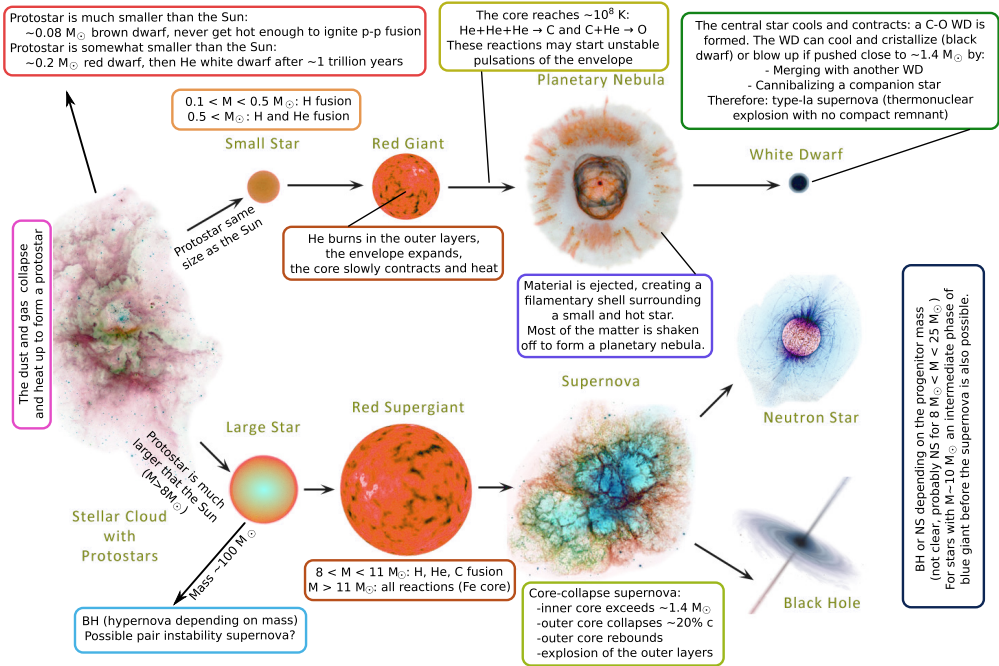
Protostar is much smaller than the Sun:
~0.08 $M_\odot$ brown dwarf, never get hot enough to ignite p-p fusion
Protostar is somewhat smaller than the Sun:
~0.2 $M_\odot$ red dwarf, then He white dwarf after ~1 trillion years

The core reaches ~10^8 K:
He+He+He → C and C+He → O
These reactions may start unstable
pulsations of the envelope

The central star cools and contracts: a C-O WD is
formed. The WD can cool and cristallize (black
dwarf) or blow up if pushed close to ~1.4 $M_\odot$ by:
- Merging with another WD
- Cannibalizing a companion star
Therefore: type-Ia supernova (thermonuclear
explosion with no compact remnant)

$0.1 < M < 0.5$ $M_\odot$: H fusion
$0.5 < M_\odot$: H and He fusion

Small Star   **Red Giant**

Planetary Nebula

White Dwarf

The dust and gas collapse
and heat up to form a protostar

Protostar same
size as the Sun

He burns in the outer layers,
the envelope expands,
the core slowly contracts and heat

Material is ejected, creating a
filamentary shell surrounding
a small and hot star.
Most of the matter is shaken
off to form a planetary nebula.

Supernova

Neutron Star

BH or NS depending on the progenitor mass
(not clear, probably NS for 8 $M_\odot$ < M < 25 $M_\odot$)
For stars with M~10 $M_\odot$ an intermediate phase of
blue giant before the supernova is also possible.

**Stellar Cloud
with
Protostars**

Protostar is much
larger that the Sun
(M>8$M_\odot$)

Large Star   **Red Supergiant**

Mass ~100 $M_\odot$

$8 < M < 11$ $M_\odot$: H, He, C fusion
M > 11 $M_\odot$: all reactions (Fe core)

Core-collapse supernova:
-inner core exceeds ~1.4 $M_\odot$
-outer core collapses ~20% c
-outer core rebounds
-explosion of the outer layers

Black Hole

BH (hypernova depending on mass)
Possible pair instability supernova?

Figure 1.9: Cartoon of the stellar evolution: the initial mass, composition and the possible presence of a companion determine the fate of a star. NSs are formed in core-collapse supernovae when a massive progenitor successfully sheds its stellar mantle during the explosion (O'Connor and Ott, 2011). The mass values reported as thresholds for the various processes are only indicative (different models provide different mass thresholds). It is expected that for $M < 15M_\odot$ a NS is formed, whereas stars with $M > 50M_\odot$ will die as BHs. Extremely massive stars may make pair-instability SN (still hypothetical) without leaving any remnant. The idea of a mass threshold that discriminates between BHs and NSs formation is currently debated: the outcome is though to depend mainly on the compactness of the core before the collapse, a non monotonic function of the stellar mass parameter, so that the scenario for stars with $15M_\odot < M < 50M_\odot$ is very uncertain (Sukhbold et al., 2016).

acts as a natural feedback mechanism for heating matter, thus allowing to ignite new thermonuclear reactions as the star chemically evolves. Thermal agitation provides the energy for tunneling the Coulomb barrier and exothermic nuclear fusion is possible (up to iron). This luminous part of a star's life can be considered as a "suspended collapse": the opacity of the gas increases with its density, creating temperature, composition and pressure gradients, the latter balancing almost exactly gravity. The little amount of energy that is lost by radiation through the stellar surface allows for further slow contraction[19]. This can last for millions of years, with a timescale that roughly scales with the inverse square of mass (Glendenning, 2000): gravity propels small stars at a much lower rate than large stars.

The detailed global picture of stellar population synthesis is still developing, however it

---

[19] A nice example of the so-called Kelvin-Helmholtz contraction (in the absence of exothermic reactions) is the cooling of Jupiter. It is estimated that Jupiter shrinks by two centimeters per year and radiates more energy trough this mechanism than it receives from the Sun: the virial theorem tells us that every year "one centimeter" is used to heat the interior, the other one is radiated through Jupiter's surface.

is possible to sketch a simplified cartoon of the main pathways that end with the creation of a compact object (Fig (1.9)). Neutron stars are the end points of evolved stars whose inert core's mass is greater than the upper mass limit for WDs: they form in core-collapse supernovae[20], the violent release of a fraction of the gravitational energy gained by the collapsed solar mass core. The gravitational binding energy of a neutron star is about the 10% of its mass, making the release of this binding energy an order of magnitude greater than the energy produced by nuclear fusion during the entire life of the star[21].

In massive stars[22] successive steps of core contractions increase the internal temperature, triggering the burning of carbon, neon, oxygen and silicon in a sequence that is increasingly faster. Stratified shells of nuclear ashes are left behind, with iron and nickel (which have the largest binding energy per nucleon) that deposit on an inert and nearly isothermal core supported by degenerate and relativistic electrons. When this catalyzed core approaches the Chandrasekhar limit, the core starts to contract and its temperature can increase till $\sim 10^9$ K; since electrons are relativistic, the pressure they provide increases less rapidly with density than in the non-relativistic case and the core can implode. When the temperature is about 3×10^9 K, the endothermic photo-disintegration of nuclei by thermal photons further destabilize matter and the collapse proceeds almost as a free-fall: in particular disintegration of ^{56}Fe into He

$$^{56}\text{Fe} + \gamma \rightarrow 13\,^4\text{He} + 4\,n \tag{1.1}$$

adsorbs energy very efficiently. At higher temperatures, also helium nuclei get photo-dissociated as well[23]

$$^4\text{He} + \gamma \rightarrow 2\,n + 2\,p. \tag{1.2}$$

Another important reaction is the inverse β-decay. Usually electron captures cannot take place if electrons are not highly relativistic: the 1.3 MeV rest mass difference between the neutron and the proton, well above the electron rest mass 0.5 MeV. In the collapsing core, however, electrons are degenerate, so with the increasing density also their Fermi energy rises. Therefore both nuclei and free protons continuously undergo inverse β-decay

$$(Z, A) + e^- \rightarrow (Z - 1, A) + \nu_e$$
$$p + e^- \rightarrow n + \nu_e \,.$$

---
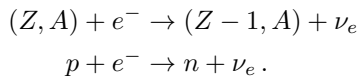
[20] Core-collapse SNe are cataloged as type-II, Ib (missing hydrogen features in the spectrum) and Ic (missing also helium features). The more stripping happened to the star, the more is likely go from type-II to Ib and then to Ic. For single stars the only way to strip is through winds; since massive stars have stronger winds, a $\sim 20\,M_\odot$ star will make a type-II SN whereas a $\sim 40 M_\odot$ star will probably undergo a Ib or Ic. For binaries this is more complicated because stripping can occur by mass transfer onto a companion, a less mass dependent process compared to winds.

[21] In a typical neutron star of mass M the binding energy is of the order $\sim 0.1\,Mc^2$, i.e. ~ 100 MeV per nucleons. This should be compared with the nuclear binding energy of 9 MeV per nucleon in a Fe nucleus, only the one percent of the ~ 1 GeV nucleon mass. The reason for why the weakest known force can bind matter more than the strong force lies in their different ranges: the nuclear force is mediated by massive bosons and has finite range but every particle in a star interacts gravitationally with all the others (Glendenning, 2000).

[22] A massive star is by definition a star that will undergo core-collapse. The actual limiting lower range is $8 \pm 1\,M_\odot$; beyond this mass core-collapse of the iron core is inevitable (Smartt, 2009).

[23] The Q-values for these two endothermic processes are $c^2(13m_{He} + 4m_n - m_{Fe}) \approx 124$MeV and $c^2(2m_p + 2m_n - m_{He}) \approx 24$MeV. Photo-dissociation is thus a very efficient way to trigger the free-fall collapse of the core. The free fall timescales depends only on the density $\sim 10^9$ g/cm^3 and is of the order of a millisecond.
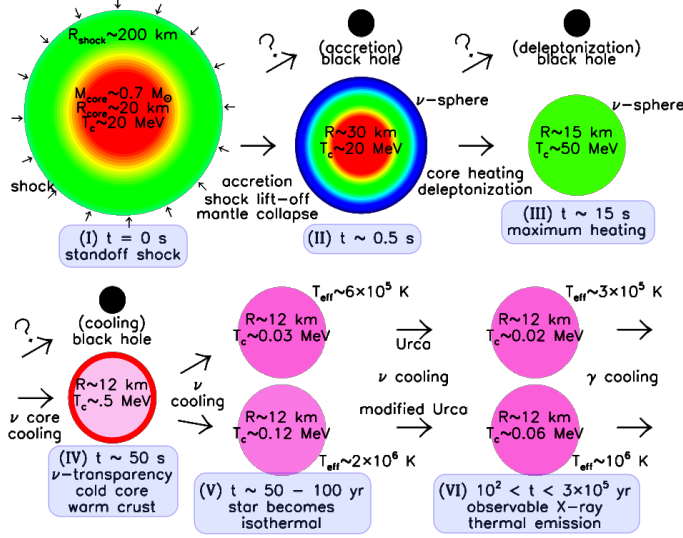
Figure 1.10: The main stages of evolution of a neutron star. In passing from the fifth to the sixth stage the two possibilities of fast (Urca) and slow (modified Urca) cooling are taken into account. Adapted from Lattimer and Prakash (2007).

Consequently the number of free neutrons grows; their degeneracy pressure can start to partially balance gravity. The collapse eventually stops thanks to the short-range repulsive component of the nuclear force, when a density comparable to that of an atomic nucleus is reached; infalling matter rebounds on the stiffened core and a shock wave originates somewhere in the outer part of the neutron rich core. However the shock wave is not strong enough to blast away the outer layers[24]: the shock loses energy by dissociating heavy elements nearby the core, and stalls at a distance of few hundreds kilometers, as shown in Fig (1.10). During these processes the central density increases up to the point that a fraction of neutrons drips out the nuclei and forms a degenerate fermion gas. At densities $10^{14}\,\mathrm{g/cm^3}$, the nuclei are almost completely dissolved into homogeneous nuclear matter mostly composed by neutrons. If the mass of the progenitor core is not too large, the pressure provided by the nucleons is finally enough to halt the collapse. This compact inner core is a hot ($T \sim 10^{11}\,\mathrm{K}$, equivalent to tens of MeV) and neutron rich *proto-neutron star*, a very dynamical object with a radius of $\sim 20\,\mathrm{km}$ that evolves in few seconds. In this early stage, the proto-neutron star is extremely opaque and bloated with energetic neutrinos produced in the continued neutronization. At these energies, the cross-section of the nuclei-neutrino interaction (that scales as the square of the mean neutrino energy) is large enough to trap them, meaning that the mean free path of a neutrino is less than the radius of the proto-neutron star. During this phase neutrinos can only escape by diffusion, a relatively slow process if compared with the timescales of the collapse. They diffuse out during the first tens of seconds (stages II and III in Fig (1.10)).

As matter gets enriched in neutrons, neutrinos are copiously produced and drain energy from inside on the diffusion timescale: the initially opaque proto-neutron star,

---

[24] Once the collapse of the core is triggered, a decompression wave travels outside the red giant at the speed of sound, diffusing the outer layers. However this sonic signal is very slow compared to the free-fall timescales of the imploding core and to the subsequent shock produced by the rebound.

with a temperature of tens of MeV, looses its trapped neutrinos (deleptonization) over an interval of some seconds and cools to about $1\,\mathrm{MeV}$ or less. The final chemical equilibrium is then reached and the newly-born neutron star cools down to $\sim 10^9\mathrm{K}$ within days. During the subsequent weeks or months, the outer layers crystallize due to the repulsive Coulomb forces between the neutron-rich ions. As the temperature decreases, the neutrino emission processes can become less efficient, but they still govern the cooling during the first $10^4 - 10^5$ yr. Only when the inner temperature goes below $\sim 10^8\mathrm{K}$ in mature neutron stars, the photon emission from the surface becomes the main cause of cooling.

In some cases the proto-neutron star might not survive its early evolution, collapsing instead into a black hole. The first scenario is that proto-neutron stars can accrete mass fallen through the shock. If the maximum mass is exceeded, the star collapses and the neutrino signal abruptly ceases. Alternatively, since the progenitor has enhanced maximum sustainable mass (thanks to extra leptons and thermal energy) with respect to cold neutron stars, black holes can be created just because of deleptonization, cooling or spin-down of the proto-neutron star. Within this scenario, the proto-neutron star is born with a mass greater than that of the cold neutron star that is going to generate, undergoing a collapse to black hole that is delayed with respect to the first case by $\sim 20\,\mathrm{s}$, a timescale settled by the neutrino diffusion time. This second scenario could explain why in SN 1987A no compact remnant has been observed, while the $\sim 10\,\mathrm{s}$ duration of the detected neutrino signal confirmed at least the birth of a proto-neutron star (Burrows and Lattimer, 1987). Of course, a supernova is not necessarily a spherically symmetric phenomenon: because of this, neutron stars can acquire a high proper motion, as Vela (Fig (1.3)). A kicked pulsar is another of the hypotheses why the neutron star of SN 1987A has not been observed.

Study of supernovae is an active and complex field of modern astrophysics and the detailed mechanism that enhances the explosion is not well understood, as reviewed by Woosley and Janka (2005). It seems that the pure rebound of infalling matter cannot power the supernova and that neutrino transport is essential(Bethe and Wilson, 1985). The free-falling material abruptly breaks as it meets the stalled shock, turning it into an accretion shock where huge amount of heat is produced; thus a rarefied bubble region develops in between the core and the accretion front. Here the neutrino pairs, which have diffused from the core, can annihilate, powering the expanding bubbles which, in turn, can transfer the gravitational binding energy gained by the core to the accretion front. Symmetry also plays a fundamental role: 1D simulations (spherical symmetry) create rarefied bubbles that are concentric shells, while 2D simulations (axisymmetric) produce toroidal bubbles; in 3D simulations turbulence destroys any symmetry of the flow, resulting in a delayed explosion with respect to the 2D case (Müller, 2017).

1.3 Neutron star cooling

The theory of neutron star cooling was motivated by the first evidence of X-ray emission from the surface of NSs in the Sixties (Chiu and Salpeter, 1964) and is reviewed by Page et al. (2006) and Yakovlev et al. (2005).

Once formed, the newly born NS cools down during its neutrino-transparent era. The core rapidly cools via neutrino emission, while the temperature of the thermally decoupled crust remains nearly constant, at least for the first $\sim 10^5$ yr. A cooling wave slowly travels from the core to the surface, bringing the NS interior to a nearly isothermal state (this relaxation time can take ~ 10-100 yr, see stage V in Fig (1.10)); thanks to the high thermal conductivity of degenerate matter, NSs older than some decades are though to have an

almost uniform internal temperature, except within an envelope that acts as an insulating blanket in between the hot interior and the colder surface.

The fast or slow rate of cooling in young as well as in mature NSs is intimately linked to the reactions that produce neutrinos [the total neutrino emissivity is dominated by processes that occur in the core (Yakovlev and Levenfish, 1995)], like the fast direct Urca and the modified Urca [for a table of the relevant processes and their dependence on temperature see e.g. Page et al. (2013)]. Where direct Urca is forbidden at low temperatures, the modified Urca can still operate, as advantage is taken of a neighboring nucleon in the medium to guarantee the momentum conservation: five degenerate particles participate in this kind of reaction, making modified Urca a less efficient channel for neutrino creation.

Indeed NSs cooling is far from being linear and is realized via two main channels: by neutrino emission from the entire stellar body and by transport of heat from the interior to the surface, resulting in the thermal emission of photons. Therefore the long-term thermal history of a NS is mainly determined by the neutrino luminosity and by the heat capacity of the core, as well as by the composition (i.e. the thermal conductivity) of the outer layers, which control the photon emission. The main open issues concern the presence of hyperons, meson condensates, superfluidity and superconductivity which strongly affect the neutrino production rate; possible use of cooling observations to constrain the internal equation of state and superfluid properties is summarized by Lattimer and Prakash (2007).

Only when temperature reaches values of the order $\sim 5 \times 10^7$ K, the neutrino emissivities start to be irrelevant and the photons radiated from the surface become the main cooling channel of the so-called photon-cooling era. The overall time that NSs remain visible is not yet know but some cooling scenario were proposed so far.

Standard cooling scenario - It's a relatively slow cooling, in which the dominant neutrino processes are the neutron and proton branches ($N = n$ and $N = p$) of the modified Urca processes

$$N + n \rightarrow N + p + e + \bar{\nu}\,, \qquad N + p + e \rightarrow N + n + \nu\,.$$

However, neutrino production can be boosted if the proton fraction is large, or in the presence of exotic matter like hyperons, kaons or deconfined quarks, which would switch on the direct Urca processes. In this scenario, the total emissivity is dominated by slow processes in the core, such as modified Urca and the many realizations of bremsstrahlung[25].

Minimal cooling scenario - In this restrictive scenario all the possible fast neutrino emission processes (from direct Urca involving baryons or exotic matter) are excluded a priori. This basic assumption is justified since the enhanced neutrino emission processes are quickly quenched by superfluidity or superconductivity. The neutrino emission and specific heat are indeed exponentially suppressed by superfluidity when $T \ll \Delta$, where β is the inverse temperature and Δ is the pairing gap of the superfluid phase (roughly the energy needed to break a Cooper pair). However in the early life of the neutron

---

[25] Bremsstrahlung differs from modified Urca processes in that it results in the production of a $\nu\bar{\nu}$ pair which can have any flavor. The typical process has the form $N_1 + N_2 \rightarrow N_1 + N_2 + \nu + \bar{\nu}$, where N_1 and N_2 are both nucleons, or $p + e \rightarrow p + e + \nu + \bar{\nu}$. The presence of strong magnetic field opens a new channel, in which neutrino pairs can be produced by electrons $e + e \rightarrow e + e + \nu + \bar{\nu}$ (Aguilera et al., 2008). Although bremsstrahlung reactions generally turn out to be less efficient than the modified Urca, they still can make important contributions in the case that the Urca processes are suppressed by pairing.

star, when the temperature $\beta^{-1} \approx \Delta$ and matter undergoes a phase transition to a superfluid state, the fluctuations in the number of Cooper pairs can enhance neutrino cooling: as the young neutron star cools below the transition temperature, fluctuations in the number of paired nucleons can lead to a burst of neutrino emission (Page et al., 2013).

Calculations of the detailed cooling scenarios have to be contrasted with the data of neutron stars of known age and effective temperature which have not been reheated by accretion[26]. In a cooling simulation, the evolution of the temperature profile in the star is followed, staring from some initial data after the early thermal relaxation. Thermal radiation from isolated neutron stars, among which Crab and Vela, has indeed been observed but the extraction of the thermal component from the measured spectra is complicated and debated. For example, processes in the magnetosphere of young pulsars $\sim 10^3$ yr old result in strong non-thermal emission that is likely to bury the thermal emission. On the other hand, in older objects of age $\sim 10^6$ yr the radiation from hot polar spots can be stronger than the thermal radiation from the colder rest of the stellar surface[27]. Moreover observations of cooling NSs are restricted to measuring the individual temperatures at one point in time. As NSs may differ in their masses, envelope and magnetic fields, only a measurement of the cooling rate of a young NS can determine its cooling trajectory, making comparison between cooling simulations and astronomical data is not simple in principle.

The cooling trajectory has been resolved, up to date, only for the neutron star in Cassiopeia A (Fig (1.6)). This remnant is associated to the historical supernova SN 1680 and soft X-ray spectrum indicates a surface temperature of $\sim 10^6$ K; therefore the age of Cas A is precisely determined, making it the youngest neutron star known in the Milky Way. Analysis of nearly a decade of archival data reported that the surface temperature of Cas A has rapidly decreased from 2.12×10^6 to 2.04×10^6 K (Andersson et al., 2010), a cooling rate which is significantly larger (by a factor of ten) than expected from the standard cooling scenario. Such a fast cooing must be a transitory event that can be explained by invoking transition of internal layers to a superfluid state and the subsequent enhanced neutrino cooling due to Cooper pair fluctuations; moreover the onset of this fast cooling transient should be recent as, on the contrary, the star wold be so cold to be now unobservable.

The numerical simulation of realistic cooling scenarios is also of great interest for neutron star population unification, where the magnetic fields can strongly modify the cooling curves: application of refined magneto-thermal 2D simulations have been recently used by Viganò et al. (2013) to propose a unified interpretation of the neutron star zoo (Fig (1.5)).

---

[26] It is fundamental to properly take into account for effects of general relativity when interpreting observational data and in simulations as well. Since the source is a very compact object, the observations have to be corrected for redshift, by considering the apparent effective temperature, radius and luminosity, as detected by a distant observer (Shapiro and Teukolsky, 1983), usually indicated by T_∞, R_∞ and $L_\infty = 4\pi R_\infty^2 \sigma T_\infty^4$ (see also Fig (1.7)). The distance of the neutron star (necessary to estimate the luminosity from the measured flux of photons) can be deduced either from the radio signal dispersion measure (due to the interstellar medium) or from the distance of an associated supernova remnant.

[27] In the presence of a strong magnetic field, the majority of electrons occupies the lowest Landau level, implying an enhancement of the longitudinal thermal conductivity of the electron fluid. This effect can be very pronounced near the magnetic pole, where the field is normal to the surface and more intense, so that heat propagates preferentially along the field lines, making the polar cap region considerably hot.

1.4 Pulsar phenomenology

Although pulsar physics is by now half a century old, and many aspects of their radiation emission have been understood, there still remain many unsolved problems concerning the very mechanism of generation of the coherent (i.e. non-thermal) radiation.

Once neutron stars are magnetized with fields of the order of $B \sim 10^{12}$ G, they become radio emitters and can be detected at much lower frequencies trough the pulsed signal from the rotating beacon. Folding hundreds of pulses allows to measure the period P of a pulsar with an accuracy up to ten digits and long follow-ups allow to measure accurately also the period derivative $\dot{P}$. Such radio pulsars appear to emit short pulses with periods between 1.4 ms and 10 s.

Despite the beamed emission mechanism is not well understood, radio observations are of fundamental importance. From accurate timing of neutron stars we can infer the dipolar component of the magnetic field, as recalled in App (B). Moreover, the pulse period can be measured with accuracies that allow sensitive measurements of small quantities such as gravitational perturbations from planetary-mass objects orbiting a pulsar. This remarkable property also lead to the discovery of the first confirmed exoplanets (Wolszczan and Frail, 1992).

The rapid rotation of the magnetosphere gives rise to strong electric fields, particle acceleration and pulsed radiation across the whole EM spectrum, so that beamed radio emission and thermal X-rays are not the only means by which a pulsar emits. The basic model, namely the vacuum-dipole model, is reviewed in App (B). Despite its simplicity it gives a first interpretation of the P-$\dot{P}$ diagram, as shown in the left panel of of Fig. (1.5).

1.4.1 Pulsar classes

Thanks to the conservation of angular momentum and of magnetic flux during the collapse, neutron stars gain intense magnetic fields and high angular velocities. Things are however not so simple: magnetic flux conservation during the collapse cannot explain the large number of neutron stars with very high inferred magnetic fields. Therefore the magnetic field is thought to be enhanced during the core-collapse, probably via dynamo mechanism. As it stands the generation and evolution of the magnetic field in neutron stars is a very open field of research.

Two attributes, rotation and a strong dipolar component of the magnetic field, are the means by which NSs can be observed, thanks to the onset of beamed emission that powers the magnetosphere. Observations of thermal emission from NSs is rare and difficult, in most cases hidden by the complex and energetic phenomena that occur in the magnetosphere. Recent observations, particularly in X-rays and γ-rays, have shown a great diversity of neutron star types which can be broadly classified, according to the primary source of energy that powers their electromagnetic and particle emission, into the following classes:

Rotation-powered pulsars have a period distribution centered around ~ 0.1 s. These objects are believed to be isolated neutron stars with a dipolar magnetic field of the order $\sim 10^{12}$ up to $\sim 10^{14}$ G. The rotational energy loss of the pulsar powers the radiation via creation and acceleration of e^+e^- pairs in a strong magnetic field. Rotation-powered pulsars make up the majority of the neutron stars detected and sometimes exhibit glitches. Also the so-called recycled millisecond pulsars, no longer accreting, are clearly powered by they rotational energy
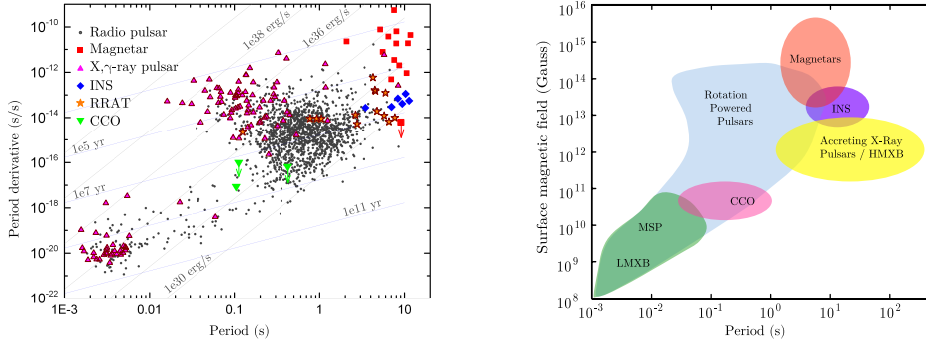
Figure 1.11: *Left* - Similarly to the Hertzsprung-Russell diagram for classical stars, the population of pulsars can be plotted on the P-$\dot{P}$ diagram, where the quantities $I\Omega\dot{\Omega}$ and the characteristic age τ are over-plotted using the relations given in App (B). RPPs are represented by black dots. *Right* - Schematic diagram of the NS zoo with respect to their periods and derived surface magnetic field strengths. The magnetic field of accretion-powered NSs cannot be measured from their spin down rate, but cyclotron lines seen in their spectra provides an alternative way to estimate the surface field. Note that only LMXB have small periods, since in HMXB there is no mass transfer (the interaction with the companion is mediated by the stellar wind of the massive main sequence star). Adapted from Harding (2013).

Thermally-powered pulsars are neutron stars that do not show magnetic activity and are sometimes called INSs. However thermal emission from their surface is observable in soft X-rays. It is thus the fossil heat of the proto-neutron star that powers the main feature of the observed spectrum. Of course all neutron stars are expected to have a thermal component of the emission, but only for objects of this class the cooling is the most important responsible of emission.

Accretion-powered are found in binary systems and globular clusters. Since the binary companion transfers material onto the spinning neutron star, it is the gravitational potential energy that powers the bulk of the observed emission. The infalling matter can bury the magnetic field, so that the dipolar component is expected to be weak for neutron stars standards, implying that their surface magnetic field cannot be faithfully estimated by using the dipole formula, Eq. (B.3). This class of binary objects can be seen as a part of the greater astronomical class of X-ray binaries that are usually divided into many subcategories, according to the mass of the companion star: the high mass X-ray binaries (HMXB, the NS is a companion of a massive main sequence star and interacts with its wind) and the low mass X-ray binaries (LMXB, mass transfer from the less massive donor fills the Roche lobe). In particular the LMXBs are though to be the progenitors of the rotation-powered millisecond pulsars (Papitto et al., 2014).

Magnetars (AXPs and SGRs), with typical periods centered in the range $1 - 10\,\text{s}$, are the strongest magnets in the present universe, as described in App (B).

Magnetars surface dipole field is inferred to be no higher than $10^{13}\,\text{G}$ with the fallback disk model (Chatterjee et al., 2000); (Alpar et al., 2013). However, the total surface field including all multipoles needs to be of the order of 10^{14}-$10^{15}\,\text{G}$ to power the magnetar bursts. The quiescent X-ray emission is powered by the ohmic decay of their large magnetic fields but magnetic stresses can eventually crack the star's crust, powering the bursting

activity (Thompson and Duncan, 1996).

The paradigm that magnetar's activity is associated with a high dipolar field has been challenged by the discovery of few neutron stars that displayed SGR-like activity (burst emission from SGRs was soon recognized to repeat, at variance to what was observed in GRBs, setting the two phenomena apart) but with an inferred dipolar magnetic field comparable with that of standard radio pulsars Turolla et al. (2015). This implies that magnetars are not only spread in the high-dipolar field region of the P-$\dot{P}$ diagram, as shown in (1.11) since these particular sources may be aged magnetars with a strong toroidal field in their interior.

Astronomical manifestations of magnetars can come in different guises: burst active X-ray pulsars, anomalous X-ray pulsars and soft gamma repeaters, that were identified as magnetars (Thompson and Duncan, 1995). In particular, SGRs emitted also three giant flares, extremely powerful events during which luminosities can reach up to 10^{47} erg/s for about one second. On the other hand, AXPs (dubbed "anomalous" because their high X-ray luminosity cannot be easily explained in terms of accretion from a binary companion or injection of rotational energy in the pulsar wind) were identified as X-ray pulsar in the soft X-ray range (Mereghetti, 2008). Subsequent observations revealed some similarities between AXPs and SGRs, including the unifying discovery that AXPs too emit short, SGR-like bursts.

This dissertation focuses on the rotation-powered pulsars which have not been recycled. In particular we are interested in those pulsars that have displayed large glitches, approximately the 10% of the total radio pulsar population.

1.5   Timing irregularities

The pulsar rotation frequency $\nu(t) = 1/P(t)$ can be measured at a given reference time t by means of pulsar timing techniques, namely the continuous recording of the time of arrival (TOA) of each pulse at the telescope. Pulses can be detected at different frequencies of the electromagnetic spectrum and constitute the fingerprint of the pulsar: the shape of the pulse profile, the number of recorded cycles needed to reach its required stability and its dependence on the photon energy and polarization are characteristic of each pulsar. Although individual pulse shapes can vary considerably, averaging over many recorded pulses yields a stable profile, with a high signal-to-noise ratio. This average profile is then correlated with the template profile for that given pulsar, so that the phase offset (which is related to the TOA via multiplication by the instantaneous pulse period) can be determined. Since the period evolves very slowly, a spin-down model $P(t)$ can be obtained by fitting the single TOA with a Taylor expansion around the reference time, so that the pulsar rotational dynamics can therefore be tracked (Lorimer and Kramer, 2004). The pulsars that are regularly monitored are typically observed every few days or weeks.

The period derivative is small but positive for non-accreting pulsars, implying that the angular velocity decreases steadily and in a predictable manner thanks to external electromagnetic braking torque which is nearly constant during the observational survey. Improved rotational parameters are obtained from the new TOAs by minimizing the discrepancies between the predicted and observed phases.

However, the evolution is not so smooth and linear: timing irregularities are seen in the pulse phase residuals after subtracting a polynomial fit (i.e. the spin down model valid at the reference time).
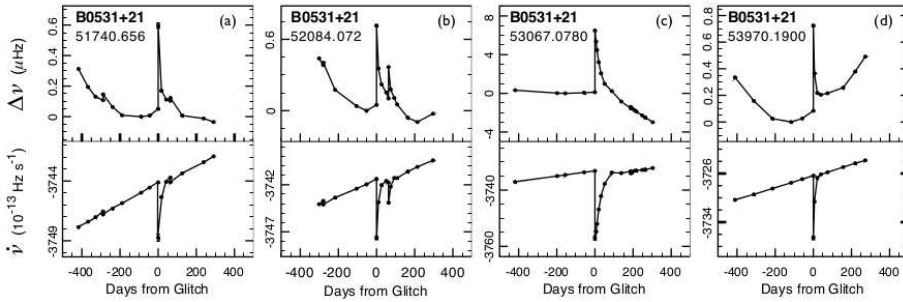
Figure 1.12: Four large glitches in the Crab pulsar ($\nu \approx 33$ Hz and $\dot{\nu} \approx -3.7 \times 10^{-10}$ Hz/s). Every glitch is shown by plotting the frequency residuals, of the order of 10^{-6}Hz (top) and frequency rate (bottom) against observation time. Day zero corresponds to the glitch epoch, which is indicated in MJD (Espinoza et al., 2011).

1.5.1 Pulsar glitches

Occasionally the rotational frequency of a pulsar undergoes sudden jumps of amplitude $\Delta\nu > 0$, which are followed by a period of slow recovery that may last for days or months, the so-called glitches. The signature of a glitch in the timing residuals is rather clear for relative jumps bigger than $\Delta\nu/\nu \gtrsim 10^{-7}$: when a glitch occurs, the model $P(t)$ previously obtained can no longer predict the TOAs, which have to be described by a different timing solution and a jump (a discontinuity) in ν and $\dot{\nu}$ at the epoch of the glitch needs to be included, as sketched in Fig (1.12).

The first glitches were observed very soon after the discovery of pulsars, in the Vela and in the Crab (these two objects are still the most studied). To date, there are 482 events in 168 objects recorded in the Jodrell Bank catalogue, including few glitches in magnetars and millisecond pulsars and a single very small glitch[28] of a pulsar in a binary system (Serim et al., 2017).

Glitches with large amplitudes ($\Delta\nu \approx 10^{-5}$ Hz) are sometimes observed as sudden spin-ups of the Vela pulsar, accompanied by an increase in the spin-down rate of about 1%. The long subsequent recoveries (lasting from days to months) were interpreted as manifestations of the existence of an internal component that is very loosely coupled to what we can observe (i.e. the emission of the magnetosphere). Most of the times, the full investigation of the recovery is prevented by a new glitch that occurs and dominates the residuals.

As the interaction between normal fluids provided by viscosity would result in very short coupling timescales, glitches are thus considered to be the probes for the existence of superfluid phases of dense hadronic matter; indeed, superfluids can flow without friction (up to a certain point) and are also theoretically expected in degenerate systems of interacting particles, as recently reviewed by Haskell and Sedrakian (2017).

Glitches can vary significantly from one another, not only among different objects: even single pulsars can show glitches that recover in a different manner. The variability of these event affects not only the size and the frequency of the events (some pulsar glitch

---

[28] This glitch has been discovered in the $\nu \approx 10^{3}$ s and $\dot{\nu} \approx 4 \times 10^{-14}$ pulsar SXP 1062 and provides the first confirmation of the existence and observability of this type of timing irregularities among accretion-powered pulsars. Thanks to the unusually low value of ν, this glitch has the largest value of the fractional change of pulse frequency ($\Delta\nu/\nu \approx 1.4 \times 10^{-3}$) reported up to now.

sporadically, other frequently), but also the post glitch response of the star: some glitches appear as simple steps, while others display an increase in spin-down rate after the glitch (which implies a change in the internal torques which does not relax over the inter-glitch timescale), as shown in Fig (1.13).

In few cases several exponentially relaxing components in the post-glitch recovery have been recognized, indicating that different layers of the star are involved in the process, each with its own typical coupling timescale (see App (C)).

The basic phenomenological model for pulsar glitches, proposed by Baym et al. (1969) and based on two interacting components [see also the description given by Shapiro and Teukolsky (1983) or Eqs (C.1) and (C.2)], tells us that the recovery can be fitted with a function of two parameters, the relaxation timescale τ^R and the healing parameter Q:

$$\Omega(t) \, = \, \Omega_{pre}(t) + \Delta\Omega \, Q \, e^{-t/\tau^R} + \Delta\Omega(1 - Q), \qquad (1.3)$$

where the instantaneous spin up occurred at $t = 0$, while $\Omega_{pre}(t)$ is the spin down model valid before the glitch. Usually $\Omega_{pre}(t) = -|\dot{\Omega}|t + \Omega$ for values of the spin down rate $|\dot{\Omega}|$ and angular velocity Ω measured before the glitch. The interpretation of the parameter τ^R is given in Eq (C.2), while a pictorial interpretation of the healing parameter Q is sketched in Fig (1.13). In the Vela pulsar the glitches occur as sudden steps of permanent offset, described by the healing parameter $Q \approx 1$, differently from what has been observed in the Crab where Q is typically small (Crawford and Demiański, 2003).

This early model for the recovery is however incomplete; in most of the large glitches where there are enough observations, also a component of Ω of constant second time derivative is observed throughout the inter-glitch data. The Vela pulsar provides the clearest example: the offset in the second derivative of the rotation rate takes over after the fast exponential relaxation. This particular behavior needs to be accounted for in the correct way in order to estimate the braking index of the pulsar (Akbal et al., 2017).

Leaving aside AXPs, where glitches and anti-glitches can be accompanied by burst activity (Archibald et al., 2013), glitches in RPPs show no evidence for electromagnetic counterparts: some initial suggestions featured external mechanisms, such as plasma explosions in the magnetosphere, but the lack of evident pulse profile changes associated with these events was soon taken as the clue for an internal origin[29]. It is therefore usually assumed that glitches in RPPs have a different origin than those in magnetars, and are not originated by effects involving the magnetic field, which is though to play no significant role or adjustment during the glitch event. The scenario for AXPs is briefly discussed in App (B), while a unified scenario for both usual glitches in RPPs and anti-glitches in magnetars have been recently proposed by Haskell and Antonopoulou (2014) and Kantor and Gusakov (2014).

While the post-glitch relaxation can be followed, the rise time cannot be properly resolved, making it an instantaneous event to the accuracy of data; to date, the best resolved event placed a limit of $\sim 40\,\text{s}$ for the rise time of a glitch in the Vela pulsar (Dodson et al., 2002). This implies the angular momentum is transferred to the crust in less than a few hundred rotation periods (McCulloch et al., 1990); (Dodson et al., 2009).

In this dissertation it will be useful to divide glitching pulsars into two broad categories. The first one corresponds to RPPs which have glitched only once and comprises more

---

[29] In the following chapters we will always assume a constant external torque on the inter-glitch timescale, an hypothesis that is justified only for RPPs: magnetars and HMXB have very variable external torques. Magnetar and HMXB glitches may be due to external torque events with internal torque response, a scenario that is not considered in the present work.
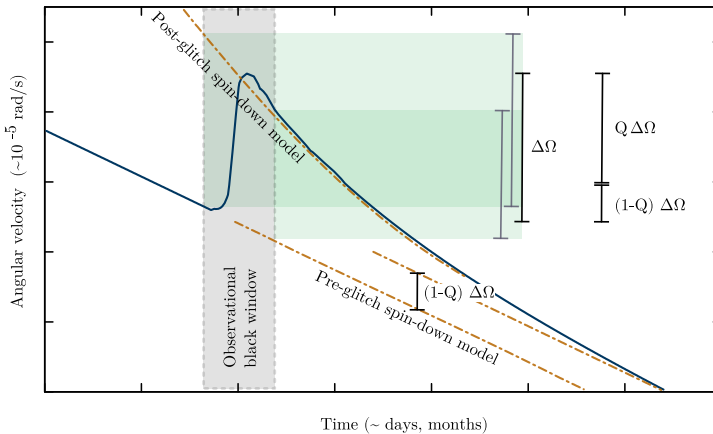
Figure 1.13: Schematic diagram of a glitch, following the notation introduced in the seminal work of Baym et al. (1969): the spin up phase is instantaneous to the accuracy of data so that the glitch amplitude is found by considering the jump between a pre-glitch model and the fitted relaxation. The healing parameter Q represents the fraction of the extrapolated jump that recovers before the next glitch. In every model that does not allow for permanent changes in the properties of the star, $Q = 0$ at infinity (typically another glitch is triggered before complete recovery is approached). The three parameters $\Delta\Omega$, τ^R and Q in Eq. (1.3) allow to fit the post glitch relaxation, but they vary from glitch to glitch, even of the same pulsar (eventually more timescales can be fitted but the general idea is unchanged).

than the 60% of the known glitching pulsars. The second one is that of the *frequent glitchers*, like Vela, Crab or the current record holder PSR J1740-3015 (which have been seen glitching more than thirty times). Unfortunately very few pulsars have been seen glitching more than a dozen times, making statistics in single objects quite poor. Of those objects which are observed to glitch repeatedly, most do so at unpredictable dates, but two (PSR J0537-6910 and Vela) are claimed to be quasi-periodic (Haskell and Melatos, 2015); (Melatos et al., 2008). The most studied neutron star is Vela (which frequency is $P^{-1} \approx 11.2\,\mathrm{Hz}$): since the first observed event in 1969, it has exhibited a quite regular sequence of similar size glitches $\Delta\Omega/\Omega \sim 10^{-6}$, about one every 2.8 years. There are however no solid statistical studies of the glitching behavior of single pulsars, due to intrinsic difficulties and to the paucity of data.

Activity parameter - A fundamental quantity for pulsars that have glitched several times is the activity parameter

$$\mathcal{A} = \frac{P}{T_{obs}} \sum_i \Delta\nu_i \qquad (1.4)$$

where T_{obs} is the duration of the observation survey during which the glitches of amplitude $\Delta\nu^i/\nu$ have been observed. In the above equation $P = \nu^{-1}$ is the benchmark period of the pulsar: since $\Delta\nu \ll \nu$, the exact value of the ever changing ν is unimportant. Note that T_{obs}/P is the total number of cycles observed, therefore the activity is the average spin up due to the observed glitches in a rotational cycle.

An interesting observational correlation between the absolute activity $\nu\mathcal{A}$ and the spin down rate $|\dot{\nu}|$ has been observed (Lyne et al., 2000), (Espinoza et al., 2011); (Fuentes et al., 2017); (Ashton et al., 2017). Moreover middle-aged pulsars with characteristic age
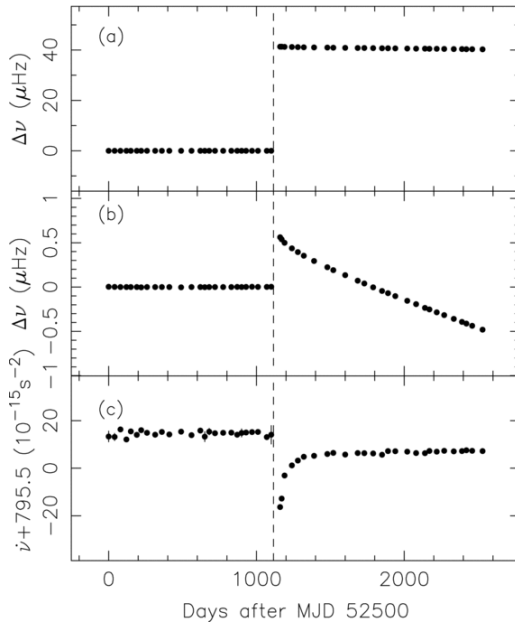
Figure 1.14: The glitch with the largest $\Delta\nu/\nu$ ever detected in a RPP, discovered in the timing of PSR B2334+61 (Yuan et al., 2010). The vertical dashed line marks the glitch epoch. Panel (a) shows variations of rotational frequency $\Delta\nu$ relative to the pre-glitch solution, (b) an expanded plot of $\Delta\nu$ where the mean post-glitch value has been subtracted from the post-glitch data, and (c) variations of the frequency first derivative $\dot{\nu}$. The plotted points represent fits of ν and $\dot{\nu}$ to 5-10 adjacent TOAs, with $\Delta\nu$ being the difference between the fitted value of ν and the value from the pre-glitch solution (extrapolated after the glitch). Image taken from Yuan et al. (2010).

$\tau \approx 10^4$ yr seem to glitch the most, while activity is smaller for significantly younger and older pulsars (Shemar and Lyne, 1996), as can be seen also in Fig (3.14). This fact may be linked to an evolution of the superfluid reservoir as the star cools (Ho et al., 2015).

The activity parameter can be linked to the moment of inertia of the region that stores the angular momentum released in a glitch, as first proposed by Datta and Alpar (1993) and later by Link et al. (1999). In particular, for a pulsar of total moment of inertia I, the following constraint must hold:

$$2\left(I - I_{res}\right)\mathcal{A} \;<\; I_{res}\,\tau^{-1}\,,$$

where I_{res} is the moment of inertia of the pinning region (Datta and Alpar, 1993) and τ is the characteristic age of the pulsar, as defined in App (B). This inequality can be used to infer an indirect constrain (after the EOS has been fixed and the pinning region identified) on the pulsar mass by using observations of the glitch activity. In the following chapters we will develop an alternative method to constrain the mass of a pulsar.

Glitch randomness - Glitch sizes are generally reported as a fractional increase of the pulsar frequency and can span several magnitudes, ranging from $\Delta\Omega/\Omega \approx 10^{-12}$ to $\Delta\Omega/\Omega \approx 10^{-5}$. The absolute increase in Ω spans seven decades across the total glitch population of all detected pulsars, $3 \times 10^{-11} \lesssim \Delta\Omega \lesssim 2 \times 10^{-4}\,\mathrm{rad/s}$ (Espinoza et al., 2011), and up to four decades in a single object.

Due to this variety of possible values and the absence of a preferred timescale for the waiting times, glitches are sometimes seen in analogy with earthquakes: the stochastic nature of glitches is a strong clue for an instability for which the star prepares over the waiting interval. Although the magnitudes of individual glitches seems to vary in accordance with fat tailed PDF (Melatos et al., 2008), the maximum-sized glitches have stable sizes, probably a direct manifestation of the presence of a well defined reservoir of angular momentum. Conversely, also the claimed presence of a well defined *minimum size* for a glitch is a remarkable property (Espinoza et al., 2014): recent analysis of the lower end of the Crab's size PDF, suggests the existence of a minimum size around $\Delta\nu/\nu \sim 10^{-9}$, well above the smallest resolvable event. (Espinoza et al., 2014) reviewed almost thirty years of data for the Crab, finding that the number of events with $\Delta\nu < 0.05\,\mu$Hz is significantly less than expected from extrapolating downwards a power-law PDF. Whether or not this implies a true limit in the small glitches of the Crab depends on the form of the extrapolated PDF, which is at present quite uncertain because of the relatively small number statistics. Moreover, the lower end of the distribution may be contaminated by a different population of timing noise events (possibly of magnetospheric origin) and further studies are required to rule out this possibility.

Much of this rich phenomenology still needs to be organized into a coherent picture and our understanding of pulsar glitches, as well as their modelling, is still evolving. There are two main mechanisms which have been examined in the literature.

Starquake model - The outer layers of a neutron star form a crystalline crust that can support stress. This crust crystallizes after the early protoneutron stage, when the star is almost rigidly rotating. During the subsequent spin down, the liquid core adjusts its shape to the rotation rate, while the solid crust counteracts via elastic deformation: the shape of the star is very near but not exactly equal to the shape of a rotating fluid in hydrostatic equilibrium: because of the decreasing centrifugal force, the internal fluid tends to relax to a slightly less oblate star shape, but this is hindered by the elastic feedback of the stressed crust. This yield to a point where there will be a sudden relaxation of the stress, with the consequent very slight change in stellar shape and moment of inertia. Therefore, glitches can occur because the star suddenly reduces its momentum of inertia, which is done via a crustal fracture, as first proposed by (Ruderman, 1969). The calculated accompanying jump in angular velocity is close to that observed in small events, making it a viable model for the Crab pulsar (Alpar et al., 1994; Alpar et al., 1996), but cannot explain the great variety of giant Vela-like glitches, which are much more energetic events: the Vela quake would be a cataclysmic event since this would correspond to a shifted of the crust by about 10 meters. Apart from the difficulty seen in storing this huge amount of energy into the elastic response of the crust, the main problem of the starquake model is the difficulty in explaining frequent glitches: the majority of glitchers spin down too slowly and enough stress cannot be built is the star relaxes completely in a quake, making quakes very rare events (Smoluchowski, 1970).

Vortex avalanche model - Since no such spin-up phenomena had ever been observed in other astronomical objects, Cameron and Greenstein (1969) proposed that glitches had to do with specific properties of neutron stars. They proposed that the first glitch in the Vela was due to the onset of a fluid instability (due to the core rotating faster than the crust) and assumed the viscous effects to be unimportant. The spin-down rate of Vela
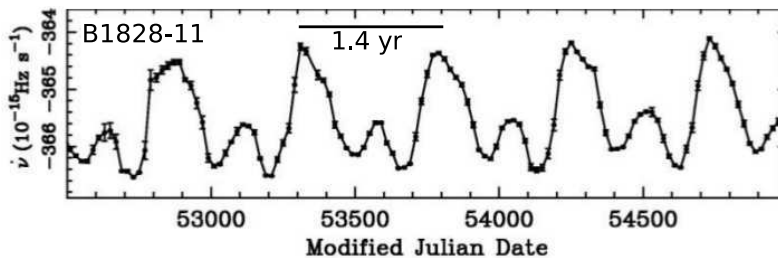
Figure 1.15: The quasi periodicity detected in the spin-down rate of PSR B1828-11 (a young pulsar with period $P = 405\,$ms), which is also a well studied free precession candidate (Ashton et al., 2016). The average value of the spin down of this pulsar is approximatively $\nu(t)/$Hz ≈ 2.46 -3.6 $\times 10^{-13}\,(t/$s), corresponding to a rate of $\dot{P} \approx 5.9 \times 10^{-14}$. The observed variations of $\Delta\dot{\nu}/\dot{\nu} \approx 0.7\%$ have a periodicity of $\sim 1.4\,$yr. Some pulsars have pronounced periodic modulations not only in their timing residuals, but also the shape of pulsations: B1828-11 is probably the best example of this. As a result, this pulsar has been used as evidence for both precession and periodic magnetospheric torque switching.

relaxed to the value it had before the glitch after one year; Baym et al. (1970) interpreted this very long relaxation time as an evidence for neutron-star superfluidity.

To date, the most accepted scenario is based on the prediction that neutrons in the interiors of cold NSs are in a superfluid state. Anderson and Itoh (1975) proposed a vortex mediated exchange of angular momentum between a normal and a superfluid component. In this case, the low cutoff in the PDF of glitch sizes observed by (Espinoza et al., 2014) could be related to the vortex knock-on process (Warszawski and Melatos, 2012) and to the threshold above which an avalanche of moving vortices can propagate (Haskell and Melatos, 2016); (Haskell, 2016).

Starquakes can still have a role, being a possible trigger for the vortex avalanche, but it is the avalanche itself that is responsible for the spin-up of the crust, not the moment of inertia change during the quake. Both the spin-up of the crust and the post-glitch relaxation are thus manifestations of superfluid vortex dynamics, while in the starquake model of Baym et al. (1969), one of the first models involving superfluidity, the superfluid is introduced only to explain the long recovery.

1.5.2   Timing noise

Pulsars are stable on an accuracy of one part in 10^{10} or even better, apart from glitches that represent sporadic discontinuities. Moreover, we know from radio pulsar timing that the spin down of a pulsar differs from a purely polynomial spin down due to a phenomenon called timing noise, a continuous low-frequency structure in the residual between the best-fit timing model and the observed pulsations. The longterm monitoring (lasting several years, up to 30) of some pulsars has indeed revealed little and slow modulations in their rotational frequencies ν, which appear as a wandering of the rotation rate around the predictions of a simple polynomial slow-down model. Also the spin down rate $\dot{\nu}$ shows periodicities (even more clearly), as shown in Fig (1.15). Moreover the little variations in $\dot{\nu}$ are not only periodic in time but also bounded by well-defined low and high values. A comprehensive review of timing noise is provided by Hobbs et al. (2010).

While glitches are rapid and sporadic events with sudden changes in ν and $\dot{\nu}$, timing noise appears as a slow and continuous process. This wide-spread phenomenon, first seen in the Crab pulsar and later found in the timing of both normal and millisecond pulsars, has nowadays been established as a general characteristic of pulsar rotation rates (Lorimer and Kramer, 2004).

For long, timing noise was thought to be random and non-deterministic but some examples of repeating patterns have been detected. Therefore, this was attributed to a problem of free precession but the question is still open. Other possibilities are the presence of unseen binary companions (in particular planets), clouds of particles that induce fluctuations in the radiated beam, post-Newtonian orbital effects, free precession of the star, or magnetospheric effects (Lyne et al., 2010). In particular, the tentative explanation of timing noise in terms of free precession has to consistently include the effect of the superfluid interior: the pinned superfluid vorticity induces gyroscopic precession and secular or stochastic torques do not necessarily average to zero over many precession cycles (Shaham, 1977).

The fact that these slow fluctuations are detected mainly in young[30] pulsars, for which the spin down rate is larger than for older pulsars, is interpreted as a clue that timing noise arises from an irregular transfers of angular momentum between the crust and the liquid interior due to superfluid turbulence (Melatos and Link, 2014).

Although it seems clear that timing noise is not an aberration due to our current methods of collecting timing data, this phenomenon is still poorly understood to date. One possibility is to find a way to rule out some of the explanations proposed so far. For example, Bayesian analysis tools can be used to discriminate between competitive models for the timing noise models of PSR B1828-11, as recently proposed by Ashton et al. (2016).

---

[30] Here "young" refers to the dipole age $\tau = \nu/(2\dot{\nu})$, which may not be a good estimate for the pulsar true age. The dominant contribution to timing noise for young pulsars with $\tau < 10^5$ yr can also be explained as being caused by the recovery from previous glitches (Hobbs et al., 2010).

Axially-symmetric model for pulsar rotation

In this chapter a general class of models for pulsar rotation, based on the assumption of axial symmetry, is described: despite many glitch models in literature are effectively constructed under the hypothesis of cylindrical symmetry, the translational invariance along the rotation axis is destroyed simply because the star is spherical and stratified. It is thus important to account for the non-homogeneous structure due to the stratification of matter, in particular in models where the superfluid can develop a differential rotation rate. In this Chapter we work out the details in the simplest situation, where vortex lines are straight and parallel to the rotation axis; in App (E), it is shown how this restrictive scenario can be generalized.

The main result is a system of differential equations that set the mathematical framework in which to test quantitatively the macroscopic consequences of the presence of a stable array of vortices, a working hypothesis widely used in glitch models. Even without solving the equations explicitly, we are able to draw some general quantitative conclusions.

2.1   Motivation

The detection of glitch events in many RPPs indicates that a large amount of angular momentum is first stored and then exchanged between an internal component and the observable crust: a neutron star has to be made of (at least) two components which can interact via some type of mutual friction in order to allow exchange of angular momentum. As aforementioned in the previous chapter, observations of long post glitch relaxations indicate that one of these components is superfluid.

With this in mind, these recurring and random period instabilities are usually explained as a manifestation of the internal superfluid vortex dynamics. Anderson and Itoh (1975) posed the basis for this interpretation; large glitches are vortex avalanches, global events in which an extended portion of previously pinned vorticity is suddenly expelled from the superfluid bulk on a short timescale: the vortices, in their outward motion, transfer their angular momentum to the crust. The nature of the avalanche trigger is still debated: it could be a starquake (Ruderman, 1976; Ruderman et al., 1998), a local increase in the temperature of the star (Link et al., 1993; Link, 2014), an hydrodynamical instability (Glampedakis and Andersson, 2009) or a manifestation of a self-organized critical system (Melatos et al., 2008).

Since the pioneering two-component model of Baym et al. (1969), dynamical models have evolved in order to incorporate effects of multifluid hydrodynamics, as superfluid entrainment (Carter, 1989; Comer and Langlois, 1994) and dissipation (Andersson and Comer, 2006). Although the hydrodynamical equations are known (Prix et al., 2002), the majority of studies of glitches have been carried out in the approximation of a rigidly rotating star and there has been little progress on making the pulsar glitch models quantitative.

The currently accepted formalization of the multi-fluid problem in the interior of a neutron star is based on the seminal works on the hydrodynamics of Helium-II of Hall and Vinen (1956) and Bekarevich and Khalatnikov (1961); the governing equations are nowadays quite clear and developed but lead to a computationally hard 3D problem [e.g. Peralta et al. (2006) for hydrodynamical simulations in Couette geometry]. We therefore reduce it to a simpler 1D model by making two widely used assumptions: axial symmetry and straight vortices. This choice has, however, two drawbacks:

- Quoting Andersson et al. (2012), virtually every discussion of neutron star vortex dynamics has made the assumption that the vortex array is straight. The assumption of axial symmetry around the rotational axis of the pulsar is a widespread working hypothesis that allows to reduce the dimensionality of the problem: we can quantitatively test the consequences of this scenario with our model. Moreover, it can be possible that some of the details of the hydrodynamical problem become irrelevant at the global stellar scale.

- We can not study the nature of the trigger event, since it may be related to some non-trivial effect arising in the full three-dimensional problem, like the onset of turbulence. In our model, almost all the dynamical freedom of the superfluid is frozen, as only laminar flows are allowed.

The main motivation to start from such a simplified scenario stems from the fact that in literature we can only find rigid models with uniform entrainment [e.g. Sidery et al. (2010)] or differential models without entrainment [e.g. Haskell et al. (2013)]. In particular, vortex-creep models [since the seminal work of Alpar et al. (1984) and Alpar et al. (1984a)] do not account for entrainment or stratification. Similarly, global models based on the two-fluid formalism have either neglected entrainment Haskell et al. (2013) or have been studied under the assumption of uniform entrainment and rigid rotation of the neutron superfluid Prix et al. (2002); Sidery et al. (2010). The present model addresses these lacks in the literature and provides a rigorous formulation of the previous work of Haskell et al. (2013), extending it to the case of density-dependent superfluid entrainment.

2.2   Mesoscopic input

The two physical ingredients that currently challenge the description of pulsar glitches, both at the mesoscopic scale of vortex lines as well as at the macroscopic stellar scale, are entrainment and pinning. Another input is the EOS, which sets the stellar structure and composition at the macroscopic scale. However, the choice of the EOS does not affect in a fundamental way the dynamics the of superfluid vortices, which is the means by which the angular momentum can be transported during the glitch.

2.2.1 Entrainment

A key feature of superfluidity is the possibility for the normal and superfluid components to flow independently. The formalization of this multi-fluid problem in the interior of NSs is based on the seminal works on the hydrodynamics of He-II that extended the early two-fluid models of Tisza and Landau (Hall and Vinen, 1956); (Bekarevich and Khalatnikov, 1961). Later, with the aim to study ^{3}He-^{4}He superfluid solutions, Andreev and Bashkin developed a three-fluid framework where two superflows and a normal flow exist simultaneously (Andreev and Bashkin, 1975). They found that entrainment (a non-dissipative effect that couples the two species) can be described in the frame of reference comoving with the normal flow as a *density-matrix* which relates the momentum of one constituent to the kinematic velocities of both constituents [see also Chamel (2017) for a nice introduction to the modern formalism with applications to the hydrodynamics of NS interiors]. From the practical point of view, entrainment is described, in the core as well as in the crust, in terms of *effective masses*, which definition depend on the frame of reference used.

Entrainment in the inner crust - Dripped neutrons in NS crusts are analogous to electrons in ordinary metals and their properties can be determined by the band theory of solids (Chamel, 2006, 2012). Only neutrons in the conduction band can move throughout the crust: the density of conduction neutrons can be much smaller than the density of unbound (i.e. dripped) neutrons. This reduction of the number of neutrons that can be effectively considered free (by an order of magnitude in some layers) is due to Bragg scattering. The conclusion is that, even if dissipative effects were not taken into account, the crust still resists the neutron current.

Bragg scattering is a non-local and non-dissipative effect: neutrons are scattered by individual clusters and can then interfere constructively or destructively; in the latter case neutrons cannot propagate, as if they were very massive Carter et al. (2005). Indeed neutron diffraction due to scattering on a crystalline structure is a well known topic in condensed matter physics. Scattering experiments with thermal neutrons are routinely performed to explore the structure of materials: a neutron can be coherently scattered if $k > \pi/d$, where d is the typical lattice spacing and k the wavenumber of the neutron. The main difference between electrons in metal and neutrons in neutron star crusts is that neutrons are highly degenerate: neutrons have momenta up to k_F and typically $k_F > \pi/d$ in all regions of the inner crust but the shallowest.

Entrainment in the outer core - The scenario is very different in the core, where neutrons and protons can only be locally scattered by the surrounding nucleons Chamel and Haensel (2006): in this case entrainment between the two baryon species is due to the strong interaction. This mechanism results in a lower effective mass of neutrons in the core, a behavior that be interpreted in terms of a back-flow of nucleons. This local effect also exists in the crust but it is negligible when compared to Bragg scattering. Following the suggestion of Vardanyan and Sedrakyan (1981) that the the Bashkin and Andreev idea would be applicable in neutron stars, the first calculation of the strength of entrainment for the neutron-proton superfluid mixture in the core was carried out by Alpar et al. (1984b) in the framework of an extension of the Ginzburg-Landau theory for a superfluid mixture.

Entrainment challenges our understanding of pulsar glitches: the recent large values found for entrainment in the crust indicate that such a phenomenon cannot be ignored

in the physics of pulsar glitches. In particular Vela glitches have been thought to arise
from the superfluid in neutron-star crust (Alpar et al., 1984b; Datta and Alpar, 1993;
Link et al., 1999). However superfluid can be strongly entrained by the crust and this
results in a decreased mobility of the crustal superfluid that cannot carry enough angular
momentum to explain large glitches (Chamel, 2012, 2013; Andersson et al., 2012). In our
numerical examples we use the effective neutron masses calculated by Chamel and Haensel
(2006) and Chamel (2012) for the core and the crust respectively.

Hydrodynamics with entrainment - As said, the two-fluid model of Landau for superfluid
hydrodynamics at $0 < T < T_c$ was generalized to a "three-fluid" one, i.e. a normal compo-
nent (excitations) and two components (irrotational) that describe the superfluid mixture.
This was done for finite temperature $T < T_c$ in the context of superfluid ^{4}He-^{3}He solutions,
where T_c is the critical temperature for the onset of the superfluid phase of ^{3}He. If ^{3}He is
the dilute and ^{4}He the solvent, the effective mass of ^{3}He turns out to be 2.3 times greater
than its bare mass (Meierovic, 1984); a by result of the strong interaction between a ^{3}He
atom with the surrounding ^{4}He (for the dilute, the ^{3}He-^{3}He interaction can be neglected).
However the low miscibility of these two fluids makes this system hardly achievable in
experiments and the measurement of the effective mass is difficult.

Therefore, the mass current for each of the two species must be expressed as a
combination of the three velocities[1] $\mathbf{v}_3$, $\mathbf{v}_4$, $\mathbf{v}_N$ (the first two are the gradients of the order
parameters, N stays for "normal"). At the hydrodynamical level (and for small relative
velocities) the mass currents in the frame of reference of the normal fluid turn out to be

$$\boldsymbol{\pi}_4 = \rho_{44}(\mathbf{v}_4 - \mathbf{v}_N) + \rho_{43}(\mathbf{v}_3 - \mathbf{v}_N)$$
$$\boldsymbol{\pi}_3 = \rho_{34}(\mathbf{v}_4 - \mathbf{v}_N) + \rho_{33}(\mathbf{v}_3 - \mathbf{v}_N)$$

where the mass-density matrix is symmetric: $\rho_{43} = \rho_{34}$ since they are second derivatives
of the energy of the mixture with respect to the relative velocities $\mathbf{v}_3 - \mathbf{v}_N$ and $\mathbf{v}_4 - \mathbf{v}_N$.
Unfortunately, the discussions in the literature have been usually obscured by the confusion
between momentum and velocity: in order to adapt the original formalism to the NS core
the velocity of a constituent has to be reinterpreted as the momenta per particle divided
by the corresponding bare mass [see e.g. Chamel and Haensel (2006) for a very concise
but clear treatment].

In a neutron star core we have an analogous situation with the presence of the neutron
superfluid and the proton superconductor (and a normal component): the bare protons
(but also the neutrons) are dressed by a polarization cloud of nucleons comprised of both
species. Despite a precise hydrodynamical formalism has been developed [we will follow
the quite standard terminology described by Chamel and Haensel (2008) or Haskell and
Melatos (2015)], very little is known about realistic entrainment parameters ϵ_n and ϵ_p in
neutron stars, which are often used to construct the density-matrix. These parameters are
not independent but have to fulfill the relation $\rho_p\,\epsilon_p = \rho_n\,\epsilon_n$ which is quite natural: the
most present component (the one with higher density) is less entrained by the other. The

---

[1] This terminology is not standard: in the original article of Andreev and Bashkin, the gradients of
the phase of the superfluid order parameter are referred to as "velocities". This would be an appropriate
description of the neutron star interior if both protons and neutrons condensed into an $^1S_0$ state; the
complications associated with the $^3P_2$ order parameter are typically not considered.

In this work we use a different terminology (geometrically motivated, as discussed in chapter (4)) and
consider the gradients of the phase as "momenta per particle". As discussed by Glampedakis et al. (2011)
the definition of the entrainment matrix is a matter of personal choice and detailed comparison between
the two different approaches is provided by Andersson and Comer (2001a).

relation between effective masses m_x^* and entrainment is given by $\epsilon_x = 1 - m_x^*/m_x$, where m_x is the bare mass of a free x-species particle (Carter et al., 2006).

The precise hydrodynamical formalism that is adopted in this works is detailed in many references [see e.g. Glampedakis et al. (2011) or the review of Andersson and Comer (2007)] and will be introduced when needed. We just stress that the difference between the momenta per particle and the velocity is essential in the case of *interacting perfect multifluids* (Rezzolla and Zanotti, 2013): the kinematic velocity of each species is introduced by considering the two (conserved) number densities or particle currents j_x^i, so that $v_x^i = j_x^i/n_x$, while the momenta per particle p_{xi} is introduced through the usual conservation of energy and momentum (Prix, 2004).

2.2.2 Pinning

Vortex pinning arises in many areas, such as in superfluid He, terrestrial superconductivity, ultracold atomic gases and classical hydrodynamics. The case of superfluid ^{4}He is instructive since the interaction between the vortex and the pinning site can be understood in terms of ideal fluid dynamics: when a vortex filament terminates on a flat surface which contains a pinning site in the form of a local protrusion, it gets captured if it approaches to within a critical distance (Schwarz, 1988). Once a vortex is pinned, it requires a finite background flow velocity with respect to the pinning center to free it.

Pining arises because, in the presence of an inhomogeneity or a lattice, not all the configurations have the same energy: depending on situations, it may be more convenient to confine the inhomogeneities into the core of a vortex. Within a perfect fluid approach, pinning can be described as arising from the competition between pressure and kinetic energy of the flow induced by the vortex. In the case of quantum vortices one also has to consider that the confinement of normal matter into the vortex core changes the condensation energy contribution, as pointed out in the first calculation of pinning energies and forces in a NS crust made by Alpar (1977): the energy cost per particle of normal matter in the vortex core is expected to scale as $\sim \Delta^2/E_F$, where E_F is the Fermi energy of the dripped neutron fluid.

Pinning in terrestrial superconducting layers - Generally the pinning mechanism of a "defect" that is blocked by a "pinning center" is based on the fact that the amount of inhomogeneity is reduced when the defect is superimposed on it. Most often (and more importantly for what we are going to discuss), pinning refers to the frozen positions of magnetic vortices (defects in the order parameter) in the Shubnikov phase of hard superconductors[2] (Campbell and Evetts, 1972). In this case the pinning centers are provided by the disorder that is always present in the form of atomic defects, like vacancies in doped cuprates or surfaces between crystallites.

Strong pinning is a desirable property for technological applications of superconductors since it hinders *flux-creep*, a thermally activated mechanism introduced in the seminal paper of Anderson (1962). Creep of fluxtubes can induce a pseudo-resistance of the

---

[2] The vortex-vortex interaction of hard superconductors in the Shubnikov phase is generally repulsive, leading to the well-known phenomenon of the Abrikosov lattice. However, for materials with a low Ginzburg-Landau parameter (e.g. Nb), also a sizeable short range attractive interaction is present. As a consequence, the transition from the Meissner to the Shubnikov phase at the lower critical field is first order and is accompanied by a discontinuity in the intervortex lattice spacing. In some samples an intermediate *mixed-state* phase is formed in which isolated Shubnikov domains are nucleated, surrounded by the field-free Meissner state.

superconducting sample and depresses both the critical current density and the upper critical field[3]. On the other hand, when fluxtubes are strongly pinned and a current (of superfluid electrons) is applied to the sample, the material can sustain dissipationless currents (Huse et al., 1992).

An ideally hard superconductor is a type-II superconductor with infinite pinning force (Bean, 1962). It is interesting to note that such an idealized material behaves in two different ways when cooled below the transition to the Shubnikov phase:

> *Zero field cooled* - We first cool the material so that it enters into its mixed-state without any external magnetic field. Now the external field is switched on: we observe complete shielding of the magnetic field, i.e. there are no fluxtubes. This is the behavior of a perfect diamagnet, where skin-depth currents on the surface shield the field.

> *Field cooled* - We apply an external magnetic field first, then cool down the sample; the initial total magnetic flux is frozen into the sample in the form of fluxtubes.

Therefore an ideally hard superconductor screens perfectly the change of the magnetic field flux rather than the magnetic field itself. This is very different from the case of type-I superconductors that behave always as a perfect diamagnet[4].

The recent work of Thomann et al. (2017) provides an analytical and numerical study of the effects of pinning on the dynamics of a vortex lattice in a type II superconductor in the strong-pinning situation: the authors determine the force-vortex velocity (or current-voltage) curve in the limit of zero temperature, finding that a finite background current has to be applied in order to unpin the fluxtubes.

Pining in NS - Something analogous to the field cooling case happens in NSs; in this case both the superfluid and the proton superconductor are cooled in the field regime since the protoneutron star is magnetized and rapidly rotating [the angular momentum provides the "external field" for superfluidity, see Eq (2.7): the angular velocity is analogous to the magnetic field flux from the mathematical point of view]. Therefore, the superfluid in a neutron star can be regarded as a hard superfluid and, in the limit of "ideally hard", any change in the vorticity flux (which is proportional to the large-scale angular velocity, as in Eq (2.8)) is suppressed. This is indeed the early idea of Anderson and Itoh (1975): pinning is particularly important in glitch modelling since it is the mechanism that allows to build up the angular momentum reservoir. When vortices are blocked, the normal component slows down due to radiation losses while the pinned superfluid maintains its state of motion, storing the angular momentum which can then be released in a glitch (Anderson et al., 1982).

Typically in NSs pinning refers to the interaction of vortices with the crustal lattice and pinning centers are the nuclei of the inner-crust. Strong pinning in NSs allows to support higher neutron currents before the dissipative effects generated by the motion of vortices enter the game (a mechanism dubbed vortex-creep, in analogy with the flux-creep

---

[3] If the magnetic field is too high (at the point the distance between fluxtubes is of the same order of the coherence length), superconductivity is destroyed. This is the upper critical field of type-II (dubbed "hard") superconductors.

[4] The fact that soft superconductors always show the Meissner-Ochsenfeld effect tells us that the diamagnetism in such materials is a property of thermodynamical equilibrium, i.e. it does not depend on the story of the system. We have thus two extrema: soft superconductors which expel the magnetic field and ideally hard superconductors that oppose changes of the magnetic flux.

observed in superconductors); this implies that a bigger angular momentum reservoir can be stored into the current of superfluid neutrons, allowing to explain the large glitches of the Vela pulsar (Datta and Alpar, 1993).

From densities $\rho_d \sim 4 \times 10^{11}\,\text{g/cm}^3$ (where neutrons begin to drip out of nuclei) to $\rho_c \sim 0.5\rho_0$ (where individual nuclei disappear) the neutron $^1S_0$ superfluid coexists with a lattice of neutron rich heavy nuclei. A convenient semiclassical approach to calculate pinning energy per pinning site E_p is to restrict the vortex-lattice system to only two adjacent Wigner-Seitz cells of radius R_{WS} and, for a given density zone, to consider the energy difference between two extreme (benchmark) configurations: the one with one of the two nuclei confined into the vortex core and the symmetric one in which the vortex core lies onto the interface between the two WS cells (Donati and Pizzochero, 2004).

For different densities, the difference between the free energy (or the internal energy since we are at $T = 0$) of these two configurations determines which type of pinning is favorable:

- Nuclear pinning: the vortex passes through one of the two nuclei; this turns out to be the most energetically convenient situation for densities $\rho \lesssim \rho_c$.

- Interstitial pining: at lower densities, $\rho \gtrsim \rho_d$, it is more convenient for the vortex core to avoid normal impurities (nuclei).

When estimating E_P it is fundamental to account for the condensation energy that depends quadratically on the pairing gap Δ of superfluid dripped neutrons. Currently, the major uncertainties about evaluation of Δ arise from polarization effects of nuclear matter that strongly suppress the pairing gap. This uncertainty is non-rigorously cured by introducing a suppression factor $\beta \sim$ 1-3 which rescales the BCS pairing gap calculated without taking into account polarization effects: $\Delta_{BCS} \to \Delta_{BCS}/\beta$. The case $\beta = 1$ leads to stronger pinning since the effective interaction with the medium is neglected; the choice $\beta = 3$ describes the case in which the effect of the polarization is maximum, leading to weaker pinning forces.

Since the pinning energetics is determined by four main contributions (the kinetic energy associated to the background flow induced by the vortex, the Fermi energy for free neutrons, the energy of the nuclei and condensation energy) which have different density dependencies, the rescaling of the pairing gap with β has also the effect of changing the range of densities at which pinning is stronger.

Donati and Pizzochero (2006) found that pinning energies per site are in the interval $0 < E_p < 3.5\,\text{MeV}$ and are significant only in a restricted density range, for $0.07\rho_0 < \rho < 0.2\rho_0$. The rest of the crust presents either interstitial pinning or extremely weak pinning: intuition for this is provided by the fact that distances between nuclei are comparable to the coherence length $\xi \sim 10\,\text{fm}$, implying that there is not a definite and convenient position of the vortex with respect to the lattice.

Mesoscopic pinning forces - While the concept of pinning energy E_P is quite clear (it is the energy difference between two benchmark configurations), it is less clear what should be a pinning force: no detailed and accepted methodologies to calculate this quantity exist in literature at present. Despite the name, we interpret it as a scalar quantity which represents the threshold for unpinning, namely f_P is the maximum modulus of the forces acting on a unit length of vortex line forced to flow with the normal component. Within this interpretation, the pinning force is analogous to static friction, which adjust itself to the external force up to a maximum value where motion sets in.
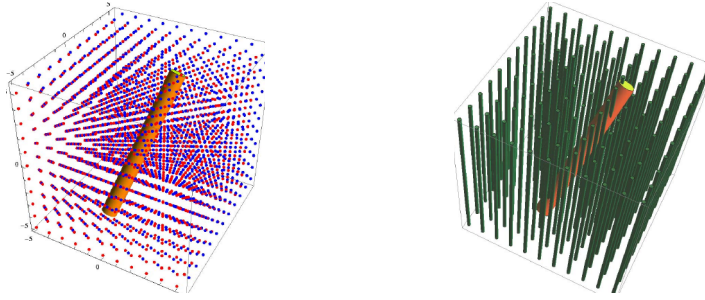
Figure 2.1: Snapshot of the average procedure used to estimate mesoscopic pinning forces per unit length f_P. The domain of the simulation is not arbitrary but is settled by physical properties of the vortex: the coherence length ξ gives an estimate of the core radius, whereas the vortex tension sets the length L of the segment. For $L \to \infty$ an infinite domain is necessary and the average procedure gives zero pinning. *Left* - The vortex is immersed into the crust. *Right* - The same procedure can in principle be used also for estimating the pinning to fluxtubes in the core. Figures modeled after Seveso (2015).

The strength of pinning is thus described by a mesoscopic quantity $f_P(n_B)$ that defines the depinning threshold and sets the strength of thee lattice-vortex interaction at a given density n_B in the crust: its value is the module of the maximum lift force on vortices that the lattice can sustain per unit length of vortex line.

Pinning can be a collective phenomenon: the effects of lattice rigidity on the summation of pinning forces is considered by Campbell and Evetts (1972) for type-II superconductors. In neutron stars, however, we also have to deal with the rigidity of a single vortex line [see e.g. Link and Epstein (1991)].

We briefly recall here the results of Seveso et al. (2016). The number of interactions of a vortex (see Fig (2.1)) with a nucleus in the lattice are counted for every random orientation of the vortex line: translations and rotations of the cylinder modify the number of nuclei touched by the vortex core. Hence pinning arises because of energy fluctuations due to the finite length L, which in turn is related to the finite tension of the vortex. Three different regimes are found, whose occurrence depends on the interplay between physical parameters such as $\xi_n(n_B)$ and the lattice spacing $b(n_B)$:

- Strong pinning forces are found where $\xi_n < b$ and the microscopic vortex-nucleus interaction is so strong to displace nuclei. Results in these strong pinning regions are quite insensitive to the debated nature of microscopic pinning (nuclear or interstitial); this is a drawback of the average procedure, but it is also physically reasonable.

- Weak pinning occurs where vortex-nucleus interaction is too weak to compete with the elastic properties of the lattice: since nuclei cannot be displaced, the vortex interacts with less nuclei than in the previous case.

- Regions in the crust where pinning is negligible correspond to a density interval such that $\xi(\rho) > b(\rho)$; the vortex core can always encompass a quite constant number of nuclei, so no energetically preferred configurations arise.

As expected, the mesoscopic pinning force becomes weaker for longer (more rigid) vortices and is generally much smaller than early estimates (based on vortices that are unrealistically aligned with the crystal) by a factor 10^3 or more. Nevertheless the forces obtained still

have maximum values of order $f_P \sim 10^{15}$ erg/cm², still enough to explain large glitches. The quantity f_P turns out to depend very little on whether the microscopic force is attractive or repulsive in a given region of the star, which compensates for the present lack of consensus on the sign of the vortex-nucleus interaction as a function of density (Wlazlowski et al., 2016).

2.3 Hydrodynamical model: straight lines

The microphysical input that describe the stellar structure are functions of the *baryon number density* n_B: to study the rotational dynamics of the two components we need the *free neutron fraction* y_n (that is zero below the drip density), the *normal fraction* $y_p = 1 - y_n$, the dimensionless *entrainment parameter* $\epsilon_n = 1 - m^*$ [where m^* is the dimensionless effective mass of neutrons in the frame of the crust, see Eq (2.5)], the *pinning force per unit length* f_P and the *mobility* η arising from the dissipative processes acting on vortex lines (Alpar et al., 1984b; Alpar and Sauls, 1988; Bildsten and Epstein, 1989). Given an EOS and the spherical stellar structure, all these profiles are functions of the spherical radius r.

2.3.1 Simplification of the full problem

Under the assumption of axial symmetry it is possible to project exactly the 3D hydrodynamical problem to a cylindrical one. This symmetry can be consistently implemented only in a restrictive scenario, that of a paraxial array of straight vortices which collectively resist bending induced by the non homogeneous forces exerted in the different layers of the star. In this way, however, we rule out a priori possible turbulent motion and forms of the mutual friction between the two different from the one usually used (Andersson et al., 2007): this is a limit of the model to be kept in mind. More precisely:

- *No precession* - We consider RPPs that spin around a definite axis, called the z-axis.

- *Equilibrium structure* - The equilibrium structure is given by solving the TOV equations by using a $T = 0$ barotropic EOS that provides the pressure $P(n_B)$, the internal energy density $\mathcal{E}(n_B)$ and the neutron fraction $y_n(n_B) = n_n(n_B)/n_B$, where n_n is the number density of non-bound neutrons. However, we need the superfluid fraction x_S. The pairing gap is highly unknown in the core, where it may vanish or be so little that finite temperature destroys superfluidity. For simplicity we take $x_S = y_n$ inside the superfluid domain (e.g. the inner crust and the outer core). The radius at which the neutron drip starts, R_d, corresponds to a density of $\rho_d \approx 4.3 \times 10^{11}$ g/cm³): thus x_S can be non-zero only for $m_n n_B > \rho_d$.

- *Rigid normal component* - The solid crust, the charged component and the portion of the neutron fluid that is outside the support of x_S are frozen into the magnetic field on very short timescales. This is justified as long as the normal component is locked on timescales much shorter than the spin-up timescale of the glitch (Easson, 1979). This rigid component is dubbed *p-component*; using cylindrical coordinates (x, φ, z), its velocity is given by $\mathbf{v}_p = x\Omega_p \hat{\mathbf{e}}_\varphi$. Following standard notation, the complement to the p-component is called *n-component*.

- *Inconsistency with GR* - As a first step, we construct a Newtonian dynamics on top of the relativistic TOV structure. This leads to a fundamental inconsistency:

from the Newtonian point of view the inertia is represented by the mass m_n, in GR by the enthalpy per particle $(\mathcal{E} + P)/n_B$ (as will be discussed in chapter (4)). In the layers where $P \ll \mathcal{E}$ we may consider $m_n n_B \approx \mathcal{E}/c^2$. We extend this non-rigorous identification, somewhat used in studies of the crust, to the whole star. We thus define a quantity ρ, the mass density, which in principle (at least in a strict Newtonian interpretation) should be $\rho = m_n n_B$, so that the partial mass density of the n-component is $\rho_n = m_n n_n = m_n y_n n_B$. In practice we leave ρ undefined and, in the numerical estimates, we will use $\rho = \mathcal{E}/c^2$, a choice resembling the interpretation of mass-energy density provided by the TOV equations. Of course the energy $\mathcal{E}$ cannot be split into the partial contribution from neutrons (since the proton-neutron gas is highly interacting). However we will use $\rho_n = y_n \mathcal{E}/c^2$ in the numerical estimates as well. We call this spurious prescription *quasi-Newtonian*. Full discussion of this approximation is possible only by introducing the appropriate relativistic corrections, as done in chapter (4).

- *Straight lines* - In order to project the 3D problem into a cylindrical one, we are forced to consider straight and paraxial vortex lines that extend trough the superfluid domain (identified by $y_n > 0$, or $x_S > 0$ if the actual superfluid fraction is provided by the EOS). In this case, in order to reduce the dimensionality of the problem, the momentum of the fluid is forced to have only azimuthal component, constant on cylindrical shells.

In numerical estimates we consider an *extreme scenario*: the superfluid component fills the spherical volume of radius R_d and is threaded by straight vortices, each carrying a quantum of circulation $\kappa = h/(2m_n)$, namely we take $x_S = y_n$ everywhere from the center to the drip point. The extreme scenario implements the hypothesis that normal matter vortex cores pass continuously through the crust-core phase transition, where no normal matter layer is expected (Zhou et al., 2004). This possibility of continuous vortex lines was already suggested by Ruderman (1976) as an alternative to the scenario of distinct vorticity in the crust and the core. However only the latter assumption has been implemented in the subsequent literature until the attempt to explain quasi-periodicity in the Vela glitches by Pizzochero (2011). Recent studies on vortex lines that pass trough the A-phase and B-phase of superfluid ^{3}He indicate a more complex behavior of vortices at the AB interface (Finne et al., 2006).

Therefore we are far from describing the hydrodynamical problem of a NS interior. However some of of these simplifications are tacitly assumed in the literature; for example, very few models of glitching pulsars exist in full GR and the rotational dynamics is typically Newtonian.
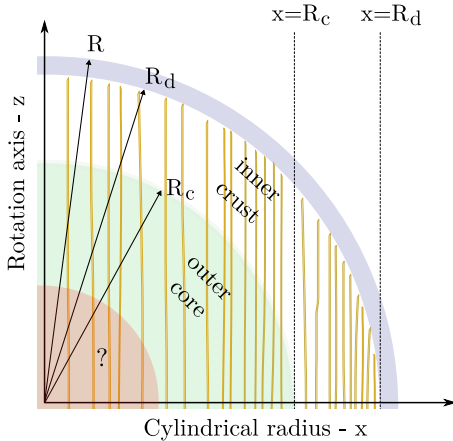
Figure 2.2: Sketch of the stellar structure (out of scale), with the geometrical definitions used. In the cylindrical shell $R_c < x < R_d$ the vortex lines are completely immersed in the inner crust. The outer crust (the thin blue layer in the figure) is part of the p-component. In principle vortices can stop at any spherical radius and all the input quantities of the model are automatically adjusted by following the integral prescriptions detailed in the text.

It is useful to introduce the following integrations along a straight line γ_x placed at distance x from the rotation axis [5]

$$a(x) = \int_{\gamma_x} \rho_n \, , \qquad b(x) = \int_{\gamma_x} \frac{\rho_n}{1 - \epsilon_n} \, , \qquad d(x) = \kappa^{-1} \int_{\gamma_x} \eta \, , \qquad (2.1)$$

where $\rho_n = y_n \rho$. It is also useful to introduce a normalized weight g that describes the distribution of moment of inertia of a cylindrical shell of radius x, defined as

$$\langle f \rangle = \int_0^{R_d} dx \, g(x) \, f(x) \, , \qquad g(x) = 2\pi \, x^3 \, b(x)/I_v \, . \qquad (2.2)$$

The normalization factor

$$I_v = \frac{8\pi}{3} \int_0^{R_d} dr \, r^4 \, \frac{\rho_n(r)}{1 - \epsilon_n(r)} \qquad (2.3)$$

reduces to the moment of inertia of the n-component if there is no entrainment. The presence of the factor y_n, automatically defines the region where superfluidity is present: for this reason in all these and subsequent definitions we fix the limits of radial integration to their extreme values, the interval $[0, R_d]$, without any loss of generality. Of course

$$I = \frac{8\pi}{3} \int dr \, r^4 \, \rho \qquad (2.4)$$

is the total Newtonian moment of inertia of the star.

---

[5] *Coordinates conventions* - We use standard spherical coordinates (r, θ, φ), where $\theta = 0$ denotes the positive direction of the rotational axis and $\theta = \pi/2$ is the equatorial plane. The coordinate φ is the azimuthal angle. We also use cylindrical coordinates (x, φ, z), defined as $x = r \sin \theta$ and $z = r \cos \theta$. The z-axis coincides with the rotational axis, whereas the inner-outer crust interface is the sphere of radius R_d, namely $(x, \varphi, \pm z(x))$ with $z(x) = (R_d^2 - x^2)^{1/2}$. The volume element d^3x in flat space is $d^3x = dx d\varphi dz \, x$ or $d^3x = dr d\theta d\varphi \sin \theta r^2$. Within the relativistic slow-rotation formalism of the last chapter, the spherical coordinates are Schwarzschild-like coordinates: in particular the coordinate $r = (x^2 + z^2)^{1/2}$ represents the circumferential radius.

2.3.2   Conservation of vorticity

In order to derive the dynamical equations we could start from the Euler equations for multifluid hydrodynamics, as in Haskell et al. (2013). However this kind of procedure is less transparent with respect to a direct construction of the equations of motion: in the hydrodynamical equations the mutual friction force is already given, here we derive it consistently with the assumed vortex dynamics. For this reason we prefer to present a constructive derivation, similar to that early proposed in the seminal work by Alpar et al. (1984). The effect of entrainment and of the non-homogeneous stellar structure have not been considered previously in such kind of constructions.

Macroscopic Feynman-Onsager relation (Stokes' theorem) - Following Prix et al. (2002), the superfluid momentum per particle is a linear superposition of the local kinematic velocities of the two components:

$$\mathbf{p}_n = m_n \left[(1 - \epsilon_n) \, \mathbf{v}_n + \epsilon_n \mathbf{v}_p \right] \quad \Rightarrow \quad \mathbf{p}_{np} = m_n m^* \mathbf{v}_{np} \,. \tag{2.5}$$

We use the general notation f_{xy} to indicate that the quantity f_x is seen in frame labeled by y. For example, the macroscopic vorticity $\boldsymbol{\omega}_n$, when seen in the frame of the normal component, is

$$\boldsymbol{\omega}_n = m_n^{-1} \, \nabla \times \mathbf{p}_n \quad \Rightarrow \quad \boldsymbol{\omega}_{np} = \boldsymbol{\omega}_n - 2 \, \Omega_p \, \hat{\mathbf{e}}_z \,. \tag{2.6}$$

At the mesoscopic scale, the momentum per (dripped) neutron $\mathbf{p}_n$ is related to the configuration of vortex lines via the Bohr-Sommerfeld quantization rule (Prix, 2004); at the macroscopic scale (i.e. for a large number of vortices) we can introduce a function $\mathcal{N}(\gamma)$ that is proportional to the flux of the macroscopic vorticity, namely

$$\int_\gamma \mathbf{p}_n \cdot d\mathbf{x} = \frac{h \mathcal{N}(\gamma)}{2} \,. \tag{2.7}$$

The Bohr-Sommerfeld quantization requires $\mathcal{N}(\gamma)$ to be the number of vortex lines enclosed by a generic closed path γ (therefore $\mathcal{N}(\gamma) \infty \mathbb{Z}$ is an index); the factor of 2 accounts for Cooper pairing of neutrons. Since $|\mathcal{N}(\gamma)| \gg 1$ at the macroscopic scale, we can safely neglect the integer nature of $\mathcal{N}$ and consider

$$m_n^{-1} \int_\Sigma \nabla \times \mathbf{p}_n = \kappa \mathcal{N}(\partial \Sigma) = \kappa \int_{\Sigma_\perp} n_v \, d^2 \Sigma_\perp, \qquad \mathcal{N}(\partial \Sigma) \in \mathbb{R} \,, \tag{2.8}$$

where $\Sigma_\perp$ is a surface normal to the vorticity field. Since $\mathcal{N}$ is interpreted as number of vortex lines, n_v is interpreted as the number of vortex lines per unit area of $\Sigma_\perp$.

A (non-preceding) neutron star has a definite total angular momentum of direction $\hat{L}$, imposed at birth. The macroscopic angular momentum can thus be considered as an external field that defines a preferred direction: we can use it to define an *auxiliary* variable Ω_v which has the dimensions of an angular velocity. Consider the flux of the macroscopic vorticity trough a surface Σ_L normal to $\hat{L}$

$$\Omega_v(\Sigma_L) = m_n^{-1} |\Sigma_L|^{-1} \int_{\Sigma_L} \nabla \times \mathbf{p}_n \,.$$

This non-local definition of the average angular velocity as the flux of vorticity, explains in a very natural and straightforward way the factor 2 between vorticity and angular velocity

for rigid-body rotation. Since this definition of Ω_v is not local, we do not have to expect that Ω_v coincides with the usual definition of angular velocity of a particle. Note however that in general the notion of angular velocity always needs a prescribed direction to be present, i.e. $\hat{L}$.

Since the surface Σ_L is orthogonal to a preferred direction, Σ_L is uniquely identified for every generic curve $\partial\Sigma$ which is the boundary of an oriented surface; therefore the alternative definition $\Omega_v(\partial\Sigma) = \kappa \, |\Sigma_L|^{-1} \mathcal{N}(\partial\Sigma)$ is completely equivalent.

On the other hand, the modulus of the vorticity $\kappa n_v = m_n^{-1} |\nabla \times \mathbf{p}_n| = \omega_n$ is an intrinsic quantity since no preferred direction has to be imposed; n_v is the density of vortices per unit area of a surface normal to the vorticity lines.

Macroscopic Feynman-Onsager relation (straight vortices) - We now specialize the above expressions to the particular case under study. Since $\mathcal{N}(\gamma)$ does not change if γ is translated along the z-axis, the azimuthal component of the momentum, $p_n^\varphi(x)$, is a function of the cylindrical radius only. Therefore the circulation of Eq (2.7) around a ring of radius x reads

$$x \, p_n^\varphi(x) \;=\; \frac{h}{2} \int_0^x dy \, y \, n_v(y) \,. \tag{2.9}$$

It is convenient to introduce a columnar angular velocity $\Omega_v(x)$ that automatically satisfies the usual single-component Feynman relation

$$\Omega_v(x) = \frac{p_n^\varphi(x)}{m_n \, x} \qquad \Rightarrow \qquad \Omega_v(x) = \frac{\kappa \, \mathcal{N}(x)}{2\pi \, x^2} \,. \tag{2.10}$$

From Eq (2.5), it immediately follows that $\Omega_{vp} = m^* \, \Omega_{np}$. More explicitly, $\Omega_{np}(x, z) = \Omega_{vp}(x)/(1 - \epsilon_n(r))$ namely the velocity field of the neutrons in not columnar. Stokes' theorem applied to Eq (2.9) implies that the density of vortex lines $n_v = 2h^{-1} |\nabla \times \mathbf{p}_n|$ is related to Ω_v via

$$\kappa n_v(x) = \omega_n = 2\Omega_v(x) + x\partial_x\Omega_v(x) \,. \tag{2.11}$$

This equation is not general but a consequence of the axial symmetry assumed in our model.

The definition in Eq (2.10) tells us that the dynamics of $\Omega_v(x, t)$ is indeed equivalent to the dynamics of $\mathcal{N}(x, t)$: loosely speaking Ω_v is the angular velocity of an abstract "vortex-component" or, better, it just counts the amount of vortex lines inside the radius x. The variable Ω_v can thus vary in time only if we let vortices to move trough the boundary of the cylindrical region of radius x.

Let $\mathbf{v}_L$ be the local average velocity of vortex lines. Since vortices cannot end into the bulk, we impose the conservation of the number of intersections of vortex lines with the

equatorial plane[6]

$$\partial_t n_v + \frac{1}{x}\partial_x(x\, n_v\, v_L^x) = 0 \quad \Rightarrow \quad \partial_t \Omega_v = -\left(2\Omega_v + x\partial_x\Omega_v\right)\frac{v_L^x(x,t)}{x} \ . \tag{2.12}$$

This is the equation that regulates the mutual friction torque between the superfluid and normal components: if vortex lines are perfectly pinned (i.e. $v_L^x = 0$), Ω_v cannot change and angular momentum transport is impossible: the two "v" and "p" components are completely decoupled.

2.3.3 Total angular momentum balance

The evolution of a non-magnetized and isolated neutron star is driven by the secular spin-down. The total angular momentum is radiated via some mechanism (see the appendix (B)), which is modeled by an external braking torque:

$$\int d^3x \ \mathbf{x} \times [\rho_n(r)\dot{\mathbf{v}}_n(x,z) + \rho_p(r)\dot{\mathbf{v}}_p(x)] \ = \ \mathbf{T}_{ext}\,, \tag{2.13}$$

where $\rho_y = x_y\rho$ for $y = n, p$. Under the no precession hypothesis the analysis is trivial and we can always write $\mathbf{T}_{ext} = -I|\Omega_\infty|\hat{\mathbf{e}}_z$ for some positive number $|\Omega_\infty|$. By ignoring the difference in the mass per baryon of two components, the local property $y_n\epsilon_n = y_p\epsilon_p$ (Carter et al., 2006) allows to write the second equation of the dynamical model as

$$I_p\, \partial_t\Omega_p(t) + \int d^3x\ (\rho_n/m^*)\, x^2\, \partial_t\, \Omega_v(x,t) \ = \ -|\Omega_\infty|\, I\,. \tag{2.14}$$

Note that this equation is very different from that proposed by Link (2014), where an extra torque due to a third component (which is supposed to be almost always completely decoupled) is introduced. Such an additional term is de facto an impulsive external torque that is introduced to generate a glitch. On the other hand, in our model the angular momentum is always strictly conserved if the electromagnetic emission is switched off: a glitch can thus be triggered by a temporal discontinuity, or rapid change, in v_L^x.

2.3.4 Relation between vortex velocity and lag

Equations (2.12) and (2.14) provide a close set of partial differential equations for Ω_v and Ω_p only after some reasonable dependence of the local velocity v_L^x from the dynamical

---

[6] Consider the curl of Euler equation for a barotropic fluid with conservative forces. In this case the barotropic term in the associated vorticity equation vanishes and we are left with $\nabla \times (D_t\mathbf{v}) = 0$, that can be written as

$$\omega^i \ = \ \epsilon^{iab}\,\nabla_a\, v_b\,, \qquad \partial_t\,\omega^i \ + \ \epsilon^{iab}\,\epsilon_{lmb}\,\nabla_a\,(\omega^l\, v^m) \ = \ 0\,,$$

meaning that the vorticity is frozen into the fluid (Kelvin's theorem). Consider the above equation but let v^i be a generic velocity, say v_L^i. Because of the cross product we can restrict ourselves to consider only those v_L^i that have no components parallel to ω_i. In our case $\omega^i = \kappa n_v \delta_z^i$ and we obtain a simpler form of the vorticity transport,

$$\partial_t n_v + \nabla \cdot (n_v\mathbf{v}_L) - \partial_z(n_v v_L^z) = 0\,.$$

For both straight and curved vortices, the local velocity of a vortex segment is defined to be normal to the vortex line. This is quite intuitive since if the particles that comprise the vortex's core flow along the core itself, the vortex does not move. The transport velocity $\mathbf{v}_L$ is thus assumed to be orthogonal to the vorticity and the last term in the above equation can be dropped.

variables Ω_v and Ω_p is given: we need to find out a plausible form of the mutual friction. As we are going to see, this is the most difficult point and some arbitrary choices are unavoidable.

In complete generality we can introduce a functional $\mathcal{B}$, defined as

$$v_L^x = x\,\mathcal{B}[\Omega_v, \Omega_p, x]\,(\Omega_v(x) - \Omega_p)\,. \tag{2.15}$$

The explicit form of $\mathcal{B}$ depends on the details of vortex dynamics. We study the standard case proposed by Epstein and Baym (1992), based on earlier works on the motion of vortices in liquid ^{4}He and superconductors [see e.g. Nozières and Vinen (1966)]: in the frame of the crust a vortex line experiences a viscous drag force per unit length $\mathbf{f}_D$ and a Magnus force $\mathbf{f}_M$ that are locally expressed as

$$\mathbf{f}_D(\mathbf{x}) = -\eta(r)\,\mathbf{v}_{Lp}(\mathbf{x})\,, \tag{2.16}$$

$$\mathbf{f}_M(\mathbf{x}) = \rho_n(r)\,\kappa\,\hat{\kappa} \times [\mathbf{v}_{Lp}(\mathbf{x}) - \mathbf{v}_{np}(\mathbf{x})]\,. \tag{2.17}$$

The parameter η is sometimes referred to as *mobility* in studies of vortex dynamics in type-II superconductors: in this case the Magnus force is replaced by the Lorentz force on a vortex (Thomann et al., 2017).

As discussed in Andersson et al. (2006), the presence of entrainment does not modify the form of the Magnus force, providing that the unit vector $\hat{\kappa}$ is directed along $\nabla \times \mathbf{p_n}$. In the present case of straight vortices we have that $\hat{\kappa} = \hat{\mathbf{e}}_z$, which is *not* along $\nabla \times \mathbf{v_n}$ unless $\epsilon_n = 0$.

The Kelvin's circulation theorem for ideal and barotropic fluids implies that free vortices in a background flow are transported with the fluid, thus behaving like massless particles. However in a superfluid, the presence of normal matter into the vortex core can be taken into account by introducing an effective mass per unit length (Baym and Chandler, 1983). We will ignore this correction: since there is no inertia, the equation of motion for straight and rigid vortices is postulated[7] to be

$$\int_{\gamma_x} \mathbf{f}_M + \mathbf{f}_D = 0 \quad \Rightarrow \quad \begin{aligned} &\int dz\,\left[\eta v_{Lp}^x(x) + \kappa\rho_n(v_{Lp}^\varphi(x) - v_{np}^\varphi(x,z))\right] = 0 \\ &\int dz\,[\eta(v_L^\varphi(x) - x\Omega_p) - \kappa\rho_n v_L^x(x)] = 0\,. \end{aligned}$$

Replacing the variable Ω_n in favor of Ω_v and using the definitions given in Eq (2.1), the solution of this system is

$$v_{Lp}^x = \mathcal{B}^x\,x\,\Omega_{vp} \qquad\qquad \mathcal{B}^x(x) = \frac{d(x)\,b(x)}{d(x)^2 + a(x)^2} \tag{2.18}$$

$$v_{Lp}^\varphi = \mathcal{B}^\varphi\,x\,\Omega_{vp} \qquad\qquad \mathcal{B}^\varphi(x) = \frac{a(x)\,b(x)}{d(x)^2 + a(x)^2}\,. \tag{2.19}$$

where the x-dependence is understood. Coherently with the general notation used here, the lag Ω_{vp} has been defined as

$$\Omega_{vp}(x,t) = \Omega_v(x,t) - \Omega_p(t) = (1 - \epsilon_n)^{-1}\Omega_{np}(x,z,t)\,. \tag{2.20}$$

---

[7] It is this assumed non-local form of the equation of motion for vortex lines that provides a definition of our concept of rigidity: the sum of all the local forces along a rigid line must vanish. It is worth to note that, given this definition of infinite tension, the vortex dynamical equations turn out to be formally equivalent to the equations of motion for a single tensionless vortex, as discussed in (Haskell and Melatos, 2016).

In this simple example the functional $\mathcal{B}$ is only dependent on the cylindrical radius x, namely it is just a function $\mathcal{B}[\Omega_v, \Omega_p, x] = \mathcal{B}^x(x)$. Equations (2.18) and (2.19) imply that, in the frame of reference of the crust, the velocity of vortex lines at radius x forms an angle $\tan d(x)/a(x)$ with respect to $\hat{\mathbf{e}}_\varphi$. The fastest expulsion of vortex lines occurs when η is such that $d(x) \approx a(x)$. Of course the present analysis, that generalizes the early local approach of Epstein and Baym (1992) in the presence of entrainment and for a non-uniform star, can very easily made local when the rigidity assumption is dropped, as discussed in App (D).

A final remark is due: the non-linear effect of pinning has not already been introduced, so that the present analysis (provided that the parameter η is known) is valid far from the unpinning transition. The equations (2.18) and (2.19) can be interpreted as the asymptotic (average) velocity of vortex lines when the lag Ω_{vp} is well below a certain threshold.

2.3.5   Effective pinning

When a pinning force per unit length $\mathbf{f}_P(\mathbf{x})$ acts on a segment of vortex line at $\mathbf{x}$, the general equation of motion for rigid vortices becomes

$$\int_{\gamma_x} \mathbf{f}_M(\mathbf{x}) + \mathbf{f}_D(\mathbf{x}) + \mathbf{f}_P(\mathbf{x}) = 0\,.$$

The vectorial quantity $\mathbf{f}_P(\mathbf{x})$ is unfortunately unknown and probably not even well defined, even if there are attempts to model it at the mesoscopic scale as the gradient od a spherical pinning potential (Warszawski and Melatos, 2012; Haskell and Melatos, 2016). As it stands, the general and complete form of the functional $\mathcal{B}$ resulting from the solution of the above equation is precluded, due to the uncertain nature of the pinning term. We thus have to follow another route, based on the physical intuition rather than on a well-defined mathematical formalization.

The threshold effect of pinning is expected to introduce explicit and non-smooth dependence of $\mathcal{B}$ on the dynamical variables Ω_p and Ω_{vp}. We have to face to two alternatives:

Creep-like prescription - Pinning can be modeled by considering that only a fraction Y of (unpinned) vortex lines is free to move. This is equivalent to say that the functional $\mathcal{B}$ can be approximated by

$$\mathcal{B}[\Omega_v, \Omega_p, x] \approx Y[\Omega_{vp}, x]\, \mathcal{B}^x(x)\,. \tag{2.21}$$

The factor $Y \in [0, 1]$ modulates the mutual friction and can be equally interpreted as a parameter that slows the expulsion of vortex lines or as the fraction of (unpinned) vortex lines that are free to move under the combined action of $\mathbf{f}_M$ and $\mathbf{f}_D$. By considering a large population of vortices around the radius x, we can also interpret Y as a *probability for unpinning* (Jahan-Miri, 2006). The simplest way to encode pinning at the macroscopic scale is thus to construct Y in such a way that

$$Y[\Omega_{vp}, x] \approx 0 \qquad \text{if} \quad |\Omega_{vp}(x)| < f_Y(x) \tag{2.22}$$

$$Y[\Omega_{vp}, x] \approx 1 \qquad \text{if} \quad |\Omega_{vp}(x)| \simeq f_Y(x)\,, \tag{2.23}$$

for some function $f_Y(x)$ that must be chosen or estimated with an argument external to the model. Since $f_Y(x)$ has cylindrical symmetry, it cannot be a fundamental

input of the model, unless a local spherical model for slack (i.e. tensionless) vortex lines is considered, as discussed in the next chapter.

This is indeed the prescription used in vortex-creep models, where the effect of the velocity lag between the two components is to modulate the typical velocity of free vortices: finite temperature, quantum effects[8] and finite vortex tension take part in smoothing the step-like form of Y. As an explicit example, the original non-entrained model of Alpar et al. (1984) in the regime $0 < \Omega_{np} < f_Y$ is realized by

$$Y[\Omega_{np}] \approx \exp\left(\frac{\Omega_{np} - f_Y}{\alpha \, f_Y}\right),$$

where α is a dimensionless temperature that tunes the local rigidity of the pinning and f_Y is an opportune critical lag estimated from pinning energies. Within this model, Alpar et al. (1989) showed that the vortex-lattice interaction can also lead to strong linear drag, a particular realization of thermal creep which can be linearized under certain conditions in the crust. Also the more recent and detailed treatment of thermally-activated creep proposed by Link (2014) uses a similar parametrization of the mutual friction force (however the inclusion of entrainment and spherical stratification in this kind of cylindrical is non-rigorous).

Drag prescription - Pinning can be modeled as very strong drag, at the point that the vortex is carried into corotation with the crust. An infinite drag is dissipationless since $\mathcal{B}^x$ goes to zero for $\eta \to \infty$. To model pinning we can drop $\mathbf{f}_P$ and consider instead a local functional $\eta[r, v_{Ln}]$ in Eq (2.16), where $v_{Ln} = |\mathbf{v}_{Ln}|$. In this case, depending on the form of η, the solution of the equation of motion can be difficult to study, even in its non-local form $\mathbf{f}_D + \mathbf{f}_M = 0$. The solution of the equations in their non-local form is even more tricky. In a local hydrodynamical model with no particular symmetries, we could attempt to solve the vortex dynamics by considering a generic mobility η such that

$$\eta[r, v_{Ln}] \simeq \eta(r) \qquad \text{if} \quad v_{Ln} \simeq f_\eta(r)$$
$$\eta[r, v_{Ln}] \gg \kappa \rho_n(r) \qquad \text{if} \quad v_{Ln} < f_\eta(r),$$

where f_η sets the strength of the local pinning mechanism and $\eta(r)$ is the local drag parameter of Eq (2.16) which arises far from the pinned state. The two regimes defined by $v_{Ln} < f_\eta(r)$ (quasi-conservative regime) and $v_{Ln} \gtrsim f_\eta(r)$ (dissipative regime) are discussed in the appendix (D).

As long as vortices are meant to be rigid we will not consider here the second possibility which seems more suitable for tensionless vortex lines. We thus use Eq (2.22) in which the threshold $f_Y(x)$ is provided by the prescription proposed by Pizzochero (2011): the Magnus force and the unknown pinning force $\mathbf{f}_P$ are integrated to obtain an estimate of their total values on a vortex.

The quantity $f_P(\rho)$ studied in Seveso et al. (2016) is not interpreted as the modulus of $\mathbf{f}_P$. Rather, it represents the maximum value that the pinning force can sustain before letting the vortex free to move, much like the static friction force: we thus set $f_Y(x) = \Omega_{vp}^{cr}(x)$ in Eq (2.22), where

$$\kappa \int_{\gamma_x} \rho_n \, x \, \Omega_{vp}^{cr} = \int_{\gamma_x} f_P \quad \Rightarrow \quad \Omega_{vp}^{cr}(x) = \frac{1}{\kappa \, x \, b(x)} \int_{\gamma_x} f_P. \tag{2.24}$$

---

[8] Quantum tunneling sets a lower limit to the creep rate at low temperatures (Link et al., 1993).

In principle there is no fundamental reason for saying that $f_Y(x) = \Omega_{vp}^{cr}(x)$; this point could be taken as a further defining property of the ideally rigid vortices. From the phenomenological point of view this prescription has been tested in the hydrodynamical simulations of Haskell et al. (2013) and Seveso (2015). However we will provide a check of the interpretation $f_P = |\mathbf{f}_M|_{max}$ by studying also an alternative scenario of completely loose vortex lines in the next chapter.

Improving the friction term - Vortices in an hydrodynamical model only serve to construct a particular form of the mutual friction torque in terms of the dynamical variables (in our global model we shifted this problem on $\mathcal{B}$ which regulates the coupling between the components). A glitch can then be triggered by perturbing $\mathcal{B}$ or, more specifically, by suddenly increasing the Y fraction in some interval of x; this would mimic the sudden artificial unpinning of many vortices. At the mesoscopic scale however things are much different and more complex, as simulations of the vortex unpinning mechanism suggest (Link and Epstein, 1991; Link, 2009). Moreover a compete model should account for the possible auto-regulation of the unpinning process at the mesoscopic and macroscopic scale.

Other contributions to the vortex dynamics (that could have a significant impact on mutual friction) arise from the finite tension force of vortices originating from the quantized superflow around the core, as well as their mutual interaction (Haskell and Melatos, 2016; Wlazlowski et al., 2016): dropping the straight vortex description, the sum of all the local forces acting on a vortex (including tension on a bent line and eventually a mean-field force induced by the vortex-lattice) should vanish on a segment of vortex line.

Self-interaction forces that further complicate the picture are present for lines with a small curvature radius, as it is clearly recognizable within the vortex-line filament model of Schwarz (Barenghi et al., 2001).

Moreover the radiation of phonons during the pinning and unpinning of a vortex line and proximity effect when two lines are close are important at a microscopic scale Warszawski and Melatos (2012): these precesses may provide the physics needed to explain the claimed self-organized criticality of glitching pulsars Melatos et al. (2008). All these aspects are mesoscopic, and to date none of them can be modeled as by means of fundamental quantum mechanics: this may not a big problem since we still have to understand how to include the physics of the mesoscopic scale into hydrodynamical formulations. Further work is therefore needed to understand how these issues impact on the form of the macroscopic mutual friction. Better understanding of the effective modellization of the motion of vortices can come from the study of laboratory type-II superconductivity (Geller et al., 1998; Mints and Papiashvili, 2005).

2.3.6   Dynamical equations of the model

With the aid of the definition given in Eq (2.2) we can rewrite the Eqs (2.12) and (2.14) in a more compact form as

$$I_p \dot{\Omega}_p = -I |\dot{\Omega}_\infty| - I_v \langle \dot{\Omega}_{MF} \rangle \tag{2.25}$$

$$I_v \dot{\Omega}_v = I_v \dot{\Omega}_{MF} \tag{2.26}$$

where the cylindrical average is that of in Eq (2.2) and the mutual friction torque $I_v \dot{\Omega}_{MF}$ has been introduced:

$$\dot{\Omega}_{MF} = -\mathcal{B} \left(2\Omega_p + 2\Omega_{vp} + x\partial_x \Omega_{vp} \right) \Omega_{vp} . \tag{2.27}$$

It is also interesting to write the above equations as a system for a differential variable, $\delta\Omega_{vp} = \Omega_{vp} - \langle\Omega_{vp}\rangle = \delta\Omega_v$, and two rigid variables, $\langle\Omega_{vp}\rangle$ and Ω_p:

$$I\,\dot{\Omega}_p + I_v\langle\dot{\Omega}_{vp}\rangle = -I|\dot{\Omega}_\infty| \tag{2.28}$$

$$I_p\,\langle\dot{\Omega}_{vp}\rangle = I\,|\dot{\Omega}_\infty| + I\,\langle\dot{\Omega}_{MF}\rangle \tag{2.29}$$

$$\delta\dot{\Omega}_{vp} = \delta\dot{\Omega}_{MF}\,. \tag{2.30}$$

Clearly, the rigid part of the system is consistent with the general form expected for two-components glitch models in absence of precession, see App (C).

Steady state - Provided that the braking torque itself is not evolving, the value of $|\dot{\Omega}_\infty|$ coincides with the absolute value of the observed spin-down rate, averaged over a long period of time (even if in this period the pulsar glitched several times). By requiring that the star spins down as a whole, we obtain a very restrictive definition of steady state: $\dot{\Omega}_p = \dot{\Omega}_v$ everywhere, namely

$$\mathcal{B}\left(2\Omega_p + 2\Omega_{vp} + x\partial_x\Omega_{vp}\right)\Omega_{vp} = |\dot{\Omega}_\infty| \quad\Rightarrow\quad \Omega_{vp}^\infty(x) \approx \frac{|\dot{\Omega}_\infty|}{2\,\Omega_p\,\mathcal{B}_\infty}, \tag{2.31}$$

where the implicit solution of the equation depends on the properties of the function $\mathcal{B}_\infty(x) = \mathcal{B}[\Omega_{vp}^\infty, x]$, which (in this case) depends on x only.

It is possible to relax this notion of steady state by inserting $\Omega_p = -|\dot{\Omega}_\infty|$ into Eq (2.28); we obtain a less restrictive realization of the steady state,

$$\langle\,\mathcal{B}\left(2\Omega_p + 2\Omega_{vp} + x\partial_x\Omega_{vp}\right)\Omega_{vp}\,\rangle = |\dot{\Omega}_\infty| \quad\Rightarrow\quad \langle\Omega_{vp}^\infty(x)\rangle \approx \frac{|\dot{\Omega}_\infty|}{2\,\Omega_p\,\langle\mathcal{B}_\infty\rangle}, \tag{2.32}$$

where the approximations involved are sketched in the next section (this can also be checked a posteriori by inserting the numerical profiles). In this case $\delta\Omega_{vp}$ can have its own dynamics, provided the constraint in Eq (2.32) is fulfilled.

We can adapt a simple reasoning proposed by Greenstein (1975) to calculate the energy dissipated at the steady state in presence of entrainment. In our case the dissipated kinetic energy $\dot{\mathcal{E}}_k = \partial_t(\rho_n v_n^2 + \rho_p v_p^2)$, which at the order $O(\Omega_{vp})$ can be written as

$$\dot{\mathcal{E}}_k = -\rho x^2\Omega_p|\dot{\Omega}_\infty| + (x^2\rho_n/m^*)\,(\delta\dot{\Omega}_{vp}\Omega_p - |\dot{\Omega}_\infty|\Omega_{vp}^\infty) < 0\,.$$

Integrating this local contribution over the whole star we obtain

$$-\int d^3x\,\dot{\mathcal{E}}_k = I\Omega_p|\dot{\Omega}_\infty| + I_v|\dot{\Omega}_\infty|\langle\Omega_{vp}^\infty\rangle\,.$$

The first term is the spin-down luminosity [the power radiated via the braking mechanism (Alpar and Baykal, 2006)]; the second term can be evaluated using Eq (2.32) and gives an estimate of the total rate of heat generated by friction: since it is second order in the small spin-down rate, the kinetic energy of a RPP is lost mostly by the radiation mechanism, while the internal torque provides only a very small correction. However the heat generated in the bulk by the mutual friction can still play an important role in more refined hydrodynamical models, where the coupled thermo-rotational evolution is considered. Also the energy released in a neutron star interior during the glitch event

produces extra heat, part of which diffuses trough the outer layers and may result in a thermal afterglow from the surface. However, simple estimates indicate that the detection of the thermal afterglow in pulsars is unlikely because their non-thermal radiation is much more intense.

Reduction to a rigid model - The standard rigid model defined by Eqs (C.1) and (C.2) can be a reasonable approximation of the Eqs. (2.26) and (2.25) when the Eqs (2.29) and (2.28) decouple from Eq (2.30). Clearly, this possibility depends on the particular form of $\dot{\Omega}_{MF}$. We restrict our attention to a finite time interval during which the friction functional $\mathcal{B}$ does not vary. Eventually the friction term can be approximated with an effective function of x only, $\mathcal{B} \approx \mathcal{B}_{\text{eff}}^x(x)$. With this assumption, the decoupling of the rigid equations is obtained by dropping the term $x\partial_x\delta\Omega_{vp}$ and taking in $\dot{\Omega}_{MF}$ only the terms that are up to first order in the deviations from the cylindrical average:

$$\langle\dot{\Omega}_{MF}\rangle \approx 2\langle\mathcal{B}_{\text{eff}}^x\rangle\langle\Omega_{vp}\rangle\Omega_p\,. \tag{2.33}$$

In this way the dynamics of Ω_p and $\langle\Omega_{vp}\rangle$ does not depend on $\delta\Omega_{vp}$. Now, if we identify Ω_o with Ω_p and Ω_i with $\Omega_p + \langle\Omega_{vp}\rangle$, the Eqs (2.29) and (2.28) are equivalent to Eqs (C.1) and (C.2). It also follows that the relaxation time τ^R and the coupling time τ^C can be estimated as

$$\tau^R = \frac{1}{2\langle\mathcal{B}_{\text{eff}}^x\rangle\Omega_p} \qquad\qquad \tau^C = \frac{I_p/I}{2\langle\mathcal{B}_{\text{eff}}^x\rangle\Omega_p}\,. \tag{2.34}$$

The relaxation time given here should be intended as the characteristic timescale of a body-averaged model in a particular dynamical phase described by $\langle\mathcal{B}_{\text{eff}}^x\rangle$. This also gives a microphysical interpretation of the phenomenological parameter τ^R, that can be fitted from observations.

2.4   Numerical estimates

The dynamical equation that have been derived depend on various inputs that van be found by using the integration prescriptions: in this section we briefly discuss the inputs that we use.

As already mentioned, for a given central mass density and given EOS, the stellar structure is fixed by solving the TOV equations, , reviewed in App (A). However, since we are dealing with Newtonian moments of inertia, we do not implement the general relativistic conversion between the baryon number density n_B and the energy density $\rho = \mathcal{E}/c^2$. *EOS* - We use the SLy EOS proposed in Douchin and Haensel (2001) as a unified description of the whole star (except for the outer crust that is almost irrelevant in glitch models). The EOS provides the relation $P(\rho)$ and the fraction of non-bound neutrons $y_n(\rho)$ (shown in Fig. (2.3)). This equation of state predicts a first order phase transition where nuclear clusters dissolve into homogeneous matter at baryon density $n \sim 0.76\,\text{fm}^{-3}$, corresponding to $\rho_c \approx 1.3 \times 10^{14}\,\text{g/cm}^3$. To value of R_d marks the onset of neutron drip (a second-order phase transition) at the mass density $\rho_d = 4.3 \times 10^{11}\,\text{g/cm}^3$ (Haensel et al., 2007).

At the crust-core interface, matter strongly stiffens due to the disappearance of nuclei: a two-phase nucleon system changes into a single-phase one, and repulsive nucleon-nucleon interaction is no longer countered by softening effects resulting from the presence of the lattice-gas phase coexistence. For the SLy EOS, the crust-core transition turns out to
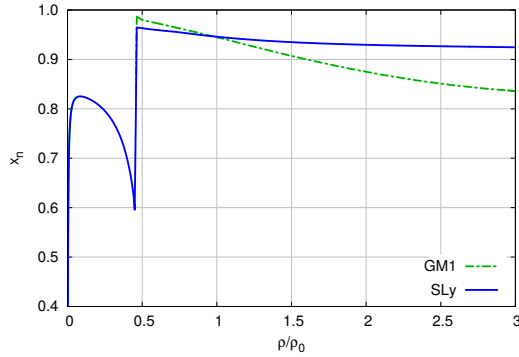
Figure 2.3: The fraction $y_n = n_n/n_B$ as a function of ρ used in our examples: the blue solid line is the fraction provided by the Sly EOS, obtained by joining the data in Table 1 and Table 4 of Douchin and Haensel (2001). Here we show also the superfluid fraction consistent with the GM1 EOS in the core (dashed line). Below the drip point we have $y_n = 0$ since no free neutrons are present. In the inner-crust y_n is the fraction of superfluid nucleons in the neutron gas outside nuclei: this quantity has a sharp dip at the crust-core interface since nuclei dissolve and all the neutrons contribute to the superfluid liquid.
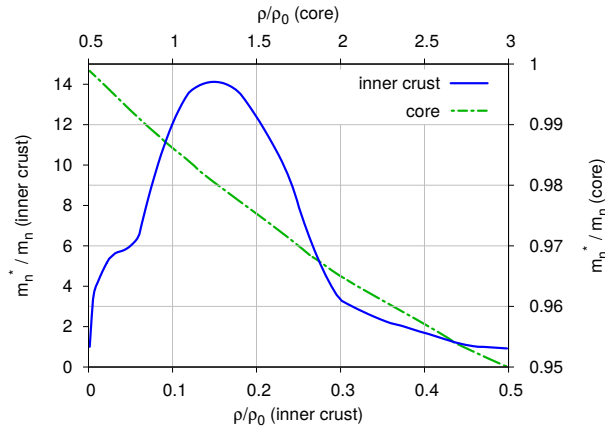
Figure 2.4: The effective neutron mass m^* in the crust (solid line), obtained by interpolating the values reported by Chamel (2012), and in the core [from Chamel and Haensel (2006), dashed line]. The crust-core interface corresponds to $\rho_c \approx 0.47\,\rho_0$. The original entrainment profile has been interpolated.

be a very weak first-order phase transition, with relative density jump predicted by the Maxwell construction of about one percent.

For comparison we also use the stiffer GM1 equation of state of Glendenning and Moszkowski (1991) in the core (i.e. for $\rho > \rho_c$), while keeping the SLy to describe the crust. The corresponding y_n fraction is shown in Fig (2.3).

Entrainment - We use the effective neutron mass m_n^* given in Chamel and Haensel (2006) and in Chamel (2012) for the crust and the core respectively, see Fig. (2.4). It is evident from the figure that m^* depends strongly on density in the inner crust. The
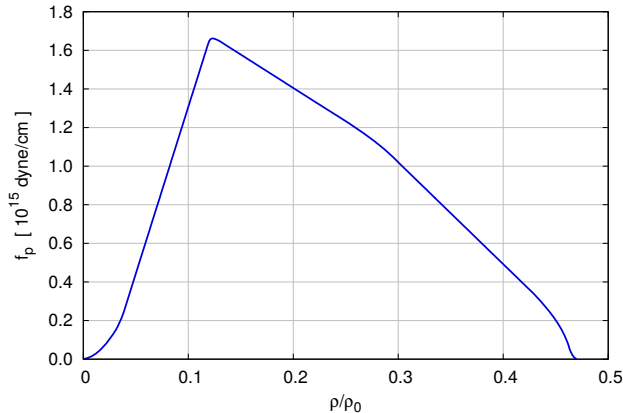
Figure 2.5: The pinning force profile per unit length f_p used to calculate Ω_{vp}^{cr} in units of 10^{15} dyne/cm. We constrain the pinning force profile to be zero outside the density range $\rho_d < \rho < \rho_c$. The original profile has been interpolated.

entrainment parameters that we use in this work are obtained from the effective masses as $\epsilon_n = 1 - m_n^*/m_n$ and $\epsilon_p = y_n \epsilon_n/(1 - y_n)$. At the transition between crust and core the effective mass is settled to unity.

Pinning force - In order to estimate the critical profile in Eq (2.24), we need the pinning threshold f_p resulting from the vortex-lattice interaction in the inner crust. Seveso et al. (2016) have proposed a numerical simulations to evaluate $f_p(n_B)$ at different densities n_B in the inner crust, which accounts for finite *single* vortex tension and random orientation with respect to the lattice. We use the pinning profile corresponding to in-medium suppressed pairing gap [the case $\beta = 3$ and $L = 5000$ of Seveso et al. (2016), see table 3 therein], as shown in Fig (2.5).

Pinning to fluxtubes - Theoretical estimates based on the proton coherence length suggest that the protons in the core could form a type-II superconductor (Baym et al., 1970); hence the vortex motion could also be impeded by the interaction with the magnetic fluxtubes. The current estimates, based on aligned vortex-fluxtube configurations, suggest strong pinning in the core comparable to crustal pinning (Ruderman et al., 1998). However, following the phenomenological study of Haskell et al. (2013), this extra pinning interaction should be small except for magnetars. We are currently studying this issue along the same lines of Seveso et al. (2016) and the first findings have been reported in Seveso (2015): much like crustal pinning is weaker once non-aligned configurations are taken into account, preliminary results indicate a similar reduction for pinning in the core too, with only ultra-strong magnetic fields which are likely to provide considerable vortex-fluxtube interaction.

Core pinning is a very open and debated point that has deep impact on the dynamics of the superfluid vortices in the core (Sidery and Alpar, 2009). Here we force f_P to be zero outside the crust; our general model, however, allows different prescriptions to be tested. Note that even pinning forces in the crust are very poorly known, since at the moment the only detailed and density-dependent estimate of the mesoscopic vortex-lattice
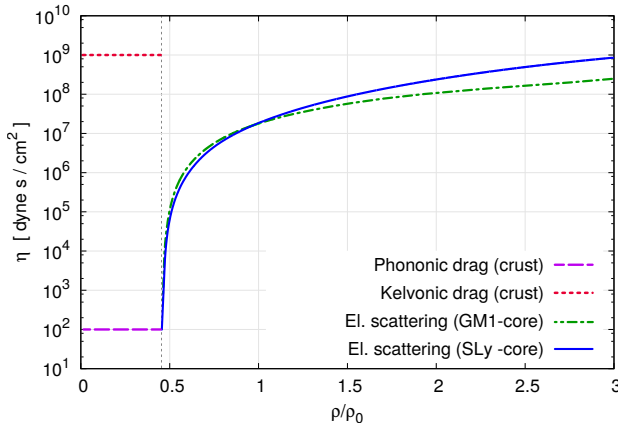
Figure 2.6: Example of viscous drag parameter $\eta(\rho)$: in the core ($\rho > 0.47\rho_0$) the dominant dissipative channel is provided by the electron scattering off magnetized vortex lines. In this case $\eta(\rho)$ is given by Eq (2.35). In the crust ($\rho_d < \rho < \rho_c$) we consider two dissipative mechanisms: the excitation of phonons in the crustal lattice (purple dashed line) or the excitation of Kelvin waves in the vortex cores (red dotted line).

interaction at the mesoscopic scale is that of Seveso and coworkers.

Drag parameter - The drag parameter η is probably the less studied microphysical input that we need: any realistic treatment of the drag exerted on vortices implies the study of many dissipative channels (both at the mesoscopic and quantum scale), including the excitation of quasiparticles in the vortex core. Eventually we can take into account only the dominant ones in each region of the star. Andersson et al. (2006) proposed an estimate of the drag on vortex lines due to the electron scattering off vortex lines:

$$\eta_{es} \approx 6.1 \times 10^{-5} \, \kappa \, y_n \, y_p^{7/6} \, \rho^{7/6} \, \frac{\epsilon_p^2}{\sqrt{1-\epsilon_p}} \left(\frac{\text{cm}^3}{\text{g}} \right)^{1/6} , \qquad (2.35)$$

where $y_p = 1 - y_n$, $\epsilon_p = y_n \epsilon_n / y_p$ (Chamel and Haensel, 2006). According to this picture, the mobility coefficient η_{es} is calculated by considering that the vortices in the core are magnetized due to the entrainment effect between the neutron superfluid and the proton superconductor [see also Alpar et al. (1984b)]. Electrons can thus be scattered by the magnetized vortex, imparting a drag on the normal matter which fills the vortex core. For this reason the above estimate is valid only for $\rho > \rho_c$, while $\eta_{es} = 0$ in the crust since no dripped protons are present.

On the other hand, for $\rho < \rho_c$ the vortices excite phonons[9] in the crustal lattice during their unpinned motion (Jones, 1990; Epstein and Baym, 1992).

---

[9] Following Jones (1990), the mobility coefficient due to the excitation of lattice phonons is given by

$$\eta_{ph} = 0.053 \, \frac{a}{\xi^3} \frac{E_p^2}{M_i \, c_s^3} \approx 0.16 \, \frac{f_p^2}{\rho_p \, \xi \, c_s^3} ,$$

where a is the lattice spacing, $\xi \sim 5 - 100$ fm is the coherence length of the superfluid, M_i is the mass of the ions, E_p the pinning energy per nucleus and $c_s \sim 10^9$ cm/s is the local speed of sound in the inner crust. Assuming a bcc lattice and neglecting the mass contribution of the electrons, i.e. $\rho_p = 2M_i/a^3$. In

Table 2.1: Some stellar structure parameters are given for three different masses. Neutron drip starts at $r = R_d$, where $\rho_d \approx 1.53 \times 10^{-3}\,\rho_0$. Similarly R_c is the core radius and corresponds to $\rho_c \approx 0.47\,\rho_0$. The upper panel refers to the SLy EOS. In the lower panel we use the GM1 EOS, together with its consistent $y_n(\rho)$ in the core. In the crust nothing changes with respect to the SLy case.

M	R_d	R_c	$I/10^{45}$	I_v	I_v
($M_\odot$)	(km)	(R_d)	(g cm^2)	(I)	(I_p)
1.1	11.41	0.936	0.86	0.928	12.9
1.4	11.43	0.953	1.09	0.941	16.1
1.9	10.92	0.974	1.35	0.958	22.9
1.1	13.08	0.926	1.14	0.901	9.2
1.4	13.28	0.945	1.51	0.913	10.5
1.9	13.24	0.966	2.04	0.916	10.9

This effect is the likely dissipation channel when the relative velocity between the vortex line and the lattice is small ($|\mathbf{v}_L - \mathbf{v}_p| < 10^2$ cm s^{-1}). When the velocity of vortex lines relative to the lattice nuclei is much higher, other dissipative processes come into the play, like the creation of Kelvin waves in the vortex cores (Jones, 1992).

At present only rough estimates of the drag parameter in the crust can be found in the literature. For this reason, we decide to take as a title of example a fiducial constant value for the phonon-drag parameter in the inner crust, namely $\eta_{ph} \sim 10^2$ g s^{-1}cm^{-1}. The drag associated to excitation of Kelvin waves is roughly seven orders of magnitude greater than the phonon-drag, thus we consider $\eta_{kw} \sim 10^9$ g s^{-1}cm^{-1}. This choice is made on the basis of the inferred phenomenological parameters presented in Haskell et al. (2013), see Table 1 therein. Figure (2.6) shows the two full drag profiles as a function of the density; in both cases the mechanism that dominates dissipation in the core is still given by Eq (2.35).

The fact that for different vortex velocities we have to interpolate between the phonon-drag and a kelvon-drag is a direct manifestation of the fact that the power dissipated per unit length by a vortex is not in general of the form $\eta(\mathbf{v}_L - \mathbf{v}_p)^2$.

2.4.1 Estimate of the cylindrical profiles

We use the physical input described in the previous section to construct the profiles $\mathcal{B}^x$, Ω_{vp}^{cr} and g. To study how the input of our model are sensitive to a change of the EOS in the core, we use SLy and the much stiffer GM1. For both cases (SLy for the whole star or GM1 in the core plus SLy in the crust), the structural parameters are summarized in Table (2.1).   We present the results for the SLy case only, since the profiles obtained using GM1 in the core are qualitatively similar. Since the radius x can rescaled at will in our dynamical equations, the actual value of R_d is irrelevant in our model and it is thus rescaled to unity in the plots: this allows to compare stars with different mass-radius relations.

Moment of inertia density - In Fig (2.7) we plot the weight $g(x)$, the fundamental

---

principle, we can directly use the values of E_p calculated by Donati and Pizzochero (2006), or estimate the parameter E_p according to the prescription of Alpar et al. (1984), namely $E_p \sim f_p\, a\, \xi$, so that the second (approximate) equality follows. All these quantities are not constant in the inner crust and the above formula is only an order of magnitude estimate for η_{ph}, which depends on the local velocity of sound (and therefore on the EOS).
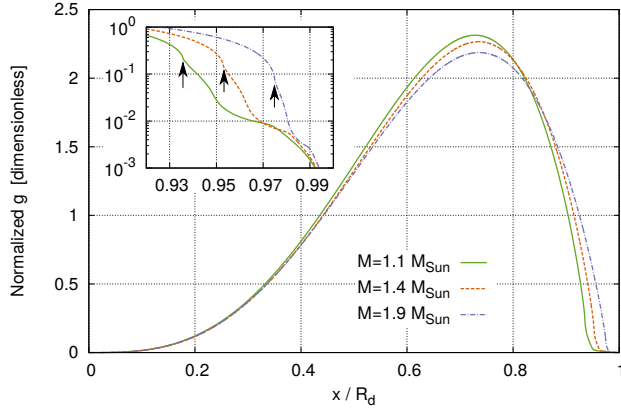
Figure 2.7: The dimensionless weight $g(x)$ for three neutron stars with mass 1.1, 1.4 and 1.9 $M_\odot$ using the SLy EOS. The analytical formula is given in Eq (2.2). Here, in order to compare stars with different masses, g is normalized on the interval $[0,1]$, since the actual value of the radius is unimportant in the set of Eqs (2.25) and (2.26). In the insert we focus on the outermost cylindrical shell: the arrows indicate the surfaces $x = R_c$.
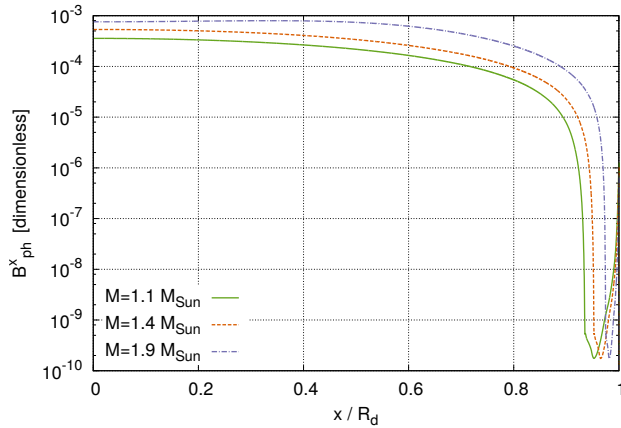

Figure 2.8: The profile $\mathcal{B}^x_{ph}(x)$ for three neutron stars with mass 1.1, 1.4 and 1.9 $M_\odot$, using $\eta(\rho) = \eta_{ph}(\rho) + \eta_{es}(\rho)$ for SLy. Note that we started from a discontinuous η at $\rho = \rho_c$ but the integration over the vortex length provides a smooth profile.
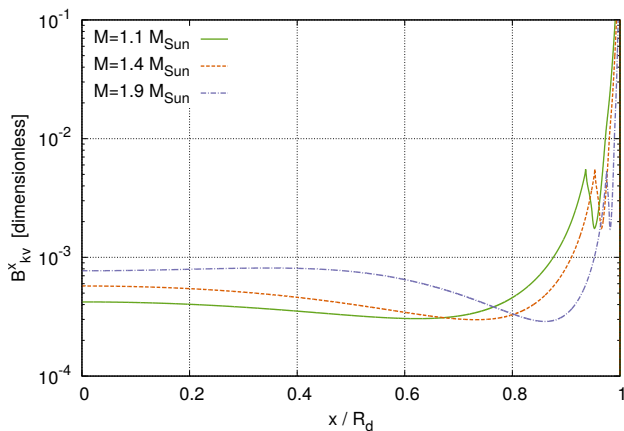
Figure 2.9: The dimensionless profile $\mathcal{B}_{kv}^x(x)$ for three neutron stars with mass 1.1, 1.4 and 1.9 $M_\odot$, using $\eta(\rho) = \eta_{kv}(\rho) + \eta_{es}(\rho)$ with the SLy EOS. For vortex lines near the rotation axis the electron scattering dominates and there is nearly no difference with respect to $\mathcal{B}_{ph}^x(x)$.
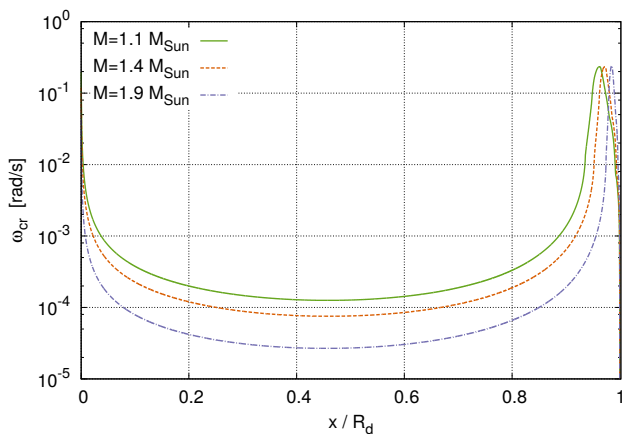

Figure 2.10: Critical lag profile $\Omega_{vp}^{cr}(x)$ for three neutron stars with mass 1.1, 1.4 and 1.9 $M_\odot$ and the SLy EOS. The critical lag calculated without taking into account the entrainment effect is lower by one order of magnitude in the crust (Seveso et al., 2012).
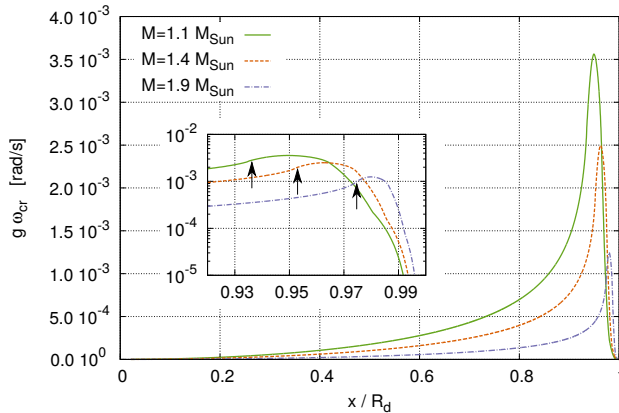
Figure 2.11: The angular momentum reservoir $g\,\Omega_{vp}^{cr}$ of a cylindrical is plotted for three neutron stars with mass 1.1, 1.4 and 1.9 $M_\odot$ using the SLy EOS. The area enclosed by each curve represents the average critical lag $\langle\Omega_{vp}^{cr}\rangle$, listed in Table (2.2). The insert sows the outermost cylindrical shell and the arrows indicate the surfaces $x = R_c$. According to the Rayleigh's criterion, if the actual lag is near the critical lag, the region where $\partial_x(g\,\Omega_{vp}) < 0$ may be unstable, slightly reducing the total angular momentum reservoir.

quantity used to project the non-uniform spherical stricture it onto a cylindrical 1D model. The behavior of g near the origin is ruled by the factor x^3, while the drop after the maximum depends both on the decreasing density and on the spherical shape of the star. It is worth to note that the mass of the star does not have a deep impact on the overall shape of the normalized profile g, thanks to the fact that in our model the actual value of the cylindrical radius is unimportant. For massive stars, g weights more the outermost cylindrical layers. The cylindrical shells that are completely immersed into the crust ($x > R_c$) contribute very little to the total moment of inertia of the v-component, see the insert of Fig (2.7).

Drag parameters - Figures (2.8) and (2.9) show the $\mathcal{B}^x$ profile calculated with electron scattering in the core and either phononic or kelvonic drag in the crust. We label the total dimensionless drag $\mathcal{B}^x$ in these two cases as $\mathcal{B}_{ph}^x$ and $\mathcal{B}_{kv}^x$. The dominant contribution from electron scattering in the core makes these two profiles quite similar for $x \lesssim 0.6\,R_d$. Note that switching from phononic drag to kelvonic drag in the crust is relevant also for vortex lines that are not completely immersed in the crust ($0.8\,R_d \lesssim x < R_c$).

Critical lag - The critical lag Ω_{vp}^{cr} given by Eq (2.24) is shown in Fig. (2.10) for the SLy EOS. When GM1 is used in the core the result is qualitatively similar: the critical lag profiles, even in presence of entrainment still have the typical peak of the snowplow model. This peak gets closer to the cylindrical shell $x = R_d$ as we increase the mass of the star. When GM1 is used in the core, the main difference with respect to the SLy case is the higher value of the central plateau between $0.2 \lesssim x/R_d \lesssim 0.8$.

Cylindrical angular momentum reservoir - In Fig. (2.11) we show the product $g\,\Omega_{vp}^{cr}$; the area enclosed by each curve is the mean critical lag $\langle\Omega_{vp}^{cr}\rangle$, listed in Table (2.2). It is worth noting that the main contribution comes from regions with $x > 0.6\,R_d$, which do

not contain the possibly exotic inner core: in this scenario of rigid vortices the cylindrical
angular momentum reservoir is spread across the inner crust and the outer core of the
neutron star.

2.4.2   Global quantities: spin-up timescale and angular momentum reservoir

Some of the results developed in the previous section can be used to make quantitative
estimates even without solving explicitly the dynamical equations (2.26) and (2.25).

Spin-up timescale - Firstly we estimate of the spin-up timescale, assuming that the
effective dissipation channel is the excitation of kelvons: the fastest possible time variation
is obtained if all vortex lines unpin, so that $Y \approx 1$ everywhere. Within the rigid approxi-
mation of Eq (2.34), the relaxation and coupling timescales of a pulsar of period P during
the spin up can be defined as

$$\tau_{kv}^R = \frac{P}{4\pi \langle \mathcal{B}_{kv}^x \rangle} \qquad\qquad \tau_{kv}^C = \frac{P}{4\pi \langle \mathcal{B}_{kv}^x \rangle} \frac{I_p}{I} \, < \, \tau_{kv}^R, \qquad\qquad (2.36)$$

in complete analogy with Eq (2.34). The parameter τ_{kv}^R can be interpreted as the expo-
nential timescale of the rise time for an extreme glitch where all the vortices suddenly
unpin. This is reliable as long as a change in the value of the friction functional occurs
on timescales greater than τ_{kv}^R, as discussed in App (C). Similarly we can calculate τ_{ph}^R,
the same quantity but using $\mathcal{B}_{ph}^x$. We list these values (in units of the pulsar period P)
in Table (2.2). The listed spin-up timescales are referred to the extreme situation where
all the vortex lines are unpinned ($Y = 1$ everywhere): for the Vela pulsar, using a period
$P \sim 0.09$ s, all the listed spin-up kelvonic timescales τ_{kv}^R are less than a minute or so.
Therefore τ_{kv}^R is comparable to the present observational "blind window" of about 40 s
(Dodson et al., 2002). The first seconds of a glitch event thus provide an indirect insight
into the dynamics of superfluid vortices inside a pulsar and give a clue of the dominant
dissipation mechanism in the crust.

Angular momentum reservoir - From Eq (2.28), the conservation[10] of total angular
momentum before and after the glitch reads

$$I\Omega_p + I_v \langle \Omega_{vp}^{pre} \rangle \, = \, I(\Omega_p + \Delta\Omega_p) + I_v \langle \Omega_{vp}^{post} \rangle \quad \Rightarrow \quad \Delta\Omega_p = \frac{I_v}{I} \, \langle \Omega_{vp}^{pre} - \Omega_{vp}^{post} \rangle \, .$$

The angular momentum reservoir is maximal when the whole star is just subcritical. We
can therefore define a *maximum* glitch amplitude $\Delta\Omega_{\max}$ by taking $\langle \Omega_{vp}^{pre} \rangle = \langle \Omega_{vp}^{cr} \rangle$ and
$\langle \Omega_{vp}^{post} \rangle = 0$. Note that we do not require the postglitch lag to be everywhere null, but
only that it averages to zero at some instant after the vortex avalanche has been triggered.
We thus obtain

$$\Delta\Omega_{\max} \, = \, \frac{I_v}{I} \, \langle \Omega_{vp}^{cr}(x) \rangle \, . \qquad\qquad (2.37)$$

This kind of maximal glitch is probably never realized dynamically (we have to start from
an initial lag that is everywhere nearly subcritical and admit the possibility of overshoot
which depends on the less studied repinning process). Moreover, in an generic glitch the
postglich lag is not null in the average but just less than the average preglitch lag. However
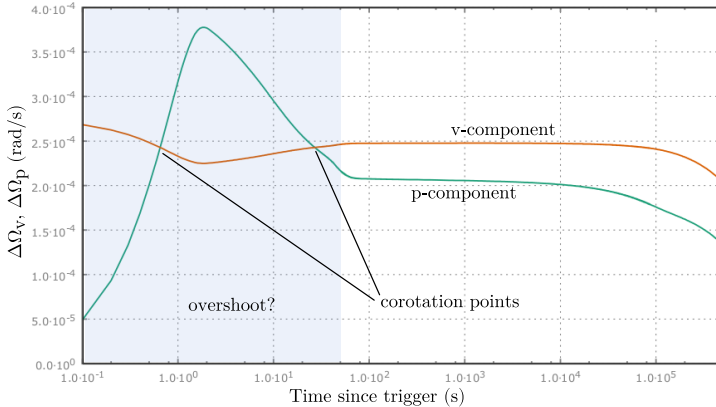
Figure 2.12: Simulation of a maximum glitch of the Vela, obtained by artificial unpinning of the whole reservoir ($M = 1.4\,M_\odot$, SLy EOS). Ve used the prescription provided by Eq (2.21). The (very uncertain) drag parameter in absence of pinning has been fixed to $\mathcal{B}^x = 10^{-2}$, as suggested by Haskell et al. (2013); therefore, the spin-up occurs on the very fast timescale of $\sim 1\,\mathrm{s}$, and differs from the timescales given in Tab (2.2). Once the event is triggered the possibility to obtain an overshoot depends on the details of the repinning prescription. However the height of the corotation points is completely fixed by angular momentum conservation. These points always fall inside the first minute, the observational black window (shaded region), thus providing an upper limit to the observed glitch amplitudes (the white region). The glitch amplitude at the instantaneous corotation is exactly the $\Delta\Omega_{\mathrm{max}}$ defined in the text.

the quantity $\Delta\Omega_{\mathrm{max}}$ sets an upper limit to the observed glitch amplitudes. Clearly $\Delta\Omega_{\mathrm{max}}$ is not really the maximum value of the frequency jump since an overshoot may be present, as shown in Fig (2.12).

The short spin-up timescales that we find imposing $Y = 1$ suggest that for a large glitch the overshoot is realized on timescales of few seconds for Vela, depending on mass. Therefore, the actual measurement of the amplitude $\Delta\Omega$ is likely to occur after the realization of instantaneous corotation (see Fig (2.12)): $\Delta\Omega_{\mathrm{max}}$ is just a theoretical upper limit for the observed glitch amplitude.

Some values of $\Delta\Omega_{\mathrm{max}}$ are listed in Table (2.2): a mass of $1.4\,M_\odot$ is enough to reproduce the largest observed glitch of the Vela ($\Delta\nu \approx 3 \times 10^{-5}\,\mathrm{Hz}$) when the SLy EOS is used ($M_{Vela} < 1.8\,M_\odot$ for the GM1 EOS). The identification of the Vela as an intermediate-mass neutron star has also been proposed on the basis of its surface cooling [see e.g. the review of Yakovlev et al. (2005) and references therein].

2.5 Turbulence and the importance of stratification

A central feature of the quantitative example (but not of the model) described in the previous section concerns the nature of superfluid vortices extending across the crust-core interface: this extreme scenario of straight lines that pass trough the core would be of great interest if change in the symmetry of the order parameter doesn't decouple the S-wave from the P-wave superfluids. This is at variance with most of the existing literature, in which the neutron superfluids in the core and the crust of the NS are assumed to be

---

[10] Electromagnetic angular momentum loss occurs on much longer timescales.

Table 2.2: Timescales and maximal glitches as a function of stellar mass are calculated using the SLy EOS (upper panel) and the GM1 EOS in the core (lower panel). The phonon and kelvon relaxation time are obtained using Eq (2.36) and are given in units of the pulsar period P. For the GM1, the phonon relaxation timescales τ_{ph}^R are systematically too long to explain the fast (unresolved) spin-up of Vela glitches which occur in less than a minute or so.

M	τ_{ph}^C	τ_{ph}^R	τ_{kv}^C	τ_{kv}^R	$\langle \Omega_{vp}^{cr} \rangle$	$\Delta\Omega_{max}$
$(M_\odot)$	(P)	(P)	(P)	(P)	$(10^{-4}\mathrm{rad/s})$	$(10^{-4}\mathrm{rad/s})$
1.1	62.1	807	13.2	171	4.17	3.87
1.4	29.2	478	12.1	193	2.51	2.37
1.9	9.0	207	7.2	165	0.92	0.89
1.1	445	4450	13.9	139	6.99	6.30
1.4	261	2871	17.1	188	4.37	3.92
1.9	136	1632	26.3	315	2.04	1.87

separated, with the core P-wave superfluid strongly coupled to the normal component and only the S-wave crust superfluid accumulating angular momentum for the glitch.

However the extreme scenario that has been studied numerically in the previous section is still a possibility, at least in the absence of a normal matter layer at the core-crust interface which separates the two superfluid domains. In this section we critically analyze this extreme scenario, proposed e.g. by Ruderman and Sutherland (1974) and Pizzochero (2011).

Arguments for a core-crust reservoir - The strong entrainment found in the crust challenges the standard picture based on a reservoir confined into the crust: the crust is not enough to explain large glitches (even though this conclusion is not universally accepted due to uncertainty on the entrainment parameters and on the EOS). It is therefore natural to seek for a larger superfluid domain which extends into the core (Ho et al., 2015). Moreover, consistent microscopic calculations of the neutron pairing gap so far do not show any shell of normal matter that could physically separate the two superfluids and disconnect the respective vortices (Zhou et al., 2004). This has also implications on the internal temperature distribution: the absence of normal neutrons requires the temperature in the outer core to be lower than the critical temperature for P-wave superfluidity (otherwise superfluidity in the crust would be destroyed).

Microscopic calculations of neutron pairing gaps in the triplet channel (i.e. P-wave) give $T_{cr}^P > 5 \times 10^8$ K for densities $n > 0.08 \, \mathrm{fm}^{-3}$ (Taranto et al., 2016); on the other hand, simulations of cooling constrained by observations of Cas A (Ho et al., 2015) predict isothermal outer cores with temperatures always smaller than 2.2×10^8 K$< T_{cr}^P$ for all the pulsars considered (for Vela, the estimated temperature is $T = 1.2 \times 10^8$ K): if the crust contains a superfluid region, the outer core is expected to be in a superfluid state as well. Hence our choice of a single superfluid component in the numerical estimates that extend through the core is thus, at the moment, consistent with our understanding of neutron star interiors.

Unfortunately, the constraints on superfluid properties in NS cores obtained from observations of fast cooling in the central compact object in Cas A (Heinke and Ho, 2010; Elshamouty et al., 2013) are still not conclusive, since different physical scenarios are able

to explain the observations (Taranto et al., 2016); moreover, even the presence of the fast cooling itself is questioned, although not firmly excluded (Posselt et al., 2013).

Turbulent superfluid core - We saw that the crust and the core are both expected to be in a superfluid state and that no normal matter in between is expected: at least in principles vortices can pass trough the rust-core transition. We now question the assumption that vortex lines are straight on the global stellar scale.

Turbulence is a well known phenomenon in He-II, where it gives rise to a complex tangle of vortex lines (Barenghi et al., 2001), a phenomenon also known as quantum turbulence (Tsubota et al., 2013). Tangling of vortices is likely to develop in some regime also in NSs, but its relevance for glitch models is still unclear. In the case of neutron stars this tangle must have a preferential direction (imposed by large scale rotation): hence *polarized turbulence* is expected (Andersson et al., 2007), as well as intermittence between laminar regimes (rectilinear vortex array) and turbulent ones (Peralta et al., 2006).

We thus try to clarify why turbulence should be expected in our model with extended vortices that pass trough different layers of stratified matter. A first insight is provided by a classical fluid, where the Taylor columns (that in homogeneous systems are a by effect of the Coriolis force) become unstable in presence of stratification (Hollerbach, 2009).

Following a criterion for the onset of turbulence based on the estimate of a single vortex tension, originally devised for Helium-II, the core is susceptible to become turbulent. For simplicity we assume that there is no entrainment and that vortices pass trough the core-crust interface, like in the extreme scenario. Since vortex pinning in the core is neglected, each vortex can be considered a string with both ends held fixed by pinning forces in the crust. Hence the only forces acting on a vortex segment immersed into the core are the Magnus $\mathbf{f}_M$ and the tension $\mathbf{f}_T$ forces, which are given by

$$\mathbf{f}_M = \rho_n \kappa \, \hat{\kappa} \times \mathbf{v}_{np} \qquad\qquad f_M \sim \rho_n \kappa \, x \, \Omega_{np} \qquad (2.38)$$

$$\mathbf{f}_T = \kappa \, \nu_n \, \rho_n \, (\hat{\kappa} \cdot \nabla) \, \hat{\kappa} \qquad\qquad f_T \sim \frac{\rho_n \, \kappa^2}{4 \, \pi \, L} \ln\left(\frac{d_n}{\xi_n}\right) \qquad (2.39)$$

where $d_n \approx n_v^{-1/2}$ and ξ_n are the average neutron vortex separation and coherence length, respectively; the factor $\nu_n = (\kappa/4\,\pi) \ln(d_n/\xi_n)$ is a *kinematic viscosity* and L is the local vortex curvature radius[11]. The sum of these forces on the core must vanish (Link, 2014). Assume first, for our pinned and straight line, that $\Omega_{np} \sim 10^{-4}\,\mathrm{rad/s}$ for $x \sim R_d/2$, which is a typical value for the critical lag well inside cylindrical the region defined by $x < R_c$, see e.g. the critical profiles calculated by Seveso et al. (2012) which do not include entrainment. The typical inter-vortex separation d_n and the neutron coherence length can be written as (Mendell, 1991)

$$d_n \approx \sqrt{\frac{\kappa \, P}{4 \, \pi}} \approx 1.3 \times 10^{-3} (P/10\,\mathrm{ms})^{1/2}\,\mathrm{cm} \qquad (2.40)$$

$$\xi_n \approx 16 \, y_n^{1/3} \rho_{14}^{1/3} \Delta_n (\mathrm{MeV})^{-1} \mathrm{fm}\,, \qquad (2.41)$$

where we have neglected the entrainment in the core and ρ_{14} is the density expressed in $10^{14}\mathrm{g/cm^3}$ units. By taking the benchmarks values typical of the core of a NS, $\Delta_n = 1\,\mathrm{MeV}$,

---

[11] For a curve $\gamma(s)$ parametrized by the arc length s we have $\gamma' \cdot \gamma'' = 0$, so that its extrinsic curvature is just $K = |\gamma''(s)|$. In our case $\gamma'(s) = \hat{\kappa}$, i.e. $K = |\hat{\kappa} \cdot \nabla \hat{\kappa}|$. In the plane it is easy to see that $K = L^{-1}$, where L is the radius of the osculating circle. For a straight vortex $L \to \infty$.

$y_n = 0.95$, $\rho_{14} = 2.8$ and $P \approx P_{Vela} \approx 100\,\text{ms}$, we obtain $\xi_n \approx 22\,\text{fm}$ and $d_n \approx 4 \times 10^{10}\text{fm}$, namely $\ln(d_n/\xi_n) \approx 20$.

Since the sum of the forces must vanish we impose $f_M \sim f_T$, which implies $L \sim 10^{-5}\,\text{cm}$, an extremely small radius of curvature.

The inverse reasoning gives that $L \sim R$ and $f_M \sim f_T$ only if $\Omega_{np} \sim 10^{-13}$, namely for corotating superfluid and normal components. We can conclude that, since the tension of a single line is much smaller than the hydrodynamical force in the core acting on it when pinned, the core is susceptible to become turbulent.

However, in the extreme scenario, a huge amount of vortex lines is organized into a paraxial configuration: the combined effect of many vortex lines in this particular geometry may resist bending. Indeed, the previous argument is strictly valid only for a single vortex and does not include the possible presence of a restoring elastic force of the vortex array (Baym and Chandler, 1983).

Deformations of the vortex array on scales much larger than its lattice constant are described in terms of shears and compressions of a 2D crystal and have their own continuum elastic theory (Williams and Fetter, 1977; Sonin, 1987, 2014). The macroscopic shear modulus of the vortex lattice is estimated as $\mu \sim \kappa \Omega_n \rho_n$, while force density associated to a displacement u turns out to scale as $F_e \sim \mu u/R^2 \sim \mu_s L^{-1}$. The curvature radius L can be easily estimated as $L = (R^2 + u^2)/(2u) \sim R^2/u$, where R is the length of the segment that has been displaced in the middle by u, holding the two ends fixed. The elastic force density F_e has to be compared with the Magnus force density $F_m \sim \rho_n R \Omega_n \Omega_{np}$, the mutual friction force in the quasi-conservative regime discussed in App (D): the requirements $F_e \sim F_m$ and $u \sim R$ (i.e. $R \sim L$) imply an extremely small lag.

Finally, an hydrodynamical argument is provided by the HVBK equations [12] with mutual friction and vortex tension, valid when bent vortices are far apart so that no reconnections can take place. The mutual friction force given in Eq (D.8) in the case of a bent vortex array, takes the form

$$\mathbf{F}_{MF} = \rho_n \tilde{\mathcal{B}}_c \left(\boldsymbol{\omega}_n \times \mathbf{v}_{np} - \mathbf{T} \right) + \rho_n \tilde{\mathcal{B}}_d \, \hat{\omega}_n \times \left(\boldsymbol{\omega}_n \times \mathbf{v}_{np} - \mathbf{T} \right), \qquad (2.42)$$

where $\rho_n \mathbf{T} = -\rho_n \nu_n \boldsymbol{\omega}_n \times (\nabla \times \hat{\omega}_n) = \rho_n \nu_n \boldsymbol{\omega}_n \cdot \nabla \hat{\omega}_n$ is the tension of the vortex array. We thus have to compare $\mathbf{T}$ with the term $\boldsymbol{\omega}_n \times \mathbf{v}_{nb}$, namely we have to find the value of L such that

$$|\mathbf{T}| \approx |\boldsymbol{\omega}_n \times \mathbf{v}_{nb}| \qquad \Rightarrow \qquad \nu_n L^{-1} \approx \Omega_{np} R.$$

We thus obtain a result very similar in all the three cases presented: these are also the major obstructions for the explanation of long period oscillations of the pulsar period in terms of Tkachenko waves[13], proposed by Ruderman (1970).

---

[12] To avoid confusion we recall that, consistently with Appendix (D), the Hall-Vinen-Bekarevich-Khalatnikov equation of motion for the superfluid component is (Barenghi and Jones, 1988; Barenghi et al., 2001)

$$D_t \mathbf{v}_n + ... = \mathbf{T} + \rho_n^{-1} \mathbf{F}_{MF},$$

where entrainment is zero and $\mathbf{v}_n$ refers to the superfluid velocity (it is actually a model for a single superfluid at $T > 0$, not for a superfluid mixture at $T = 0$). Unfortunately the HVBK equations are sometimes presented with sign misprints in the friction of tension terms.

[13] Tkachenko waves are very well known collective oscillation modes of the vortex array in laboratory superfluids: Coddington et al. (2003) directly imaged Tkachenko waves in waves in a vortex lattice in a dilute-gas Bose-Einstein condensate; see Sonin (2014) for a short review. Ruderman (1970) associated the observed ~ 4 months oscillations of the Crab pulsar's period with Tkachenko waves. If the wavelength of the mode to is comparable with the pulsar radius and the wave vector is perpendicular to the vortices, then these oscillations result in a modulation of the observed period on the timescale of months. (Fetter,

Taylor-Proudman theorem - The possibility of dynamical phases in which the existence of an array of vortices is possible is not completely ruled out: Ruderman and Sutherland (1974) claimed that the early argument of Greenstein (1970) for the onset of turbulence in neutron stars did not account for the stabilizing effect of rotation, a caveat also reported by Andersson et al. (2007). The main argument of Ruderman is that the increased effective tension of a bundle of vortices as compared to a single vortex resists bending: the array of vortex lines could remain parallel to the rotation axis, providing a realization of the Taylor-Proudman theorem to axisymmetric and spinnig-down frictionless fluids. This idea is widely (sometimes tacitly) used in most of the mesoscopic and hydrodynamical studies of superlfuid neutron stars. As it stands, all the work on the topic of turbulence in neutron stars is at the moment exploratory and there is far from a consensus as to which regimes will lead to turbulence and how this will develop. For this reason, but also for its convenience, the working assumption of a straight array of vortices is still commonly used. Indeed, this practice allowed us to implement stratification in a consistent model and then to test *in the aftermath* the validity of the hypothesis.

2.6 Possible generalizations

We developed a dynamical model that takes into account the layered structure of the star, the differential rotation of the superfluid and the presence of density-dependent entrainment, consistently with the working hypotheses presented at the beginning of the chapter. In our treatment we pointed out that all the complex behavior of the rearrangement of the vortex configuration is hidden into the functional $\mathcal{B}$, introduced in Eq (2.15). The model is defined by the dynamical equations, Eqs (2.26) and (2.25): they describe the exchange of angular momentum between two effective components, characterized by the moments of inertia I_v and I_p, whose angular velocities are $\Omega_v(x,t)$ and the observable $\Omega_p(t)$. Both I_v and $I_p = I - I_v$ account for the entrainment corrections exactly.

In the previous section, we pointed out that the theoretically expected absence of a normal matter layer at the crust-core interface suggests that the quantized vortices can continuously pass from the S-wave region to the P-wave region, even though this is not guaranteed: vortices in ^{3}He actually provide an example of a much rich behavior (Finne et al., 2006).

In particular, given the assumption that vortex lines continuously extend from the inner crust into the core, we still cannot deduce that the two superfluids rotate at the same rate providing a realization of the Taylor-Proudman theorem: a mechanism of the kind proposed by Greenstein (1970) can still operate to decouple the core from superfluid in the crust. The mechanism of Greenstein is suppressed if vortices cannot bend and wind around the rotation axis, so that columnar rotation is realized only for vortices (or, better, bundles of vortices) that are extremely rigid at the hydrodynamical scale, a debated possibility.

1970) pointed out a difficulty associated with the three-dimensional nature of the pulsar and the neglected effects of mutual friction between the vortices and the normal component in the original Ruderman's calculation. The interest to interpretation of pulsar oscillations in the terms of vortex array oscillations declined to some extent, but recently Noronha and Sedrakian (2008) reopened the issue (also this model however does not account for stratification). A formalism that extends the hydrodynamical model of Baym and Chandler (1983), valid for a $T = 0$ superfluid (i.e. a superfluid comprised of a single inviscid component), is presented in Haskell (2011). In this preliminary study however the vortex array is immersed into a comoving background, so that the existence of a vortex array is possible.

Indeed, the ^{4}He argument proposed in the previous section points in the direction of vortex lines that are tensionless and can thus bend on very short lengthscales without considerable energy cost.

Three-component model - Fortunately our model can be very easily generalized to a 1D model with three components, where there are two sets of vortex lines and two auxiliary variables $\Omega_v^{crust}(x,t)$ and $\Omega_v^{core}(x,t)$ for the crust and the core respectively. In this case, the core superfluid interacts with the normal component trough the dissipation mechanism mediated by the electron scattering, given in Eq (2.35), and can possibly be pinned to fluxtubes.

   Within this picture, the vortex-rigidity hypothesis is relaxed to some extent: since there are two geometrically distinct superfluid domains with columnar rotation, the straight vortex bundles in the core do not have to match the (possibly) pinned vortices in the crust, so that it is easier for them to remain straight.

   The derivation of the corresponding dynamical equations is trivial since the mathematical framework is unchanged with respect to what discussed in the present chapter. A detailed numerical study of the coupling timescales between the normal component and the two superfluids, following the general multi-component formalism presented in App (E), can be of interest: this would provide a more detailed and consistent study of the early estimate of core-crust coupling proposed by Alpar et al. (1984b).

Axially-symmetric 2D model - Alternatively, it is possible to drop the assumption of straight vortices and consider a single variable $\Omega_v(x,z,t)$: this description can be rigorously implemented under the hypothesis of tensionless vortices[14]. The angular momentum balance takes the usual form

$$I_p\,\dot{\Omega}_p(t)\,+\,\int dI_v\,\dot{\Omega}_v(x,z,t)\,=\,-I|\dot{\Omega}_\infty|\,,$$

where $dI_v = 2\pi\,x^3\,(\rho_n/m^*)\,dx\,dz$ and $I_p = I - I_v$; the parameter I_v is still given by Eq (2.3): eventually the inner core can be excluded by the superfluid domain in the case the pairing gap vanishes at high densities. For tensionless vortices the term $\dot{\Omega}_{MF}$ introduced in Eq (2.26) is purely local, so that

$$\dot{\Omega}_v(x,z,t)\,=\,-\mathcal{B}[\Omega_{vp},r]\,(2\Omega_v + x\partial_x\Omega_v)\,\Omega_{vp}\,.$$

The general functional $\mathcal{B}$ reduces to a local function of the lag and of the spherical radius and, as long as some tension-mediated interaction between superfluid layers is introduced, does not involve derivatives of the dynamical variables. The simplest possibility is to consider

$$\mathcal{B}[\Omega_{vp},r]\,=\,Y[\Omega_{vp}(x,z) - \Omega_{vp}^{cr}(r)]\,\mathcal{B}^x(r)$$

where $\Omega_{vp}^{cr}(r)$ and $\mathcal{B}^x(r)$ are the obvious local analogues of $\Omega_{vp}^{cr}(x)$ and $\mathcal{B}^x(x)$, see e.g. Eq (3.15). An explicit example of this kind of construction is provided in the next chapter.

   From the macroscopic point of view, a finite tension of vortex bundles, or the well known phenomenon of effective superfluid viscosity mediated by the tangling of vortices at the mesoscopic scale (Barenghi et al., 2001), will introduce derivatives along the z-axis which couple vertically the different superfluid layers.

---

   [14] Since in this case of tensionless vortices (dubbed "slack" in the next chapter) we do not have to perform any integration along the z-axis, it is sufficient to consider a single superfluid component. Distinction between the S-wave and P-wave superfluids is indeed implicit into the assumed coupling with the normal component provided by $\mathcal{B}$.

Constraints on pulsar masses

The central issue of this chapter is a general method that can be used to constrain the mass of glitching pulsars, using observations of the largest glitch recorded.

As usual in astrophysics, extrapolation of this information is an indirect process, which result depend on a bunch of input parameters (like the EOS) provided by the current literature.

The proposed methodology is quite different from other studies which concentrate on pulsar activity. In order to give an explicit example we describe the general method by using a unified (and very simplified) model for the replenish of the angular momentum reservoir. This provides a quantitative test for global models of rotating neutron stars, as well as microphysical inputs present in literature, in particular pinning forces.

3.1 Maximum glitch amplitude: Newtonian framework

In the previous chapter we discussed a Newtonian model for pulsar glitches that is consistent with the stratified structure of the neutron star, the presence of non-uniform entrainment and pinning.

We considered a rigidly rotating component (labeled by p) and a superfluid component (labeled by n) that can rotate non-uniformly with angular velocity $\Omega_n = \Omega_p + \Omega_{np}$ but still around a common and constant rotation axis. Using standard cylindrical coordinates, the angular velocity lag between the components is a function $\Omega_{np}(x, z)$ that can vary in time but does not depend upon the coordinate φ, as can be shown by considering the continuity equation for the n-component for a fixed spherical background density, i.e. $\nabla \cdot (\rho_n \mathbf{v}_n) = 0$. Entrainment is introduced according to the Newtonian formalism of Prix (2004), where the momenta per baryon $\mathbf{p}_n$ and $\mathbf{p}_p$ are linear combinations of both velocities: in particular, their azimuthal components are given by [see Eq (2.5)]

$$p_{n\varphi} = m_n \, x \, (\Omega_p + (1 - \epsilon_n)\Omega_{np}) \,, \tag{3.1}$$

$$p_{p\varphi} = m_p \, x \, (\Omega_p + \epsilon_p \Omega_{np}) \,, \tag{3.2}$$

the other components being zero (this allows for the cylindrical reduction). Here m_n and m_p are the mass per baryon of the two fluids and the dimensionless entrainment parameters ϵ_n and ϵ_p obey the constrain $m_n n_n \epsilon_n = m_p n_p \epsilon_p$, where n_n and n_p are the baryon number densities of the two-fluid (the total baryon density is $n_B = n_n + n_p$). Since the superfluid is composed entirely of neutrons, we can consider m_n to be the neutron

bare mass. Things are more subtle for the normal component, which is a neutral mixture of protons, leptons (in particular electrons), thermal excitations of the neutron superfluid and crustal neutrons that are not in the conduction band (Carter et al., 2006). The β-equilibrium for a three-component star (electrons, protons and neutrons) tells us that m_p should be at least the sum of the proton bare mass and of the electron bare mass [see also the discussion in Sourie et al. (2016)]. Further contributions from the non-superlfuid neutrons are expected to rise the value of m_p even closer to m_n. In general, by using the definition of the entrainment parameters, the total momentum density $\boldsymbol{\pi}$ can be expressed in terms of the velocities $\mathbf{v}_n$ and $\mathbf{v}_p$ as the sum of the two conserved currents $\rho_n \mathbf{v}_n$ and $\rho_p \mathbf{v}_p$, i.e.

$$\boldsymbol{\pi} = n_n \mathbf{p}_n + n_p \mathbf{p}_p = m_n n_n \mathbf{v}_n + m_p n_p \mathbf{v}_p \,. \tag{3.3}$$

The azimuthal component, once $m_n = m_p$ has been assumed, is

$$\pi_\varphi = n_n p_{n\varphi} + n_p p_{p\varphi} = m_n x (n_B \Omega_p + n_n \Omega_{np}) \,. \tag{3.4}$$

The angular momentum reservoir of the system can be easily found by considering the total angular momentum L written as the volume integral of the angular momentum density $x \pi_\varphi$:

$$L = \int x \pi_\varphi \, d^3 x = I \, \Omega_p + \Delta L[\Omega_{np}] \,, \tag{3.5}$$

where I is given in Eq (2.4) and

$$\Delta L[\Omega_{np}] = \int d^3 x \, (r \sin\theta)^2 \rho_n \, \Omega_{np} \tag{3.6}$$

is the angular momentum reservoir due to the lag Ω_{np}. The *maximum* glitch amplitude (see Fig (2.12)) corresponding to a given lag Ω_{np} is

$$\Delta\Omega_p[\Omega_{np}] = I^{-1} \Delta L[\Omega_{np}] = \frac{I_n}{I} \langle \Omega_{np} \rangle \,. \tag{3.7}$$

To make contact with the terminology used in the previous chapter, we introduced the average lag

$$\langle \Omega_{np} \rangle = I_n^{-1} \Delta L[\Omega_{np}], \quad \text{with} \quad I_n = \frac{8\pi}{3} \int dr \, r^4 \, \rho_n \,. \tag{3.8}$$

It is thus possible to define the moment of inertia I_n relative to the superfluid reservoir[1] as the normalization factor of the distribution ΔL defined in Eq (3.6): this definition is coherent with the interpretation of angular velocity as vorticity flux, given in Eq (2.8). Not surprisingly, the glitch amplitude in Eq (3.7) does not explicitly depend on entrainment: it is a direct consequence of Eq (3.3). However the lag Ω_{np} is a dynamical variable of the model and its evolution is affected by entrainment. We want to maximize $\Delta\Omega_p$, in order to obtain a theoretical upper bound to the observed glitch amplitudes, extending the reasoning already presented in the previous chapter. This is done by considering the critical lag for unpinning Ω_{np}^{cr} when all the vortices are pinned, even if perfect pinning is probably never realized in real neutron stars.

---

[1] This is not the standard approach commonly used to define the quantity I_n in body averaged models with entrainment, see e.g. Sourie et al. (2016).

The upper limit $\Delta\Omega_{\max}$ on the glitch amplitude is thus obtained by artificially emptying the whole reservoir of pinned superfluid, namely

$$\Delta\Omega_{\max} \,=\, \Delta\Omega_p[\Omega_{np}^{cr}]\,. \tag{3.9}$$

Estimates of Ω_{np}^{cr} are based on the still poorly known physics of vortices in the crust, as well as in the core of neutron stars, as pointed out in the last section of the previous chapter. Therefore we construct the critical lag in two different physical scenarios; when vortex lines have an overall rigidity so that they collectively organize into a stable array of paraxial vortex lines (Ruderman and Sutherland, 1974), and when vortices are slack (i.e. tensionless) at the hydrodynamic scale, so that any macroscopic portion of superfluid can flow quite independently from the others.

3.1.1 Rigid vortices

While the general treatment with bent vortices is given in App (E), here we restrict ourselves to the straight lines case. The angular momentum reservoir of Eq (3.6) in terms of Ω_{vp} is

$$\Delta L[\Omega_{vp}/m^*] \,=\, 2\pi \int dx\, x^3 \int_{\gamma_x} dz\, (\rho_n/m^*)\, \Omega_{vp}\,, \tag{3.10}$$

implying that Eq (3.9) reads

$$\Delta\Omega_{\max} \,=\, \frac{I_v}{I}\, \langle \Omega_{vp}^{cr} \rangle\,. \tag{3.11}$$

Here the moment of inertia I_v is the normalization factor of the distribution in Eq (3.10): of curse it is consistent with Eq (2.3).

Again, let us test the prescription proposed by Pizzochero (2011) and used in Eq (2.24) for straight lines, i.e. the magnitude of the local mesoscopic Magnus force

$$|\mathbf{f}_M| = \kappa\, \rho_n\, x\, \Omega_{vp}/m^* \tag{3.12}$$

integrated along $\gamma_x(z)$ must equal the pinning force f_P integrated along the same curve. The critical lag is thus given by

$$\int_{\gamma_x} |\mathbf{f}_M| = \int_{\gamma_x} f_P \quad \Rightarrow \quad \Omega_{vp}^{cr}(x) \,=\, \frac{\int_{\gamma_x} f_P}{\kappa\, x \int_{\gamma_x} \rho_n/m^*}\,. \tag{3.13}$$

Proper generalization to the case of bent vortices is provided by Eq (E.1). Since the integral factor in the denominator of Ω_{vp}^{cr} is the same that appears in Eq (3.10), we obtain

$$\Delta\Omega_{\max} \,=\, \frac{\pi^2}{\kappa\, I} \int_0^{R_d} dr\, r^3\, f_P(r)\,, \tag{3.14}$$

where R_d is the radius corresponding to the interface between the inner and the outer-crust (drip-radius). In the Appendix (E) we discuss in detail why, in this case of rigid lines, it is important to use Ω_{vp} instead of Ω_{np}.
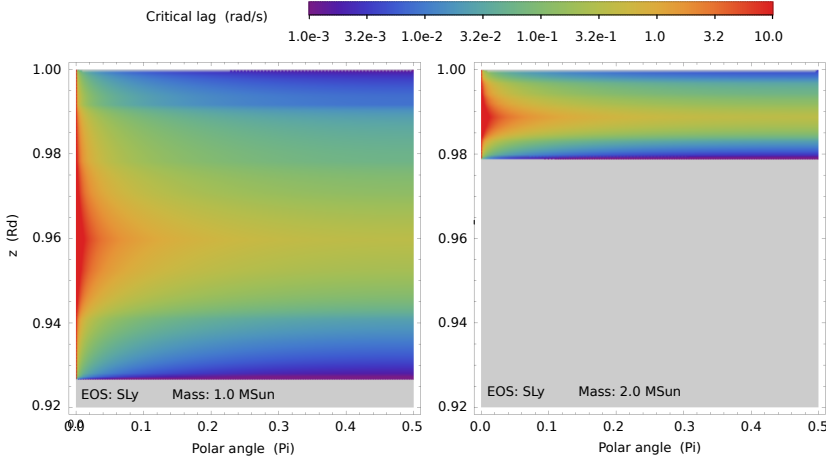
Figure 3.1: The critical lag for unpinning Ω_{vp}^{cr} in the case of macroscopically slack vortices given by Eq (3.15). The vertical scale is the relevant part of rotation axis that intersects the inner crust (distances along the axis are measured in units of R_d) while the horizontal coordinate is θ/π. The critical lag diverges for $\theta = 0$, a feature that is not captured by the color map. *Left* - We considered the SLy EOS and a pulsar of mass $1\,M_\odot$. *Right* - The same but for a much more massive star of $2\,M_\odot$; qualitatively the plot is the same but the crust really shrinks and the possibility to store angular momentum is reduced.

3.1.2   Slack vortices

Within our main hypothesis of zero meridional circulation, the maximum glitch $\Delta\Omega_{\mathrm{max}}$ is exactly independent on entrainment in two different physical situations: for vortex lines in a paraxial array and for completely slack vortices that only feel the local pinning and the mesoscopic Magnus force. In this latter case we assume a local unpinning condition given by

$$|\mathbf{f}_M| = f_P(r) \quad \Rightarrow \quad \Omega_{vp}^{cr} = \frac{f_P(r)\,m^*(r)}{\kappa\,\sin\theta\,r\,\rho_n(r)}\,. \tag{3.15}$$

An example of critical lag Ω_{vp}^{cr} is shown in Fig (3.1).

We remark that a completely slack vortex at the microscopic scale would bend even over lengths of the Wigner-Seitz radius in the crust, making unrealistic the analysis of vortex pinning carried out by Seveso et al. (2016) that incorporates the presence of non-zero single-vortex tension to estimate the mesoscopic pinning force per unit length of vortex line. Moreover, differently from the previous case, this scenario of vortices that are tensionless at the macroscopic scale can lead to the development of superfluid turbulence: if vortices pass through the crust-core interface, the non-pinned section of the vortex immersed into the core can wrap around the rotation axis as described by Greenstein (1970) and vorticity can develop toroidal components.

Under the assumption of slack vortex lines there is no real advantage in preferring Ω_v instead of Ω_n: the same line of reasoning can be followed by using directly Eq (3.7) and recalling that $\Omega_{np}^{cr} = \Omega_{vp}^{cr}/m^*$. Moreover any local phenomenological unpinning condition can be used in place of Eq (3.15). For example it could be interesting to replace it with the form for the mutual friction proposed by (Gorter and Mellink, 1949) for isotropic turbulence, see also (Barenghi et al., 2001). However isotropic turbulence is unlikely to be

relevant for neutron stars (Andersson et al., 2007), thus we stick ourselves to the more usual choice of Magnus-like mutual friction. Eventually it is always possible to refine the present treatment, in particular Eq (3.15), with a suitable unpinning condition when a better understanding of polarized turbulence in neutron stars will be achieved. By using Eq (3.11) we end up with the same result given in Eq (3.14): the maximum glitch amplitude depends only on the mass of the star and on the pinning force profile.

In both cases of slack and rigid vortices, the critical angular velocity lag diverges as $\sim 1/x$ near the rotation axis. This is however not a flaw of the model: firstly we do not expect the reservoir to be completely filled in real neutron stars, secondly this kind of divergence is cured by the fact that near the rotation axis the moment of inertia density on a meridional slice of the star (the x-z plane) goes to zero as $\sim x^3$.

3.2 Upper limit on pulsar masses

The maximum glitch amplitude $\Delta\Omega_{\mathrm{max}}$ of Eq (3.14), valid for both straight and slack vortices, can depend only on the mass of the star and pinning forces. After the pinning profile has been fixed, this provides a way to constrain the mass of a pulsar for which one may expect to have measured the largest glitch: here we apply this method to all the observed large glitchers.

The procedure is shown in Fig (3.2), where we plot the function $\Delta\Omega_{\mathrm{max}}(M)$ together with the largest *observed* glitch $\Delta\Omega$ for a selection of pulsars, listed in Tab (3.2). For comparison we use three unified equations of state: SLy Douchin and Haensel (2001), Bsk20 and Bsk21 Goriely et al. (2010), see also Fantina et al. (2013) for a comparative study. The curve $\Delta\Omega_{\mathrm{max}}(M)$ displays yet the main property of our model for the reservoir, namely an inverse relation between the NS mass and the maximum allowed glitch: as expected, larger glitches require smaller masses.

The curves for the three unified EOSs are quite similar, but stiffer EOSs can significantly move the curve upward and yield weak upper limits for the masses; e.g. the very stiff GM1 EOS gives for the Vela an upper limit of $1.8M_{\odot}$ (Antonelli and Pizzochero, 2017). Since the pinning forces have estimated errors of order $\pm 10\%$ arising from the statistical uncertainty associated to the counting procedure used by Seveso et al. (2016), we also expect a certain shift of the curves. In general, the rescaling of the pinning force by an overall factor is equivalent to multiply the curves by the same factor. The results are thus intimately related to the microphysics used, which are non-tuned and independently calculated data available in the literature for the EOS, pinning and entrainment. Different microphysical input can change the numerical values obtained here for the masses, but will maintain the general inverse relation.

By looking at Fig (3.2), it can be seen that masses between $\sim 1.1\,M_{\odot}$ and $\sim 2.2\,M_{\odot}$ can account for maximum glitches spanning one order of magnitude: the maximum glitch amplitude relative to the maximum mass allowed by the EOS sets the threshold used to define the *large* glitchers: out method allows to constrain the mass of all pulsars with $\Delta\Omega \geq 5 \times 10^{-5}\,\mathrm{rad/s}$, as shown in Fig (3.3).

We indicate with M_{abs} the *absolute upper limit* to the mass of a pulsar, defined by $\Delta\Omega_{\mathrm{max}}(M_{\mathrm{abs}}) = \Delta\Omega$. Future observations of even larger glitch amplitudes can only lower this upper limit to the mass, leading to stronger constraints. Note also that the possible presence of turbulence in the crust could reduce the maximum glitch amplitude, thus lowering the curves of Fig (3.2) and leading to stronger constraints (eventually we could
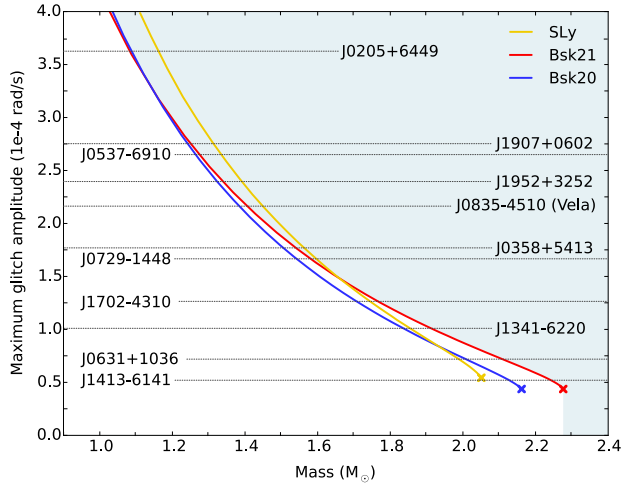
Figure 3.2: The estimated maximum glitch $\Delta\Omega_{\mathrm{max}}$, given by equation (3.14), is plotted as a function of the stellar mass: SLy (yellow), Bsk20 (blue) and Bsk21 (red). The horizontal lines, labeled by pulsar names, indicate the largest glitch amplitude $\Delta\Omega$ recorded in the corresponding pulsar. The mass values M_{abs} are given by the intersection of the horizontal lines and the curves $\Delta\Omega_{\mathrm{max}}(M)$. The upper limit for the mass defines a forbidden region, shown here for the case of Bsk21 (shaded). The curves are terminated by the maximum mass allowed by each EOS (crosses): this determines the minimum $\Delta\Omega$ that can be constrained by the corresponding EOS, namely $\sim 5 \times 10^{-5}\,\mathrm{rad/s}$.

find that we are using unrealistic low pinning forces): it seems reasonable to expect that the increase in the vortex length density due to the development of complex vortex tangles weakens the collectively enhanced pinning of the vortex array.

At present, out of ~ 130 objects that have displayed at least one glitch, there are 51 observed large glitchers for which a mass limit can be obtained, listed in Tab (3.2); the remaining pulsars with smaller observed maximum glitch are not constrained, since any mass can account for these small events. In some case, this could be due to observational selection effects arising from the short time of observation or from the very slow evolution due to small spin-down. Some of these objects may be constrained in the future.

Most of these 51 objects are *single* glitchers, pulsars that so far have displayed a unique large event that is considerably greater than all the other recorded glitches. Hence, the typical timescale between large glitches (as well as the glitch activities) are as yet undetermined in these objects, until new observations will improve the statistics. Among these 51 neutron stars, there are 17 large glitchers that have displayed at least a couple of large events of similar magnitude: they are listed in table (3.1). For these pulsars, we further determine a speculative lower limit for the mass by using also their observed average timing behaviour.

3.3   Constraints imposed by the reservoir dynamics

It is possible to try to lower the upper bound of the mass by using extra information from the observed timing properties. Starting from corotation, forward integration in time of the *assumed* dynamical equations [e.g. Eqs (2.25) and (2.26)] allows to follow the
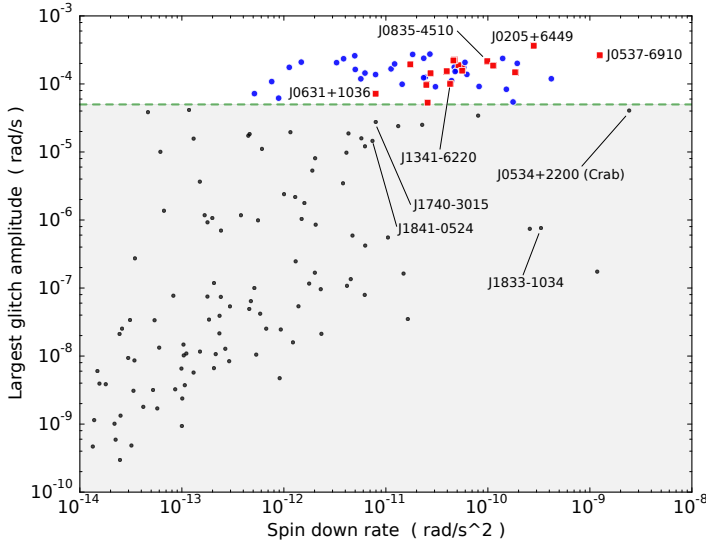
Figure 3.3: Scatter plot of the largest glitch recorded in a pulsar and its spin down rate. Here the whole glitchers population is considered. The shaded area indicates the region below $0.5 \times 10^{-4} \, \mathrm{rad/s}$. The 17 objects for which we can give a mass constrain are indicated in red, the remaining 34 large but single glitchers are indicated with blue marks. Note that the lower right corner is not populated but it is difficult to say whether or not this is due to an observational bias.

evolution of the lag $\Omega_{vp}(x, z, t)$ and of the associated quantity $\Delta\Omega_{\max}(t)$: since the time evolution starts from the corotation point at $t = 0$ (see Fig (2.12)), the prescription used to obtain $\Delta\Omega_{\max}(t)$ can be sketched as

$$\langle\Omega_{vp}(x, z, 0)\rangle = 0 \quad \rightarrow \quad \Omega_{vp}(x, z, t) \quad \rightarrow \quad \Delta\Omega_{\max}(t) = I^{-1}\Delta L[\Omega_{vp}], \tag{3.16}$$

where the first step represents the forward simulation of the dynamical equations, while the second step represents the definition given in Eq (3.9). The quantity $\Delta\Omega_{\max}(t)$ sets a theoretical upper limit for the glitch amplitude at time t, given that a large glitch occurred at $t = 0$. More precisely, $\Delta\Omega_{\max}(t)$ gives the amplitude of a *maximal* glitch[2], triggered at time t after the emptying of the reservoir because of an initial large event. We immediately have to face three difficulties:

- The general form of the natural set of dynamical equations is known (see the appendix (C)) but not the details of the mutual friction, which encodes the unknown vortex dynamics, i.e. drag, pinning, tension, interaction between vortices and so on. Within the creep scenario modified by pinning, we may assume some prescription similar to the one provided by Eq (2.21). The dynamical equations are therefore always assumed at a certain level[3]. Therefore we have to choose the form of mutual friction in the dynamical equations.

---

[2] The maximal glitch of (3.9) is the maximum glitch that can be triggered at that time with that particular reservoir. The maximum glitch of Eq (3.14) is of course a maximal glitch, but triggered when the reservoir is completely filled.

[3] As discussed in the previous chapter, the best we can do is to make working hypotheses and then construct a consistent dynamical model. Despite this, we still have to make quite arbitrary simplifications

- The initial condition $\langle \Omega_{vp}(x, z, 0) \rangle = 0$ is unknown (only the average is given). However the instantaneous relaxation timescales far from steady state are all quite small in our model: since we want to integrate forward in time for the typical inter glitch waiting time there is no problem in assuming $\Omega_{vp}(x, z, 0) \rangle = 0$. Eventual transients due to this unnatural initial condition are rapidly smoothed out and the system evolves towards the steady state, as preliminary numerical simulations indicate. Clearly this problem does not exist if the assumed dynamical equations are based on a body-averaged rigid model.

- Imagine we now want to make comparison with the observational data: we choose a pulsar spinning at Ω, with observed mean spin down rate $\dot{\Omega}$ and showing a sequence of N_{gl} glitches $\{\Delta\Omega_i, t_i\}_{i=1,\dots N_{gl}}$. We integrate the dynamical equations in time as described, setting $\Omega_p(0) = \Omega$ and $|\Omega_\infty| = |\dot{\Omega}|$ but we do not know when the observed pulsar actually empties its reservoir of angular momentum (maybe never). In principle there is no systematic argument for saying that the star reaches corotation during the largest observed event: we have to assume this (note that this assumption is not needed when we calculate the mass upper bounds, conversely M_{abs} could be interpreted as a punctual estimate of the mass rather than an upper bound).

The first two points are unavoidable difficulties that can be addressed only by the systematic study of many and different forms of the mutual friction, as well as for different inputs (like the EOS): here we restrict our attention to variations of the EOS and of the total mass, while entrainment and pinning are fixed. More refined dynamical models may need more inputs.

The third point is probably the most interesting, since it rises fundamental questions concerning the nature of glitches and their trigger. Clearly, a sequence of maximal glitches would result in a correlation between the glitch amplitudes and the waiting time between them. This ceases to be a scenario that has something to do with reality if there are no pulsars in which reservoir effects are important. If this the case, the sequence of glitch amplitudes and waiting times shows no correlations between events, which is probably true for small glitches (that comprise the major part of the whole sample among the pulsar population).

Within the hypothesis that maximal glitches are (at least in some objects) possible and that are not *dragon-king* events, we have to conclude that the observations of small glitches pollute the observed glitch series in a pulsar: since there is no need to wait for the reservoir to replenish significantly to trigger them. Statistical studies cannot be reliably done at the moment due to the paucity of collected glitches in single objects: some outstanding candidates, like J0537-6910 or the Vela could be studied by searching for correlation between large events only, differently from what is typically done without discriminating events according to their impact on the underlying superfluid reservoir. This work goes beyond the scope of this chapter, so we just give some hints that are useful to clarify the method proposed in the next section. The present discussion can also be considered a personal note to the work already published (Pizzochero et al., 2017).

The analogue of seismicity for glitches - In geology the concept of *stationary* seismicity is often used: this concept underlies an homogeneity in time, which implies that the statistical properties of the random process (a sequence of earthquakes) does not depend

---

when we have to model the mutual friction term; better comprehension of the dynamical phases of many vortices in a pinning landscape will probably provide useful hints to construct realistic friction functionals.

on the window of observation. In particular, the mean rate must be practically constant in time. It is however quite obvious that an aftershock sequence is not stationary, but observational evidence (at least for earthquakes) shows that seismicity can be well described by a stationary process (e.g. example the world-wide seismicity in a decade). The idea of pulsar activity $\mathcal{A}_a$ fits well this concept. For some pulsars the observational window is so limited and the number of glitches detected so small that it may be unsafe to conclude that the observed value of $\mathcal{A}_a$ correspond to the (stable) value that would be extrapolated by looking at a longer sequence of glitches. For simplicity we assume[4] that the value of $\mathcal{A}_a$ extracted from the available datasets correspond to a stationary sequence of glitches where aftershocks and more quiet periods of activity are both present many times, intertwined in such a way to produce an overall stationary spin up rate (eventually also many very small and undetected glitches may be included, as their contribution to the cumulated glitch amplitude is negligible).

Waiting times between glitches are not well-defined - The waiting time $\delta t_i = t_{i+1} - t_i$ between two glitches of amplitudes $\Delta\Omega_i$ and $\Delta\Omega_{i+1}$ is a highly discontinuous function of the glitch amplitudes: it immediately jumps to a different value when $\Delta\Omega_i$ (or $\Delta\Omega_{i+1}$) approaches zero: $\delta t_i \rightarrow \delta t_i + \delta t_{i-1}$ (or $\delta t_i \rightarrow \delta t_i + \delta t_{i+1}$). This may not be a serious flaw if glitches have a definite character, i.e. there exist a minimum glitch event that can be triggered (Espinoza et al., 2014). Minimum size of a glitch is actually claimed for the Crab pulsar, but its size is so small that its effect on the superfluid reservoir can be safely considered to be zero (cf. this lower limit with the maximum glitch amplitude recorded in the Crab). For the same reason, also the mean waiting time makes little sense: the more our continued timing observation is sensitive with respect to small glitches, the more the mean waiting time decreases.

A better quantity would be the mean waiting time between events of similar size. A rough estimator for such an observable can be defined as follows: starting from the glitch $\Delta\Omega_i$ at time t_i, we have to consider the date t_l of the event such that for the first time the condition $\sum_{j=i+1}^{l} \Delta\Omega_j > \Delta\Omega_i$ is realized. Of course an average of the quantity $t_i - t_l$ does not really provide the mean waiting time between glitches of similar sizes, which is expected to be longer: it is however a useful lower limit.

Current statistical studies of pulsar glitch sequences - In the case that even large glitches empty negligibly the reservoir, a completely random sequence of rare events (i.e. Poissonian) is expected. However, J0537-6910 and Vela have been proven to be exceptional objects: systematic study of glitches in individual pulsars seem to indicate that the distribution of waiting times is Poissonian while the distribution of glitch amplitudes is a power law (even though the value of the exponent is not universal across the pulsar population), but Vela and J0537-6910 showed evidence for quasi-periodicity (Melatos et al., 2008). It is worth to note that the aforementioned intrinsic problem in the definition of the waiting time has been ignored in this kind of statistical studies. As an example, consider the results of Melatos et al. (2008) about the quasi periodicity in J0537-6910: subsequent re-analysis of

---

[4] This point is not of fundamental importance for what we are going to show: the general set of ideas behind our model remains valid, even in if future observations will significantly change the inferred values of $\mathcal{A}_a$ used in this thesis. This is because our model uses $\mathcal{A}_a$ as an external input, the tuning of the model depends only on the microphysical input from literature. Of course more reliable estimates of the stationary activity for a large set of pulsars are desirable, also for reasons that go beyond the scope of the present description.

archival data[5] doubled the number of glitches found in this object (Ho et al., 2015). We have to expect this to be the rule for all the known glitchers.

Definition of a timescale associated to the glitch's amplitude - Consider the proposed generalization of waiting time, which now depends also on the glitch amplitude:

$$\Delta t_i = \delta t_i + \sum_{j=i+1}^{N_{gl}} \delta t_j \, \theta \left(\Delta \Omega_i - \sum_{k=i+1}^{N_{gl}} \Delta \Omega_k \right) ,$$

where θ is the usual Heaviside step function. In the present treatment we focus on the largest observed glitch, so we fix $i = m$ and $\Delta \Omega_{\mathrm{max}} = \Delta \Omega_m$. The expected timescale between events of a given intensity (say $\Delta \Omega_m$ for definiteness) can be roughly extrapolated by considering pulsars of (stationary) absolute activity $\mathcal{A}_a$:

$$\mathcal{A}_a = \frac{1}{T_{obs}} \sum_{i=1}^{N_{gl}} \Delta \Omega_i , \qquad\qquad (3.17)$$

where $T_{obs} \approx t_{N_{gl}} - t_1$ is the temporal duration of the observation[6]. Actually $\mathcal{A}_a$ is fitted from data, rather than found by using the above definition, as shown in Fig (3.15). We can thus define a fictitious number N_m of glitches of amplitude $\Delta \Omega_m$ and an associated timescale Δt_m as

$$N_m = \frac{1}{\Delta \Omega_m} \sum_{i=1}^{N_{gl}} \Delta \Omega_i \qquad \Rightarrow \qquad \Delta t_m \approx \frac{T_{obs}}{N_m} \approx \frac{\Delta \Omega_{\mathrm{max}}}{\mathcal{A}_a} . \qquad (3.18)$$

Note that this makes sense with the proposed definition of Δt_i: this timescale represents the mean waiting time between glitches of a fictitious object that is observed to have the same activity $\mathcal{A}_a$ but can only trigger glitches of size $\Delta \Omega_m$.

To the best of the author's knowledge, the argument behind the definition of Δt_i as estimator of the waiting time between similar glitches of amplitude $\Delta \Omega_i$ is original[7] (even though still quite heuristic); an improved formalization of these ideas is required for a precise and systematic statistical study.

We now proceed to describe how the timescale between large events can be used to refine the estimates M_{abs}, as anticipated in Antonelli and Pizzochero (2017) and detailed in Pizzochero et al. (2017).

3.3.1   Unified scenario

In the following we present a more speculative set of ideas. To keep the description as simple as possible we stick to the extreme scenario discussed in the the previous chapter:

---

[5] The new glitches are all small events that were initially not recognized, thus ignored.

[6] The approximation $T_{obs} \approx t_{N_{gl}} - t_1$ is true only for the Vela, J0537-6910 and few other pulsars that glitched many times. If the total observation consists of many disjoint temporal intervals of duration T_i, each containing several glitches, we have to consider $T_{obs} = \sum_i T_i$. The activity is thus computed as the weighted arithmetic mean of the activities $\mathcal{A}_a^i$ fitted during each interval, namely $\mathcal{A}_a = T_{obs}^{-1} \sum_i T_i \mathcal{A}_a^i$.

[7] Additional ideas can also be found in the recent work of Akbal et al. (2017): correlations between large events only has been proposed for studying the interglitch dynamics of Vela within the vortex-creep scenario.
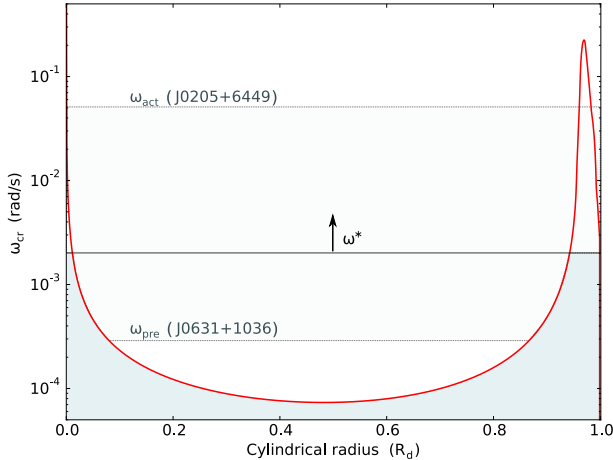
Figure 3.4: The critical lag profile $\Omega_{vp}^{\mathrm{cr}}$ (red solid curve) for a NS with mass $1.4\,M_\odot$ using the Bsk21 EOS and the extreme scenario of straight vortices that pass through the core. The horizontal line indicates the increasing nominal lag $\omega^* = t\,|\dot{\Omega}|$, the shaded area below it is bounded by the function $\Omega_{vp}(x,\omega^*)$ of Eq (3.19). The distance from the rotational axis of the star is expressed in units of the neutron drip radius R_d, which delimits the superfluid. The range of observational lags used in the present study is also indicated (lighter shading) corresponding to the values listed in the last two columns of table (3.1).

in particular we are interested in the form of the critical profile; it is equivalently possible to adapt the model in order to consider the case of rigid vortices that extend only in the crust, or the case of slack vortices discussed in the last section of the previous chapter.

Instead of solving the dynamics of Eq (3.16), with the particular rotational parameters for each pulsar, we rely on the simplified scenario sketched in Fig (3.4): starting from corotation at $t = 0$, we can measure time in terms of a *nominal lag* defined as $\omega^* = t\,|\dot{\Omega}|$; in this way we can treat all pulsars within a unified model, regardless of their specific spin-down $\dot{\Omega}$. The increasing ω^* determines the lag built up between the two components in an interval ω^* since corotation. Therefore for a pulsar of spin down rate $\dot{\Omega}$, the lag evolves as

$$\Omega_{vp}(x,t) = \min\left[\Omega_{vp}^{\mathrm{cr}}(x)\,,\, t|\dot{\Omega}|\right] \quad \Rightarrow \quad \Omega_{vp}(x,\omega^*) = \min\left[\Omega_{vp}^{\mathrm{cr}}(x)\,,\, \omega^*\right] \tag{3.19}$$

and the corresponding maximal glitch amplitude, according to Eq (3.16), is

$$\Delta\Omega_{\max}(\omega^*) = \frac{I_v}{I}\left\langle\min\left[\Omega_{vp}^{\mathrm{cr}}\,,\, \omega^*\right]\right\rangle. \tag{3.20}$$

An example of the critical lag profile in a NS is shown in Fig (3.4): it has been calculated according to the extreme scenario presented in the previous chapter. It should be now clear that for each pulsar we measure time in terms of the nominal lag ω^*: this allows for a definition of a *unified timescale* for pulsars with very different spin down rates. The curves defined by Eq (3.20) are shown in Fig (3.5) for different masses and two EOSs. On top of this, we plot the single glitches $\Delta\Omega_i$ of some pulsars[8] versus waiting times to the previous glitch δt_{i-1} multiplied by the absolute value of the spin-down rate $|\dot{\Omega}|$. The

---

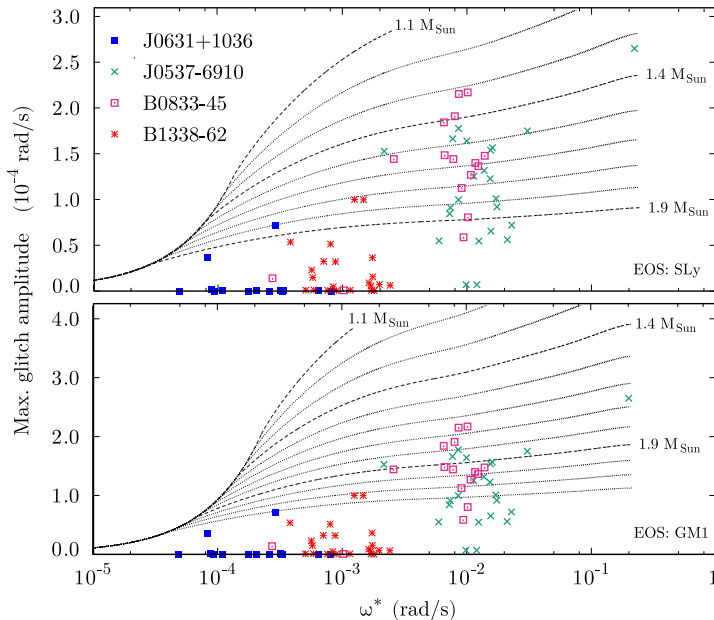[8] Among which Vela, J0537-6910 and J1341-6220 that seems to have a bimodal behavior. According

Figure 3.5: *Upper panel* - The lines $\Delta\Omega_{\max}(M, \omega^*)$ defined in Eq (3.20) are shown as a function of the nominal lag ω^* for different masses M relative to the SLy equation of state. For comparison we superimpose the single glitches $\Delta\Omega_i$ of four different pulsars; the nominal lag of each glitch is given by $|\dot{\Omega}|\delta t_{i-1}$, with δt_{i-1} the waiting time since the previous event and $|\dot{\Omega}|$ the spin down rate measured in the corresponding pulsar. *Lower panel* - the same but using the GM1 equation of state.

largest glitch of J0537-6910 is also the first one, so we plotted it at the end of the ω^* axis, where $\Delta\Omega_{\max}(\omega^*)$ saturates at the value given by Eq (3.14).

It is interesting to note that, even if the fundamental problem concerning the waiting times is ignored in Fig (3.5), it is always the largest glitch that touches the curve corresponding to the model with smaller mass, even if the data are scattered.

For each glitch we used the nominal lag corresponding to the time since the previous event, without taking into account the amplitude of this event, even if it is unlikely that small glitches are maximal. Therefore, this only serves as a clue of the fact that the largest glitch recorded in a pulsar can constrain its mass: at this level no conclusions can be taken on the actual (possibly time-correlated) occurrence of large glitches in pulsars. *A remark on the unified model* - We stress that when we simulate the full dynamical equations Eqs (2.25) and (2.26), starting from perfect corotation at $t = 0$, the lag of the in the extreme scenario evolves in a fashion very similar to the lag sketched in Fig (3.4): the nominal lag ω^* grows from zero until it locally approaches $\Omega_{vp}^{\mathrm{cr}}(x)$, where sub-critical vortex creep shapes the actual lag Ω_{vp} around the unpinning threshold. It is thus possible to recast

to Haskell and Melatos (2015), J0537-6910 is the only pulsar showing a correlation between the glitch amplitude and the waiting time to the next glitch: this suggests that the amplitudes are random, but set the time it takes to reach the threshold again (as in the crust quake model). However, also this analysis has made without considering the problem concerning the waiting times between events of very different size.

the dynamical evolution of the lag $\Omega_{vp}(x,t)$ into the form

$$\Omega_{vp}(x,t) \approx \min[\Omega_{vp}^{\mathrm{cr}}(x),\, \omega^*(t)].$$

However this only serves to *define* $\omega^*(t)$, a function of time that can be easily extrapolated from $\Omega_{vp}(x,t)$ once the actual evolution is known from the forward integration in time of the dynamical equations[9].

On the other hand, the unified model assumes $\omega^*(t) = |\dot{\Omega}_\infty|t$ for every pulsar: this choice is convenient since it is possible treat different pulsars within a unified prescription; in this way there is no need to solve the dynamical equations with the specific rotational parameters $\Omega_p(0) = \Omega$ and $|\dot{\Omega}_\infty| = |\dot{\Omega}|$ for every different object. However there are no rigorous arguments for doing this, except for the fact that the slow dynamics of Ω_{vp} toward the steady state is driven by $|\dot{\Omega}_\infty|$. This unified prescription based on a linear relation between the actual time and the nominal lag ω^* was already used (in a different context and with a different idealization of the lag dynamics) in some previous works that use the same form of the critical profile, but without entrainment (Pizzochero, 2011; Seveso et al., 2012; Haskell et al., 2013). *Effect of entrainment* - To make explicit the possible
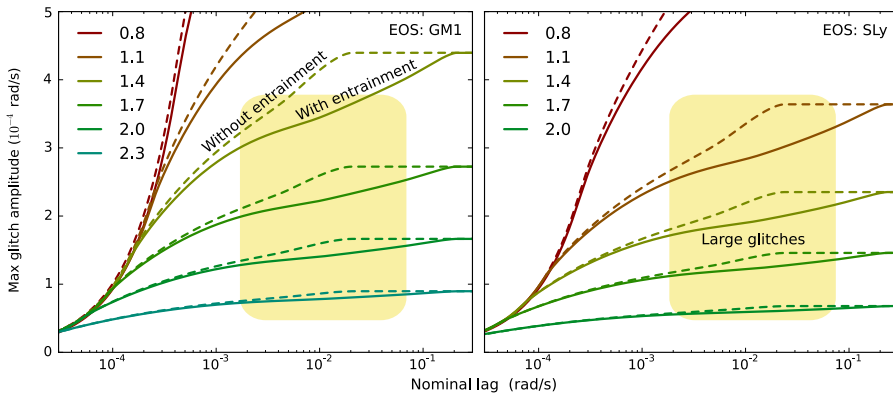

Figure 3.6: *Left* - Comparison between the maximal glitch amplitudes $\Delta\Omega_{\max}(M,\omega^*)$ given by Eq (3.20) when entrainment effect is taken into account and when $\epsilon_n = 0$ everywhere. The EOS used is GM1 and the different curves refer to the different mass values (in units of $M_\odot$) listed in the key. The region where large glitches are expected is shaded: it extends circa to the value of the largest glitch recorded in J0205-6449. The ω^* scale on the horizontal axis spans the range $3 \times 10^{-5} \div 0.3\,\mathrm{rad/s}$. *Right* - the same but using the SLy equation of state.

drawbacks of the dynamics defined by Eq (3.20), we switch off entrainment imposing $m^*(r) = 1$ everywhere and calculate the curves $\Delta\Omega_{\max}(M,\omega^*)$ by Eq (3.20) for different masses M: these curves are considerably steeper than their "entrained" counterparts, as shown in Fig (3.6). This is not surprising since the strong crustal entrainment sensibly raises the peak of the critical lag, so that the final plateau at the value $\Delta\Omega_{max}$ is reached for smaller values of ω^*. The flaw of this unified scenario is evident: entrainment should modify as well the relation between time and nominal lag $\omega^*(t)$. This is an artificial effect due to the assumed form of $\omega^*(t) = |\dot{\Omega}|t$. Nonetheless this artificial result is still physically reasonable: it is more difficult for strongly entrained superfluid neutrons to lag behind

---

[9] Once the evolution of Ω_{vp} is known, $\omega^*(t) \approx \Omega_{vp}(x_m,t)$ where x_m is the cylindrical radius corresponding to the peak of ω_{cr}.
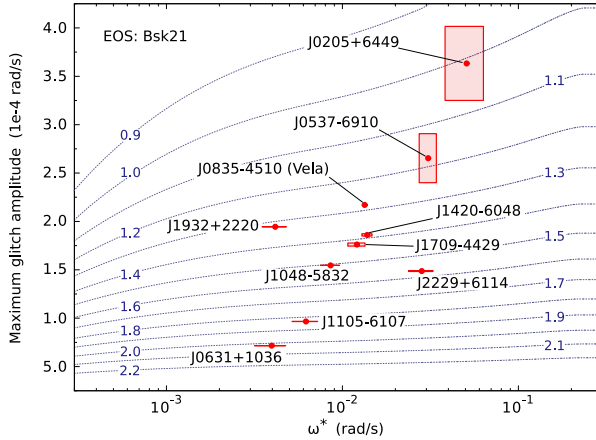
Figure 3.7: Glitch amplitude as a function of the nominal lag since corotation: the function $\Delta\Omega_{\mathrm{max}}(M, \omega^*)$ is plotted as a function of ω^* (dotted curves) for different values of the mass (indicated for each line). The EOS used is Bsk21. We also show the location of a sample of pulsars (red dots), used to estimate M_{act}: each pulsar is characterized by its maximum observed glitch $\Delta\Omega$ and the associated waiting lag ω^*_{act}, as listed in table (3.1). The observational uncertainties on these quantities, also listed in Tab (3.1), are reported as error bars or shaded regions.

the crust. Clearly a true comparative study of entrained and non-entrained dynamics can only be made by solving consistently the assumed set of dynamical equations.

3.3.2   Bracketed mass estimates

To proceed, let us make the strong additional assumption that the largest observed glitch in a pulsar depletes the whole reservoir. This approximation is generally made for all glitches in the Vela pulsar (Dodson et al., 2007) and in J0537-6910 which shows a preferred size for the events and is quasi-periodic (Melatos et al., 2008). However also the remarkable regularity in systems like J1420-6048 or J1803-2137 is a strong indication of a superfluid reservoir that is fully spent and replenished quasi-periodically, as can be seen in (3.15). Here we (tentatively) extend this claim to all the large glitchers, but *only* for their largest glitch; small glitches in these objects occur randomly (since are just irregularities in the local vortex creep rate, not extended vortex avalanches) and without any correlation with the previous glitch.

   Within the unified model and assuming the extreme scenario, we calculate the function $\Delta\Omega_{\mathrm{max}}(M, \omega^*)$ for different EOSs; as already noted in Fig (3.6), this expression depends on entrainment.

   In Fig (3.7) we plot the curve $\Delta\Omega_{\mathrm{max}}(M, \omega^*)$ as a function of the nominal lag for different values of the mass in the range $0.9 - 2.2 \, M_\odot$ and for the Bsk21 EOS; the other EOSs produce qualitatively similar results. For large enough ω^*, the curves reach their maximum value $\Delta\Omega_{\mathrm{max}}(M)$ [already shown in Fig (3.2)] which is independent on entrainment.

   For each pulsar, we consider the waiting time t_{pre} between the largest observed glitch and the one preceding it. The corresponding nominal lag is thus $\omega^*_{\mathrm{pre}} = t_{\mathrm{pre}} \, |\dot\Omega|$. Each pulsar is then characterized by two measured quantities, the amplitude $\Delta\Omega$ and the nominal lag ω^*_{pre}. These two values allow to locate the pulsar in the plane of Fig (3.7),

thus determining a corresponding mass M_{pre}, defined by $\Delta\Omega_{\max}(M_{\text{pre}}, \omega^*_{\text{pre}}) = \Delta\Omega$. The value for M_{pre} is a *lower limit*[10] on the mass of the pulsar: unless the glitch preceding the largest one has emptied the entire reservoir (thus ensuring initial corotation, which in general is *not* the case), the angular momentum accumulated since the previous glitch is larger than ΔL_{pre}; therefore a mass larger than M_{pre} is enough to reproduce $\Delta\Omega$. As already noted, this constraint on the mass in principle depends on entrainment, unlike the upper limit M_{abs}.

Summarizing, the angular momentum transferred during the maximum glitch is expected lie between two extrema: the minimum amount that can have been built up since the previous glitch, and the maximum that the pinning force can sustain. We thus estimate the mass of a pulsar by bracketing it between the corresponding values M_{pre} and M_{abs}.

Using the activity parameter - The same procedure can be used to fit a mass value M_{act} that can reproduce the pulsar absolute activity $\mathcal{A}_a$, the average rate of spin-up due to all glitches. If the angular momentum is released in a succession of glitches of fixed maximum size $\Delta\Omega$ the mean waiting time between glitches that reproduces the activity is Δt_m, which has been defined in Eq (3.18). The corresponding nominal lag is $\omega^*_{\text{act}} = \Delta t_m |\dot\Omega|$; as before, it is possible to invert the relation $\Delta\Omega_{\max}(M_{\text{act}}, \omega^*_{\text{act}}) = \Delta\Omega$ to obtain the corresponding estimate of the mass M_{act}.

This is shown in Fig (3.7), where the observational values $\Delta\Omega$ and ω^*_{act} are indicated for a sample of pulsars, together with their reported observational errors.

3.3.3 Results

The glitch data used in the analysis are given in table (3.1) and the results for the mass estimates are shown in Fig (3.8) for the Bsk21 EOS; the other EOSs produce similar results. The input used in numerical estimates are briefly described below.

Microphysical inputs - We start by considering the maximum amount of angular momentum that can be stored in the superfluid for a given model of the pinning force $f_P(n_B)$. In our calculations we use the results of ref. Seveso et al. (2016) for $f_P(n_B)$ in the NS crust; in particular we use the pinning forces corresponding to in-medium suppressed pairing gap (the case $\beta = 3$ and $L = 5000$); incidentally, this crustal gap is similar to the SFB model for S-wave neutron superfluidity used by Ho et al. (2015).

Stellar structure - The radial density profile $\rho = \rho(r)$, is found by integrating the TOV equations with an EOS for the composition and pressure of dense matter as a function of the baryon density[11]. We study three unified EOSs: SLy4 Douchin and

---

[10] Under the strong assumption that the largest glitch observed in a pulsar is a maximal glitch, it is possible to write $\Delta L^*[M^*, t_{pre}] = I^* \Delta\Omega$, where M^* is the true mass of the pulsar and $\Delta L^*[M^*, t]$ is the true evolution of the reservoir of angular momentum (time is measured since the glitch previous to the biggest one). Both ΔL^* and M^* are unknown, however the initial hypothesis tells us that we know the value of the function $\Delta\Omega^*_{\max} = \Delta L^*/I^*$ at least in a single point, i.e. when $t = t_{pre}$. We consider $\Delta\Omega_{\max}[M, t]$ such that $\Delta\Omega_{\max}[M, 0] = 0$, calculated from a specific model by using Eq (3.16). Since in general $\Delta\Omega^*_{\max}[M^*, 0] > 0$, we have $\Delta\Omega^*_{\max}[M^*, t] > \Delta\Omega_{\max}[M, t]$ for all $t > 0$ and $M \leq M^*$: this is guaranteed by the monotonicity of $\Delta\Omega_{\max}[M, t]$ in both the time and mass arguments and by the fact that $\Delta\Omega_{\max}[M_{abs}, \infty] = \Delta\Omega$ with $M_{abs} > M^*$. Therefore, to ensure the equality $\Delta\Omega^*_{\max}[M^*, t] = \Delta\Omega_{\max}[M, t]$, we have to choose $M < M^*$: the value of M that realizes $\Delta\Omega^*_{\max}[M^*, t_{pre}] = \Delta\Omega_{\max}[M, t_{pre}]$ is the M_{pre} defined in the text.

[11] One of the projects of the NewCompstar COST action was to create a database of EOSs and related data (e.g. consistent compositional information) for use in astrophysical simulations: the web

Haensel (2001), Bsk20 and the stiffer Bsk21 Goriely et al. (2010), with maximum allowed masses of 2.05 $M_\odot$, 2.16 $M_\odot$ and 2.27 $M_\odot$ respectively, and hence all compatible with the observation of Demorest et al. (2010). These EOSs (which does not contain hyperons) describe in a unified way both the crust and the core of the star, and they are compatible with all the constraints on nuclear matter properties around saturation obtained from experiments; moreover, they give NS radii that are consistent with present observational limits Lattimer and Steiner (2014), see also Fantina et al. (2013).

Extreme scenario - As already done in the previous chapter, we consider the extreme scenario: the total pinning force is derived by integration of f_p along the straight vortex lines. While vortices can probably pass trough the core, we already described in the previous chapter the argument for which it is unlikely that vortices remain straight in the core. We thus consider also the possibility of rigid vortices that are confined into the crust, a scenario that is still described by the dynamical Eqs (2.25) and (2.26).

Results - Although there are quantitative differences between EOSs, several qualitative features are evident for all models. Firstly, for most pulsars we find tight constraints for the mass of the star. One exception is J0537-6910, which only has an upper limit on the mass, as the maximum glitch was also the first observed glitch.

   More interesting, we note that a quite tight range of masses (approximately between 1.1 and 2 $M_\odot$) can explain a spread of an order of magnitude in glitch sizes: this difference is only due to the different structure between very compact and less compact structures. In particular, the results for M_{pre} (the lower bound on the mass) and M_{act} (the mass estimate constrained by the activity) still show the inverse relation between mass and maximum glitch size, noted previously for the maximum reservoir only. These mass values correspond to a partially filled reservoir and are determined using additional independent observational quantities (i.e. t_{pre} and $\mathcal{A}_a$), so that they could have been scattered randomly. Their consistency with the maximum curve provides a little[12] clue for the validity of the unified scenario; if this is the case, it indicates that mass can be an important ingredient to understand the different behavior of glitching pulsars (in addition to age, temperature and rotational parameters).

   As already observed, the mass values found here correspond to present, state of the art microphysical input: future theoretical advances may rescale the masses but maintain the qualitative general relation. Direct mass measurements of glitching pulsars are necessary to verify the mass-amplitude relation, but a single observation would already allow to calibrate the curve and give a fundamental constraint on the pinning force.

3.3.4   Discussion of the results

The framework proposed suggests a unified scenario for pulsars exhibiting large glitches, with the NS mass playing a key role; this is indeed a *minimal scenario* in which the

---

site `compose.obspm.fr` offers a collection of EOS tables, not only for cold beta-equilibrated neutron stars. Most of the currently available general purpose EOS models for use in simulations of core-collapse or NS merger are given in tabular form. The equations used here are listed as "cold neutron star EOS", namely barotropic EOSs for catalyzed nuclear matter at $T = 0$.

   [12] It is worth to note that the angular momentum reservoir is replenished quite fast, so that for most of the typical inter glitch timescales it is near saturation: in other words the curves $\Delta\Omega_{\mathrm{t}}(\omega^*, M)$ are not very steep in the region highlighted in Fig (3.6), implying that the small bracketed mass values are a drawback of the simplified dynamics and (possibly) of the methodology used to estimate M_{pre}.
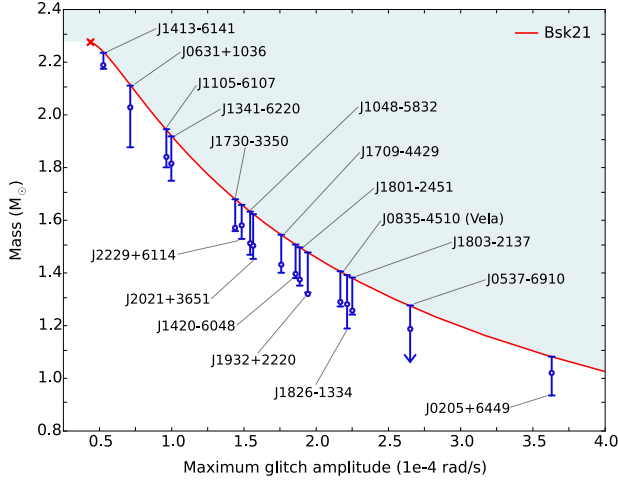
Figure 3.8: Mass estimates for 17 large glitchers with the Bsk21 equation of state. The red solid curve gives M_{abs} as a function of the maximum observed glitch $\Delta\Omega$; as in figure 2, the shaded region indicates the forbidden region and the cross corresponds to the maximum mass (2.27 $M_{\odot}$) allowed by the Bsk21 EOS. For each pulsar listed in table (3.1) and characterized by its observed $\Delta\Omega$, the mass interval $[M_{pre}, M_{abs}]$ is indicated by blue vertical bars, while the estimate for M_{act} is shown as a blue circle. The lower bound M_{pre} is undetermined for J0537-6910.
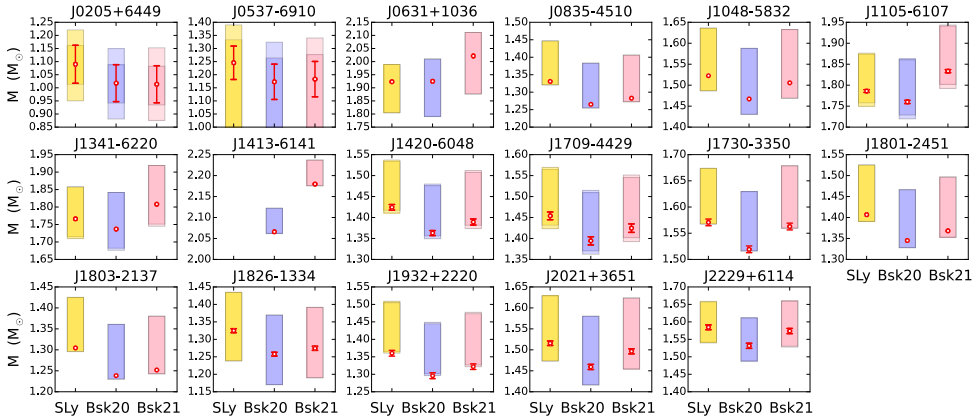

Figure 3.9: Mass estimates for the 17 large glitchers of Fig (3.3). The extreme scenario (vortex lines that are straight into the crust and core) has been used. The interval $[M_{pre}, M_{abs}]$ is highlighted with different shadings. The red circles indicate the values of M_{act}. The mass values are given with their corresponding errors, red error bars for M_{act} and lighter shading for the interval $[M_{pre}, M_{abs}]$; they are obtained from standard error propagation of the uncertainties associated to the observed glitch parameters, reported in table (3.1). In several cases, the error is smaller than the symbol used and thence not reported. As explained in the text, J0537-6910 has no lower bound M_{pre}. Due to its small largest glitch, J1413-6141 is not constrained by the soft Sly EOS: any mass is compatible with its maximum event.
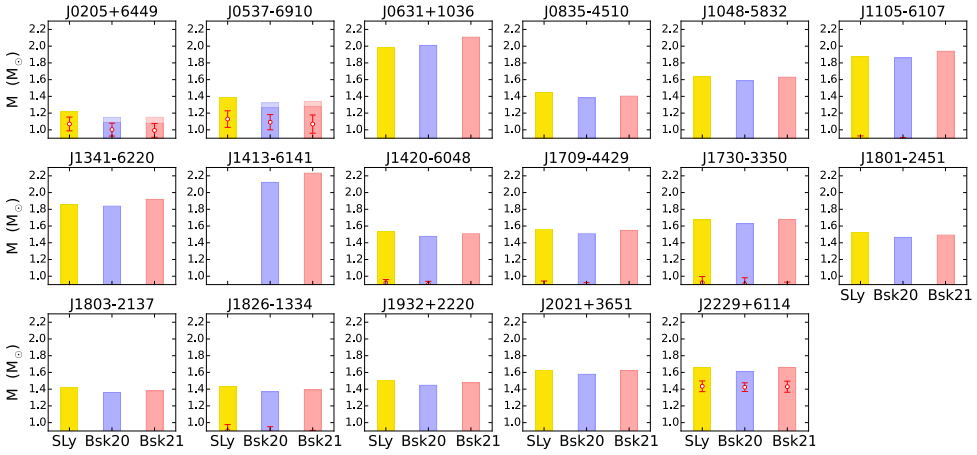
Figure 3.10: Mass estimates for the 17 large glitchers, calculated by restricting the superfluid domain to the crust (straight vortices fill the S-wave superfluid domain, while the totality of the core is assumed to be part of the normal component). Explanation of symbols is given in the caption of Fig (3.9). In the majority of cases M_{act} is below the range of observed masses (e.g. for Vela we have $M_{act} \approx 0.8\,M_{\odot}$).

importance of the mass for glitch models can be tested: no complications deriving from internal temperature (hence the pulsar age) or the particular value of the rotational parameters enters the game.

The values of the upper limit M_{abs} are quite robust, while M_{act} can be refined with the aid of hydrodynamical simulations in place of our simplified model. As it stands, the small mass intervals presented in Fig (3.9) are due to the fact that the dynamical reservoir is replenished very fast in the unified scenario, so that the observed pulsars fall in the region where the curve $\Delta\Omega_{max}(M, \omega^{*})$ is nearly flat. The estimates of M_{act} are thus less reliable than M_{abs}; moreover, it is difficult to interpret M_{act} as a punctual estimate of the stellar mass[13].

The complete range of derived masses for the three EOSs is displayed in Figs (3.9) and (3.10) for two different cases: straight vortices that pass trough the core and crust-confined vortices (note that the upper limit M_{abs} is the same in both cases). The reported errors result only from observational indeterminacies in the glitch data, listed in Tab (3.1). With the exception of two objects, these observational errors are very small, implying that the actual uncertainty in the mass estimates are completely related to the uncertainty in the assumed microscopic inputs.

We note that, in general, the mass value M_{act} is higher than the lower mass estimate M_{pre}; in the quasi-periodic Vela pulsar (as well as in several others that are not usually regarded as quasi-periodic) its value is quite close to M_{pre}: this may suggest that the reservoir of angular momentum is nearly depleted during each large glitch, even though it is impossible to draw some robust conclusion on the particular glitch behavior of a pulsar from our numerical estimates. It has however been suggested by Haskell (2016) that pulsars of low mass may have a narrower distribution of glitch sizes, centered around larger events: the present analysis seem to provide an extra clue that this is likely to be

---

[13] The mass M_{act} is more likely to be a refinement of the upper limit M_{abs}.

the case.

While things work very well for the so-called extreme scenario (Fig (3.9)), in the case of superfluidity restricted into the crust we again find the well known result that the crust is not enough: M_{act} is in general very low, around $0.8\,M_\odot$ in most cases, and M_{pre} is systematically even lower.

A word of caution is due: we proposed the extreme scenario in order to overcome the difficulty posed by strong crustal entrainment, finding a large enough angular momentum reservoir. According to the recent work of Watanabe and Pethick (2017), the effects of band structure on the neutron superfluid density are modest when pairing is properly taken into account[14]. Moreover, the uncertainties in the EOS provide enough flexibility for the construction of models that predict a large crustal thickness (Piekarewicz et al., 2014), implying both large crustal moment of inertia and a wider domain of integration for pinning forces in Eq (3.14). Moreover, calculations of strong entrainment assume a bcc lattice that may not be valid: in some regions of the crust the interstitial neutrons give rise to an attractive interaction between nuclei that can make the bcc lattice unstable (Kobyakov and Pethick, 2014).

The extent to which pulsar-timing observations can be reconciled with the standard glitch theory and strong entrainment is also explored by Chamel (2016) by considering the lack of knowledge of the dense-matter EOS: even if crustal entrainment is ignored, the standard vortex-mediated glitch scenario has been challenged by the observation of a huge glitch in PSR 2334+6 (Yuan et al., 2010) from which the constraint $I_{crust}/I > 9.4\%$ was inferred (Chamel, 2016).

Therefore, while some observations suggest that the neutron superfluid in the core of a NS contributes to glitches, glitch models based on the superfluid in the inner crust are still tenable: our model can provide a test for the newly calculated microscopic inputs and numerical estimates can be easily carried out by considering crustal superfluidity only.

Moreover we stress that the only robust mass constraint is that provided by the upper limit M_{abs}: it is entrainment independent and does not depend on the unknown extension of the superfluid domain in the core. However the general idea seems promising and can be tested with refined dynamical models and newly calculated microphysical inputs.

Broad distribution of pulsar masses - Our model predicts a broad distribution of masses, centered around $1.4M_\odot$. We note that populations studies also recover a broad distribution, that however depends on the evolutionary path of the system, with masses in NS-NS binaries tightly distributed around $1.4M_\odot$ and masses in WD-NS binaries much more broadly distributed around higher values (Özel and Freire, 2016); the inferred mass distributions for these different categories[15] of neutron stars is shown in Fig (3.11), see also (Kiziltan et al., 2013).

Future radio and gravitational waves observations are likely to probe the mass distribution in more detail, and may allow to investigate the evolutionary history of systems with glitching pulsars. This possibility is of wide interest as the mass distribution of the NS

---

[14] Hint on this open point is likely to come from cold atomic gases in optical lattices, which are a useful system for investigating experimentally the suppression of band structure effects by pairing: both the strengths of the periodic potential and of the pairing interaction can be varied in such systems.

[15] Certain sub-populations (as those in double neutron stars and in binaries with high mass companions) are thought to have experienced little or no accretion over their lifetimes. On the contrary, NSs in low-mass X-ray binaries and millisecond pulsars (typically in close orbits around WDs) undergo extended accretion periods that can increase neutron star mass from its birth value.
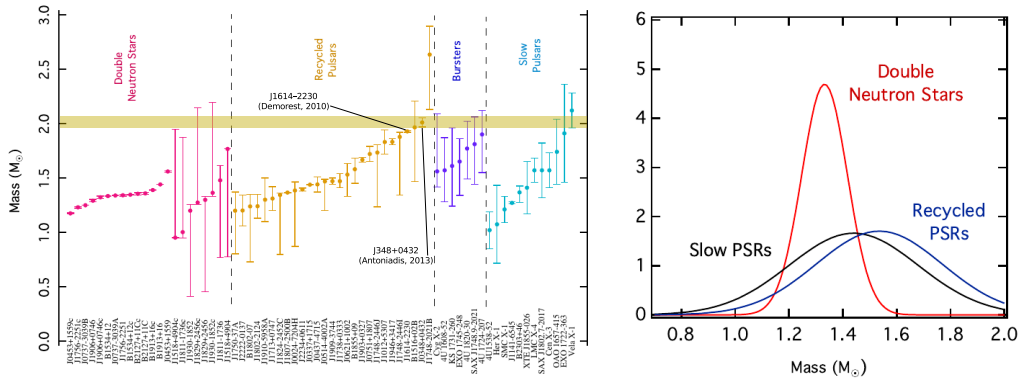
Figure 3.11: Empirical distribution of NS masses. *Left* - The most recent measurement of neutron star masses, grouped in subclasses: double neutron stars (magenta), recycled pulsars (yellow), bursters (purple), and slow pulsars (blue). *Right* - The mass distributions for the different populations of neutron stars, inferred using a Bayesian techniques to measure the most likely values of the mean dispersion for these systems. Figures adapted from (Özel and Freire, 2016).
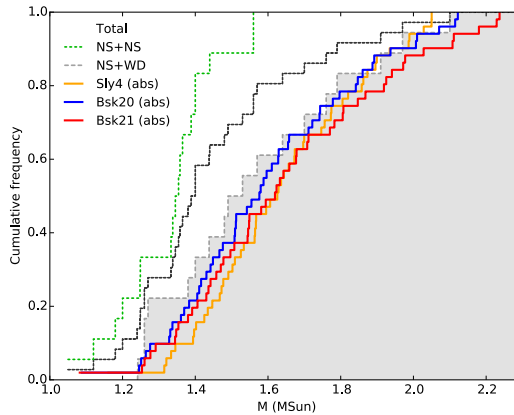
Figure 3.12: Cumulative frequency for the set of measured masses and for the 51 M_{abs}. We indicate the results for the three EOSs used, using the usual color code. The green dotted line is the cumulative frequency of NS masses that belong to a double system comprised of two neutron stars, the gray dotted curve refers to the NS that have a DW companion: this curve defines a shaded region: our estimated masses seem to fit well the distribution of this subclass. The black solid line is the cumulative frequency obtained by considering all the measured masses, irrespectively of the subclass of the object.

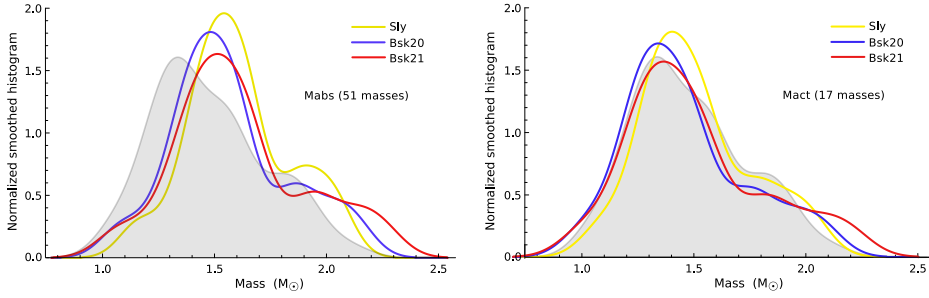**Figure 3.13:** Smoothed normalized histogram of four datasets: the distribution of the all pulsar masses, taken irrespectively of their origin (i.e. joining all the sets relative to different subclasses), and the three distributions relative to the EOSs used. The shaded region is delimited by a curve that is the distribution corresponding to the black curve of Fig (3.12). *Right* - We consider the 51 values of M_{abs}. *Left* - The 17 values of M_{act} produce a distribution that is very superimposed to the empirical distribution. While this is certainly very interesting, it is still not a proof of the goodness of M_{act}. In both cases the accordance is remarkable and deserves to be deepen.

population can also give information about the core-collapse, the EOS, and the accretion history of each neutron star.

In Fig (3.12) we show the cumulative frequency for the dataset comprised of the 51 masses M_{abs} fitted for the large glitchers.

Comparison with other models - The present approach is alternative to the methodology described by Ho et al. (2015), that relies on the mean behaviour over many decades of pulsar evolution (i.e. the activity) coupled to indirect estimates of the NS internal temperature. While our maximum angular momentum reservoir is determined by the profile of the pinning force, their reservoir is fixed by both the density and the temperature dependencies of the neutrons pairing gaps in the singlet channel alone.

A comparison of our results with the masses estimated by Ho and collaborators is possible, since the two studies have 2 EOSs and 8 pulsars in common. Even considering errors and although we both interpret the Vela as a middle-mass object, our results are completely at variance with those of Ho et al. (2015): their estimates and ordering of masses bear no resemblance to ours, the mass values are much more dependent on the EOS used as input. They find a mass distributions that is poor in low-mass objects (all their estimated masses are larger than $1.6 M_\odot$ for the Bsk21 EOS). The difference is due to the additional complication introduced by using an angular momentum reservoir that depends on thermal properties as well as to the very different methodologies adopted in the two studies.

3.4 Observational data

The glitch parameters and their observational uncertainties were extracted from the database maintained by the Jodrell Bank Observatory, http://www.jb.man.ac.uk/pulsar/glitches.html; they are reported in Tab (3.1), where we list the relevant data used in our method for the 17 non-single glitchers: spin down rate $\dot{\Omega}$, absolute activity $\mathcal{A}_a$, maximum observed glitch $\Delta\Omega$, nominal lags ω^*_{act} and ω^*_{pre}. The observational errors on the glitch parameters are also considered but no errors are listed when they do not affect the mass estimates. Moreover, the errors in the mass estimates are calculated by

J-name	$|\dot{\Omega}|$	$\mathcal{A}_a$	$\Delta\Omega$	ω^*_{act}	ω^*_{pre}
	10^{-4} rad/(yr s)	10^{-4} rad/(yr s)	10^{-4} rad/s	10^{-4} rad/s	10^{-4} rad/s
J0205+6449	88.97	0.63 ± 0.11	3.63 ± 0.38	508 ± 125	88 ± 20
J0537-6910	394.97	3.41 ± 0.06	2.65 ± 0.25	307 ± 34	-
J0631+1036	2.51	0.04 ± 0.01	0.72	41 ± 11	2.91 ± 0.03
J0835-4510	31.07	0.50 ± 0.01	2.17	134 ± 2	101
J1048-5832	12.49	0.22 ± 0.03	1.55	86 ± 11	28.1 ± 0.4
J1105-6107	7.86	0.12 ± 0.03	0.97 ± 0.01	62 ± 10	21.3 ± 3.23
J1341-6220	13.43	0.22 ± 0.02	1.00	59 ± 4	12.5 ± 1.3
J1413-6141	8.10	0.13 ± 0.02	0.53	32 ± 3	25.8 ± 0.9
J1420-6048	35.47	0.47 ± 0.03	1.86 ± 0.01	138 ± 9	112 ± 9
J1709-4429	17.56	0.25 ± 0.05	1.76 ± 0.02	121 ± 14	59 ± 4
J1730-3350	8.65	0.11 ± 0.02	1.44	107 ± 16	97.2 ± 0.7
J1801-2451	16.25	0.28 ± 0.03	1.89	106 ± 8	62.5 ± 0.5
J1803-2137	14.91	0.29 ± 0.03	2.25	116 ± 10	95.8 ± 0.1
J1826-1334	14.49	0.20 ± 0.04	2.22	159 ± 24	19.0 ± 0.1
J1932+2220	5.47	0.25 ± 0.05	1.94	42 ± 7	50 ± 1
J2021+3651	17.63	0.31 ± 0.06	1.57	89 ± 17	24.9
J2229+6114	58.23	0.30 ± 0.05	1.49 ± 0.01	282 ± 45	74.5 ± 0.5

Table 3.1: Observational parameters for the 17 pulsars considered that are both large and non-single glitchers. The definition of the quantities is given in the previous sections. We do not report any error when it is so small that the resulting mass estimate is unaffected.

standard error propagation and reflect only the observational uncertainties (the theoretical microphysical inputs are considered "exact").

The properties relative to the sample of the 51 large glitchers (The Crab pulsar is added at the end of the table for comparison purposes) are reported in Tab (3.2). The threshold $\Delta\Omega > 5 \times 10^{-5}$ rad/s that discriminates between large glitchers and the rest of the pulsar population is settled by the pinning forces used: with weaker pinning forces or newly detected large glitches, other pulsars will join the sample in Tab (3.2).

As an explicit example, consider J0729-1448: this pulsar seems a perfect candidate for our study, but it is categorized as a single glitcher: N_m is very close to 1, a fact that is reflected into the huge uncertainty of the fitted value of $G = \mathcal{A}_a/|\dot{\Omega}|$, as can be checked also in Fig (3.15). Following this line of reasoning, only 17 non-single large glitchers with definite activity and with (at least) two glitches of the comparable size remain.

For completeness we also present, in Fig (3.14), a summary of the properties of the known sample of RPPs that have been observed to glitch.

The whole glitching RPPs population is organized as follows: we consider the three base quantities used in our model, namely $|\dot{\Omega}|$, $\mathcal{A}_a$ and $\Delta\Omega_{\mathrm{max}}$, which are used to calculate M_{abs} and M_{act}. These three quantities are obtained directly from observations: possible correlations between them can be manifestations of a common physical property of the sample. We also consider two derived quantities, the characteristic age $\tau = P/(2\dot{P})$, that indirectly accounts for the pulsar period (or for the angular velocity Ω). The angular velocity has not been used in the unified scenario but we know that the steady state lag, in the absence of strong pinning, depends on both Ω ad $|\dot{\Omega}|$. In principle it is thus interesting to consider also this quantity, via τ. Finally we consider ω^*_{act}, the nominal lag corresponding to the timescale between maximal glitches: this quantity is derived by using all the three basic quantities $|\dot{\Omega}|$, $\mathcal{A}_a$ and $\Delta\Omega_{\mathrm{max}}$; therefore possible correlations between this quantity and the others are artificial.
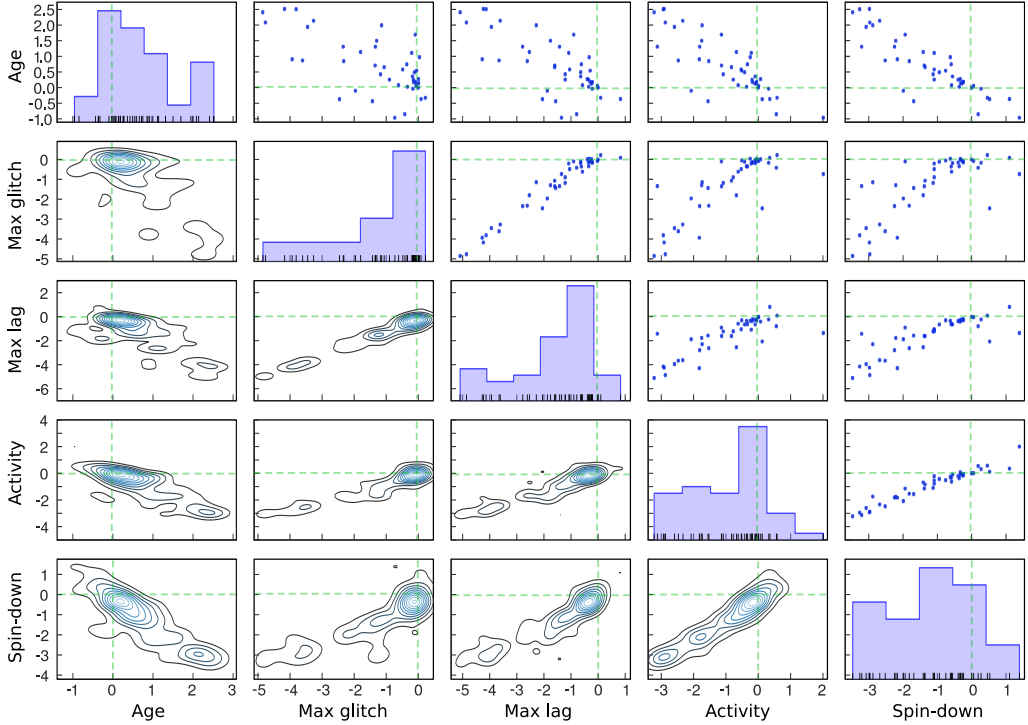
Figure 3.14: Cross correlations between some phenomenological quantities of the RPPs that have been observed to glitch and for which it is possible to define the activity parameter. The considered variables are: the characteristic age $\tau = \Omega/(2|\dot{\Omega}|)$, the maximum glitch $\Delta\Omega_{\mathrm{max}}$, the nominal lag ω_{act}^*, the activity $\mathcal{A}_a$ and the spin down rate $|\dot{\Omega}|$. As explained in the text, for every pulsar in the sample we normalized the relative quantities to the values of Vela, so that Vela is always represented by the point of coordinates (0,0), indicated by the dashed lines. Some evident correlations are artificial, namely the ones envisaged between τ and $|\dot{\Omega}|$ or between ω_{act}^* and $\Delta\Omega_{\mathrm{max}}$ (simply because τ and ω_{act}^* are derived quantities). It is however interesting to note that at the moment (due to the paucity of data and selection effects) there are no evident correlations in the sample of the large glitchers, except from the clear (and well known) relation between $\mathcal{A}_a$ and $|\dot{\Omega}|$.

The dataset presented in of Fig (3.14) is organized as follows: firstly we consider the quantities τ^V, $\Delta\Omega_{\mathrm{max}}^V$, ω_{act}^{*V}, $\mathcal{A}_a^V$ and $|\dot{\Omega}^V|$ relative to the Vela pulsar. For every pulsar for which we can fit $\mathcal{A}_a$, we plot the quantities Age=$\log_{10}(\tau/\tau^V)$, Max glitch=$\log_{10}(\Delta\Omega_{\mathrm{max}}/\Delta\Omega_{\mathrm{max}}^V)$, Max lag=$\log_{10}(\omega_{act}^*/\omega_{act}^{*V})$, Activity=$\log_{10}(\mathcal{A}_a/\mathcal{A}_a^V)$ and Spin-down=$\log_{10}(|\dot{\Omega}|/|\dot{\Omega}^V|))$. In this way we can see how the population of the known glitching RPPs is scattered with respect to the coordinate (0,0), which represents the Vela pulsar. On the diagonal of Fig (3.14) we draw histograms, showing the rough phenomenological distribution of the corresponding quantity. The other non-diagonal inserts are scatter plots. We can note some cross correlations between the five phenomenological quantities that have been used. Some evident correlations are artificial, namely the ones envisaged between τ and $|\dot{\Omega}|$ or between ω_{act}^* and $\Delta\Omega_{\mathrm{max}}$ (simply because τ and ω_{act}^* are derived quantities). It is however interesting to note that at the moment (maybe due to the paucity of data and to selection effects) there are no evident correlations in the

sample, except from the clear and already known correlation between $\mathcal{A}_a$ and $|\dot{\Omega}|$ (Fuentes et al., 2017). This fundamental property of the sample is translated into the (weaker and partially artificial) correlation between $\Delta\Omega_{\mathrm{max}}$ and ω^*_{act}.

Moreover, there is a remarkable clustering of the scattered data around Vela in the τ-$\Delta\Omega_{\mathrm{max}}$ panel (τ and $\Delta\Omega_{\mathrm{max}}$ are independent measured quantities), a clue that the pulsars that display large glitches are really "Vela-like" pulsars, with similar characteristic age and maximum glitch amplitude.

A systematic statistical analysis will be possible in a future, if new-generation radio telescopes will lead to an interesting increase of the glitch dataset in RPPs. The direction to follow from the observational side is quite clear: we need more sources that are observed to glitch several times more than many single glitchers.
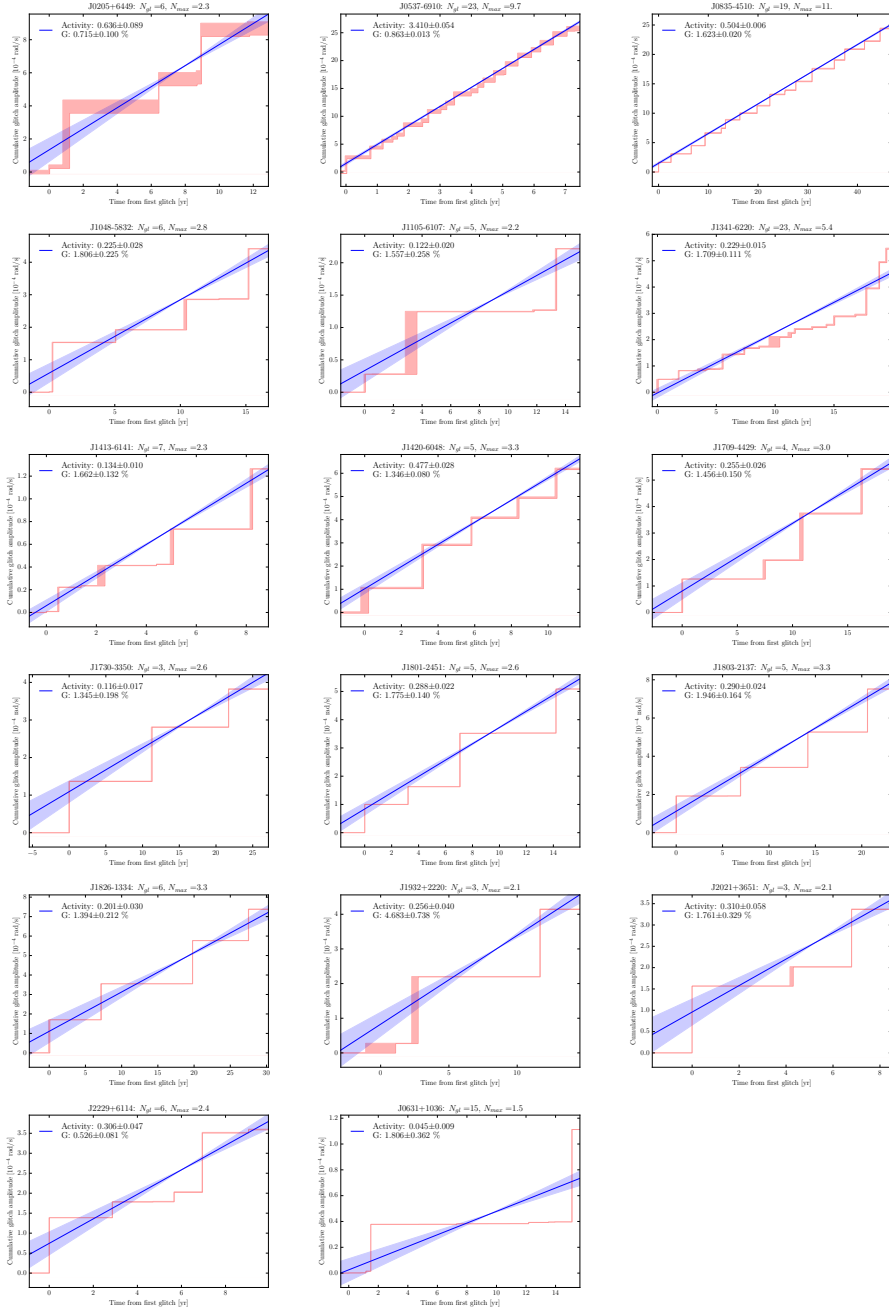
Figure 3.15: The cumulated glitch activity (red line) for the 17 pulsars considered as a function of time: its vertical width indicates the absolute uncertainty on the measured amplitude, the horizontal width refers to the uncertainty on the glitch date. The blue line is a least square fit (the uncertainty on the slope is indicated as an angle).

Table 3.2: Observational values for the 51 large glitchers considered, see also Fig (3.3). We report the rotational parameters Ω and $|\dot{\Omega}|$, the dipole characteristic age τ, the number of glitches N_{gl}, the largest jump size $\Delta\Omega_{\max}$ and the corresponding fraction of large glitches N_m/N_{gl}. Here $G = \mathcal{A}_a/|\dot{\Omega}|$, so that the nominal lag corresponding to the largest glitch can be equivalently written as $\omega^*_{act} = \Delta\Omega_{\max}/G$.

J-Name	Age (dipole) 10^3 yr	Ω rad/s	$|\dot{\Omega}|$ 10^{-4}rad/(s yr)	G %	$\Delta\Omega_{max}$ 10^{-4}rad/s	N_m/N_{gl}	N_{gl}
J0205+6449	5.4	95.61	88.97	0.72 ± 0.10	3.63 ± 0.38	**0.40**	**6**
J0358+5413	560	40.18	0.36	17.98 ± 6.03	1.75	0.17	6
J0537-6910	4.9	389.72	394.97	0.86 ± 0.01	2.65 ± 0.25	**0.42**	**23**
J0631+1036	44	21.83	2.51	1.81 ± 0.36	0.72	**0.10**	**15**
J0729-1448	35	24.97	3.55	3.27 ± 2.34	1.67 ± 0.00	0.20	5
J0835-4510	11	70.34	31.07	1.62 ± 0.02	2.17	**0.59**	**19**
J1016-5857	21	58.51	13.90	*	1.12	0.92	2
J1023-5746	4.6	56.37	61.23	*	2.01	*	1
J1048-5832	20	50.81	12.49	1.81 ± 0.23	1.55	**0.48**	**6**
J1052-5954	140	34.79	1.21	*	2.35	*	1
J1105-6107	63	99.43	7.86	1.56 ± 0.26	0.97	**0.46**	**5**
J1112-6103	33	96.72	14.78	*	1.77 ± 0.02	0.83	2
J1119-6127	1.6	15.40	47.90	0.17 ± 0.06	0.83 ± 0.12	0.35	3
J1301-6305	11	34.05	15.53	*	1.58 ± 0.01	0.79	2
J1341-6220	12	32.50	13.43	1.71 ± 0.11	1.00	**0.24**	**23**
J1357-6429	7.3	37.83	25.88	*	0.92	0.86	2
J1412-6145	51	19.93	1.97	*	1.45	*	1
J1413-6141	14	22.00	8.10	1.66 ± 0.13	0.53	**0.34**	**7**
J1413-6205	63	57.25	4.56	*	0.99	*	1
J1420-6048	13	92.16	35.47	1.35 ± 0.08	1.86 ± 0.01	**0.67**	**5**
J1531-5610	97	74.62	3.84	*	1.97 ± 0.01	*	1
J1539-5626	800	25.82	0.16	*	0.72	*	1
J1614-5048	7.4	27.12	18.28	*	1.75 ± 0.02	0.98	2
J1617-5055	8.1	90.59	55.70	*	0.54 ± 0.00	*	1
J1702-4310	17	26.12	7.67	*	1.26 ± 0.03	*	1
J1709-4429	17	61.32	17.56	1.46 ± 0.15	1.76 ± 0.02	**0.77**	**4**
J1718-3718	33	1.86	0.28	*	0.62	*	1
J1730-3350	26	45.05	8.65	1.35 ± 0.20	1.44	**0.88**	**3**
J1740+1000	110	40.78	1.79	*	1.19	0.50	2
J1757-2421	290	26.84	0.47	*	2.09	*	1
J1801-2451	15	50.30	16.25	1.78 ± 0.14	1.89	**0.54**	**5**
J1803-2137	16	47.01	14.91	1.95 ± 0.16	2.25	**0.67**	**5**
J1806-2125	63	13.04	1.04	*	2.06	*	1
J1809-1917	51	75.93	7.39	*	1.23	*	1
J1813-1246	43	130.70	15.07	*	1.52	*	1
J1826-1334	21	61.91	14.49	1.39 ± 0.21	2.22	**0.55**	**6**
J1833-0827	150	73.67	2.50	1.69 ± 0.89	1.37	0.33	3
J1837-0604	34	65.25	9.66	*	0.91 ± 0.00	0.51	2
J1838-0453	52	16.50	1.58	*	1.63 ± 0.06	0.50	2
J1838-0537	4.9	43.12	44.06	*	2.37	*	1
J1838-0655	23	89.13	19.65	*	1.38 ± 0.06	*	1
J1846-0258	0.73	19.24	132.13	*	1.19 ± 0.06	0.50	2
J1856+0113	20	23.49	5.78	*	2.72	0.67	2
J1856+0245	21	77.66	18.81	*	2.08 ± 0.00	*	1
J1907+0602	19	58.92	15.14	*	2.75	0.50	2
J1921+0812	620	29.83	0.24	*	1.08	*	1
J1932+2220	40	43.49	5.47	4.68 ± 0.74	1.94	**0.71**	**3**
J1952+3252	110	158.94	7.42	3.18 ± 0.76	2.38	0.17	6
J2021+3651	17	60.57	17.63	1.76 ± 0.33	1.57	**0.72**	**3**
J2229+6114	10	121.71	58.23	0.53 ± 0.08	1.49 ± 0.00	**0.40**	**6**
J2337+6151	41	12.68	1.56	*	2.60	*	1
J0534+2200	1.2	189.91	765.75	0.0030 ± 0.0004	0.406 ± 0.002	0.10	25
J1833-1034	4.9	101.53	104.59	0.0043 ± 0.0004	0.00761	0.51	4

Relativistic corrections to pulsar glitch amplitudes

In this chapter we investigate the general relativistic corrections to pulsar glitch amplitudes. Numerical estimates will be carried out within the slow rotation approximation of Hartle (1967): the slow rotation approximation allows for a simple calculation of the maximum amount of angular momentum that can be stored into the pinned superfluid, consistently with the stratified structure of the star and the presence of a background axially symmetric curved spacetime. We thus provide a relativistic generalization of the Newtonian model described in the previous chapters.

It is found that the effect of general relativity on the maximum glitch amplitude, at least in the pinning paradigm that we consider here, is quite small. Therefore the Newtonian upper bounds on the mass presented in the previous chapter only differ by few percent with respect to the same upper bounds calculated within the relativistic framework.

The present analysis can also serve as a basis to construct more sophisticated models of angular momentum reservoir in a relativistic context. The relevant concepts of two-fluid hydrodynamics are briefly reviewed and a generalization of the famous Feynman-Onsager relation (when both entrainment coupling between the fluids and strong gravity are present) is derived.

In the following we use the "mostly plus" convention, i.e. the metric signature is $(-, +, +, +)$. Except for the final results that have to be numerically evaluated (where th constants G and c are explicit), geometrized units are used in the calculations.

4.1 The perfect fluid in general relativity

A concise introduction to relativistic hydrodynamics is given by Gourgoulhon (2006), while modern extended treatment (including astrophysical applications and numerical schemes) is presented in the book of Rezzolla and Zanotti (2013). A particularly NS-oriented review of relativistic hydrodynamics is that of Andersson and Comer (2007). Applications to relativistic rotating stars and a clear general introduction to the perfect fluid in GR can be found in the book of Friedman and Stergioulas (2013), while the notes of Gourgoulhon (2010) are more focused on the theoretical foundations and provide a detailed discussion of the spacetime and flow symmetries.

4.1.1   Observers in general relativity

An observer in general relativity is a worldline, namely the set of events recorded by a test (massive) particle. This particle can be freely-falling (like the Earth) or use its internal energy (like a rocket) or interaction with fields and matter (like us, sustained on the surface of Earth by Coulomb forces) to deviate from the geodesics motion. An observer can carry a frame, a set of four basis elements of the tangent space that are locally defined at each point on the observer's worldline. A family of observers thus provide a frame field, a collection of frames that span the tangent bundle: this provides the so-called "tetrad formalism", an alternative to the more usual "chart approach". Following standard terminology, points belonging to the spacetime manifold will be sometimes referred to as events. In the chart of coordinates[1] $\{x^\mu\}$, the worldline is a timelike curve $\mathcal{L}$ parametrized as $x^\mu(\lambda)$. Given a particular event $A \in \mathcal{L}$, the events that are simultaneous to A (i.e. that are considered to be simultaneous to A by the given observer) is the set of points belonging to a hypersurface passing trough A and orthogonal to $\mathcal{L}$.

A particular choice of the parameterization defines the proper time τ, the length along the curve $c\,d\tau = \sqrt{-g_{\mu\nu}\partial_\lambda x^\mu \partial_\lambda x^\nu}\,d\lambda$. Note that in this definition d is not the exterior derivative operation but simply indicates an infinitesimal increment. The four-velocity $u = u^\mu \partial_\mu$ of the particle is the unique unit tangent vector to $\mathcal{L}$ oriented toward the future, $u^\mu = dx^\mu(\tau)/d\tau$: the 4-velocity is indeed always normalized as $u_\mu u^\mu = -1$ and unique, thanks to the fact that proper time has been chosen among all the possible parameterizations. This 4-velocity u is a tensor defined by using only $\mathcal{L}$ and the absolute structure of spacetime provided by g: it is therefore intrinsic to the particle under consideration. This is in contrast with the usual notion of relative velocity, namely u is not defined in relation to some observer. Also the 4-acceleration a, which natural components are given by $a^\mu = u^\nu \nabla_\nu u^\mu$, is an intrinsic property of the particle as well. The normalization of u implies that $g(u,a) = 0$, a property that can be realized only if a is spacelike, i.e. $g(a,a) > 0$.

If we want to introduce the relative velocity we have to consider two observers (i.e. two point masses) that share the same tangent space at some point: we thus introduce the worldline $\mathcal{L}'$ with 4-velocity u' and proper time τ' that intersects $\mathcal{L}$ at a certain event, say A. After some elapsed proper time $d\tau$ since A, the observer relative to $\mathcal{L}$ will touch the event B. The second observer will see this to happen after the time $d\tau'$ has elapsed, at event B'. Exactly as in special relativity, the Lorentz factor W is defined as $d\tau' = W d\tau$. We just have to understand how to express W it in terms of u and u'. Both observers start at A and after a little bit they are separated by the displacement $B'B$

$$u\,d\tau = u'\,d\tau' + B'B\,.$$

However B is an event that is simultaneous to B' for the observer $\mathcal{L}'$, therefore $g(B'B, u') = 0$. We thus multiply the above equation by u'_μ and obtain

$$W = -u'_\mu u^\mu \qquad\qquad\qquad (4.1)$$

---

[1] The so-called *natural basis* relative to the coordinates $\{x^\nu\}$ is, as usual, indicated by $\{\partial_\mu\}$, i.e. a set of four vector fields of coordinates δ^μ_α, where μ can be regarded as the "name" of the vector ∂_μ. The natural co-basis is $\{dx^\nu\}$, a set of four one-forms of coordinates δ^μ_α, where μ is the "name" of the form dx^μ. The exterior derivative df of a scalar field f is notoriously a one-form, namely the gradient of f. Use of the symbol d for the exterior derivative justifies the use of the symbol dx^μ for the co-basis elements, namely $df = \nabla_\mu f\,dx^\mu$, where $\nabla_\nu f$ are four numbers which represent the components of df with respect to the basis $\{dx^\mu\}$.

The velocity U of $\mathcal{L}$ as seen by $\mathcal{L}'$, when they meet at A, is naturally defined as

$$U = \frac{B'B}{d\tau'} \qquad \Rightarrow \qquad u = W\left(U + u'\right) .$$

The square of the above equation (remember that $g(U, u') = 0$ due to simultaneity definition) gives that W is identical to the well-known expression from special relativity

$$W = \left(1 - U_\mu U^\mu\right)^{-1/2} . \tag{4.2}$$

The velocity U^μ generalizes the usual concept of relative velocity of the particle in B with respect to the particle in B'. Note that now U^μ is not normalized to -1.

Finally it is useful to introduce the projector[2] $\perp$ onto the 3-dimensional vector space orthogonal to u, which can be considered as the local rest space of the observer:

$$\perp_{\alpha\beta} = g_{\alpha\beta} + u_\alpha u_\beta . \tag{4.3}$$

It is simple to see that $\perp(u) = 0$. Let $\perp'$ be the projector onto the space orthogonal to u', then $\perp'_{\alpha\beta} u^\beta = W U_\alpha$ and $\perp'_{\alpha\beta} u^\alpha u^\beta = U^2/(1 - U^2)$.

4.1.2 Basic thermodynamics

In order to discuss the hydrodynamics of the perfect fluid in general relativity (fluids for which viscous effects and heat fluxes are zero, and the pressure is isotropic), it may be useful to briefly review some basic thermodynamics. This is more authoritatively done in many textbooks, including the classic books of Misner et al. (1973) and Shapiro and Teukolsky (1983); however this section will allow to set some notation.

The laws of thermodynamics provide information about the changes in the thermodynamic properties of the system as they evolve in quasi-equilibrium, along a sequence of states where the thermodynamic variables are related trough an equation of state. The EOS plays a fundamental role in hydrodynamics because it provides a closure relation in the set of dynamical equations and, at the same time, represent the realistic input in the description of a given physical system (Rezzolla and Zanotti, 2013).

Given a fluid element, there will be a number of thermodynamic quantities defined at a certain event and measured in the element's rest frame. Not all of the thermodynamic quantities are independent, e.g. the state of a single-component fluid can be expressed in terms of only two independent parameters, usually the density and temperature.

For a simple and single-species system the first and second laws of thermodynamics can be combined[3] to give

$$dE = T\,dS - P\,dV + \mu\,dN , \tag{4.4}$$

where the internal energy E, entropy S, volume V, and particle number N are the extensive variables related by the equation of state $E = E(S, V, N)$. The energy must scale together with all the other quantities, implying that $kE = E(kS, kV, kN)$ for a constant k: the local thermodynamic state (modulo entrainment that we do not consider here) is a function

---

[2] The operator $\perp$ is idempotent ($\perp^\alpha_\mu \perp^\mu_\beta = \perp^\alpha_\beta$) and self-adjoint (simply because it is real and symmetric), therefore it is an orthogonal projection.

[3] As pointed out by (Andersson and Comer, 2007), the first law is a statement about heat and work, and says nothing about the entropy, which enters through the second law.

of the extensive variables per unit volume (or per particle). This scaling is based on the hypothesis that surface effects are negligible for the volume V. Total differentiation gives

$$dkE + kdE = Td(kS) - Pd(kV) + \mu d(kN)$$
$$= (TS - PV + \mu N)dk + k(T\,dS - P\,dV + \mu\,dN)$$

which implies the Euler relation $E = TS - PV + \mu N$. The equation of state $E = E(S, V, N)$ is valid in small (but macroscopic) patches across which the changes in the gravitational field are negligible[4]. It is thus sufficient to determine the properties of matter in special relativity; the thermodynamic variables of the fluid are defined in the set of frames locally comoving with the fluid. From the geometrical point of view the thermodynamic quantities are scalar fields by construction. The reason for this construction stems from the equivalence principle: the first and second laws of thermodynamics are local statements made by an observer (see the next section) that is at rest with respect to the fluid element under consideration. The Euler relation divided by V (the proper volume of a little portion of fluid) reads

$$E/V = \mathcal{E}(n, s) = \mu(n, s)\,n + T(n, s)\,s - P(n, s). \tag{4.5}$$

We now denote with X a generic extensive variable, while $x = X/V$ is its value per unit volume and $\tilde{x} = X/N$ is its value per particle (that is proportional the specific quantity); differentiation gives

$$dx = d(X/V) = d(n\tilde{x}) = dn\,\tilde{x} + n\,d\tilde{x} = \frac{dn}{n}\,x + n\,d\tilde{x}. \tag{4.6}$$

When we want to describe a stationary star in equilibrium, n is the conserved baryon number density: $dN = 0$ implies $dV/V = -dn/n$ and from the above equation it follows that

$$d\mathcal{E} = dE/V - \mathcal{E}\,(dV/V)$$
$$= -P\frac{dV}{V} + \mu\frac{dN}{V} + T\frac{dS}{V} + \mathcal{E}\,\frac{dn}{n} \qquad (\text{use } dS/V = ds - s\,dn/n \text{ and } dN = 0)$$
$$= \frac{\mathcal{E} + P - Ts}{n}\,dn + T\,ds.$$

Consider now the standard definition of enthalpy, $H = E + PV = TS + \mu N$, the thermodynamic potential which is minimized when the system reaches chemical equilibrium at constant pressure. Following the aforementioned "tilde notation", the enthalpy per baryon is

$$\tilde{h} = \frac{E + PV}{N} = \frac{\mathcal{E} + P}{n} \quad \Rightarrow \quad d\mathcal{E} = \tilde{h}\,dn + T\,n\,d\tilde{s} \qquad (\text{for } dN = 0),$$

---

[4] We adapt an argument by Glendenning (2000): consider $g_{rr}(R) = (1 - 2M/R)^{-1}$ and $g_{rr}(0) = 1$, therefore the metric changes over the distance R by a typical factor

$$\frac{g'_{rr}}{g_{rr}}R \sim \frac{g_{rr}(R) - g_{rr}(0)}{(g_{rr}(R) + g_{rr}(0))/2} = 2M/(R - M) \approx 1.$$

The estimate has been made for a high-mass neutron star of $2\,M_\odot \approx 3\,\text{km}$ and $R \approx 10\,\text{km}$. The average Wigner-Seitz radius r_{WS} scales as $r_{WS}^3 \sim R^3/A$ which, for typical values $A \sim 10^{57}$ and $R \sim 10^6$ cm, gives $r_{WS} \sim 1\,\text{fm}$. Therefore

$$\frac{g_{rr}(r + r_{WS}) - g_{rr}(r)}{(g_{rr}(r + r_{WS}) + g_{rr}(r))/2} \approx \frac{g'_{rr}(r)}{g_{rr}(r)}r_{WS} \sim \frac{r_{WS}}{R} \sim 10^{-19}.$$

the relative change of the metric over many Wigner-Seitz cells is negligible. Friedman (1992) gives an interesting and complementary argument but based on the scaling of the Ricci scalar.

where the relation between the differentials dx and $d\tilde{x}$ has been used. The rest mass density mc^2n is included in the mass-energy density $\mathcal{E}$ and so in μ and $\tilde{h}$. Moreover, in the zero temperature limit, the enthalpy per baryon coincides with the chemical potential[5], $\tilde{h} = \mu$ as should be evident by confronting Eq (4.5) for $T = 0$ and the definition of $\tilde{h}$.

Sometimes the specific quantities, in particular the specific energy, are also used. Consider Eq (4.4) with $dN = 0$ and divide it by N. Since N is constant, this operation commutes with differentiation and the fundamental relation is

$$d\tilde{\mathcal{E}} = T\,d\tilde{s} - P\,d\tilde{v} \qquad \Rightarrow \qquad P = n^2 \frac{\partial \tilde{\mathcal{E}}}{\partial n}. \tag{4.7}$$

Following the notation in Eq (4.6), $\tilde{v} = n^{-1}$ is the mean volume per baryon.

4.1.3 Dynamical equations

The world-line of a fluid element defines a 4-velocity $u^\alpha = dX^\mu(A_0, \tau)/d\tau$, where A_0 is some event that can be used as a label: this is the so-called Lagrangian formulation of hydrodynamics. For our scope the Eulerian formulation more suitable: the fluid motion is described by a tensor field u that at every event of coordinates x^ν associates a vector of coordinates $u^\mu(x^\nu)$ which belongs to the tangent space at that event. General relativity is ruled by the Einstein equations that are conveniently written as

$$R_{\alpha\beta} - \frac{1}{2}R\,g_{\alpha\beta} + \Lambda g_{\alpha\beta} = \frac{8\pi G}{c^4}\,T_{\alpha\beta}\,,$$

where the 8π factor is needed to ensure the correct Newtonian limit. Since the energy-momentum tensor (also sometimes called stress-energy) $T^{\alpha\beta}$ has dimension of an energy per unit volume and the metric is dimensionless, the Ricci tensor $R_{\alpha\beta}$, scalar R and Λ have the dimension of the inverse of an area (and so the Einstein tensor $G_{\alpha\beta} = R_{\alpha\beta} - \frac{1}{2}R\,g_{\alpha\beta}$). This is in accordance to the fact that Einstein equations are second order equations for the metric g. The Bianchi identity[6] $\nabla_\mu G^{\mu\alpha} = 0$ implies $\nabla_\mu T^{\mu\nu} = 0$. This is sometimes regarded to as the equation of motion of matter. However things are not so simple: if the fluid is comprised of a single component, the conservation of the energy-momentum is equivalent to the three usual Euler equations plus the energy equation. However if we have to deal with a multifluid we need more than four equations.

An important case of energy-momentum tensor is that of a perfect fluid. A non-viscous isotropic fluid flowing along the velocity field u is described by an energy-momentum tensor of the form

$$T^{\alpha\beta} = \mathcal{E}\,u^\alpha u^\beta + P \perp^{\alpha\beta} = h\,u^\alpha u^\beta + g^{\alpha\beta}P\,, \tag{4.8}$$

where the tensor field $\perp_{\alpha\beta} = g_{\alpha\beta} + u_\alpha u_\beta$ projects onto the three-space at rest with respect to the fluid element, in complete analogy with the projector of Eq (4.3). Following the notation introduced in Eq (4.6), $h = n\,\tilde{h}$ is the enthalpy density. The fact that we used the energy density and the pressure measured by a comoving observer makes sense, as can be

---

[5] From Eq (4.4) with constant N, the chemical potential is $\mu = \tilde{\mathcal{E}} + P/n - T\tilde{s} = \tilde{h} - T\tilde{s}$.

[6] Since Λ is a constant, the invariance of the metric with respect to covariant derivatives $\nabla_\alpha g_{\mu\nu} = 0$ assures that the presence of $g\Lambda$ does not modify the fact that the Bianchi identity implies the vanishing of the divergence of the energy-momentum tensor. Moreover on the stellar scale the cosmological constant can be dropped.

checked by noting that $T_{\mu\nu}u^\mu u^\nu = \mathcal{E}$ [for the derivation of the energy-momentum tensor and its 3+1 decomposition see e.g. (Rezzolla and Zanotti, 2013) or (Gourgoulhon, 2010)].

The particle current of the fluid is defined like in special relativity, $n^\mu = n\,u^\mu$. In this way, the general-relativistic conservation of rest mass (i.e. of particle number), the conservation of energy and momentum are given by the hyperbolic system of equations

$$\nabla_\alpha T^{\alpha\beta} = \nabla_u (n\,\tilde{h}\,u^\beta) + u^\beta \nabla_\alpha (n\,\tilde{h}\,u^\alpha) + \nabla^\beta P = 0 \qquad (4.9)$$

$$\nabla_\alpha n^\alpha = \nabla_u n + n\nabla_\alpha u^\alpha = 0 \,, \qquad (4.10)$$

where $\nabla_u = u^\alpha \nabla_\alpha$ is a derivative along the fluid worldline. Equations (4.9) and (4.10) provide a total of five equations for six unknowns: the three components of the four-velocity (the fourth one is obtained through the normalization), the number density n and two thermodynamic quantities, say, the pressure P and the enthalpy per baryon $\tilde{h}$. An equation of state relating the pressure to other thermodynamic quantities is the sixth equation necessary to close the system. The conservation equations (4.9) and (4.10) can be written in a form that resembles the conservation of energy (energy equation) and momentum (Euler equation). Projection along u of $\nabla_\alpha T^{\alpha\beta} = 0$ gives

$$u_\beta \nabla_\alpha T^{\alpha\beta} = \nabla_u \mathcal{E} + h \nabla_\alpha u^\alpha = 0 \,,$$

while projection orthogonal to u gives the three Euler equations

$$h\,a^\nu + \perp^{\nu\beta} \nabla_\beta P = 0 \,, \qquad (4.11)$$

where $a^\nu = \nabla_u u^\nu$ is the 4-acceleration. The fact $u_\mu \nabla_\nu u^\mu = 0$ has been used in the derivation. The Euler equation is written in such a way to recall its non-relativistic counterpart: here the enthalpy h plays the role of inertia.

4.1.4   Zero temperature limit and Kelvin's theorem

It is interesting to study the zero temperature limit of the Euler equation. For $T = 0$ we have $d\mathcal{E} = \mu\,dn$ and $\mu = \tilde{h}$ which imply[7]

$$n^{-1}\,dP = d\tilde{h} \qquad \Rightarrow \qquad n^{-1}\,\nabla_\nu P = \nabla_\nu \tilde{h} \,.$$

By using this result, the zero temperature relation $h = n\mu$ and the fact that $\nabla_\nu\,\nu = -u^\beta \nabla_\nu(\mu\,u_\beta)$, it is simple to rewrite the Euler equation (4.11) as

$$\mu\,a_\nu + \perp^\beta_\nu \nabla_\beta \mu = 0 \qquad \Rightarrow \qquad u^\beta \nabla_\beta (\mu\,u_\alpha) - u^\beta \nabla_\alpha (\mu\,u_\beta) = 0$$

that has clear interpretation in terms of differential forms (Friedman and Stergioulas, 2013): we define the 1-form $p_\nu dx^\mu$ and its exterior derivative, the 2-form dp, in components:

$$p_\nu = \tilde{h}\,g_{\nu\rho}\,u^\rho \qquad\qquad (dp)_{\alpha\beta} = \partial_\alpha p_\beta - \partial_\beta p_\alpha \,. \qquad (4.12)$$

---

[7] By using the language of differential forms, n, P, $\mu = \tilde{h}$ are 0-forms. Therefore $dP = \nabla_\alpha P\,dx^\alpha$ and $d\mu = \nabla_\alpha \mu\,dx^\alpha$. The wedge product is usually understood for 0-forms but it is possible to write $dP = n \wedge d\mu$ as well as $d\mathcal{E} = \mu \wedge dn$. Here the covariant derivative ∇_ν can be replaced by the partial derivative ∂_ν since the two notions coincide for exterior calculus (and, moreover, we only have to take derivatives of scalar functions).

More formally, the form $p = \tilde{h} \wedge g(u)$ is sometimes called *momentum* per particle while $dp = d\tilde{h} \wedge g(u) + \tilde{h} \wedge dg(u)$ is known as *vorticity*[8]: as the external differentiation of a scalar provides a generalization of the notion of gradient, external differentiation of a 1-form provides the generalization of the curl. These definitions are always valid, independently from the fact that here we restricted the argument to the perfect fluid at zero temperature.

Suppose now that the field u^μ is a solution of the relativistic Euler equations, it follows that the fluid's 4-velocity is an eigenvector of the vorticity with eigenvalue zero, namely the equation of motion is

$$u^\beta \nabla_\beta \, p_\alpha \, - \, u^\beta \nabla_\alpha \, p_\beta \, = \, 0 \qquad \Rightarrow \qquad (dp)_{\mu\nu} \, u^\nu \, = \, 0 \, .$$

This is a rather strong statement: the Euler equation is equivalent to the fact that vorticity is conserved along fluid worldlines, as it can be shown by using the language of differential forms. We need to use the Cartan's formula, which states that the Lie derivative[9] $\mathcal{L}_v$ of a generic differential form σ along v can always be expressed in terms of the exterior derivative d as $\mathcal{L}_v \sigma \, = \, v \, d\sigma + d(v\sigma)$. In the case σ is a 0-form (a scalar field) we have $d(v\sigma) = 0$ and $\mathcal{L}_v \sigma \, = \, v^\mu \partial_\mu \sigma$. Consider the Lie derivative along u of p: $\mathcal{L}_u p \, = \, u \, dp + d(u \, p) \, = \, -d\mu$. In the second equality the Euler equation $u \, dp = 0$ and $up = u^2 \mu = -\mu$ have been used. Note that $\mathcal{L}_u p + d\mu = 0$ is just another way to interpret the Euler equation. Subsequent differentiation gives $d\mathcal{L}_u p = -ddh = 0$. A general and important result is that the Lie derivative and the exterior derivative commute, thus $\mathcal{L}_u dp = 0$: the vorticity dp is Lie-dragged along u. This is indeed the *Kelvin's theorem* for the perfect fluid in general relativity.

A final note: we derived the Kelvin's theorem in the zero temperature limit, while at the classical level it is only required for the fluid to be perfect (i.e. in the Euler equations there are only conservative forces) and barotropic. However a perfect fluid at $T = 0$ is indeed barotropic, therefore the important point in the relativistic case is that it is possible to define the momentum p via the thermodynamical relation $dP = nd\tilde{h}$. More general conditions under which the isobaric surfaces and the surfaces of constant $\tilde{h}$ coincide are provided by the Carter-Lichnerowicz equation of motion (Rezzolla and Zanotti, 2013; Friedman and Stergioulas, 2013). A slight generalization of the Carter-Lichnerowicz equation of motion for a multiconstituent perfect fluid and its relation with the non-relativistic Crocco equation (that is an alternative to the Newtonian Euler equation) is discussed by Gourgoulhon (2010).

Relativistic vorticity inside a rigidly rotating NS - We know that a classical and rigidly rotating body is filled with a constant vorticity field parallel to the rotation axis. We try to give a picture of the analogous case but in GR: we consider a rigidly rotating NS described by the metric (4.29), in the approximation of slow rotation: the structure is therefore given by solving the TOV equations, reviewed in App (A), from which we can calculate the specific enthalpy profile $h(r)$. The usual concept of vorticity is that of a vectorial field, but now we have to consider the 2-form dp: to draw the vorticity lines we have to restrict our attention to a 3D spacelike subspace. Vortex lines are therefore found

---

[8] This notion of vorticity must not be confused with the so-called *kinematic vorticity*, which does not contain the enthalpy contribution. It may sound strange that in relativity the vorticity contains the enthalpy, since in a non-relativistic context the vorticity is just $\nabla \times \mathbf{v}$. However in the Newtonian limit $\tilde{h} \approx mc^2$ is a constant since $\mathcal{E}$ is dominated by the rest-mass and $\mathcal{E} \gg P$.

[9] In this brief survey, did not properly introduced the three notions of derivative: exterior, covariant and the Lie derivative $\mathcal{L}_v$ with respect to a vector field v. However their definitions are standard.
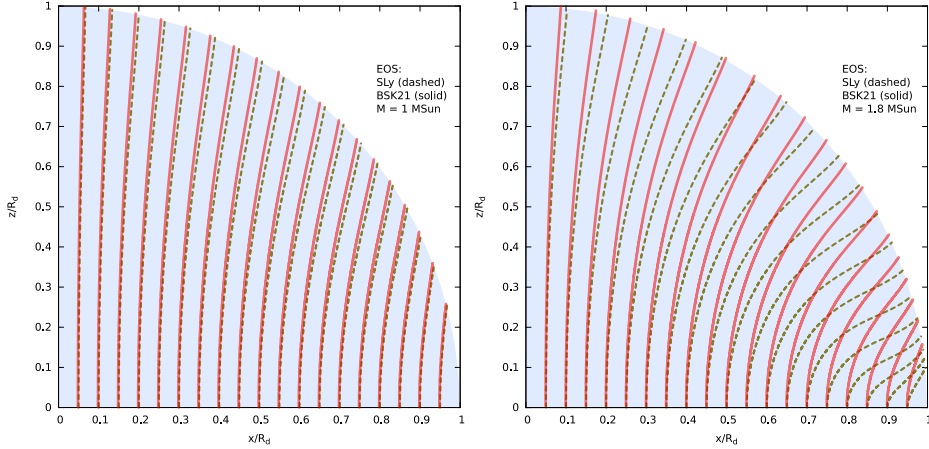
Figure 4.1: Configurations of *macroscopic* vorticity lines for a rigidly rotating star with realistic structure provided by the SLy (dashed lines) and Bsk21 (red lines, solid) EOSs. We make comparison between a $1\,M_\odot$ and a $1.8\,M_\odot$ stars: the relativistic vorticity lines are bent (even for rigidly rotating stars) due to the presence of stratification and curved spacetime, see also Eq (4.35). The vorticity lines are plotted starting from evenly spaced positions on the equatorial plane or graphical reasons: this does not reflect another property of the vorticity field: n_v is in principle not constant on the equatorial plane, even for rigidly rotating stars.

by employing the 3+1 decomposition on the vector $\omega^\mu = \frac{1}{2}\epsilon_{\mu\nu\alpha\beta}dp^{\alpha\beta}u_\nu$, where ϵ is the usual volume form (it is a tensor, not just the completely antisymmetric symbol). Quite long calculations in the Schwarzschild chart provide the explicit form of ω^μ: in Fig (4.1) we plot its field lines in the (r,θ) plane, where r is the circumferential radius.

4.1.5   Feynman-Onsager relation

The formulation of vorticity in terms of differential forms is general and valid in both flat and curved spacetime, as well as in the three-dimensional space of standard vector-analysis. According to the Landau picture of superfluidity, the superfluid flow is potential: its velocity **v** is curl-free: $\nabla \times \mathbf{v} = 0$. Onsager in 1949 and Feynman in 1955 found that this statement must be generalized: $\nabla \times \mathbf{v} = 0$, except for singular lines around which the phase of the order parameter winds by an integer multiple of 2π. The discovery of superfluid ^{3}He-A generalized further the rule: the order parameter can be more complex than the usual $U(1)$ phase. Despite also nuclear superconductivity provides a realization of an exotic superfluid with a complicated order parameter-field, the attention is most of the times restricted to the crustal superfluid, where the Cooper pairs are in the singlet state, so that they behave as a spin-0 boson. In this case the usual Feynman quantization rule, which is valid for the He-II, is assumed also for the neutron S-wave superfluid.

Topological argument - The Feynman-Onsager quantization provides a constraint on the analytical properties of p at the mesoscopic scale (i.e. this description breaks down at the scale of the coherence length): the form p is postulated to be exact, namely there is a potential $\Phi : D \to C$ such that $p = d\Phi$. This automatically implies zero vorticity, since $dp = dd\Phi = 0$. The fundamental point is the topology of the codomain C. Irrotational flow of the type $p = d\Phi$ exists for classical fluids as well and typically $C = \mathbb{R}$. However,

for a quantum fluid like He-II or the S-wave superfluid neutrons, Φ is usually interpreted as the phase of the complex order parameter: in this case $C = S^1$. This allows to define the *winding number* of a closed path $\gamma \subset D$: it is the number of turns performed in S^1 when γ is completely run once and mapped via Φ. Imagine now that γ can shrink to a single point $x_o \in D$ in which Φ is continuous; in this case the image of γ in S^1 is a small oscillation around the value $\Phi(x_0)$: no winding. To obtain a non zero winding number of γ we have to break this (purely topological) continuity argument; we thus need an unavoidable singularity of Φ: only if γ shrinks around some singular point x_0, the image $\Phi(\gamma)$ does not necessarily fall into a neighborhood of $\Phi(x_0)$, making winding possible.

Stokes' theorem - We can integrate the momentum 1-form over a spacelike curve γ. We expect, thanks to the Stokes' theorem, that the circulation of p should be zero. However D may be not be simply-connected due to the singularities of Φ: if γ cannot shrink to a non-singular point without leaving D, there is no surface $\Sigma \subset D$ such that $\partial\Sigma = \gamma$. More precisely, it is only guaranteed that there is a surface Σ such that $\gamma \in \partial\Sigma$, namely Σ has additional boundaries (due to holes) in order to avoid the singularities. For such an oriented Σ, the Stokes' theorem applies, provided the fact that the integration of p is carried out along all the boundaries that comprise $\partial\Sigma$ with the correct orientation: in this case we always obtain zero. On the other hand, if we consider only the initial closed curve γ, the result must depend on the total winding number of γ. It should be clear that this winding number counts the number of oriented holes in Σ, namely

$$\int_\gamma p = \frac{h}{n_b} \mathcal{N}_\gamma , \qquad \mathcal{N}_\gamma \in \mathbb{Z} . \tag{4.13}$$

In the above expression $\mathcal{N}_\gamma$ represents the sum of the winding numbers of γ around each topological defect present in D, n_b is the mass of the "bosonic molecule" that undergoes quantization in units of the single-particle mass m. For example, when the baryon density n_B is used, we have $n_b = 4$ in the case of He-II, $n_b = 6$, for ^{3}He and $n_b = 2$ for neutron and proton superfluids. The Feynman-Onsager quantization thus consists of two statements: that the potential of p is a phase that takes values in $[0, 2\pi]$ and that curves with winding number equal to 1 give a contribution to the total circulation of h/n_b.

In the case the gauge field A_μ is also present and the single particles have charge q (i.e. $q = -e$ for the electron fluid), the canonical momentum 1-form given in Eq (4.12) takes the form

$$p_\mu = \left(\tilde{h} u_\mu + q\, A_\mu \right) . \tag{4.14}$$

Constants make sense since qA is an energy, like $\tilde{h}$, while u is dimensionless (to obtain a genuine momenta a factor c should be introduced at the denominator of the rhs). The circulation is:

$$\int_\gamma (\tilde{h} u_\mu + q\, A_\mu)\, dx^\mu = \kappa\, m\, c \mathcal{N}_\gamma = \frac{1239\,\text{MeV fm}}{n_b} \mathcal{N}_\gamma \tag{4.15}$$

where $\kappa = h/(n_b\, m)$ is the so-called quantum of circulation (we reintroduced the c factors, so that the rhs and the lhs are both energies times a length) and the numerical value is $h\, c$. In the non-relativistic limit we do not have to care about the temporal components (γ is spacelike) and $\tilde{h} = mc^2$, $u^i = v^i/c$. The above expression gives

$$\int_\gamma (m v_i + c^{-1} q\, A_i)\, dx^i = \kappa\, m \mathcal{N}_\gamma . \tag{4.16}$$

For $q \to 0$ we see that the flux of vorticity ($\omega = dv$) is measured in units of $\kappa = h/m_b$, for $m \to 0$ we have that the flux of magnetic field ($B = dA$) is is measured in units of $\Phi_0 = hc/q_b$, where $q_b = q \, m_b/m$ is the charge of the boson molecule.

4.2   Relativistic perfect multifluids

We briefly review the two-fluid description of degenerate neutron stars, where a single normal fluid coexists with the superfluid neutrons. We will consider only the simplest case of this framework, that is, the one in which the fluids are not conducting, there are no dissipative forces between them and the temperature is zero. This limited two-species scenario is a starting point to study cold superfluid neutron stars, a scenario that has been developed in close analogy with a single-species superfluid at $T > 0$, where the normal part represents the thermal excitations.

The modern covariant formulation for many interacting fluids has been developed thanks to the variational formulation of relativistic hydrodynamics championed by Carter (1989) and collaborators, where the clear distinction between transport currents and momenta allows for a simple implementation of the entrainment effect. Application of this formalism to the hydrodynamics of neutron stars is discussed by Langlois et al. (1998). Since the historical development of the subject can be quite hard to follow, it is worth to mention the more recent reviews of Andersson and Comer (2007) and Chamel and Haensel (2008), as well as Rezzolla and Zanotti (2013). A concise review of the formalism with application to the glitch problem is also present in Sourie et al. (2016).

As in chapter (2), the two fluids are loosely denoted by "neutrons", flowing with 4-velocity u_n^μ and "protons", flowing with u_p^μ. Both 4-velocities are normalized to -1. The respective 4-currents and scalar number densities are related to the velocities in the usual way,

$$n_n^\mu = n_n u_n^\mu \qquad\qquad n_p^\mu = n_p u_p^\mu \,.$$

A fundamental quantity is the Lorentz factor relative to the frames carried by the two fluids: if we define the Lorentz factor to be

$$\Gamma = -u_n^\alpha u_{p\alpha} \,, \tag{4.17}$$

the equation (4.1) immediately gives that the relative velocity of the superfluid with respect to the normal component is

$$U_{np}^\mu = \Gamma^{-1} u_n^\mu - u_p^\mu \,.$$

Clearly this provides, via Eq (4.2), a natural definition of Δ, the speed of neutrons as seen in the frame of the protons

$$\Delta^2 = U_{np}^\mu U_{np\mu} = 1 - 1/\Gamma^2 \,, \tag{4.18}$$

We called this quantity Δ instead of the more evocative name U_{np} since this terminology is quite standard, see for example the discussion, in the Newtonian limit, given by (Prix et al., 2002) where $\Delta = |\mathbf{v}_n - \mathbf{v}_p|$. The quantity Δ is essential since it provides the correct generalization of the velocity lag between the normal component and the superfluid. It is important as well that this velocity lag is actually computed in the frame of the protons: all the microscopic physics, like the pinning of vortices, is local and is more transparent if described in the frame of the crust.

4.2.1 Master function approach

The variational approach allows to derive the hydrodynamic equations of any relativistic mixture of interacting fluids. However following the development of these ideas on the original literature can be difficult: the review of Andersson and Comer (2007) is thus an helpful reference.

The formalism relies on the Hilbert action where the Lagrangian of matter Λ is a invariant function of scalars built from the currents. For a single fluid $\Lambda(n^\mu)$, also known as *master function* (Andersson and Comer, 2007), can be constructed by using the scalar $n^\mu n_\mu$. The complete action for matter and gravity is (Misner et al., 1973) takes the form

$$\int d^4x \sqrt{-\det(g)} \left[\Lambda(n) + \frac{c^4}{16\pi G} R(g, \partial g, \partial^2 g) \right].$$

As first reviewed by Carter (1989), the ordinary non-conducting perfect fluid models can be comprehended to a large extent as resulting directly from the existence of a variational formulation pioneered by Taub, which proposed an action integral for the perfect fluid where the pressure turns out to be the on-shell value of the Lagrangian density Λ.

Variations of Λ are carried out by considering how the density changes when fluid worldlines are displaced by a generic displacement field (hence this method was dubbed "convective"). One of the simplest examples of this methodology is probably provided by Carter and Langlois (1995), where the authors derive the relativistic generalization of Landau's two constituent superfluid theory in Lagrangian terms. In this paper, the authors also clearly discuss the different variational approaches (based on different choices of the fundamental variables) that have been proposed for the relativistic fluids in terms of the Legendre transform.

Cowling approximation - In the following we will drop the gravitational part of the full action: in many astrophysical situations of interest, like stellar oscillations, the test-fluid approximation is enough to get an accurate description of the underlying dynamics. Within this approximation the self-gravity is neglected in comparison to the background gravitational field. In the case of the oscillations of relativistic stars the fluid is auto-gravitating but the spacetime can still be considered fixed, in the sense that the star is only perturbed with respect to the hydrostatic equilibrium. In stellar pulsation theory this approximation is known as Cowling approximation. We will thus neglect the effects of a dynamical spacetime: even though during glitches the pulsar rotates differentially and at different rates, we will keep the metric fixed. However we still have to understand how to construct the master function Λ.

Perfect fluid - A first insight on how should be Λ is given by considering the perfect fluid at zero temperature: in this case $d\mathcal{E} = \mu \, dn_B$, where n_B is the total baryon density and $\mu = (P + \mathcal{E})/n_B$ is the enthalpy per baryon. The general idea is to promote thermodynamically conjugate variables to dynamically conjugate ones by rewriting the first law as $-d\mathcal{E} = p_\nu \, dn^\nu$. This is easy to prove with the aid of the definition $p_\alpha = \mu u_\alpha$ and of the fact that $dn = -u_\alpha dn^\alpha$. The energy density $\mathcal{E}$ defines the Lagrangian density $\Lambda(n^\mu) = -\mathcal{E}(n)$ and p_ν can be regarded as the canonical momentum per particle.

Interacting perfect fluids - Similarly, for two interacting fluids we impose that

$$- d\mathcal{E} = p_\nu^n \, dn_n^\nu + p_\nu^p \, dn_p^\nu. \tag{4.19}$$

Once we allow for a non-zero lag Δ between the components, the system cannot be strictly described by an usual barotropic EOS $\mathcal{E}(n_p, n_n)$: with the currents n_p^μ and n_n^μ we can construct three independent scalar fields: n_p, n_n and $n_p^\mu n_{n\mu}$. In place of the last one (that is $-\Gamma$) we can choose Δ. Therefore the internal energy density takes the form $\mathcal{E}(n_p, n_n, \Delta^2)$. Since the EOS can now depend on Δ, the first law must be generalized as

$$d\mathcal{E} = \sum_x \mu_x \, dn_x + \alpha \, d\Delta^2 \, ,$$

where μ_x are the effective chemical potentials of the two-fluid and $x \in \{n, p\}$ is just a label. The presence of the scalar function α gives rise to a non-dissipative interaction between the fluids called entrainment. Since

$$\mu_x dn_x = -\mu_x u_{x\,\alpha} \, dn_x^\alpha$$

and

$$d\Delta^2 = \frac{2 \, d\Gamma}{\Gamma^3} = -\frac{2}{\Gamma^3} \, d\left(\frac{n_n^\mu n_{p\mu}}{n_n n_p}\right) = 2 \sum_{x \neq y} dn_x^\mu \left(\frac{u_{x\alpha}}{\Gamma^2 n_x} - \frac{u_{y\alpha}}{\Gamma^3 n_x}\right) \, ,$$

it is straightforward to find

$$-d\mathcal{E} = \sum_{x \neq y} dn_x^\mu \left[u_{x\mu}\left(\mu_x - \frac{2\alpha}{\Gamma^2 n_x}\right) + u_{y\mu}\left(\frac{2\alpha}{\Gamma^3 n_x}\right)\right].$$

Finally, comparison with (4.19) gives

$$p_{n\alpha}/\mu_n = (1 - \epsilon_n)u_{n\alpha} + (\epsilon_n/\Gamma)u_{p\alpha} \qquad (4.20)$$

$$p_{p\alpha}/\mu_p = (1 - \epsilon_p)u_{p\alpha} + (\epsilon_p/\Gamma)u_{n\alpha} \, . \qquad (4.21)$$

Coherently with Sourie et al. (2016) and many others, the dimensionless entrainment parameters ϵ_n and ϵ_p are defined as

$$\epsilon_x = \frac{2 \, \alpha}{\Gamma^2 \, n_x \, \mu_x} \, , \qquad (4.22)$$

which implies $y_n \mu_n \epsilon_n = y_p \mu_p \epsilon_p$. The same relation hods in the non-relativistic formulation where the chemical potentials μ_x are replaced by the mass per baryon m_x: in the Newtonian limit the relativistic chemical potential μ_x approaches $c^2 m_x$. Thanks to the above relation between the entrainment parameters, the energy-momentum tensor of the system is (Langlois et al., 1998)

$$T^{\alpha\beta} = n_n \, p_n^\beta \, u_n^\alpha + n_p \, p_p^\beta \, u_p^\alpha + \Psi \, g^{\alpha\beta} \qquad (4.23)$$

and turns out to be symmetric, as it has to be. Since complete derivation of the energy momentum cannot be recalled here, we have to make comparison with the energy-momentum tensor of the perfect fluid to understand the meaning of the scalar function Ψ: the system reduces to a single perfect fluid if the lag is zero and the two species are in chemical equilibrium. More precisely when $\Delta = 0$ the fluids can be in β-equilibrium ($\mu_x = \mu^*$ and $n_x = n_x^*$). In this case $u_x^\alpha = u^\alpha$ and $\Gamma = 1$ imply that $p_{x\alpha} = \mu^* u_\alpha$. The energy-momentum tensor becomes

$$T_{\alpha\beta}^* = n_B \, \mu^* \, u^\beta u^\alpha + \Psi^* \, g^{\alpha\beta} \quad \Rightarrow \quad T_{\alpha\beta}^* u^\alpha u^\beta = n_B \, \mu^* - \Psi^* \, . \qquad (4.24)$$

From the general property of the single fluid $T^{\alpha\beta}u_\alpha u_\beta = \mathcal{E}$, now we have

$$\mathcal{E}(n_n^*, n_p^*, \Delta = 0) = n_B\,\mu^* - \Psi^*\,,$$

the expression in Eq (4.24) is the usual energy-momentum of a single perfect fluid with pressure $P = \Psi^*$ and enthalpy density $n_B\,\mu^* = \mathcal{E}(n_p^*, n_n^*, \Delta = 0) + P$.

4.3 Axisymmetric spacetime

We reviewed the theoretical basis that are needed to construct idealized two-fluid models of superfluid (non-magnetized) neutron stars. Now we have to discuss how the geometry of spacetime can be conveniently simplified, in order to avoid complex numerical solution of the full Einstein equations: we will fix some symmetries of spacetime (generated by the Killing vectors) and extend them to be also symmetries of the matter.

In depth discussion of axisymmetric spacetime around neutron stars can be found in Friedman and Stergioulas (2013) and references therein. Here we just need a few notions: out analysis is greatly simplified by some strong initial assumptions (that are however standard in the context of isolated and rotating relativistic stars). The neutron star spacetime is asymptotically flat, stationary and axisymmetric; in particular it is a *circular* spacetime, meaning that there are no meridional macroscopic currents in the fluid. This can be formalized as:

- There exist a Killing field t^μ which is timelike at spatial infinity: it is the generator of time translations. Although in realistic stellar models, t^μ is everywhere timelike, within a horizon or in an ergosphere of an exceptionally compact rotating star, t^μ will be spacelike (the ergosphere is by definition the region in which an asymptotically timelike Killing vector becomes spacelike). This is not our case.

- There exists a Killing field φ^μ that vanishes on a timelike 2-surface (the axis of rotation), is spacelike everywhere, and whose orbits are closed curves. It is the generator of rotations around the axis.

- Asymptotic flatness means the scalar products at spatial infinity tend to $t^\mu t_\mu \to -1$, $\varphi^\mu\varphi_\mu \to \infty$ if not on the spatial infinity of the rotation axis, $\varphi^\mu t_\mu \to 0$. In particular the first condition tells us that at spatial infinity t^μ is the 4-velocity of a distant observer.

Carter showed that there is no loss of generality in considering the two Killing vectors as commuting. This condition implies that a coordinate system $\{x^\mu\}$ exists where $t^\mu\partial_\mu = \partial_t$ and $\varphi^\mu\partial_\mu = \partial_\varphi$ (now it is evident that they commute); φ and t are just names for two out of the four coordinates $\{x^\mu\}$. The nonzero components of the metric involving t and φ can be written as invariant combinations of the Killing vectors: since $t^\mu = \delta_t^\mu$ and $\varphi^\mu = \delta_\varphi^\mu$ (or, better $t_\mu = g_{\mu t}$ and $\varphi_\mu = g_{\mu\varphi}$) it follows that there are three metric functions that have an invariant meaning:

- The metric function $g_{tt} = t^\mu t_\mu$ is a interpreted as *time dilatation* with respect to the aforementioned observer at spatial infinity (more precise interpretation requires the introduction of the ZAMO observer, see the next section).

- The function $g_{\varphi\varphi} = \varphi^\mu\varphi_\mu$ is the square of the *circumferential radius*: consider one of the closed orbits of ϕ^μ, namely a spacelike curve $\mathcal{C}$ defined by a slice $t = t_0$ of

the subspace relative to the two Killing vectors. The proper circumference of $\mathcal{C}$ is $\int_{\mathcal{C}} \sqrt{-g} d\varphi = \delta\varphi \sqrt{g_{\varphi\varphi}}$, where $\delta\varphi$ depends on the parametrization used for $\mathcal{C}$, usually $\delta\varphi = 2\pi$.

- The scalar $g_{\varphi t} = \varphi^\mu t_\mu$ is conveniently rewritten as $g_{\varphi t} = -\omega g_{\varphi\varphi}$. Clearly, also $\omega = -t^\nu \varphi_\nu / \varphi_\mu \varphi^\mu$ is a scalar field and it is related to the phenomenon known as *dragging of inertial frames*. The aforementioned properties of asymptotic flatness give that $\omega \to 0$ at spatial infinity.

The geometry of the orthogonal 2-surfaces is usually described by the introduction of a conformal factor A, implying that the metric can be written as

$$g = (g_{tt} - \omega^2 g_{\varphi\varphi}) dt^2 + g_{\varphi\varphi}(d\varphi - \omega dt)^2 + A(dx_1^2 + dx_2^2),$$

where $\omega = -g_{t\varphi}/g_{\varphi\varphi}$. Here x_1 and x_2 are two orthogonal coordinates that parametrize the conformally flat subspace. Coordinates of this kind are thus called quasi-isotropic coordinates. In the exterior vacuum, it is possible to reduce the number of metric functions g_{tt}, $g_{\varphi\varphi}$, ω, A, to three, but as long as one is interested in describing the whole spacetime (including the source-region of nonzero pressure), all the metric functions are required. Sometimes spherical-like coordinates r, θ are used in place of x_1 and x_2 and in the above equation $dx_1^2 + dx_2^2$ is replaced by $dr^2 + rd\theta^2$, while $g_{\varphi\varphi}$ is parametrized as $g_{\varphi\varphi} = r\sin(\theta)B(r,\theta)$ for some function B, in order to resemble usual spherical coordinates. However (t, r, θ, ϕ), despite the name, are not the usual Schwarzschild coordinates used e.g. in the TOV equations: in the non-rotating limit these coordinates reduce to the so-called isotropic spherical coordinates.

On top of this we want a spinning fluid: the flow is circular if the 4-velocity u of the fluid is toroidal, namely $u^{[\alpha} t^\beta \varphi^{\gamma]} = 0$. This immediately implies that $u^\mu = u^t t^\mu + u^\varphi \varphi^\mu$. One of these two parameters is fixed by normalization ($u^{t\,2} g_{tt} + 2u^t u^\varphi g_{t\varphi} + u^{\varphi\,2} g_{\varphi\varphi} = -1$), the other can be fixed by introducing the angular velocity of the fluid $\Omega = u^\varphi / u^t$.

In the slow rotation formalism a different form of the metric is used, requiring $g_{\theta\theta} = g_{\phi\phi}/\sin^2(\theta)$, which corresponds to the choice of the usual Schwarzschild coordinates in the vacuum region. We use Schwarzschild-like coordinates (t, r, θ, φ) for the global chart, such that the Killing vector associated with stationarity is ∂_t and the circular Killing vector is ∂_φ. Following Hartle and Sharp (1967), the metric can be written in terms of four functions Φ, Λ, Ξ and ω as

$$g = -e^{2\Phi(r,\theta)} dt^2 + e^{2\Lambda(r,\theta)} dr^2 + r^2 e^{2\Xi(r,\theta)} d\theta^2 +$$
$$+ \sin^2\theta \, r^2 \, e^{2\Xi(r,\theta)} \left[d\varphi - \omega(r,\theta) \, dt\right]^2 . \quad (4.25)$$

The coordinates θ and φ represent, respectively, the polar and azimuthal angles with respect to the rotational axis of the star[10]. We can specify the fluid velocity: coherently with the coordinates and the metric used we have

$$u = u^t (\partial_t + \Omega \, \partial_\varphi) \qquad u^t = e^{-\Phi}/\sqrt{1 - v^2}, \quad (4.26)$$

where, for convenience, we defined $v = r\sin\theta \, e^{\Xi - \Phi}(\Omega - \omega)$. The fluid covelocity is

$$g(u) = -\frac{e^\Phi + r\sin\theta \, e^\Xi \, \omega \, v}{\sqrt{1 - v^2}} \, dt + \frac{r\sin\theta \, e^\Xi \, v}{\sqrt{1 - v^2}} \, d\varphi . \quad (4.27)$$

---

[10] It is the the set of points where $g(\partial_\varphi, \partial_\varphi) = \sin^2\theta \, r^2 \, e^{2\Xi(r,\theta)}$ vanishes, i.e. $\theta = 0$ or π.

The fluid 4-acceleration has a more complex expression and involves derivatives of the metric functions. For vanishing Ω we obtain the usual acceleration of the static fluid in the Schwarzschild geometry (Ξ can be taken equal to zero in this limit): the only non-vanishing components are[11]

$$a^r = e^{2\Lambda} \partial_r \Phi + O(\Omega^2) \qquad a^\theta = e^{-2\Xi} r^{-2} \partial_\theta \Phi + O(\Omega^2) = O(\Omega^2). \qquad (4.28)$$

As expected, the first correction to the centrifugal terms scales with Ω^2, so that at the order $O(\Omega)$ matter can be considered to be in spherical hydrostatic equilibrium.

The study of rotating neutron stars is significantly simplified within the approximation of *slow rotation*, introduced by Hartle (1967): for a star with mass M and radius R spinning with an angular velocity Ω, the slow-rotation condition can be written as $R^3\Omega^2/GM \ll 1$, which implies the slightly less stringent condition $\Omega R \ll c$ (Andersson and Comer, 2001b). For a typical (like the Vela) pulsar with standard mass $M \approx 1.4\,M_\odot$ and $R \approx 10$ km, spinning at $\Omega \approx 70$ rad/s, this approximation works well. The slow-rotation framework is less safe for millisecond pulsars, but so far only two MSPs have been seen glitching [J1824-2452A (Cognard and Backer, 2004) and J0613-0200 (McKee et al., 2016)] and none of them is in our sample of pulsars, due to the small amplitude of their glitches.

At the first order in Ω the metric in Eq (4.25) reduces to (Hartle, 1967)

$$g = \left(\omega^2 \sin^2\theta\, r^2 - e^{2\Phi}\right) dt^2 + e^{2\Lambda}\, dr^2 + r^2\, d\theta^2 +$$
$$+ \sin^2\theta\, r^2\, d\varphi^2 - \omega \sin^2\theta\, r^2 (d\varphi dt + dt d\varphi). \qquad (4.29)$$

The metric functions ω, Λ, Φ that appear here depend only on r and are not the same of Eq (4.25): they are the slow-rotation limit of the metric functions of the previous section (Ξ goes to zero, so the number of functions is reduced by one). Oblateness appears when second-order corrections in Ω are taken into account: more generally, when time is reversed the velocity of the fluid is reversed as well (i.e. $\Omega \to -\Omega$) and the metric in Eq (4.25) does not change if $\omega \to -\omega$ while Φ, Ξ and Λ are unchanged. This assures that these functions can be expanded in powers of Ω^2.

In order to implement the slow rotation approximation, we thus work at the first order in Ω_p within the two-fluid formalism. Also Ω_{np} and ω are considered small; in particular, the quasi-corotation condition $\Omega_{np} \ll \Omega_p$ can be assumed for the present case of pinning-induced lag. Relaxation of this quasi-corotation assumption is studied by Andersson and Comer (2001b).

4.3.1 Tetrads (frame fields)

Frame fields correspond to a set of ideal observers immersed in the spacetime; the integral curves of the timelike field are the worldlines of the observers.

We introduced the metric of axially symmetric spacetime, e.g. Eq (4.25), on the base of the existence of a global chart of coordinates. It is also useful to introduce the tetrad formalism: the spacetime is filled with a infinite set of observers that carry a tetrad, i.e. a set of four orthonormal vectors $e_a = e_a^\mu \partial_\mu$ for $a = 0, 1, 2, 3$ that span the local tangent space (Misner et al., 1973). If the tetrad is orthonormal, the vector e_0 is the absolute

---

[11] For a spherical metric in Schwarzschild coordinates such that $g_{rr} = e^{2\Lambda(r)}$, the metric function $m(r)$ is used in place of $\Lambda(r)$, namely $\Lambda(r) = -\frac{1}{2}\ln\left(1 - 2Gm/rc^2\right)$. The radial acceleration is $a^r = rc^2/(rc^2 - 2Gm)\,\partial_r\Phi$, coherently with the TOV equations. The TOV can be conveniently derived by considering the equilibrium from the general form of the Euler equation.

4-velocity of the observer carrying that tetrad: $g(e_0, e_0) = e_0^\mu e_{0\mu} = -1$. An orthonormal tetrad provides a "square root" of the metric tensor: since $g(e_a, e_a) = 1$ for $a = 1, 2, 3$ and $g(e_a, e_b) = 0$ for $a \neq b$, we can write $g(e_a, e_b) = \eta_{ab}$, where η is a symbol (not a tensor) that indicates the Minkowski metric. Using the fact $dx^\mu(e_a) = e_a^\mu$, it follows that the metric is decomposed into its square root

$$g_{\mu\nu}\, e_a^\mu\, e_b^\nu \;=\; \eta_{ab} \quad \Rightarrow \quad g_{\alpha\beta} \;=\; e_\alpha^a\, e_\beta^b\, \eta_{ab} \quad \text{where:}\;\; e_a^\mu\, e_\alpha^a \;=\; \delta_\alpha^\mu.$$

We introduced the new set of numbers e_α^a, defined as the matrix-inverse of e_a^α; more precisely $e^a = e_\mu^a dx^\mu$ for $a = 0, 1, 2, 3$ is a set of four differential forms uniquely defined by $e_a(e^b) = \delta_a^b$. This implies that

$$dx^\mu \;=\; e_a^\mu\, e_a \quad \Rightarrow \quad g \;=\; g_{\mu\nu}\, e_a^\mu\, e_b^\mu\, e^a\, e^b \;=\; \eta_{ab}\, e^a\, e^b.$$

Hence the set of forms $\{e^a\}$ provides a local basis of covectors such that the metric tensor is that of special relativity. The Latin indexes can be transformed according to the usual Lorentz transformations, namely $\Lambda_{ab} e^a = e'^b$.

We can now use this technology on the metric (4.25): since we are constricting a tetrad relative to a specific set of observers, instead of the generic symbol e_a we use the specific names z_a. For the specific metric considered here, it is easy to find out that $g = -z^0 z^0 + z^1 z^1 + z^2 z^2 + z^3 z^3$ and $g^{-1} = -z_0 z_0 + z_1 z_1 + z_2 z_2 + z_3 z_3$ are realized for

$$
\begin{aligned}
z^0 &= e^\Phi\, dt & z_0 &= e^{-\Phi}\, (\, \partial_t + \omega\, \partial_\varphi\,) \\
z^1 &= e^\Lambda\, dr & z_1 &= e^{-\Lambda}\, \partial_r \\
z^2 &= r\, e^\Xi\, d\theta & z_2 &= r^{-1}\, e^{-\Xi}\, \partial_\theta \\
z^3 &= \sin\theta\, r\, e^\Xi\, (d\varphi - \omega\, dt) & z_3 &= (\sin\theta\, r)^{-1}\, e^{-\Xi}\, \partial_\varphi
\end{aligned}
\tag{4.30}
$$

The overall signs have been chosen in order to satisfy the defining property $e_a(e^b) = \delta_a^b$, the fact z^0 is future-directed[12] and the right-handedness of the spatial triad. Since $\omega^2 g_{\varphi\varphi} \to 0$ and $g_{tt} \to -1$ at spatial infinity by general principles, we have that $z_0^\mu \to t^\mu$: the temporal coordinate t corresponds to the time as measured by the observer at spatial infinity. It is also possible to show that the four acceleration of this set of observers is $\nabla_{z_0} z_0$ has components only along ∂_r and ∂_θ: this kind of observer is flying around the star at fixed r and θ with zero angular momentum[13] (ZAMO or "zero angular momentum observer").

---

[12] Spacetime can be foliated by considering surfaces of constant t. The gradient of t (namely dt) identifies the direction orthogonal to these surfaces. The vector field $g^{-1}(dt)$ that is dual to dt may be used to define the 4-velocity of a set of observers, the so-called *Eulerian observers*. However it is not guaranteed that this vector field is normalized to -1. In other words we want to normalize $g^{-1}(dt)$ in order to define the field e_0 of the Eulerian observers. This can be done by introducing the *lapse function* α: from $\alpha^2 g^{-1}(dt, dt) = -1$ we can find the proper normalization. This construction immediately gives that $\alpha^2 = -1/g^{tt}$, and we only have to decide an overall sign. Consider $e_0 = -\alpha g^{-1}(dt)$ and $\alpha = 1/\sqrt{-g^{tt}} > 0$. In the specific case of Eq (4.25) we have $g^{tt} = -e^{-2\Phi}$ and $\alpha = e^\Phi$, so that it turns out $e_0 = z_0$: the ZAMOs coincide with the Eulerian observers. Finally note that $z^0 = d\tau_{\text{ZAMO}} = \alpha\, dt$, implying that the function α can be equivalently given in a form of Lorentz factor with respect to the observer at spatial infinity, $\alpha = -t_\mu e_0^\mu$.

[13] The invariance of the fluid under the symmetry group generated by a Killing vector k amounts to the vanishing of the Lie derivative $\mathcal{L}_k$ of all the tensor fields associated with matter (Gourgoulhon, 2010, 2006). In particular $\mathcal{L}_k p = 0$, where p is given in Eq (4.12). Again the Cartan formula allows to show that $p(k) = k^\mu p_\mu$ a conserved quantity along fluid lines, i.e. $\nabla_u p(k) = 0$. In our case $k = \partial_t$ gives $\nabla_u \tilde{h} u_t = 0$ (the relativistic Bernoulli theorem) while $k = \partial_t$ gives $\nabla_u \tilde{h} u_\phi = 0$ (the conservation of angular momentum per baryon). This allows to interpret u_ϕ as the angular momentum of a test particle that, depending on its motion, may be conserved or not. Consider $z_{0\mu} = g_{\mu\nu} z_0^\nu = -e^\Phi \delta_\mu^t$: the fact that $z_{0\varphi} = 0$ tells us that this fluid of non-freely-falling test particles has zero angular momentum.

It can also be interesting to construct also the set $\{c_a\}$, the tetrad field carried by the fluid (that defines the corotating observers). We already know the timelike future-oriented unit vector, i.e. $c_0 = u$: it is the 4-velocity of the fluid, given explicitly in Eq (4.26). The Lorentz factor of a fluid particle relative to the ZAMO is

$$W = -g(z_0, c_0) = (1 - v^2)^{-1/2} \,, \tag{4.31}$$

namely the ZAMOs see fluid particles flowing in their laboratories with velocity v. The corotating observer is thus obtained by boosting the ZAMO with velocity v,

$$\begin{pmatrix} W & Wv \\ Wv & W \end{pmatrix} \begin{pmatrix} z_0 \\ z_3 \end{pmatrix} = \begin{pmatrix} c_0 \\ c_3 \end{pmatrix} \,. \tag{4.32}$$

The other two elements of the corotating tetrad can be taken equal to the corresponding ones of the ZAMO.

4.4 Relativistic Feynman-Onsager relation

The canonical momentum per particle of a perfect fluid at $T = 0$ is the 1-form $p = \mu \, g(u)$ given in Eq (4.12) where $g(u)$ is the fluid covelocity. The momentum can thus be naturally integrated over 1-dimensional manifolds embedded in the spacetime: here we study the circulation of the form p.

At the mesoscopic scale the superfluid flow is irrotational, $dp = 0$, thus the superfluid can rotate only if its domain is not simply connected. The topological defects correspond to world sheets into the domain whose intersection with the three-space defines a vortex line (Prix, 2000). Integration of p, given by Eq (4.12) along a closed path $\mathcal{C}$ inside the superfluid domain is assumed to obey Eq (4.13), in this case:

$$\int_{\mathcal{C}} g(u) = \frac{h \mathcal{N}}{2} \,, \tag{4.33}$$

where the factor of 2 accounts for Cooper pairing, and h is the Planck constant. This formula can be easily made more explicit within the assumption of circular spacetime. A natural choice is to consider $\mathcal{C}$ to be an orbit of ∂_φ, defined by $t = t_0, r = r_0, \theta = \theta_0$. Given the metric in Eq (4.25), the azimuthal component of the canonical momentum p_φ is the angular momentum per baryon [see Eq (4.27)]

$$p_\varphi = \mu \, W \, e^\Xi r \sin\theta \, v = \mu \, W \, e^{-\Phi} (e^\Xi r \sin\theta)^2 \bar{\Omega} \,,$$

The angular velocity does not need to be a constant, but can be a generic function $\Omega(r, \theta)$, at least as long as we consider $\mathcal{N}$ just a macroscopic function (otherwise pathological choices of $\Omega(r, \theta)$ could not guarantee the possibility to relate $\mathcal{N}$ to a reasonable vortex configuration).

The momentum restricted on the curve $\mathcal{C}$ is $p|_{\mathcal{C}} = p_\varphi(r_0, \theta_0) d\varphi$, so that the integral in Eq (4.33) is trivial and gives

$$p_\varphi(r_0, \theta_0)/m_n = \frac{\kappa \mathcal{N}(r_0, \theta_0)}{2\pi} \,.$$

The bare neutron mass m_n has been introduced in order to obtain the quantum of circulation $\kappa = h/(2m_n)$. The Feynman-Onsager relation is finally given by

$$\frac{\bar{\Omega}}{\sqrt{1 - v^2}} = \frac{\kappa \, e^\Phi \, \mathcal{N}(r, \theta)}{2\pi \, (e^\Xi r \sin\theta)^2 (\mu/m_n)} \,. \tag{4.34}$$

This relation simplifies within the slow-rotation approximation: we just have to keep at most the linear terms in Ω in order to find

$$\Omega - \omega(r) \;=\; \frac{\kappa \, e^{\Phi(r)} \, \mathcal{N}(r,\theta)}{2\pi \, (r \sin\theta)^2 (\mu(r)/m_n)} \;+\; O(\Omega^2) \,, \tag{4.35}$$

where Ω is the angular velocity measured by a distant ZAMO. Note that the Feynman-Onsager relation depends explicitly on general relativistic frame-dragging.

In the Newtonian limit the specific enthalpy is a constant and the usual non-relativistic Feynman-Onsager relation is recovered

$$\Omega(r,\theta) \;=\; \frac{\kappa \, \mathcal{N}(r,\theta)}{2\pi \, (r \sin\theta)^2} \,.$$

In this limit, when vortices are parallel to the z-axis, $\mathcal{N}$ is a function of only $r \sin\theta$ and the angular velocity Ω is columnar. This ceases to be true even at the level of the slow-rotation approximation due to the presence of the metric functions (ω and Φ) and of the stratified enthalpy μ. In the above relations, it is also possible to use the fact that the quantity $\bar{\mu} = \mu(r)e^{\Phi(r)}/m_n$ is constant throughout the star[14], so that it can be thought as a factor that rescales κ.

For our two components system, Eq (4.33) is still valid once the four-momentum per baryon p is replaced with p_n. This implies that the Feynman-Onsager relation for the two-fluid system with entrainment is obtained by replacing Ω with Ω_v in Eq (4.34). For the slow-rotation limit we can use Eq (4.35) and obtain

$$\Omega_{vp}(r,\theta) \;=\; -\bar{\Omega}_p(r) + \frac{\kappa \, e^{2\Phi(r)} \mathcal{N}(r,\theta)}{2\pi \, \bar{\mu}_n \, (r \sin\theta)^2} + O(\Omega_p^2) \,, \tag{4.36}$$

where $\bar{\mu}_n = \mu_n(r)e^{\Phi(r)}/m_n$ and $\bar{\Omega}_p(r) = \Omega_p - \omega(r)$. It is straightforward to rewrite this equation in terms of Ω_{np} via Eq (4.50) and thus see that entrainment modifies the expression for the physical velocity lag $\Omega_{np}(r,\theta)$ in a trivial way.

4.5   Maximum glitch amplitudes: slow-rotation framework

We now generalize the result given in Eq (3.14) by constructing a model of angular momentum reservoir in general relativity. The model is static: there is no need to discuss the dynamical equations of the problem that regulate how angular momentum is transferred between the two fluids. Because of this we can only discuss the mass upper bounds.

The stellar structure and composition, as well as the spacetime metric, are treated as fixed. These are not severe limitations, since our aim is just to provide an upper limit on the glitch amplitudes. However, much of the formalism and some intermediate results reported in this section can be used as a basis for constructing dynamical models of superfluid glitching pulsars (i.e. a slow-rotation relativistic version of the equations for pulsar rotation proposed in the previous chapters). An example of dynamical model for pulsar glitches with two rigid components (but in full general relativity) is discussed in Sourie et al. (2016), where the authors study the effect of GR on the characteristic rise time of large glitches.

---

[14] This can be seen as a consequence of the vorticity equation for the perfect fluid or via the standard argument given by Glendenning (2000).

4.5.1 The two-fluid model within the slow-rotation approximation

The results presented in the previous sections are valid for both rigid-body rotation as well as for differential rotation [15]. In the following, even if we have two distinct components, we shall compute the moments of inertia assuming that the superfluid is corotating with the rest of star: therefore we will take the case of a cold and uniformly rotating star as a reference case and mention additional assumptions where necessary. In this reference case the velocity u, given in Eq (4.26), is interpreted as the angular velocity of the two components, flowing with velocities u_p and u_n, at corotation. In this case the matter can be modeled as a perfect fluid: observations of pulsar glitches are consistent with departures from a perfect fluid equilibrium (due to the presence of a solid crust) of order 10^{-5} (Friedman, 1992). We are thus forced to consider small departures from equilibrium.

Given the metric in Eq (4.25), the 3-velocities v_n and v_p of the fluids measured by the local ZAMO are given by Eq (4.26), namely

$$v_x = r \sin\theta \, e^{\Xi - \Phi}(\Omega_x - \omega) \tag{4.37}$$

where $x \in \{n, p\}$ is a component label. We impose rigid-body rotation of the p-component and a quasi-corotation motion of the n-component, namely $\Omega_n(r, \theta) = \Omega_p + \Omega_{np}(r, \theta)$ and $|r\,\Omega_{np}(r, \theta)| \ll r\,\Omega_p \ll c$ for $r < R_d$ and $\theta \in [0, \pi]$. The corresponding 4-velocities in the global chart are

$$u_x = W_x \, e^{-\Phi} \left(\partial_t + \Omega_x \partial_\varphi\right) \tag{4.38}$$

where we defined, in analogy with Eq (4.31), the Lorentz factors

$$W_x = \left(1 - v_x^2\right)^{-1/2}. \tag{4.39}$$

The Komar mass[16] can be used to compute the total angular momentum as (Friedman and Stergioulas, 2013)

$$L = -\int \left(T_{\alpha\beta} - \frac{1}{2} T_\nu^\nu g_{\alpha\beta}\right) (\partial_\varphi)^\alpha z_0^\beta \, dV. \tag{4.40}$$

---

[15] In general relativity a motion is said to be rigid if the shear tensor

$$\sigma_{\mu\nu} = \nabla_{[\alpha} u_{\beta]} \perp_\mu^\alpha \perp_\nu^\beta - \nabla_\rho u^\rho \perp_{\mu\nu}/3$$

vanishes. In our case $\sigma_{\alpha\beta}$ vanishes if Ω is constant. See Rezzolla and Zanotti (2013) for construction of the shear tensor and Gourgoulhon (2006) for interpretation of the notion of rigidity via Killing vectors.

[16] Firstly, the existence of the Killing field t^μ allows to define the corresponding Eulerian observers. Secondly, t^μ allows also to foliate spacetime (pick up a chart y^μ) with surfaces of constant $f(y^\mu)$, where the scalar $f(y^\mu)$ is a solution of $\mathcal{L}_t f = t^\mu \nabla_\mu f = 1$, i.e. f is Lie-dragged along the orbits of t^μ at the constant rate 1. The 3-surface $f(y^\mu) = t_0$ identifies the subspace of all points labeled by the numerical constant t_0. At this level the coordinates are completely generic but we can perform a change of coordinates $\{y^0, y^i\} \to \{f, x^i\}$; f is usually called t, i.e. t is a function that satisfies $t^\mu \nabla_\nu t = 1$. This is trivially satisfied if the Killing field can be identified with ∂_t. The covelocity $g(e_0)$ of the Eulerian observers is proportional to the normal dt and their 4-acceleration $a = \nabla_{e_0} e_0$ is tangent to the 3-surfaces of constant t_0, namely $dt(a) = 0$.

Given this construction, the general form od the Komar mass M_k relative to a generic Killing vector k can be written as (Gourgoulhon, 2010)

$$M_k = A \int_{t_0} (2T_{\alpha\beta} e_0^\alpha k^\beta - T_\sigma^\sigma e_0^\mu k_\mu) \det(g|_{t_0})^{1/2} \, dx^1 dx^2 dx^3,$$

where $A = 1$ if k is the Killing vector associated to e_0 and $A = -1/2$ if k is a spacelike Killing vector. In our case $e_0 = z_0$, the ZAMO velocity, $k = \partial_\varphi$, $A = -1/2$, $\det(g|_{t_0})^{1/2} = \sin\theta \, r^2 \, e^\Lambda e^{2\Xi}$ and $dx^1 dx^2 dx^3 = dr d\theta d\varphi$.

We want to study L in the case where $T^{\mu\nu}$ is the energy-momentum tensor of the system of Eq (4.23) and

$$dV = e^{\Lambda+2\Xi} \, d^3x$$

is the volume form of the three-surface of constant time given by considering the square root of the determinant $-\det(g|_t = \text{const})$ [just drop the terms containing dt in Eq (4.25)]. By using the energy-momentum defined in Eq (4.23) and remembering that $W_x = -g(u_x, z_0)$ and $g(\partial_\varphi, z_0) = 0$, it is easy to find the expression

$$L = -\int T_{\varphi\beta} \, z_0^\beta \, e^{\Lambda+2\Xi} \, d^3x$$

$$= \int (W_n \, p_{n\varphi} \, n_n + W_p \, p_{p\varphi} \, n_p) \, e^{\Lambda+2\Xi} \, d^3x \,,$$

where $p_{x\varphi}$ are the azimuthal component of the momenta defined in Eqs (4.20) and (4.21): there is a clear analogy with the non-relativistic relations of Eqs (3.3), (3.4) and (3.5). In particular, we would like to split the azimuthal component of the total canonical momentum density[17]

$$\pi_\varphi \,=\, W_n p_{n\varphi} n_n + W_p p_{p\varphi} n_p$$

as done in Eq (3.4), in order to single out the superfluid reservoir contribution hidden in L. Due to the Lorentz factors W_x and Γ, the relation between the momenta and the velocities in the above equation is non-linear, and it is not possible to separate π_φ into terms that depend only on Ω_p and Ω_{np} respectively.

To overcome this complication we now start to use the slow-rotation approximation: only terms that are at most linear in Ω_p are considered and the metric is the one in Eq (4.29). The various quantities of interest are, at the lowest order in Ω_p

$$W_x = 1 + O(\Omega_p^2) \tag{4.41}$$

$$u_x^\varphi = e^{-\Phi}\Omega_x + O(\Omega_p^3) \tag{4.42}$$

$$u_{x\varphi} = e^{-\Phi}x^2(\Omega_x - \omega) + O(\Omega_p^3) \tag{4.43}$$

$$\epsilon_x = \frac{2\,\alpha}{n_x\,\mu_x} + O(\Omega_{np}^2)\,, \tag{4.44}$$

$$\Gamma \,=\, W_n\,W_p\,(1 - v_n v_p) \,=\, 1 + O(\Omega_{np}^2) \tag{4.45}$$

$$\Delta = \frac{v_n - v_p}{1 - v_n v_p} = x\,e^{-\Phi}\Omega_{np} + O(\Omega_p^2) \tag{4.46}$$

where the Lorentz factor Γ, the lag Δ and the entrainment parameters ϵ_x are defined in Eqs (4.17), (4.18) and (4.22) respectively. The above approximations, when used in Eqs (4.20) and (4.21), give the expressions

$$p_{n\varphi} = \mu_n \, x^2 \, e^{-\Phi}(\bar{\Omega}_p + (1 - \epsilon_n)\Omega_{np})\,, \tag{4.47}$$

$$p_{p\varphi} = \mu_p \, x^2 \, e^{-\Phi}(\bar{\Omega}_p + \epsilon_p\Omega_{np})\,, \tag{4.48}$$

where $\bar{\Omega}_p \,=\, \Omega_p - \omega$ can be considered the angular velocity of the protons as seen by the ZAMO. Leaving aside the fact that now the canonical momentum $p_{x\varphi}$ is an

---

[17] Note that, differently from the Newtonian case of Eq (3.3), the total canonical momentum density in GR turns out to be entrainment dependent. Explicit dependence on entrainment, however, appears only at order $O(\Omega_p\Omega_{np}^2)$.

angular momentum instead of a linear momentum, the above equations are the relativistic generalization of Eqs (3.1) and (3.2): the mass per baryon m_n is replaced by the enthalpy per baryon μ_x, while the only effect of curved spacetime is the presence of the factor $\sqrt{-g^{tt}} = e^{-\Phi}$. Therefore, the total angular momentum in the slow-rotation approximation is

$$L = \int d^3x\, e^{\Lambda-\Phi}\, x^2 \left[(\mu_n\, n_n + \mu_p\, n_p)\bar{\Omega}_p + \mu_n\, n_n\, \Omega_{np})\right]. \tag{4.49}$$

This formula was derived by taking only the linear terms of an expansion in Ω_p and by assuming that Ω_n is of the same order of Ω_p: for its validity, there is no need to invoke the smallness of the lag expressed by the additional quasi-corotation condition (that is however important in order to justify our use of a barotropic equation).

Finally, we can introduce the auxiliary angular velocity $\Omega_v = \Omega_p + \Omega_{vp}$ (this exact equality is indeed a definition for Ω_{vp}) by imposing that

$$g_{\alpha\sigma} u_v^\sigma = p_{n\alpha}/\mu_n,$$

where u_v is the 4-velocity associated with the fictitious v-component. More precisely, u_v is defined in terms of Ω_v in the same way as done for u_n and u_p, see Eqs (4.37) and (4.38). In general, the relation between Ω_{vp}, Ω_p and Ω_{np} imposed above is complicated by the presence of the Lorentz factors W_v in u_v and Γ in p_n. However, in the slow rotation case, expansion of Eq (4.20) and of $g(u_v)$ in powers of $\bar{\Omega}_p$ reads

$$\Omega_{vp} = (1 - \epsilon_n)\Omega_{np} + O(\Omega_p^2). \tag{4.50}$$

Within the slow-rotation approximation the definition of Ω_v is the same as that given by Eq (2.10) in the Newtonian framework.

4.5.2 Relativistic corrections to the moments of inertia

By considering successive corrections in Ω, Hartle (1967) derived a methodology to calculate the metric in Eq (4.29) for a rigidly rotating star. Once the metric functions are known, the moment of inertia for a slowly and rigidly rotating star is given by

$$I = \frac{8\pi}{3c^2} \int_0^R dr\; r^4 e^{\Lambda(r)-\Phi(r)}\, h(r)\, \frac{\bar{\Omega}(r)}{\Omega}\,. \tag{4.51}$$

Here $h(r) = \mathcal{E}(r) + P(r)$ is the enthalpy density profile inside the star, $\bar{\Omega}(r) = \Omega - \omega(r)$ encodes the rotational frame-dragging and the ratio $\bar{\Omega}/\Omega$ does not depend on the angular velocity Ω and is smaller than one.

In the slow-rotation approximation at the lowest order, the background neutron star structure is a solution of the TOV equations. Given an EOS and a central density (i.e. the stellar mass), the density $h(r)$ and the metric functions $\Phi(r)$ and $\Lambda(r)$ can obtained through the standard TOV equations, while $\bar{\Omega}(r)$ follows from the integration of an additional equation. We do not review the method here, since it can be found in many previous articles or books, see e.g. Glendenning (2000) and references therein. Following this prescription, one can thus find the radial profiles, in particular $\mathcal{E}(r) = \rho(r)c^2$, $P(r)$, $n_B(r)$, $y_n(r)$; also the profiles $f_p(r)$ and $\epsilon_n(r)$ follows by obvious reparametrization from anu given microscopic expression for $f_p(n_B)$ and $\epsilon_n(n_B)$.

Although previous studies have already introduced partial moments of inertia within the slow-rotation [as done e.g. by Newton et al. (2015)], we further discuss this issue in

the present context [a complementary approach and discussion can also be found in Sourie et al. (2016)]. In order to clarify the assumptions needed to proceed, we have to come back to the total angular momentum of Eq (4.49):

- The thermodynamic Euler relation for a two-fluid system tells us that (Langlois et al., 1998)

$$\mathcal{E} = \mu_n n_n + \mu_p n_p - \Psi \,. \tag{4.52}$$

  but we need the enthalpy density of a single (possibly barotropic) fluid h, that is the quantity plays the role of inertia in Eq (4.51). We thus impose $\Psi = P$, even if a velocity lag Δ is present [see also the discussion around Eq (4.24)].

- We next remark that, by looking at Eq (4.49), one needs to know how to calculate $n_n \mu_n$ and $n_p \mu_p$. We thus impose chemical equilibrium ($\mu_p = \mu_n = \mu^*$), so that the above Euler relation reduces to the enthalpy density of a simple barotropic fluid $\mathcal{E} + P = \mu^* n_B$, where μ^* plays the role of a mean effective inertial mass per baryon (Friedman and Stergioulas, 2013). In the limit of no differential rotation ($\Psi = P$) and of chemical equilibrium, we have $n_n \mu_n = y_n n_B \mu^* = y_n h$ where $y_n = n_n/n_B$ is the superfluid fraction.

Under these two additional assumptions, the total angular momentum in Eq (4.49) can be written as

$$L = I\,\Omega_p + \Delta L[\Omega_{np}] \,, \tag{4.53}$$

where I is given in Eq (4.51) and

$$\Delta L[\Omega_{np}] = \int d^3x \; e^{\Lambda - \Phi} \, y_n \, h \, x^2 \, \Omega_{np} \,. \tag{4.54}$$

We remark that in the decomposition performed in Eq (4.53) of the total angular momentum in a global component plus the contribution of the neutron reservoir represented by the lag, only the global part contains the effect of frame-dragging: the reservoir $\Delta L[\Omega_{np}]$ has no factor $\bar{\Omega}(r)/\Omega$ (cf. also Eqs (4.47) and (4.48)).

Again, we can introduce the partial moment of inertia I_n as the normalization factor of the distribution defined by ΔL; momentarily reintroducing the c factors, it turns out to be

$$I_n = \frac{8\pi}{3c^2} \int_0^{R_d} dr \; r^4 e^{-\Phi + \Lambda} \, y_n \left(\mathcal{E} + P\right) \,. \tag{4.55}$$

This allows to define the average lag $\langle \Omega_{np} \rangle$ (weighted with I_n) and thence write the angular momentum of the reservoir as

$$\Delta L[\Omega_{np}] = I_n \langle \Omega_{np} \rangle \,. \tag{4.56}$$

We point out that, although we used the same symbol, the quantity I_n does *not* represent the moment of inertia I_n^{tot} of the entire n-component (that is not even a clearly defined quantity in our simple approach) but only that of the reservoir associated with a given lag, in the sense of Eq (4.56).

Obviously, this argument introduces the more subtle problem of justifying chemical equilibrium. Andersson and Comer (2001b) showed that chemical equilibrium between the two components in a neutron star implies corotation of them, and it is thus only approximatively realized in our context where the fluids must rotate differentially in order

to produce a glitch. On the other hand, Sourie et al. (2016) have shown the inverse reasoning: starting from the hypothesis of corotation and assuming chemical equilibrium at the center of the star, it is possible to infer chemical equilibrium throughout the entire star. The additional condition of quasi-corotation is then necessary to ensure very small departures from chemical equilibrium and from rigid rotation, and thus guarantee the consistency of Eq (4.55) with the rigid-body Hartle's formalism.

Finally, from Eq (4.54) we can derive the moment of inertia of the auxiliary v-component, although it will turn out to be less useful if dynamical equations are not discussed. This is trivial in the slow rotation limit because of Eq (4.50): the moment of inertia associated with the v-component is analogous to Eq (2.3)

$$
I_v \; = \; \frac{8\pi}{3c^2} \int_0^{R_d} dr \; r^4 e^{-\Phi+\Lambda} \; \frac{y_n \left(\mathcal{E} + P\right)}{1 - \epsilon_n} \, .
\tag{4.57}
$$

A similar (but not equivalent) definition, is also present in the derivation carried out in Newton et al. (2015): in order to account for entrainment in the crust, the authors simply divide the integrand in Eq (4.51) (limited to the neutron component) by the dimensionless effective neutron mass $m_n^*(r)/m_n = 1 - \epsilon_n(r)$.

4.5.3 Relativistic corrections to the maximum glitch amplitudes

We derived the relativistic generalization of Eq (3.5); the formula for the maximum glitch amplitude is still given by Eqs (3.9) and (3.7), but now one needs to consider the relativistic definitions of I and ΔL, as given respectively in Eqs (4.51) and (4.54).

Note that for this calculation it is *not* necessary to introduce explicitly the partial moments of inertia.

Before moving to the numerical estimates of the maximum glitch amplitudes, we still need to discuss the critical unpinning lag in a relativistic framework. We try to study the robustness of the model against entrainment and against the unknown details of the vortex line configuration by analyzing the two scenarios of rigid and slack vortex lines. In both cases, we need the Magnus force per unit length of vortex; since our model is highly symmetric, we just have to consider its modulus, given by (Langlois et al., 1998)

$$
f_M = \kappa \, m_n n_n v_{Ln} \, ,
\tag{4.58}
$$

where v_{Ln} is the speed of a segment of vortex line as seen in the local frame comoving with the superfluid flow. When lines are pinned, they are forced to move with the normal component and $v_{Ln} = \Delta$. By using Eq (4.46), the local Magnus force is

$$
f_M = \kappa \, m_n \, y_n \, n_B \, e^{-\Phi} \, x \, \Omega_{np} \, ,
\tag{4.59}
$$

the slow-rotation analogue of Eq (4.58).

Rigid vortex lines - We try to adapt the Newtonian phenomenological treatment of macroscopically rigid vortices to the relativistic context: not surprisingly, extending to GR the global unpinning condition is tricky. Again, we assume a configuration of paraxial vortex lines: in the plane defined by $t = \text{const.}$ and $\varphi = \text{const.}$, the vortices are parametrized

by $\gamma_{x_0}(z) = (x_0, z)$, and the line element along the curve is[18]

$$dl = \sqrt{g_{\alpha\beta} \frac{d\gamma_x^\alpha}{dz} \frac{d\gamma_x^\beta}{dz}} dz = \sqrt{g_{zz}} dz = \sqrt{\frac{z^2}{r^2} e^{2\Lambda} + \frac{x^2}{r^2}} dz \,.$$

While in the Newtonian framework this corresponds to columnar bulk rotation (of the v-component), such a configuration is no more consistent with columnar motion when a strong gravitational field is present, as discussed in Appendix B: due to stratification and spacetime curvature, the lag Ω_{vp} is in general a function of both the x and z coordinates, as shown in Eq (4.36). Conversely, an actual columnar bulk rotation must correspond to a configuration of bent vortices. On the other hand the actual configuration of vortices in a steadily spinning-down neutron star is unknown (provided that such a stable configuration exists).

To proceed, we somewhat ignore the result in Appendix B and we arbitrarily generalize the critical lag of Eq (3.13) in order to obtain a critical lag that is only dependent on x:

$$\Omega_{vp}^{cr}(x) = \frac{\int_{\gamma_x} dl \, f_P}{\kappa \, x \int_{\gamma_x} dl \, \frac{m_n n_n}{1 - \epsilon_n} e^{-\Phi}} \,. \tag{4.60}$$

Numerically, this critical lag does not differ significantly from those presented in Paper-I, with a marked peak in the cylindrical region immersed in the inner crust. As already stressed, the curves γ_x in the above expression do not follow the actual vortex lines configuration consistent with such a columnar lag; this could be in principle implemented, even though this is likely to make no difference at the numerical level: we just want to test the robustness of $\Delta\Omega_{\text{abs}}$ against different unpinning prescriptions and its dependence on entrainment, if any. The corresponding maximum glitch amplitude turns out to be

$$\Delta\Omega_{\text{abs}} = \frac{4\pi}{I\kappa} \int_0^{R_d} dx \, x^2 \int_0^{z(x)} dz \, \frac{y_n h}{1 - \epsilon_n} \, e^{\Lambda - \Phi}.$$
$$\cdot \left(\int_{\gamma_x} dl \, f_P \right) \left(\int_{\gamma_x} dl \, \frac{m_n n_n c^2}{1 - \epsilon_n} e^{-\Phi} \right)^{-1} \tag{4.61}$$

and is entrainment dependent. We stress that this is not a drawback of our arbitrary choice of straight curves γ_x: the dependence on entrainment cannot be canceled out: in the relativistic framework, the integrals containing the rest-mass and the enthalpy do not simplify, as they do in the Newtonian framework where $h \approx n_B m_n$. Therefore any non-local unpinning prescription will give rise to an explicit dependence on entrainment parameters. It may be interesting, but not straightforward, to study the configuration of rigid vortices γ_x consistent with a columnar $\Omega_{vp}^{cr}(x)$, by using the Feynman-Onsager relation in axisymmetric spacetime.

Slack vortices -   The case of slack vortex lines is even simpler: we do not need to consider the stable (if exists) configuration of vortex lines. By taking Eq (4.59) and

---

[18] In cylindrical coordinates the slow-rotation metric has components

$$g_{xx} = \frac{x^2}{r^2} e^{2\Lambda} + \frac{z^2}{r^2}, \qquad g_{zz} = \frac{z^2}{r^2} e^{2\Lambda} + \frac{x^2}{r^2} \qquad g_{xz} = \frac{zx}{r^2}(e^{2\Lambda} - 1)$$

.

Table 4.1: Some properties of the three EOSs used: $M_{\max}$ is the maximum non-rotating gravitational mass, while n_{edge} is the baryon density at the crust-core interface [see Fantina et al. (2013) for a study of the global properties of non-rotating neutron stars constructed with the same EOSs used here]. For comparison we also list the baryon density at which the pinning force used in this work goes to zero.

EoS	n_{edge} [fm^{-3}]	$M_{\max}$	Ref.
SLy4	0.076÷0.077	2.05 $M_{\odot}$	(Douchin and Haensel, 2001)
BSk20	0.0854	2.16 $M_{\odot}$	(Goriely et al., 2010)
BSk21	0.0809	2.28 $M_{\odot}$	(Goriely et al., 2010)
f_P	0.0776		Seveso et al. (2016)

imposing the unpinning local condition, we find

$$\Omega_{np}^{cr}(r,\theta) \;=\; \frac{f_P(r)\,e^{\Phi(r)}}{\kappa\,r\sin\theta\,m_n n_n(r)}\,.$$

Then, Eqs (3.9) and (4.54) give

$$\Delta\Omega_{\rm abs} \;=\; \frac{\pi^2}{I\kappa}\int_0^{R_d}dr\,r^3\,e^{\Lambda(r)}\,\frac{\mathcal{E}(r)+P(r)}{m_n\,n_B(r)\,c^2}\,f_P(r)\,, \tag{4.62}$$

in complete analogy with the Newtonian maximum glitch amplitude reported in Eq (3.14). In the non-relativistic limit, $P \ll \mathcal{E}$ and $\rho \approx m_n n_B$ imply that the fraction in the integral is ~ 1. With the local unpinning prescription and no factor Γ due to slow rotation, the effects of entrainment on the maximum glitch cancel out in GR as well. The critical lag is associated with a relative velocity $\Delta^{\rm cr} = xe^{-\Phi}\Omega_{np}^{cr}$, describing a laminar flow on concentric spherical shells. In particular, by considering that the pinning forces estimated by Seveso et al. (2016) display peaks of the order 10^{15} dyne/cm around $m_n n_B \approx 3 \times 10^{13}$ g/cm^3, we have

$$\Delta^{\rm cr} \;=\; \frac{f_P}{\kappa\,m_n\,y_n\,n_B} \;\lesssim\; 10^{-5}\,c\,.$$

For comparison, the slowest pulsar considered here is J0631+1036, whose angular velocity of 21.8 rad/s corresponds to an equatorial velocity of order $\approx 10^{-3}c$. Thus, the approximations of slow rotation and quasi-corotation are consistent with the pinning paradigm.

4.6 Numerical results

We now present the numerical estimates of the partial moments of inertia and the maximum amplitudes; then we estimate M_{abs}, the absolute upper bounds on pulsar masses.

The input used in the calculations is summarized in Table (4.1); we adopted three unified barotropic EOSs (SLy4, BSk20 and BSk21), for which the superfluid fraction $y_n(n_B)$ is provided together with $P(n_B)$ and $\mathcal{E}(n_B)$, consistently for all regions of the neutron star (SLy is not "unified" in the outer crust but this region is unimportant in the present work).
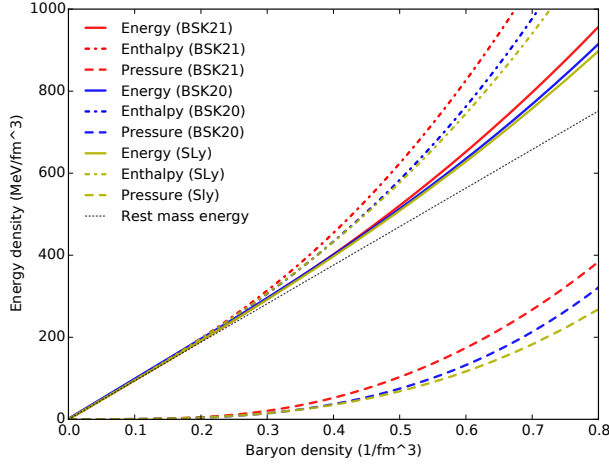
Figure 4.2: The three barotropic EOSs used: pressure P (dashed), total internal energy $\mathcal{E}$ (solid), and enthalpy $h = \mathcal{E} + P$ (dotted) densities versus the total baryon mass n_B. Some details about each EOS are reported in Table (4.1). The thin dotted black line is the rest-mass density $c^2 m_n n_B$. Some conversion factors can be useful: $10^{15} \mathrm{g/cm^3} = 0.6\,\mathrm{fm^{-3}} = 8 \times 10^{35}\,\mathrm{erg/fm^3} = 560\,\mathrm{MeV/fm^3}$. While the crust-core interface occurs for densities $\lesssim 0.1\,\mathrm{fm^{-3}}$, the central baryon density n_B^{abs} is corresponding to the maximum mass is out of scale, e.g. for the SLy we have $n_B^{\mathrm{abs}} \approx 1.2\,\mathrm{fm^{-3}}$ and $\mathcal{E}^{\mathrm{abs}}/c^2 \approx 2.9 \times 10^{15}\,\mathrm{g/cm^3}$, which implies $\mathcal{E}^{\mathrm{abs}}/(m_n c^2 n_B^{\mathrm{abs}}) \approx 1.4$; for this maximal static mass configuration the contribution of the central pressure to the central enthalpy is nearly the $\sim 50\%$.

4.6.1   Relativistic moments of inertia

It is known that the moment of inertia given in Eq (4.51) can have a marked discrepancy with respect to its non-relativistic counterpart. Although only the total moment of inertia appears in the calculation of the maximum glitch, it is interesting to discuss the relativistic corrections also to the partial ones, since they frequently appear in studies of pulsar glitches [see e.g. Delsate et al. (2016)].

A word of caution regarding the Newtonian framework is necessary: since the background configuration is actually fixed by the integration of the TOV equations, it is not clear what should be interpreted as "inertia" of the system in this spurious scenario. In a strict Newtonian definition, the inertia corresponds to rest-mass (the rest-mass density $\rho = m_n n_B$); of course this is at odds with the relativistic definition of "mass density" $\rho = \mathcal{E}/c^2$ widely used in the context of the TOV equations. The mass density ρ is indeed the energy density provided by the EOS and contains the contribution of the hadronic nucleon-nucleon interaction. Numerically, however, $m_n n_B c^2$ and ρ start to differ by more than 10%, only for densities above $10^{15} \mathrm{g/cm^3}$, as can be seen in Fig (4.2).

Indeed, some studies existing in the literature take the more consistent choice of always adopting the relativistic definition $\rho = \mathcal{E}/c^2$ of density and use it in different prescriptions, like the one discussed by Ravenhall and Pethick (1994). This was the approach of our Newtonian model and we will adhere to it in the following: in the Newtonian framework, we take $\rho = \mathcal{E}/c^2$ and $\rho_n = y_n \rho$ in Eqs (2.4), and (2.3). This prescription could be considered a "quasi-Newtonian" limit, in the sense that $h \approx \mathcal{E}$, namely $\mathcal{E} \gg P$, a standard requirement to perform the limit; however the further step $\tilde{h} \approx 1$, namely $m_n c^2 n_B \approx \mathcal{E}$ is ignored.

The purely-Newtonian maximum glitch amplitude of Eq (3.14) is not affected by our quasi-Newtonian alternative choice made here, as long as one works coherently by using the same definition of the mass density ρ_n also in Magnus force too. This ambiguity is inherent to the spurious nature of a Newtonian dynamics on top of a relativistic background and disappears in the present GR framework.

Study of the extreme scenario - It is interesting to consider the most extreme scenario of rigid vortices that fill the whole star: this is the case for which we expect the most evident deviations from the quasi-Newtonian case. In Fig (4.3) we compare the moments of inertia in the two frameworks (N and GR stand for "quasi-Newtonian" and "slow-rotation") by plotting I and I_n as a function of the gravitational mass M. For the moment of inertia I_n associated with the superfluid reservoir, we have indeed chosen the case of rigid vortices that thread the entire star, so that both the crustal and core superfluid contribute to the angular momentum reservoir. As expected from several existing studies with various EOSs, the relativistic moment of inertia is larger than its Newtonian counterpart, with discrepancies up to 50% for large stellar masses. This is even more dramatic for the reservoir, where I_n always exceeds the total moment of inertia I, indicating that the effect of $\bar{\Omega}/\Omega$ in the integrand of I is more severe than the diminishing effect of y_n in the integrand of I_n. Although unusual this result is not a physical contradiction, and becomes less and less severe as the superfluid reservoir is restricted to the outer layers only.

In Fig (4.4) we plot the ratios I_n/I and I_v/I as a function of mass in the N and GR cases for the three EOSs. When entrainment is switched-off, we have that $I_v = I_n$; therefore, comparison of the two quantities quantifies the global effect of the non-dissipative coupling for a given vortex configuration; the differences are altogether quite small, no more than some percent in the GR scenario. We can conclude that differences due to entrainment, that are severe when only the crustal superfluid is accounted for, are greatly diminished if a large reservoir is taken into the core.

Moreover, for masses larger than $\sim 1.1\,M_\odot$ we have $I_v > I_n$, while smaller masses yield $I_v < I_n$, in both the N and the GR cases: the entrainment parameters adopted here are large and negative in the crust, but small and positive in the core. The crust contribution dominates for light stars (which present a thick crust), while for more massive stars (with thinner crusts) the core contribution prevails. This is quite different than the case of crustal reservoir commonly discussed in the literature, where entrainment has always a decreasing effect on the moment of inertia of the crustal superfluid (Andersson et al., 2012); (Chamel, 2013).

4.6.2   Maximum glitch amplitudes

We now come back to the main goal of this chapter and we compare the maximum glitch amplitudes for the quasi-Newtonian and slow-rotation frameworks. Once the input has been fixed (EOS, pinning forces and entrainment coefficient), the maximum glitch amplitude can depend only on the stellar mass.

In the following, we will discuss three cases:

Model N - This is the quasi-Newtonian framework adopted in Pizzochero et al. (2017) in which inertia is given by $\rho = \mathcal{E}/c^2$: the maximum glitch amplitude as a function of mass $\Delta\Omega_{\mathrm{abs}}(M)$ is calculated according to Eq (3.14). There is no dependence on the entrainment parameters and it is not necessary to specify how vortices are arranged: both the parallel and slack vortex configurations give the same result. Moreover, also the
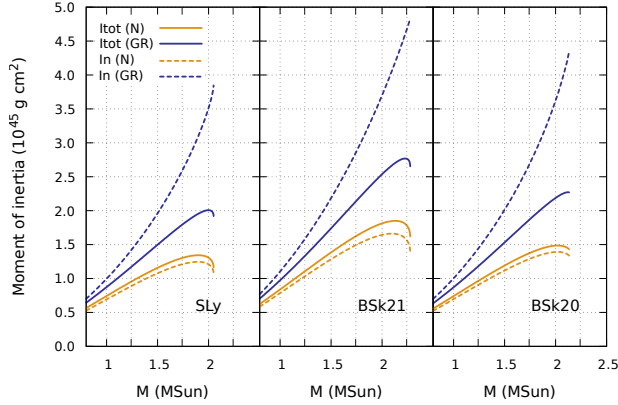
Figure 4.3: The moments of inertia I (solid lines) and I_n (dashed lines) are shown for the three EOSs considered. The mass interval starts at $0.8\,M_\odot$. In this figure, I_n is calculated for straight vortices that thread the whole star. A comparison is made between the non-relativistic moments of inertia (orange curves, labeled by N) and the relativistic ones calculated in the slow-rotation approximation (dark blue curves, labeled by GR). The curves terminate at the maximum mass allowed by each EOS, see Table (4.1).
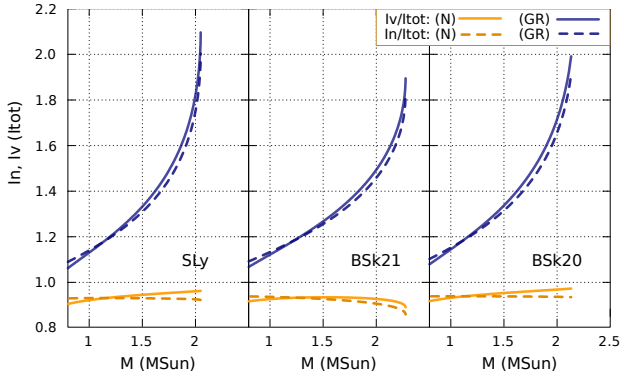
Figure 4.4: Moments of inertia of the superfluid reservoir in units of the total moment of inertia. The mass range starts at $0.8\,M_\odot$. In this figure, I_n/I and I_v/I are calculated for straight vortices that thread the whole star. We make comparison between two cases: when strong entrainment is present (I_v/I, solid lines) and when the entrainment profile is zero (in this case $I_v = I_n$ and we plot the ratio I_n/I, dashed lines). In both cases we show the curves calculated in the quasi-Newtonian framework (orange curves, labeled by N) and in the slow-rotation approximation (blue curves, labeled by GR).
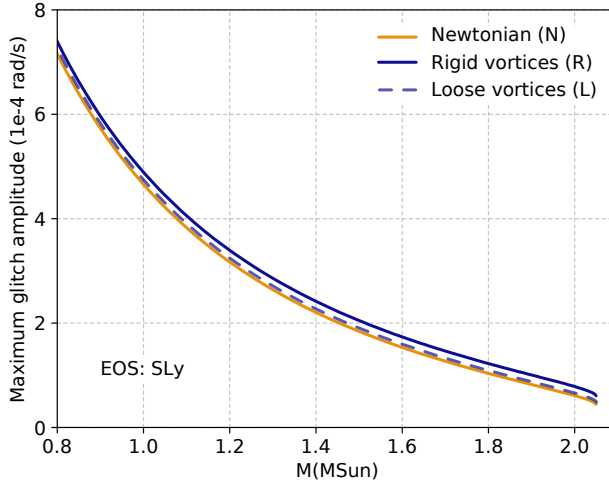
Figure 4.5: The maximum amplitude $\Delta\Omega_{\mathrm{abs}}$ relative to the SLy4 EOS is plotted as a function of mass for the three models studied: the quasi-Newtonian case (model N, orange solid line), and the two slow-rotation cases with rigid (model R, blue solid line) and slack (model L, blue dashed line) vortices. For model R, the scenario adopted is that of straight rigid vortices that thread the whole star, the extreme scenario discussed in the previous section.

extension of vortices inside the core is unimportant, as long as vortex lines extend at least across the region where pinning is present. In this paper we assumed the scenario of only crustal pinning and, as reported in Table (4.1): the region of non-zero pinning lies strictly inside the inner crust. Therefore the Newtonian results for $\Delta\Omega_{\mathrm{abs}}(M)$ are valid for both cases of continuous vortex lines and only crustal reservoir.

Model R - This is the slow-rotation version of model N for the case of rigid vortices, where the global unpinning condition is implemented. The function $\Delta\Omega_{\mathrm{abs}}(M)$ is calculated from Eq (4.61). In this case the presence of entrainment affects $\Delta\Omega_{\mathrm{abs}}(M)$. The results shown here refer to continuous vortices across the star interior. This model R is a test for the dependence of the maximum glitch amplitudes on critical lags built from non-local conditions, like Eq (4.60).

Model L - This is the slow-rotation version of model N for the case of slack vortices, where the local unpinning condition is implemented: the function $\Delta\Omega_{\mathrm{abs}}(M)$ is calculated from Eq (4.62). This seems to be a natural generalization of its Newtonian counterpart, and all the remarks made for model N are still valid.

An example of the typical result is shown in Fig (4.5): we fix the SLy4 EOS and plot the function $\Delta\Omega_{\mathrm{abs}}(M)$ for the three models. Both relativistic models give maximum glitch amplitudes that are slightly larger than their Newtonian counterpart, with model L closer to the non-relativistic case.

In Fig (4.6) we show the relative difference between the relativistic models R and L and the quasi-Newtonian one. We plot the curves $\Delta\Omega_{\mathrm{abs}}^{\mathrm{R}}/\Delta\Omega_{\mathrm{abs}}^{\mathrm{N}} - 1$ and $\Delta\Omega_{\mathrm{abs}}^{\mathrm{L}}/\Delta\Omega_{\mathrm{abs}}^{\mathrm{N}} - 1$, where the superscript indicates the model used. In model R the relativistic corrections increase with stellar mass, with values between 5% and 30% for all EOSs; conversely, for model L the dependence on mass of the corrections is weak, with values between 3% and
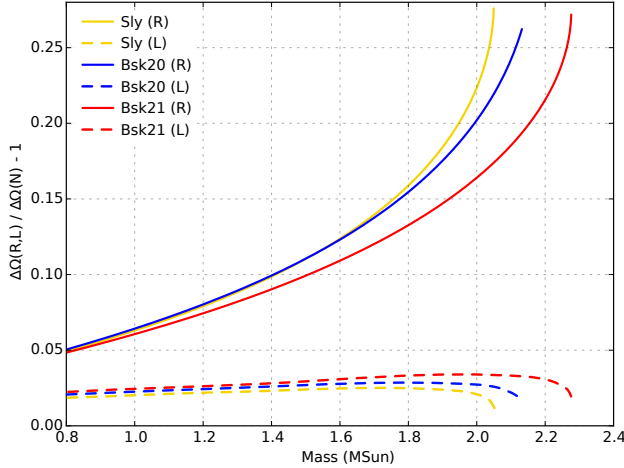
Figure 4.6:   Relativistic corrections to the amplitudes $\Delta\Omega_{\mathrm{abs}}(M)$ for the three EOSs: $\Delta\Omega_{\mathrm{abs}}^{\mathrm{R}}/\Delta\Omega_{\mathrm{abs}}^{\mathrm{N}} - 1$ (solid lines) and $\Delta\Omega_{\mathrm{abs}}^{\mathrm{L}}/\Delta\Omega_{\mathrm{abs}}^{\mathrm{N}} - 1$ (dashed lines), where the superscript indicates the model used (cf. Fig (4.5)).

5% for all the masses allowed by the EOSs.

4.6.3   Slow-rotation corrections to the upper bounds on pulsar masses

In the previous chapter it is shown how the upper limit on the stellar mass can be obtained from the maximum recorded glitch, while further timing data of the maximum event can be used to constrain the mass into a more definite range. Upper bounds are conveniently obtained by considering static models while refined constraints must rely on some, less rigorous and more uncertain, dynamical argument.

Here, we only study the upper bound on the mass, that is only dependent on the choice of the pinning force and the EOS used to calculate the function $\Delta\Omega_{\mathrm{abs}}(M)$ for models N and L, while model R requires also the entrainment coefficients. As discussed previously, however, even for model R the maximum glitch to vary at most by some percent when entrainment is set to zero: entrainment can be safely neglected (this is not the case for dynamical studies).

In Fig (4.7), where we plot the function $M = M(\Delta\Omega_{\mathrm{abs}})$ for the three EOSs; here, the curves refer to model R, the one showing the largest relativistic corrections. Qualitatively these curves are very similar in all the three models. The vertical dotted lines indicate the maximum glitch recorded. For graphical reasons, only a small sample of large glitchers are shown. The glitch amplitudes are extracted from the Jodrell Bank Glitch Catalog [19]. The largest mass M_{abs} that a pulsar can have is found by requiring $\Delta\Omega_{\mathrm{abs}}(M_{abs})$ to be equal to its maximum observed glitch. Future observations of a larger event would only lower the existing upper limit on its mass.

Instead of listing the mass upper bounds corresponding to the 51 *large* glitchers known to date (those with maximum recorded glitch larger than $5\times10^{-5}\,\mathrm{rad/s}$) and their deviation with respect to the quasi-Newtonian result, we prefer to plot in Fig (4.8) the discrepancy

---

[19] Glitch data are available at `www.jb.man.ac.uk/pulsar/glitches.html`, see also Espinoza et al. (2011).
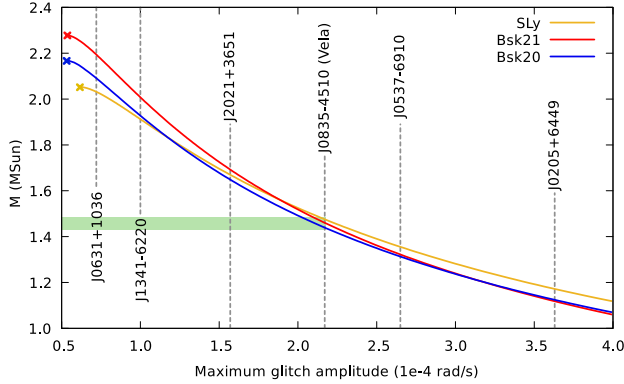
Figure 4.7: Graphical representation of the upper mass limit for a glitching pulsar. In the figure we plot the inverse of the function $\Delta\Omega_{\mathrm{abs}}(M)$ for the three EOSs; the scenario considered here is that of model R (straight rigid vortices that thread the whole star). We also report the maximum observed glitch for some of the pulsars studied in Pizzochero et al. (2017). For each pulsar, the value of the upper limit M_{abs} on the mass is found by considering the intersection of the gray dashed lines representing the maximum observed event with one of the three curves. Taking the Vela as an example, the range of M_{abs} arising from the three EOSs considered here is highlighted with a shaded band. Consider BSk21: its mean slope is $\Delta\Omega'_{\mathrm{abs}} \approx 2.9 \times 10^{-4}\mathrm{rad/s}/M_{\odot}$: this can be used to estimate how much the highlighted band changes if a bigger glitch is detected.

between the relativistic and non-relativistic values of M_{abs} as a function of the maximum glitch amplitude. The relativistic corrections to M_{abs} are always positive and small, less than 5% for all masses allowed by the EOSs (for model L the discrepancies are smaller than 1%). This is shown by considering the curves $M_{\mathrm{abs}}^{\mathrm{R}}/M_{\mathrm{abs}}^{\mathrm{N}} - 1$ and $M_{\mathrm{abs}}^{\mathrm{L}}/M_{\mathrm{abs}}^{\mathrm{N}} - 1$, where the superscript indicates the model used (Fig (4.8)).

The conclusion is that the quasi-Newtonian upper bounds on masses presented in Pizzochero et al. (2017) are quite robust: in the scenario of slack vortex lines, they are only determined by the pinning force profile and the EOS adopted, while they are independent on entrainment and on the extension of vortices in the core, and are nearly unaffected by general relativistic corrections.

4.7 Conclusions

We extended the Newtonian results of the previous chapter. The underlying model is unchanged; however in GR we are forced to put more attention into the analysis of the total angular momentum: the contribution of the differentially rotating superfluid has to be selected carefully.

The slow-rotation corrections to the maximum glitch amplitudes depend only slightly on the vortex scenario adopted (slack or rigid). In principle the rigid case has explicit dependence on entrainment input: we tested numerically that entrainment can be safely neglected for our scope. Altogether, the upper bounds on masses are increased by less than 1% in the model L when GR effects are accounted for.

Conversely, their dependence on the EOS can be further explored: alternative stellar structures (e.g. exotic interiors) would correspond to different mass constraints. In turn, these could be tested in the future against observations, as more data about glitching
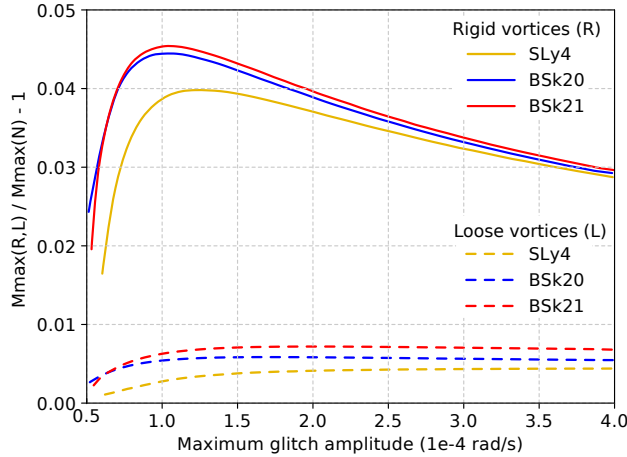
Figure 4.8: Relativistic corrections to the mass upper bound M_{abs} as a function of the maximum observed glitch for the three EOSs (identified by different colors). We plot the quantities $M_{\mathrm{abs}}^{\mathrm{R}}/M_{\mathrm{abs}}^{\mathrm{N}} - 1$ (solid lines) and $M_{\mathrm{abs}}^{\mathrm{L}}/M_{\mathrm{abs}}^{\mathrm{N}} - 1$ (dashed lines), where the superscript indicates the model used (cf. Fig (4.5)).

pulsars (possibly in binary systems) accumulate.

Mass upper bounds -   At present we are far from giving secure upper and lower constraints on pulsar masses: we only demonstrated the robustness of the upper bounds. More precisely, by robustness we mean that:

> For fixed EOS, the function $\Delta\Omega_{\mathrm{abs}}(M)$ depends only on the function $f_P(n_B)$. Mass upper limits are not affected by entrainment effects or by superfluid properties of the core-crust interface, both issues being still open at present. This is true within the pinning scenario in which the reservoir of angular momentum depends only on the static structure of the star. In this chapter we showed that these conclusions are valid for a slowly rotating neutron star in GR.

An overall rescaling $f_P(n_B) \to (1 + \epsilon)f_P(n_B)$ implies $\Delta\Omega_{\mathrm{abs}}(M) \to (1 + \epsilon)\Delta\Omega_{\mathrm{abs}}(M)$, even for finite ϵ. Imagine a change $\epsilon \sim 10\%$ in the pinning forces. The mass upper bounds are affected by

$$\delta M_{\mathrm{abs}} = -\frac{\epsilon}{1+\epsilon}\frac{\Delta\Omega_{\mathrm{abs}}}{\Delta\Omega'_{\mathrm{abs}}} \approx \epsilon\,\frac{\Delta\Omega_{\mathrm{abs}}}{3\times10^{-4}\mathrm{rad/s}}\,M_\odot$$

and the upper bound on the mass of J0205+6449 is increased by $\delta M_{\mathrm{abs}} \approx 0.1\,M_\odot$. As discussed in Antonelli and Pizzochero (2017), pinning forces in the crust are notoriously difficult to estimate, but our model (or refinements of it) can provide a direct quantitative test for newly calculated pinning profiles.

The circularity hypothesis -   Our analysis is made simple by the circularity hypothesis, i.e. the macroscopic flow of both components is laminar. However the assumed absence of macroscopic meridional circulation may be in contradiction with the fact that fluid motion in a spinning up (or down) sphere is a combination of a toroidal flow and meridional

circulation for all Reynolds numbers, as discussed with applications to neutron stars by Peralta et al. (2006) and Van Eysden and Melatos (2013).

In the case of non-zero meridional circulation (i.e. the possible presence of macroscopic toroidal vorticity), the system loses the fundamental invariance under the simultaneous inversion $t \rightarrow -t$, $\varphi \rightarrow -\varphi$ and the spacetime metric gains additional off-diagonal components. This interesting for a detailed dynamical description of the internal hydrodynamic problem, however it is not clear how this further complication would affect the values of global quantities, like the upper bound on the maximum glitch amplitudes.

Possible refinements - From the point of view of the stellar structure, our model is stationary: the presence of a differential velocity lag does not affects the background structural properties of the star (like composition or the frame-dragging angular velocity ω). A general, more refined, formalism to treat slowly rotating superfluid neutron stars can be found in Andersson and Comer (2001b), where the authors determine the effect of the differential rotation of both components on the frame dragging ω, as well as the induced changes in the neutron and proton densities and the change in shape of the star. These refinements probably worth further investigation and tests with realistic equations of state.

Future directions

This work consists of an extension and re-interpretation of some already published results (Antonelli and Pizzochero, 2017; Antonelli and Pizzochero, 2017; Pizzochero et al., 2017; Antonelli et al., 2017).

In Antonelli and Pizzochero (2017), it has been shown for the first time how the maximum glitch amplitude recorded in a given pulsar can constrain its mass when coupled to state of the art calculations of the pinning force between superfluid vortices and ions in the crust. In this work we proposed the method to calculate the theoretical (entrainment independent) relation $\Delta\Omega_{\max}(M)$, presented in Fig (3.2). This relation is the one that allows to estimate the upper limits on masses M_{abs}. This upper bound is nearly unchanged if relativistic corrections are taken into account (Antonelli et al., 2017).

The method to bracket the mass values by using observational data, which il the bulk of chapter (3), has been proposed in Pizzochero et al. (2017). After studying all known large glitchers, in particular those which have displayed at least two large events, we found that the inverse relation between mass and maximum glitch amplitude is valid as well. This happens since the mass lower limits M_{pre} are very similar to the mass upper bounds M_{abs}: this may be a drawback of the "unified model" used: we saw that this model is physically motivated but dynamically inconsistent, as also discussed in Antonelli and Pizzochero (2017).

At present, any similar study based on more refined dynamical equations (in place of the unified model) would be not definitive as well: the use of more refined dynamical equations could still be problematic, due to the uncertainties on the mutual friction term[1]. As it stands, the only way to proceed is to systematically test different prescriptions, embedded into a hydrodynamical model that consistently accounts for the realistic stellar structure.

Future work that aims to clarify these points, not only deserves a try but is fundamental for future (more reliable) implementation of the constraints on pulsar masses. The hope is that improved models for the NS superfluid properties and EOS-consistent calculations of the pinning forces will lead to more reliable mass constraints, as will further observations

---

[1] In this work the term "mutual friction" refers exclusively to the sum of terms on the hydrodynamical equations which are responsible for the momentum transport between the superfluid and normal components. In chapter (2) we derived the mutual friction term within an idealized and simplified scenario; in general this term is expected to be a non-linear and complex functional of the fluid velocities. This may still be not enough to achieve a complete description of glitches, as the trigger may have external nature (i.e. not linked to an hydrodynamical instability).

of glitching pulsars.

With this in mind, we stress that the only mass constraints that have some robustness are provided by M_{abs}, as discussed at the end of chapter (4). However, as discussed in chapter (3), it is interesting to note that our method provides a wide distribution of masses that resembles the empirical distribution of measured neutron star masses. A true breakthrough would come from an actual measurement of the mass of a glitching pulsar, which may be possible in the future if a large glitcher is discovered in a binary systems (otherwise we should ask ourselves why pulsars in binaries cannot exhibit Vela-like glitches). A number of such measurements, combined with the methods illustrated above, will allow to further constrain NS interior physics.

The problem of pulsar glitches has been faced from the perspective of two-fluid hydrodynamics. We have proposed macroscopic and deterministic models, despite glitches are unpredictable events. The dynamical model, presented in chapter (2), allows to follow the coupled response of both the normal and superfluid components due to an artificial perturbation of the system. For a given hydrodynamical model, a glitch can be initiated in many different ways, resembling the various possibilities proposed in literature, that we briefly sketch:

> *Out of equilibrium initial configuration* - It is possible to study the relaxation toward steady state for an initial arbitrary chosen Ω_p and Ω_{vp}.

> *Starquake* - Starting (for simplicity) from the steady-state condition, it is possible to artificially reduce the total angular momentum of the rigid normal component, i.e. $I_p \to (1 - \epsilon)I_p$, $\Omega_p \to (1 + \epsilon)\Omega_p$, for a small positive parameter $\epsilon = \Delta\Omega/\Omega_p$.

> *Heat deposition* - To initiate a glitch we could modify the creep rate in a certain region, mimicking heat deposition in a zone of the star: this can be done in different ways, e.g. acting on the unpinning threshold or modifying the fraction of pinned vortices.

The study of numerical simulations based on the model proposed in Antonelli and Pizzochero (2017) has been partially discussed in Seveso (2015): our 1D model, in its simplicity, shows a wide range of dynamical possibilities (exhibiting different recoveries and spin ups depending on the prescribed mutual friction and on the initial condition) but we found difficulties in handling the prescription for the repinning of vortex lines: a two-state model may be interesting, where a critical (lower) lag for the repinning is also introduced.

In the present dissertation we focused on the more robust discussion of mass-constraints, that have been carried out by means of simpler methods. The appropriate and specific remarks concerning the mass upper bounds can be found at the end of every chapter and will not be repeated here, leaving space for some additional comments and speculations.

Trigger - Our methodologies do not allow to study the intrinsic features of the trigger. The slow building of stresses driven by the thermo-rotational evolution in the crust (as well as in the vortex configuration) can play a role. The problem is to realize where these stresses accumulate in a realistic and stratified model, a still elusive task (not to account for the fact that the building of stresses is a complex phenomenon that depends on the story of the system). Another possibility is that the trigger is an hydrodynamical effect: studies in Couette geometry indicate that a fluid in a differentially rotating, spherical shell

develops meridional circulation and exerts a time-dependent torque on the outer shell (Peralta et al., 2006). This torque variability increases with the Reynolds number of the problem. Since the spherical Couette flow is an idealized model of the superfluid outer core of a neutron star (the outer sphere is the inner and outer crust), it is interesting to test whether or not the incidence of glitches depends on the expected Reynolds number in pulsars (Melatos and Peralta, 2007). This fact, together with the activity vs age correlation (Lyne et al., 2000), is one the few observed regularities in glitch phenomenology (Fuentes et al., 2017).

Avalanche - We still have to understand if the vortex avalanche can be effectively sustained: this is certainly the case if glitches are manifestations of the claimed self-organized criticality. However models proposed to put forward this hypothesis [e.g. (Warszawski and Melatos, 2008)] are unrealistic for several reasons: the models are discrete in time, have no radial dependence of pinning strengths or creep rates, do not account for the moments of inertia of the regions through which the vortices move and there is no-back reaction of the spinning-up crust on the lag. Preliminary work seem to indicate that the vortex avalanche, once triggered, is likely to propagate (Haskell and Melatos, 2016): unpinned vortices can skip multiple pinning sites and come close enough to their neighbors to initiate a knock-on reaction (Warszawski and Melatos, 2012).

Glitches as quenches - Another possibility to explain how a vortex avalanche is triggered is the back-reaction of the frictional heating that accompanies the glitch. Following the analogy with hard-superconductivity described in chapter (2), this heating further increases the already present frictional coupling. This feedback process could lead to a thermal runaway (Greenstein, 1979); (Greenstein, 1981). Such instability can spread and grow if the heat generated is comparable to the heat initially deposed in the small region relative to the seed of the avalanche. Hence, a pulsar glitch could be the superfluid realization of what is known as *quench*, the abnormal termination of the superconducting phase that occurs when part of the sample enters the resistive phase. At the best of the author's knowledge this hypothesis has never been tested, probably because the the gap energy Δ is considered to be too high. However there is no need to destroy the whole superfluid.

Heat deposition - A less violent scenario, in which a temperature perturbation causes an increase in the vortex creep rate, has been studied by Link and Epstein (1996), following the idea that the candidate mechanism which provides the initial temperature perturbation is a starquake.

In all these scenarios the central point is the coupled thermo-rotational evolution of RPPs: it is indeed known that the mutual friction between the normal and superfluid component is temperature dependent, but generates heat as-well. Better understanding of the glitch phenomenon can be achieved by considering a wider scenario in which the rotation and thermal evolution are intimately connected, similarly to what recently proposed for the magnetic field evolution among the pulsar population (Viganò et al., 2013): physical differences among pulsars, such as mass, temperature and rotational parameters, may lead to a switch between creep-like motion and avalanches, explaining the different characteristics of glitching pulsars.

In the present work we discussed only the relation between the *maximum observed*

glitch in a pulsar and the theoretically expected static[2] *reservoir of pinned vorticity* for a cold star of given mass. At the same time we do not know whether or not the instantaneous corotation condition used to define the mass-maximum glitch relation $\Delta\Omega_{\max}(M)$ can be dynamically realized. This certainly depends on the elusive mutual friction functional and on the uncertain physics of the repinning: to produce an overshoot the mutual friction term needs to incorporate a chain reaction mechanism that lowers the repinning threshold when a large amount of vortices are rapidly moving.

While general trends in the glitching behavior may be understood by means of simplified dynamical models like cellular automata, we do not have to forget that true advance will come if we will be able to contrast the phenomenology with the theoretical expectations: the primary need in the current research on pulsar glitches is the systematic test of models that can take into account in a clear manner the realistic properties of the star, such as stratification. The model discussed in this dissertation is probably oversimplified but is quantitative and consistent with the working hypothesis, as well as with some realistic aspects of NSs. However the realistic macroscopic modellization of the pulsar rotational dynamics is still in its infancy, due to the fact that nearly everything contributes to the mutual friction: crustal pinning, vortex tension, entrainment, interaction between vortices and fluxtubes, energy dissipation due to excitation of quasiparticles, turbulence. Better understanding of the mutual friction term from the "plastic phase" of hot pulsars to the "rigid phase" of colder ones could be the ultimate challenge of theoretical studies of glitches in superfluid neutron stars.

---

[2] The adjective *static* means that the reservoir is built only from energetic considerations (actually the pinning forces are derived from an average procedure on the configurations of a static vortex line immersed into an energy landscape): a nearly critical lag may never be realized dynamically.

APPENDICES

Macroscopic structure of a neutron star

The main concept behind our current understanding of neutron star structure is, in a sentence, that compressing matter liberates degrees of freedom, as sketched in Fig (0.1). As one digs deeper into a neutron star, matter becomes more homogeneous and is better approximated with a ground-state description (i.e. the fermion statistics dominates the many-body density of states, implying that thermal corrections are small).

According to the cold catalyzed matter hypothesis, matter inside cold (non-accreting) NSs is in a state of thermodynamic equilibrium with respect to all kinds of nuclear (i.e. strong) and electroweak processes at $T = 0$. Matter is therefore supposed to be in its ground state. In the $T = 0$ limit[1], the properties of a layer in the outer crust at some pressure P are given by minimizing the enthalpy per nucleon $\tilde{h}$ (or the Gibbs free energy if $T > 0$), defined as $\tilde{h} = (\mathcal{E} + P)/n_B$, where n_B is the average baryon number density and $\mathcal{E}$ is the average internal energy density.

In the zero temperature approximation the EOS is barotropic and is inferred by determining the ground state composition for every fixed density n_B. While the EOS for the outer crust has been calculated with a good accuracy, there are no widely accepted models for the composition of the inner crust and of the core.

A.0.1 Onion structure of a neutron star

The primary composition of nuclear matter in a neutron star is constantly being debated, in particular the inner core composition represents the main mystery of NS physics. A physical condition for equilibrium is that the pressure always strictly increases when going inside a NS, so the matter is stratified; properties can change continuously or abruptly if the particular density and pressure for a phase transition are realized.

Starting from the outermost layer, a neutron star is generically subdivided into four main regions: the outer crust, the inner crust, the outer core and the inner core. A complete review of the properties of the crust of neutron stars is given by Chamel and Haensel (2008).

Outer crust - The outer crust of a neutron star is solid (the most energetically favorable geometry is that of a BCC lattice) and comprised of ^{56}Fe ions and degenerate

---

[1] As reviewed by Chamel and Haensel (2008), the temperature in the interior of a NS is not zero but thermal effects are expected to mostly affect the surface layers of the star; this assumption is therefore generally satisfied in the core of mature NSs but may be less accurate in the crust, especially if the star is accreting.

valence electrons, where only an extremely thin surface layer contains a non-degenerate electron gas. Starting from $\rho \sim 10^4 \mathrm{g/cm^3}$ the iron is fully ionized owing to the high density and above $\sim 10^7 \mathrm{g/cm^3}$, the composition of the nuclei becomes more neutron rich as a result of electron captures. To maintain β-equilibrium at higher densities, electron captures by the protons inside nuclear clusters can occur, and ions get more neutron-rich.

Drip point - In order to determine the onset of neutron drip, we have to express the Gibbs free energy per nucleon for nuclei coexisting with free neutrons and electrons. Neutrons start to drip out of nuclei at some pressure P_d whenever $d\mathcal{E}/dy_n = 0$, where $y_n = n_n/n_B$ is the free neutron fraction.

Nuclear clusters are found to be unstable around $\rho_d \sim 4 \times 10^{11} \mathrm{g/cm^3}$ (corresponding to $n_d = \rho_d/m_n \approx 2.5 \times 10^{-4} \mathrm{fm^3}$), when it becomes energetically favorable for neutrons to leak out of neutron-rich nuclei. The presence of a gas of non-bound neutrons marks the beginning of the inner crust. Following the canonical work of Baym et al. (1971), the neutron drip point needs to be self-consistently calculated by minimizing the total energy density of the crust constituents (nuclei, relativistically degenerate electrons and possibly free neutrons) by using a model for the mass-energy of a nucleus with arbitrary A and Z (as in the semi-empirical mass formula) and a model for how the crystalline lattice changes the total energy density; then the neutron drip point occurs when the Fermi energy of a free neutron is comparable to its rest mass-energy, $\mu_n \approx m_n c^2$ (Chamel, 2006).

Inner crust and pasta phase - Below the neutron drip neutron-rich nuclei are still arranged in a bcc (probably polycrystalline) lattice, immersed in a gas of free neutrons in a superfluid state and normal (i.e. non-superfluid) ultrarelativistic electrons. In addition to the macroscopic liquid-drop model and the semiclassical Thomas-Fermi approximation, the inner crust have been studied also with more elaborated calculations based on the Hartree-Fock approximation with the Skyrme interaction in order to incorporate shell effects, as reviewed by Watanabe and Maruyama (2011). Competition between surface tension (of the nuclear clusters) and Coulomb interaction between protons possibly leads to a more inhomogeneous configuration than that of a bcc lattice: exotic topologies of the nuclear clusters emerge, as shown in Fig (A.1).

These so-called pasta structures can be regarded as a feature of the mixed phase during the first-order liquid-gas phase transition; in the case of a single component system, the EOS during the liquid-gas phase transition is obtained via the Maxwell construction, which allows to calculate the phase coexistence region. In systems with multiple components more complex transitions are possible: the pressure in the mixed phase is no longer constant and the Maxwell construction cannot be applied[2]. To obtain the EOS, equilibrium of partial pressures and chemical potentials (the Gibbs conditions), should be solved.

Searching for observational signatures of the pasta phase is of interest: large-scale molecular dynamics simulations show long lived topological defects that could increase electron scattering and reduce both the thermal and electrical conductivities of the pasta layer (Horowitz et al., 2015), enhancing the dissipation of magnetic field, with observable consequences on the spin-down behaviour (Pons et al., 2013). *Outer and inner core* - At densities higher than the saturation density, the ground state of nuclear matter is very uncertain, as it cannot be studied in laboratories and many-body techniques are not yet

---

[2] In a NS the pressure continuously increases, i.e. there are no macroscopically thick layers of constant pressure. If matter undergoes a first order phase transition, the density profile of the star would have a discontinuity at the radial point corresponding to the constant pressure which realizes the transition.
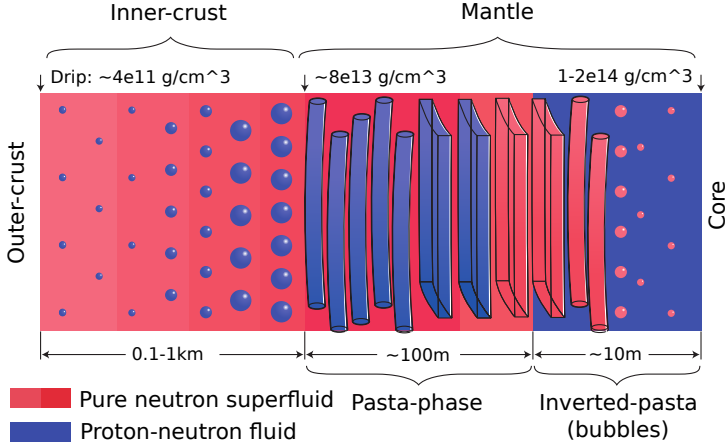
Figure A.1: Cartoon of the inner crust: at lower densities, a lattice of exotic nuclei is immersed in a superfluid of neutrons and a relativistic electron gas. At higher densities the nuclei are expected to deform and connect to form diverse topologies of nuclear clusters (pasta phases). The pasta layer is sometimes referred to as the mantle. Ranges of density and thickness are reported, and roughly represent the current theoretical uncertainties. Figure taken from Newton (2013).

so refined to allow completely reliable calculations.

The outer core starts at about a half of the saturation density ρ_0, as reported in Fig (A.1). Nuclei dissolve at the crust-core interface, outer core is mainly comprised of a neutron fluid, with small percentage of protons, electrons and muons (this mixture is sometimes dubbed extended nuclear matter). The β-equilibrium implies the equilibrium with respect to the beta decay of neutrons and inverse processes (with production of electrons or muons). All the components of this $npe\mu$-plasma strongly degenerate, with the electrons and muons that form almost an ideal Fermi gases. On the contrary, the neutrons and protons, which interact via nuclear forces, constitute a strongly interacting Fermi liquid which can be in a superfluid state. The inner core, which typically starts around $2\rho_0$, has a composition which is very model dependent; in light neutron stars it may even not exist and the outer core extends till the center. New particles can appear as density is high enough to guarantee the chemical equilibrium with more species. Several hypotheses have been put forward, as hyperonization of matter, the appearance of BEC phases (pion or kaon condensates) or a phase transition to a quark-gluon plasma comprised of up, down and strange quarks in a thermal bath of gluons. The most common hypotheses are summarized in Fig (A.2): ordinary neutron stars (with a core made of extended nuclear matter), hyperon stars (with a inner core made of hyperons and an outer core made of extended nuclear matter), hybrid stars (comprised of an inner core of QGP, eventual hyperonic matter and a shell of extended nuclear matter).

A very different family is that of quark stars: they are entirely comprised of a QGP, except for a thin external shell of ordinary matter. Differently from neutron stars, which are kept together by gravity, quark stars are bounded by the strong force. This implies that the mass-radius relation for this kind of stars has a qualitatively different shape, as can be seen in Fig (1.7).
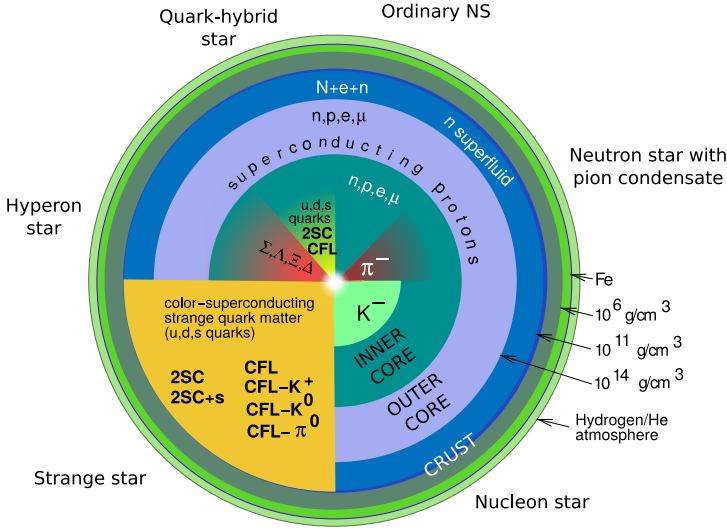
Figure A.2: Sketch of the various theoretical compositions of a neutron (or quark) star. Stellar parameters, like the thickness of the layers, strongly depend on the EOS in the neutron star core. A currently debated problem is that of hyperons: if they appear, the subsequent soften the EOS makes difficult to explain massive neutron stars (Baldo et al., 2003). While at moderate densities $\rho \sim \rho_0$ the matter inside a neutron star consists of nucleons and leptons (i.e. the fermion species present are n, p, e, μ plus escaping neutrinos), at higher densities several other species of particles appear due to the fast rise of the baryon chemical potential for ρ approaching 10^{15} g/cm^3 ~ 0.6 fm^{-3}. Not all the phases reported here are present in Fig (0.1). Figure Adapted from Weber et al. (2007).

A.1   Hydrostatic equilibrium

The interior macroscopic structure of a neutron star is governed by the exact general-relativistic equation of hydrostatic equilibrium, the Tolman-Oppenheimer-Volkoff equation:

$$\frac{dP}{dr} \;=\; -G\,\frac{(\rho + c^{-2}\,P)(m + 4\pi c^{-2}\,r^3\,P)}{r^2 \,-\, 2\,c^{-2}G\,r\,m}\,.$$

Here $m(r)$ is the enclosed mass, $P(r)$ the pressure profile and $\rho(r)$ the total mass-energy density profile, namely $\rho = c^{-2}\mathcal{E}$ with $\mathcal{E}$ the total internal energy per unit (proper) volume, as discussed in chapter (4).

To find a solution, also an EOS relating P and ρ has to be provided, together with the usual relation $m' = 4\pi r^2 \rho$, which is formally the same used to calculate the hydrostatic equilibrium of classical stars. In the limit of $c \to \infty$, the TOV equation becomes the Newtonian equation for hydrostatic equilibrium $\nabla(P + \rho\,\Phi_N) = 0$, where $\Phi_N(r) = -Gm/r$ is the gravitational potential: in this case $\rho = n_B m_B$ since the in the infinite c limit the only surviving contribution to $c^{-2}\mathcal{E}$ is that of the rest mass.

These equations allow to calculate the exact GR correction to the Newtonian gravitational potential $\Phi_N(r)$. Detailed derivation can be found in many books, as Glendenning (2000) and Misner et al. (1973): the TOV are the specification of the full Einstein equations under the assumption of static and isotropic of spacetime such as would be expected in internal and external regions of static stars. The spherically symmetric metric g is

independent of time and its most general form (using usual Schwarzschild coordinates) is

$$g = -c^2 e^{2\Phi} dt^2 + e^{2\Lambda} dr^2 + r^2 (d\theta + \sin^2\theta d\varphi^2) \,. \tag{A.1}$$

Call the circumferential radius[3] and the total gravitational mass of the star R and M respectively; the Birkoff theorem tells us that, for $r > R$, the exterior vacuum solution is that of a Schwarzschild black hole of mass M and event horizon radius $R_S = 2c^{-2}GM$, namely

$$e^{2\Phi(r)} = e^{-2\Lambda(r)} = 1 - \frac{2GM}{c^2 r} \quad \Rightarrow \quad \Phi(r \gg R_S) \approx c^{-2}\Phi_N(r) \,, \tag{A.2}$$

implying that $m(r > R) = M$ is the mass of the star as measured from Kepler's third law. Clearly the above equation is valid only for the vacuum part of the solution, implying that no physical horizon is present if $R < R_S$; for a typical NS for a neutron star we have $R \approx 0.2 R_S$, which can equivalently be written terms of gravitational binding energy $M\Phi_N(R) \approx 0.2Mc^2$. To make contact with the quantities present in the metric of Eq. (A.1), it is convenient to introduce an auxiliary variable Φ^* and write the full TOV system of equations by using geometrized units:

$$m = \frac{r}{2}\left(1 - e^{2\Lambda}\right) \qquad\qquad [\text{definition of the auxiliary variable } m\,]$$

$$\frac{dm}{dr} = 4\pi r^2 \mathcal{E} \qquad\qquad \left[\lim_{r\to 0} r^{-3}\, m = 4\pi\mathcal{E}(0)/3\right]$$

$$\frac{dP}{dr} = -\mathcal{E}\frac{d\Phi^*}{dr}\left(1 + \frac{P}{\mathcal{E}}\right) \qquad\qquad [\,P' = -\rho\,\Phi_N'\,]$$

$$\frac{d\Phi^*}{dr} = \frac{m}{r^2}\left(1 + \frac{4\pi r^3 P}{m}\right)\left(1 - \frac{2m}{r}\right)^{-1} \qquad\qquad \left[\Phi_N' = Gm/r^2\right]$$

This system has to be supplied with an EOS that gives the needed relation $P(\mathcal{E})$, namely $P(r) = P(\mathcal{E}(r))$. The third equation is also sometimes written as

$$d\Phi^* = -(P + \mathcal{E})^{-1}\, dP \,, \tag{A.3}$$

which can be used to prove an important relation between the chemical potential and Φ (Glendenning, 2000). Numerical integration is carried out from $r = 0$ to $r = R$, the radius of the stellar surface which realizes $P(R) = 0$. The central value of the density $\mathcal{E}_c = c^2\rho_c$ is a free parameter and the boundary conditions of the system are readily expressed as

$$m(r = 0) = 0$$
$$\mathcal{E}(r = 0) = \mathcal{E}_c$$
$$\Phi^*(r = 0) = \Phi_c^* \,,$$

where the exact value of Φ_c^* is unimportant[4]: after the integration of $\Phi^*(r)$, the metric function $\Phi(r)$ is found by matching Φ^* with the already known exterior solution $\Phi(r > R)$.

---

[3] The proper surface area of the star is $\int \sqrt{-\det(^2g)} = 4\pi R$; the integral is performed over a 2-surface of constant t and $r = R$. On the other hand, the proper distance between two points at constant t, φ and θ and radii r and $r + \delta r$ is $\int \sqrt{-\det(^1g)} = e^\Lambda \delta r$ (this time the integration is carried over the radial segment and Λ is evaluated at a point in $[r, r + \delta r]$).

[4] The auxiliary variable Φ^* does not appear in the system, only $\Phi^{*\prime}$ does. It is trivial to show that $\Phi^{*\prime}(r = 0) = 0$. Conversely $\Phi^{*\prime}(r = 0) > 0$ only if $m(r = 0) > 0$, which implies the existence of a physical singularity in the origin.

Explicitly this amounts to define

$$\Phi(r) \;=\; \Phi^*(r) - \Phi^*(R) + \frac{1}{2}\ln\left(1 - \frac{2M}{R}\right),$$

so that $\Phi(r) < 0$ always and the condition of asymptotic flatness is guaranteed[5]. The TOV equation also implicitly contains the fact that a maximum sustainable mass exists, as manifestation of the relativistic nature of the equation: pressure, being formally an energy density, contributes indeed to the gravitational field; if a certain threshold is reached the increasing pressure cannot contrast gravity as the increasing P makes the gradient of Φ steeper.

Pressure gradient - Suppose to have two stars, described in GR and Newtonian gravity respectively, and that these two models have the same $m(r)$, $P(r)$ and $\rho(r)$ at a certain radius r. In the GR model the proper radial distance is $e^\Lambda dr$, and we have

$$\left|\frac{dP}{e^\Lambda dr}\right| \;=\; \frac{(\rho + P)(m + 4\pi r^3 P)}{r^2\sqrt{1 - 2m/r}} \;>\; \frac{\rho\, m}{r^2}.$$

Hence going inside the star, the pressure rises faster in GR than in the Newtonian model: GR predicts stronger gravitational forces (gravity is not a force but can be still seen as something that builds up a pressure gradient) than Newtonian theory. Therefore gravitational collapse is possible, meaning that there are stable Newtonian configurations that are unstable in GR. In particular, the above equation tells us that no star in hydrostatic equilibrium can have $2m(r) \geq r$. The maximum sustainable mass turns out to be EOS dependent: softer EOS gives lower maximum masses since the star must contract in a very dramatic way to sustain pressure. The fact that the maximum mass is EOS dependent is fruitfully exploited from the observational point of view: since neutron stars with $M \approx 2M_\odot$ are observed, we can reject all the soft EOS that give smaller values for the maximum mass, as shown in Fig (1.7).

Binding energy - Nucleus of mass M_{NZ} has a definite binding energy: it is the positive amount of energy BE which has to be pumped into the system in order to destroy it. Complete destruction is achieved when the system is separated into its non-interacting basic elements (namely we have to carry the constituents far from each others), implying that

$$c^2\, M_{NZ} \;+\; BE = N m_n c^2 + Z m_p c^2 \quad \Rightarrow \quad M_{NZ} < N m_n + Z m_p.$$

The situation is analogous for a gravitating system: $M < m_B A$, where A is the number of baryons contained into the neutron star of gravitational mass $M = 4\pi \int \rho\, r^2 dr$. However, differently from what can be done for nuclei, it is not possible to interpret ρ as the gravitational mass distribution of the star: because of the Equivalence Principle, it is not possible to define a gravitational stress-energy tensor (Misner et al., 1973).

Following the presentation of Glendenning (2000), the energy associated to gravitational binding is thus always expressed as a non-local quantity (locally there is always a set of observers for which the Christoffel symbols vanish). For this reason M is called *gravitational mass*, while $\mathcal{E}(r)$ is just the thermodynamical local mass-energy. The *total mass-energy* of

---

[5] Just consider that $\ln(1 - 2M/R) < 0$, $\Phi^{*\prime} \geq 0$ and $\lim_{r\to\infty}\Phi(r) = 0^-$, as can be seen by Eq. (A.2). Clearly $\lim_{r\to\infty} g_{tt}(r) = -1$ and the Minkowski metric is recovered at spatial infinity.
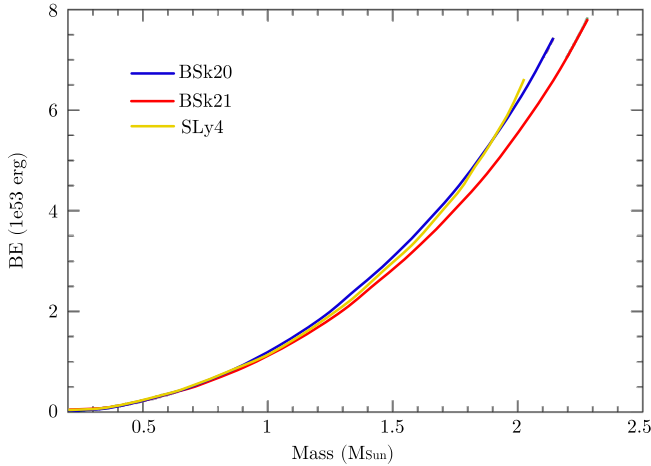
Figure A.3: Binding energy BE relative to dispersed ^{56}Fe versus gravitational mass M for the three unified EOSs that will be used in our numerical estimates presented in the next chapters. The curves are terminated at the maximum mass allowed by each EOS.

the star is

$$ E \;=\; \int \mathcal{E} \, dV \;=\; 4\pi \int_0^R dr \, r^2 \, e^\Lambda \, \mathcal{E}(r) \;>\; M \, c^2 $$

where $dV = \sqrt{-\det(^3g)}$ is the proper volume form of a 3-surface of constant t. The inequality is guaranteed by the fact that $e^\Lambda \geq 1$, as can be seen from the definition of the function $m(r)$: in particular $e^\Lambda = 1$ at the center of the star and at spatial infinity. This quantity E is however not suitable to define the gravitational binding energy of the star, as it also contains the contribution of the microscopic internal energy.

We now want to compare M (which takes into account for rest mass), the internal energy and the gravitational binding with respect to the rest mass of the NS constituents dispersed at spatial infinity. Similarly to what already done for E, it is possible to define the conserved[6] baryon number A as

$$ A \;=\; \int n_B \, dV \;=\; 4\pi \int_0^R dr \, r^2 \, e^\Lambda \, n_B(r) $$

and the relative *baryon mass* $M_A = m_B A$ of the star. It is now possible to define a quantity BE, such that $M_A = BE + Mc^2$. It is important to note that in this case the binding energy BE arises thanks to the global spacetime curvature: the volume form dV is not that of flat spacetime. The binding energy turns out to be positive (i.e. $M_A > M$ and $BE/A \sim 100\text{MeV}$) unless M is very low ($M \lesssim 0.2$ for most of the EOS). For these very light stars no creation mechanism may exist: as discussed in the previous chapter, a huge release of binding energy is required during the supernova explosion to eject most of the progenitor star and suppress the probability of black hole formation. Other authors define BE as the mass defect with respect to a dispersed configuration of a pressureless

---

[6] The total baryon number A can be interpreted (via the Gauss's theorem in curved spacetime) as the total charge associated to the conserved baryon current, see e.g. Glendenning (2000).

cloud of ^{56}Fe dust:

$$BE = \mu_{Fe} A - M c^2$$

where where A is the total number of nucleons and μ_{Fe} is the chemical potential of a nucleon in an iron nucleus, namely $\mu_{Fe} = 930.4\,\text{MeV}$ at zero pressure. According to this definition BE represents an approximation of the binding energy of neutron star with respect to the configuration of the inert core from which the neutron star was formed, as a by-product of the core-collapse. The binding energy is plotted versus M in Fig (A.3).

Magnetic fields in neutron stars

The magnetic properties of neutron stars are not yet fully understood. It is not even clear how some of these objects can have extremely high magnetic fields: simple explanation that relies on flux conservation during the collapse does not reproduce the statistics of the magnetic field strengths across the pulsar and magnetar population. The leading theory for the origin of neutron star magnetism is that dynamo action in the young star generates a strong, dominantly toroidal field. Moreover the stable internal field configuration of a rotating neutron star is still unknown and matter of debate, eve though there are strong clues that it can be a complex mix of twisted toroidal and poloidal components.

Precise pulsar timing is possible because of the coherent (i.e. non-thermal) emission from rotating and magnetized NSs, usually detected in the radio band. Although the details of the generating mechanism are still vague, the spin down of a NS can be understood in terms of the energetics of a rotating dipole.

This is not the only important effect of magnetic fields in neutron stars. Even though in this dissertation we did not take into consideration the effect of the internal magnetic field, it is however possible that the glitch behaviour is influenced by the presence of strong fields. For instance entrainment coupling in the core depends on the presence of proton superconductivity. If so, magnetic flux tubes and induced magnetization of superfluid vortices can modify (in a still not completely understood way) the internal hydrodynamics. More importantly the magnetic field drives the long term evolution of a neutron star: the most evident phenomenon, at least in RPPs, is the observed spin-down. More importantly, the presence of magnetic fields at the same time modifies cooling (by means of anisotropic heat transport and influencing neutrino emissivities) and powers the magnetosphere, thus affecting both the thermal and non-thermal (magnetospheric) features of the observed spectra[1].

Also all the complex and diverse phenomenology of magnetars is linked to dynamical aspects of the magnetic field: in particular bursts (seen in AXPs and SGRs) and the three giant flares seen in SGRs are though to be manifestations of magnetic reconnection, probably triggered by crustquakes [see e.g. Turolla et al. (2015) and Mereghetti (2008)]. This scenario is supported by the discovery of quasi-periodic oscillations (QPOs) in the X-ray flux following the giant flares from SGRs: connection of these oscillations with vibration

---

[1] As reviewed by Turolla et al. (2015), small (sub-km) hot spots are measured in certain sources, but they are more likely produced by heat deposition from the currents concentrated in magnetic bundles which emerge from the crust, rather than anisotropic internal heat transfer.

modes in the solid crust induced by the starquake has triggered interest in the field of astroseismology. Magnetic fields may also be responsible for continuous gravitational emission from isolated neutron stars that deviate from axial-symmetry since magnetic tension can induce a mass quadrupole. Both QPOs and gravitational wave emission depend on the properties of the solid crust of neutron stars, as reviewed by Chamel and Haensel (2008).

In this appendix some basic properties of magnetized neutron stars are very briefly summarized. The many aspects of neutron stars magnetic fields, including the magnetars' persistent X-ray emission and magnetic reconnection, are reviewed by Turolla et al. (2015). The more fundamental issue of how physics in strong magnetic fields can be constrained by magnetar's observations can be found in the collection of Beskin et al. (2016).

B.0.1 Energetics of a rotating dipole

Classical electrodynamics predicts that a (slowly) time varying magnetic momentum $\mathbf{m}$ looses energy as given by the non-relativistic limit of the Larmor formula[2]:

$$\dot{E}_{em} \;=\; \frac{2}{3\,c^3}\,|\ddot{\mathbf{m}}|^2,$$

which derivation is sketched in Jackson (1991) [compare also Eq (67.8) of Landau and Lifshitz (1975) and Eq (10.5.2) of Shapiro and Teukolsky (1983)]. Assume that the dipole is fixed in magnitude $|\mathbf{m}| = m$ and rotates around the direction $\hat{\mathbf{e}}_z$ with angular velocity $\Omega = 2\pi/P$, in such a way that $\mathbf{m} \cdot \hat{\mathbf{e}}_z = m\cos\alpha$. If we identify the plane orthogonal to $\hat{\mathbf{e}}_z$ with $\mathbb{C}$, the rotating dipole is modeled as

$$\mathbf{m}(t) \;=\; m\left(\hat{\mathbf{e}}_z\cos\alpha + e^{i\Omega t}\sin\alpha\right) \quad\Rightarrow\quad \ddot{\mathbf{m}} = -\Omega^2 m\,e^{i\Omega t}\sin\alpha\,,$$

which, if the dipole is not aligned with the rotation axis, implies that energy is lost as

$$\dot{E}_{em} \;=\; \frac{2}{3\,c^3}\,m^2\,\Omega^4\,\sin^2\alpha\,.$$

This is completely general, at least in the non-relativistic limit. Consider now a uniformly magnetized sphere of radius R rotating around the z-axis in vacuum. The intensity m of the magnetic dipole of the sphere can be parametrized in terms of the magnetic field at the pole B_p as $m = R^3 B_p/2$, as well as in terms of the magnetic field at the equator[3] $B_{eq} = B_p/2$; the power radiated is

$$\dot{E}_{em} \;=\; \frac{R^6(B_p\,\sin\alpha)^2}{6\,c^3}\,\Omega^4 \;=\; \frac{2\,R^6(B_{eq}\,\sin\alpha)^2}{3\,c^3}\,\Omega^4. \tag{B.1}$$

---

[2] Following Landau and Lifshitz (1975), the Pointing vector in the radiation zone for a plane wave is $S^i = c|\mathbf{B}|^2\hat{n}^i/4\pi$, where $\hat{n}^i$ points from the nearly point-like source to the far observer. In vacuum the magnetic and electric fields are conveniently expressed with the aid of the vector potential $\mathbf{A}$ as: $\mathbf{B} = c^{-1}\partial_t\mathbf{A}\times\hat{n}$ and $\mathbf{E} = \mathbf{B}\times\hat{n}$. Consider a time-varying electric dipole $\mathbf{d}$ arising from the motion (inside a region of diameter R small compared to the distance of the observer) of particles with charges q_i and velocities $\mathbf{v}_i$, then $\dot{\mathbf{d}} = \sum_i q_i\mathbf{v}_i$ is the first temporal derivative of the electric dipole moment. Non-relativistic limit of the retarded potentials in the radiation zone gives $\mathbf{A} = (cR)^{-1}\dot{\mathbf{d}}$, which implies $\mathbf{B} = c^{-2}R^{-1}\ddot{\mathbf{d}}\times\hat{n}$. The energy flux (power per unit area) in the $\hat{n}$ direction is thus $S^i\hat{n}_i = c|\mathbf{B}|^2/4\pi = |\ddot{\mathbf{d}}|^2\sin^2\alpha/(4\pi c^3 R^2)$, where the angle α is defined via $\dot{\mathbf{d}}\cdot\hat{n} = \cos\alpha$. The power radiated is the energy that leaves the boundary of the source in a time unit, namely $\dot{E}_{em} = R^2\int d^2\Omega_\alpha\,S^i\hat{n}_i$, where $d^2\Omega_\alpha$ indicates that the measure on the sphere is conveniently parametrized by using α as polar angle. Therefore the same formula $\dot{E}_{em} = 2|\ddot{\mathbf{d}}|^2/(3\,c^3)$ is valid also for the power radiated by a time-varying electric dipole. The fact $\int d^2\Omega_\alpha\,\sin^2\alpha = 8\pi/3$ has been used in the last passage.

[3] The quantities B_p and B_{eq} are often generically referred to as "dipole field" and sometimes confused. B_p is the intensity of the magnetic field produced by a pure dipole at distance R along the magnetic axis,

This is the classic result of the vacuum-dipole-model. When the effects of the magnetosphere are taken into account in the force-free models (i.e. in the low-inertia limit of MHD), the pulsar spin down luminosity is well approximated by (Spitkovsky, 2006)

$$\dot{E}_{em} = \frac{R^6 B_p^2 \Omega^4}{4 c^3} \left(1 + \sin^2 \alpha\right).$$

The power in this case is larger than for the vacuum orthogonal rotator ($\alpha = \pi/2$) and it is non-zero even in the aligned case ($\alpha = 0$). This substantial difference with respect to the vacuum case comes from the proper inclusion of the rotationally induced electric field in the magnetosphere. More generally the energy balance equation between radiation and rotational energy losses reads

$$I\,|\dot{\Omega}| = \frac{R^6 B_p^2 \Omega^3}{6 c^3} f(\alpha), \qquad [\text{e.g. } f(\alpha) = \frac{3}{2}(1 + \sin^2 \alpha), \text{ Spitkovsky (2006)}] \qquad \text{(B.2)}$$

where differences in the radiation mechanism are included in the factor $f(\alpha)$. In literature, the fiducial values $I_{45} = 1$, $R_6 = 1$ and $f(\alpha) = 1$ (vacuum orthogonal rotator) are commonly used in order of magnitude estimates: thanks to the 3D simulations of Spitkovsky (2006) it has been shown that $\dot{E}_{em}$ still scales with Ω^4, even for realistic models of the magnetosphere, the complex effects are hidden into an overall factor f.

The luminosity $\dot{E}_{em}$ must be equal to the observed decrease of rotational kinetic energy $I\Omega|\dot{\Omega}|$ of the sphere, where I is the moment of inertia. It is thus possible to infer intensity the effective magnetic field $B = B_{eq}f^{1/2}$ at the surface as

$$B = \sqrt{\frac{3 c^3 I\,|\dot{\Omega}|}{2 R^6 \Omega^3}} = \sqrt{\frac{3 c^3 I P \dot{P}}{8 \pi^2 R^6}} \approx 3.2 \times 10^{19} R_6^{-3} I_{45}^{1/2} (P \dot{P})^{1/2}\,\text{G}, \qquad \text{(B.3)}$$

where $\dot{P}$ is the spin down rate in units of s/s, P is the period in seconds, I_{45} is the moment of inertia in units of $10^{45}\,\text{g cm}^2$ and R_6 is the radius in units of $10\,\text{km}$: we use this prescription for B in our plots of the P-$\dot{P}$ diagram (Fig (B.1)).

It has been shown that neutron stars with large toroidal fields evolve into configurations, where the angular momentum of the star is orthogonal to the magnetic axis so that the relative orientation of the dipole and rotation axis is not completely random. Such configurations, which provide $\sin \alpha \approx 1$ in the dipolar rotator model, are also associated with gravitational wave emission (Cutler, 2002), due to the fact that magnetic field lines have an effective tension that can deform the star.

Gravitational waves luminosity - Intense magnetic fields can indeed sustain quadrupole deformations on a rotating neutron star but also other possibilities have been proposed [4]. Alternatively, proto-neutron stars typically born with high angular velocity, in a configuration that is likely to be triaxial: cooling and crystallization of the crust may have

---

B_{eq} is the intensity of the magnetic field on the *magnetic* equator (the angle between the equator defined by rotation and the magnetic one is indeed α). Consider usual spherical coordinates around $\mathbf{m} = m\hat{\mathbf{e}}_z$: by using $\hat{\mathbf{e}}_z = \hat{\mathbf{e}}_r \cos \theta - \hat{\mathbf{e}}_\theta \sin \theta$. The usual dipolar field $\mathbf{B} = [3(\hat{\mathbf{e}}_r \cdot \mathbf{m})\hat{\mathbf{e}}_r - \mathbf{m}]/r^3$ has components $B_r = B_p \cos \theta\,(R/r^3)$, $B_\theta = (B_p/2) \sin \theta\,(R/r^3)$ and $B_\varphi = 0$. For $\theta = 0$ and $r = R$ we have the magnetic field at the pole ($B_r = B_p$ and $B_\theta = 0$). On the magnetic equator, $\theta = \pi/2$ and $r = R$, the only non-zero component is $B_\theta = B_p/2$.

[4] Spherical bodies that vibrate radially do not radiate gravitational waves, in accordance with the Birkhoff's theorem. This is still true for an axially-symmetric neutron star. However, a rigidly rotating star with non-axial deformations radiates gravitational waves. The possible mechanisms for gravitational

frozen part of this initial asymmetry, so that the star's equatorial plane is slightly elliptical. Thus asymmetry may be due to elastic strains in the solid regions (the crust) or magnetic strains. Another mechanism has been proposed by Bildsten (1998): building of mountains proceeds via temperature and composition asymmetry in accreting stars. The viability of this mechanism has been confirmed by Ushomirsky et al. (2000) but the key unknown is the likely level of non-radial composition gradients in the crust of accreting neutron stars. Connection between gravitational wave emission and astroseismology is briefly summarized in the review of Chamel and Haensel (2008): the elastic properties of the crust play a crucial role and can be constrained by searching for continuous gravitational waves emitted by isolated and deformed neutron stars. Deformed neutron stars loose energy at a rate given by (Shapiro and Teukolsky, 1983)

$$\dot{E}_{GW} \approx \frac{32\, G}{5\, c^5} I^2 \epsilon^2 \Omega^6 \,, \tag{B.4}$$

where ϵ is a dimensionless parameter characterizing the deformation of the star[5] and I is the moment of inertia relative to the actual axis of rotation. Similarly to what have been done for the unknown magnetic field where we estimated the value of a characterizing parameter like B_p, it is still possible to use pulsar timing data to constrain the parameter ϵ: since the power radiated away in gravitational waves can be at most equal to the observed kinetic energy loss $I\Omega|\dot{\Omega}|$, this implies that

$$\epsilon \,<\, 9 \times 10^{-13}\, I_{45}^{-1/2}\, \dot{P}_{15}^{1/2}\, P^{3/2} \,.$$

Again P is the numerical value of the period in seconds. With this inequality we can also put a crude upper limit to the size of the highest mountain, that is of the order $\sim \epsilon R$. For instance, the mountains on the surface of the Crab pulsar are expected to be less than few meters. For some millisecond pulsars the constraint is even more severe: for example in the Black Widow pulsar (PSR 1957+20) mountains cannot exceed $\sim 10^{-4}$cm.

B.0.2 Characteristic spin-down age

In a rigidly rotating pulsar the kinetic energy $E_{rot} = I\Omega^2/2$ decreases my means of the electromagnetic emission[6]: $\dot{E}_{rot} = I\Omega\dot{\Omega}$ must equate the spin down luminosity. Ignoring GW emission,

$$\dot{\Omega} = -\frac{2B^2 R^6}{3\, c^3\, I}\, \Omega^3 \,, \tag{B.5}$$

where $B = f^{1/2} B_p/2$ is the effective surface field defined in Eq (B.3). Equation (B.5) can be generalized by considering a braking torque that is proportional to Ω^n. The parameter

---

wave emission from individual neutron stars that have been proposed so far are fluid oscillations, free precession (the most general motion of rigid bodies) and mountains. Mountains are actually large scale deformations with respect to the non-rotating and non-magnetized, $T = 0$ configuration with the same mass and are therefore more similar to a bulge rather than to mountains on Earth. All these mechanisms lie below the detectability threshold.

[5] As described by Shapiro and Teukolsky (1983), ϵ is the ellipticity of the equatorial plane, namely $\epsilon = 2(a - b)/(a + b)$ where a is the maximum equatorial radius and b the minimum. If the star is rotating around one of the principal axes of the inertia tensor, ϵ is given by $\epsilon = (I_1 - I_2)/I$, where I_1 and I_2 are the moments of inertia with respect to the principal axes orthogonal to the rotation axis.

[6] In a pulsar which rotates differentially the kinetic energy is degraded also by friction. This contribution is typically much less than the electromagnetic losses.

n is called braking index: $n = 3$ for pure EM-emission or $n = 5$ for pure GW-emission. We therefore consider the differential equation

$$\dot{E}_{rot} = -\alpha \Omega^{n+1} \quad \Rightarrow \quad \dot{\Omega} = -\beta \Omega^n. \tag{B.6}$$

Assuming the constancy of β, we can use the currently observed values of the rotational parameters to estimate this unknown parameter: consider $\tilde{\tau} = \Omega_o^{n-1} \beta = -\dot{\Omega}_o/\Omega_o$; the above equation is therefore written as

$$\dot{\Omega} = -\frac{\tilde{\tau}\Omega^{n-1}}{\Omega_o^{n-1}},$$

which can be integrated starting from the birth of the star (the age of the pulsar is τ_n):

$$\int_{\Omega_\tau}^{\Omega_o} \frac{\dot{\Omega}\,dt}{\Omega^{n-1}} = -\int_0^{\tau_n} \frac{\tilde{\tau}\,dt}{\Omega_o^{n-1}} \quad \Rightarrow \quad \tau_n = \frac{\tilde{\tau}}{n-1}\left[1 - \left(\frac{\Omega_o}{\Omega_\tau}.\right)^{n-1}\right].$$

Assuming that the NS was born with a very high angular velocity in the millisecond regime, $\Omega_\tau \gg \Omega_0$,

$$\tau_n \sim \frac{\beta^{-1}}{n-1} = \frac{\Omega_o}{(n-1)\dot{\Omega}_o}. \tag{B.7}$$

These results, like the inferred magnetic field and the characteristic dipole age $\tau = \tau_3 = P/(2\dot{P})$ can be used to add information in the P-$\dot{P}$ diagram, where we can draw lines of constant magnetic field B, dipole age τ and energy loss $\dot{E}_{rot}$, Fig (B.1).

However, the best-determined ages are those for which dynamical information, such as observed space velocities of the pulsar coupled with a known birthplace, is available. The characteristic spin-down ages estimated from pulsar periods P and spin-down rates $\dot{P}$ using $\tau = P/2\dot{P}$ are considered less reliable estimates of the true age: in the cases in which both kinds of age estimates are available, they generally differ by factors of two or three.

The present analysis tells us that it is also possible (though difficult) to estimate the braking index by measuring the second derivative of the angular velocity as

$$n = \frac{\Omega\,\ddot{\Omega}}{\dot{\Omega}^2}.$$

Among the radio pulsars currently known, only young pulsars have braking indexes measured with accuracy, all less than 3 (for the Crab the measured value is ~ 2.5). Some pulsars with positive second derivative $\ddot{\Omega}$ show anomalous braking indexes up to ~ 100, while many pulsars show negative values of $\ddot{\Omega}$ (e.g. $n \approx -1.5$ for J0537-6910), which can be understood in terms of missed or unresolved glitches (Alpar and Baykal, 2006).

The inferred braking indexes can also be a consequence of an evolving magnetic field (Ho, 2015): within the standard scenario for spin evolution of isolated neutron stars, young pulsars slow down with a constant surface field (i.e. constant β), implying a braking index $n = 3$ while the field is constant and $n > 3$ when the field decays. This is in contrast with observed values $n < 3$ (e.g. for Vela $n \approx 1.4$): the magnetic field can be buried soon after birth and slowly diffuses to the surface.

B.0.3 Neutron stars as the strongest known magnets

Dipolar fields inferred from the rotational parameters of pulsars are extremely high if compared to the magnetic fields we are used to, as depicted in Fig (B.2).
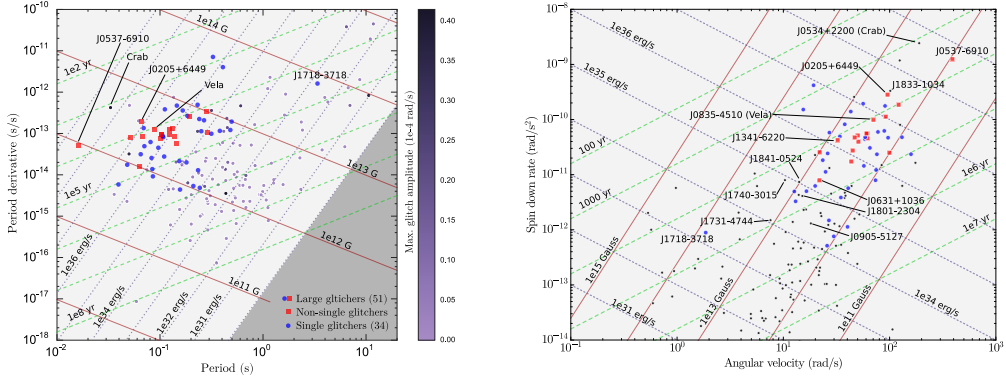
Figure B.1: The pulsars considered by Pizzochero et al. (2017) plus the 34 single glitchers presented in Tab (3.2). Lines of constant spin down luminosity, B and τ are plotted, assuming $R_6 = 1$ and $I_{45} = 1$. *Left* - The usual P-$\dot{P}$ diagram. The large glitchers are indicated by red squares (non-single) or blue circles (single). All the other known glitchers are plotted according a color scale that represents the amplitude of their largest glitch. The rough estimate of the death line indicated by Lorimer and Kramer (2004) and defined by $I\Omega\dot{\Omega} \sim 10^{30}$ erg/s bounds the shaded region [see (Chen and Ruderman, 1993) for discussion of the graveyard region]. The case of J1718-1718 is indicative of important selection effects due to the limited observations, namely in slow pulsars glitches are rare so that they appear as single glitchers or even quiet. *Right* - The same plot but using Ω and $\dot{\Omega}$. In this case, in order not to hide very weak glitchers, the color scale has been replaced by uniform black dots. It is interesting to note that the large glitchers are very clustered, with the remarkable exception of J0537-6910. The Crab is also a good candidate but, since it displayed many glitches, the detection of a considerably bigger glitch is is unlikely: this pulsar may have already shown its maximum possible glitch [since it is young and is spinning down fast, is maximum reservoir is expected to be significantly lower that the upper bound provided by Eq (3.14)].)

In the cgs system the quantity $\Phi_0 = hc/e \approx 4 \times 10^{-7}$ G cm^2 can be regarded as a quantum of magnetic field flux (Lai, 2016). Here we used the charge of the electron but it is still possible to use a generic charge as well, for example $2e$ if we want to study superconductivity may be suitable [see Eq (4.15)]. Given a macroscopic typical magnetic field strength B, it is thus possible to derive the length l_B that defines the radius of the microscopic solenoid as

$$B(l) = \frac{\Phi_0}{\pi \, l^2} \quad \Rightarrow \quad l_B = \sqrt{\frac{2\hbar c}{e\,B}}. \tag{B.8}$$

In the first equation l is just a generic length, the radius of the area relative to the flux Φ_0. The function $B(l)$ defines a relation between magnetic field strength and the length scale of the problem, and is dubbed Aharonov-Bohm scaling: since we derived it by means of dimensional considerations only, the true scaling is expected to deviate significantly from $B(l)$ at a certain (unknown) critical scale that can be easily estimated. Let's try to insert $l = \lambda_e = h/(m_e c) \approx 2.4 \times 10^{-10}$ cm, the non-reduced Compton length of the electron, into the above equation. We get $B(\lambda_e) \approx 2 \times 10^{12}$ G, a value that perfectly fits typical surface magnetic fields observed in pulsars $B \sim 10^{12}$ G. Magnetars have much higher magnetic fields, $B \sim 10^{14} - 10^{15}$ G. This means that the properties of matter at low pressure in neutron star environments is drastically modified by strong magnetic
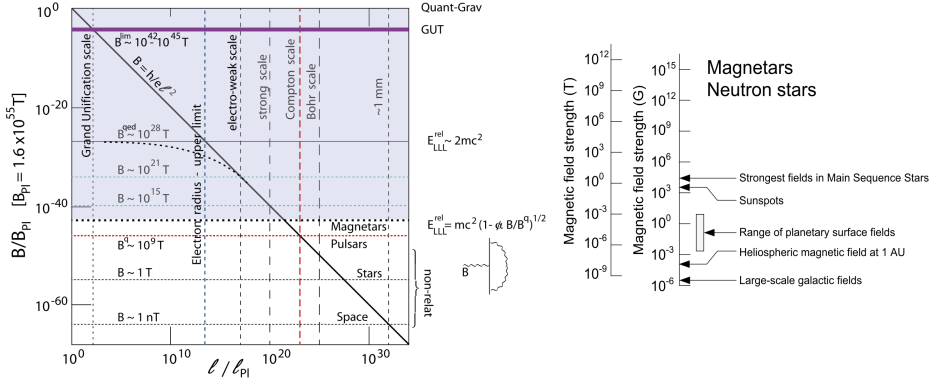
Figure B.2: Magnetic field strengths for different length scales: the ultimate field strength $B_{Pl} \sim 10^{58}$ G is given by considering the Planck length $l_{Pl} = \sqrt{\hbar G/c^3} \approx 10^{-33}$ cm, well above the expected deviation from the trivial Aharonov-Bohm scaling. *Left* - Scaling of magnetic field strength B (normalized to B_{Pl}) with respect to the typical length scale l (normalized to the Planck length l_{Pl}). The diagonal shows the relation given in Eq (B.8). The dotted red lines indicates the intersection of the electronic Compton length with the Aharonov-Bohm scaling line: this defines a field strength $B_Q \sim 10^9$ T above which QED corrections to Landau energy levels are important. For higher fields, the black dashed curve indicates a possible deviation of the Aharonov-Bohm scaling near the QED limit, where the corrections to the Landau levels are of the same order of the rest mass of the electron (namely they ceases to be corrections). This defines a limit imposed by QED for the B field (the horizontal line at $\sim 10^{28}$ T) that approximately coincides with the measured upper limit on the electron radius (vertical blue dashed line). However the (shaded) relativistic domain have never been observed. *Right* - The range of observed astrophysical magnetic field strengths, covering approximatively 21 orders of magnitude. Magnetic field is given in SI units, T= 10^4 G. For comparison, observed magnetic WDs exhibit polar field strengths in the wide range 10^3-10^9 G. Adapted from Beskin et al. (2016).

fields[7]. QED corrections to the trivial Aharonov-Bohm scaling appear when the energy gap between consecutive Landau levels is the order of the electron mass, implying that the B field is comparable to the value $B_Q \sim 10^{13}$ G. Remarkably this kind of fields are often observed in neutron stars surroundings, where a number of QED processes are important, like single-photon pair production $\gamma \to e^+ + e^-$. This process is forbidden at zero-field by momentum conservation and is one of the dominant channels for pair cascade in pulsar magnetospheres. This possibility to excite pairs is expected to make magnetized vacuum birefringent for photons propagating through it, a fact that significantly affects the x-ray polarization signals from magnetars as recently observed by Mignani et al. (2017) in RX J1856-3754. This particular object is part of the group of neutron stars known as the Magnificent Seven, radio-quiet isolated neutron star which have no stellar companions

---

[7] The typical field that is expected to alter the atomic properties of matter is $B(a_0)$, where $a_0 = \hbar^2/(m_e e^2) \approx 5.3 \times 10^{-9}$cm is the Bohr radius. Thus $B(a_0) = 2c\, m_e^2\, e^3/\hbar^3 \approx 4.7 \times 10^9$ G, much less than $B(\lambda_e)$. We defined Φ_0 and $B(l)$ in order to be consistent with Beskin et al. (2016). Alternatively, it is possible to follow another, and more common, line of reasoning: the energy between two consecutive Landau levels is $\hbar\omega_c = \hbar eB/m_e$, which implies the natural definition $B(E) = Em_e/(\hbar e)$, where E is a generic energy. The atomic magnetic field is thus given by choosing $E = e^2/a_0 \approx 27\,eV$, namely $B(e^2/a_0) = B(a_0)/2$. By choosing $E = m_e c^2$, a magnetic field of strength $B(m_e c^2) = m_e^2 c^3/(\hbar e) \approx 4.4 \times 10^{13}$ G can create electron-position pairs (vacuum polarization). This field strength is dubbed B_Q in the text; note that $B_Q = 2\pi^2 B(\lambda_e)$.

and are not surrounded by progenitor supernova material.

Inclusion of higher order QED corrections would allow for fields of up to $\sim 10^{32}$ G, deep in the (shaded) relativistic domain of Fig (B.2) which have newer been observed: strongest detected magnetar fields correspond only to the first order relativistic correction on the lowest Landau level energy (shown in Fig (B.2)) that are of the order $\sim m_e c^2 B / (4\pi 137 B_Q)$.

Rigid models

Most studies of pulsar glitches are based on body-averaged models with two rigid components: an "observable component" strongly coupled to the magnetic field and an "internal component". Some examples of this kind of approach can be found in the early work of Baym et al. (1969) or in the more recent studies of Andersson et al. (2012), Sidery et al. (2010) and Sourie et al. (2016).

The observable component is, by definition, the component of the star that corotates with the observed beamed radiation and it is typically assumed to consist of the solid crust and everything strongly coupled to it by the large-scale magnetic field.

The internal component is the so-called superfluid component. This definition is however vague enough: also the core is (at least partially) superfluid. Nevertheless the core is most of the times assumed to be part of the observable component: mutual friction arising from electron scattering couples the crust and the core superfluid in less than a minute for a glitching pulsar like Vela (Alpar et al., 1984a; Alpar et al., 1984; Alpar and Sauls, 1988; Andersson et al., 2006).

More generally the star can be comprised of many body-averaged components: distinction between such components is therefore made by considering the different processes that couple them to the solid crust. Each component (call it x, no repeated indexes summation convention is used for this component label) interacts with the others via a mutual torque $T_{MF}^{yx} = -T_{MF}^{xy}$, so that the component y induces a torque T_{MF}^{yx} on x. To resemble a form that is sometimes used in glitch modelling, we can also use the notation $T_{MF}^{yx} = I_x \dot{\Omega}_{MF}^{yx}$. Let also consider the possibility that the single components can radiate (as sometimes assumed when entrainment is present), so they loose angular momentum at a rate $T_x^{ext} = -I_x |\dot{\Omega}_x^{ext}|$.

Assume now that we can observe the star for a long time and measure its spin down rate: the most the observation is extended, the most we can push forward the claim that we are indeed measuring[1] the steady-state spin down rate $|\dot{\Omega}_\infty|$. Given the parameters I_x which represent the moments of inertia of the various components, the multi-component

---

[1] A long observation is needed to average the glitch-induced spin-ups with the post-glitch recoveries. To really fit the value of $|\dot{\Omega}_\infty|$, the moments of inertia I_x and the rates $|\dot{\Omega}_x^{ext}|$ must be considered constant during the observation timescale.

dynamics with no precession is

$$I_x \dot{\Omega}_x = \sum_y T^{yx}_{MF} + T^{ext}_x \qquad \Rightarrow \qquad \dot{\Omega}_x = \sum_y \dot{\Omega}^{yx}_{MF} - |\dot{\Omega}^{ext}_x|$$

$$\sum_x I_x \dot{\Omega}_x = -I|\dot{\Omega}_\infty| \qquad \Rightarrow \qquad \sum_x I_x |\dot{\Omega}^{ext}_x| = I|\dot{\Omega}_\infty|$$

$$\sum_x I_x = I$$

The fundamental constraints on the spin down rate and on the total angular momentum are indicated, together with the alternative notation in terms of Ω^{yx}_{MF}. Note that, since we are interested do describe the standard scenario that applies to RPPs, we forced the rates to be negative but accreting neutron stars can have positive rates.

The basic phenomenological of this kind was proposed by Baym et al. (1969), where the mutual friction is written in terms of the of the *coupling timescale*[2] $\tau^C_{yx} = \tau^C_{xy}$ as:

$$T^{yx}_{MF} = -\frac{I_y I_x}{I} \frac{\Omega_x - \Omega_y}{\tau^C_{yx}} \qquad \Rightarrow \qquad \dot{\Omega}^{yx}_{MF} = -\frac{\Omega_x - \Omega_y}{\tau^R_{yx}} \ .$$

In the equations above we introduced also the *relaxation timescale* $\tau^R_{yx} = I\tau^C_{yx}/I_y > \tau^C_{yx}$, which has the disadvantage to be a non-symmetric matrix. However some of the entries of τ^R_{yx} can be estimated directly by observing the post-glitch relaxation (in the case of two components τ^R is the timescale of the theoretical exponential relaxation).

Models with more than two components are not very used, even though they provide a variety of dynamical possibilities which could really fit the diverse phenomenology of glitches and produce overshooting of the observable component, impossible to realize with a rigid two-component model. The main problem is the identification of a third component and its coupling with the superfluid in the crust: it seems reasonable to consider the superfluid in the outer core, or the toroidal superfluid region corresponding to a region of pinning with flux tubes (Gügercinoglu and Alpar, 2014). It is trivial to generalize the differential model described in chapter (2) in order to rigorously build the integral prescriptions needed to construct such a three-component model (in this case we have to consider two sets of disjoint regions that are filled with straight vortex lines).

The simplest model for pulsar rotational dynamics is obtained by considering an internal and an observable components with angular velocities Ω_o and Ω_i. Only the observable component undergoes electromagnetic losses of angular momentum:

$$I_o \dot{\Omega}_o + I_i \dot{\Omega}_i = -I|\dot{\Omega}_\infty| \tag{C.1}$$

$$\dot{\Omega}_i = -\frac{\Omega_i - \Omega_o}{\tau^R} \ . \tag{C.2}$$

---

[2] The coupling timescale is actually the parameter used in the original article of Baym et al. (1969) and in the book of (Shapiro and Teukolsky, 1983). The terminology used here is not standard and most of the times the terms "coupling" and "relaxation" are used as synonyms. For a non-linear mutual friction torque T_{yx}, we can introduce the coupling timescale by considering the linearization of the general mutual friction term in a particular dynamical phase: $\tau^C_{xy} \approx \frac{I_y I_x}{I} [\frac{\delta T_{xy}}{\delta \Omega_{xy}}]^{-1}$. The approximation is valid on timescales shorter than τ^R_{xy} and the variation of the mutual friction has to be evaluated at the given initial lags that define the dynamical phase.

Such a linear system provides exponential relaxation if perturbed away from the steady state[3]. Values of the order $I_i \sim 10^{-2}I$ are typically found for the internal component, provided that it consists of the superfluid within the crust, enough to explain large Vela glitches (Link et al., 1999). As argued by Andersson et al. (2012) and Chamel (2013), the fraction I_i/I is significantly lowered by entrainment, leading to difficulties in explaining large glitches. This result is however debated, as it seem that it is premature to reject the longstanding hypothesis that the superfluid reservoir is confined into the crust only (Piekarewicz et al., 2014); (Watanabe and Pethick, 2017).

The entrainment effect in the above simple system of equations is usually included by introducing additional (linear) couplings between Ω_o and Ω_i. However, it has been shown in chapter (2) that entrainment does not change the form of the rigid equations; it only affects the values of I_o, I_i (leaving I unchanged) and τ, without any need to introduce new terms, differently from what it is usually done in body averaged models [e.g. (Andersson et al., 2012), (Haskell and Melatos, 2015)].

---

[3] A simple calculation shows that, within the original starquake scenario (in which the glitch is produced by artificially changing the moments of inertia at the steady state), the healing parameter Q of Eq (1.3) turns out to be $Q \approx I_i/I$. On the other hand, a transient perturbation of the value of τ_R (representing a sudden unpinning of vortices) implies $Q = 0$. In general the only way to produce a non-zero value of Q is to allow for a permanent change in one or more of parameters in the dynamical equations.

Vortex mediated mutual friction

We review the derivation of the mutual friction force in the case of superfluid ⁴He (Hall and Vinen, 1956; Bekarevich and Khalatnikov, 1961), correcting an overall sign error present in Andersson et al. (2006). This method will be applied to the standard case, where the vortex line feels a drag force and the Magnus force. The analysis is purely local, meaning that it is suitable only in an idealized scenario: the local motion of the line is uncorrelated to the forces felt by other segments of the line. This implies that the matter should be homogeneous at the mesoscopic scale of the vortex line and that the line itself is locally straight. For this reason this type of force between the normal and superfluid component is usually considered to be the standard form of vortex-induced mutual friction when an organized array of vortices is present.

General relativistic generalization of the standard result presented here is given by Andersson et al. (2016).

A superfluid vortex in 2D (i.e. a vortex in a superfluid film), or a straight vortex line in a 3D domain, is sometimes described as a point massless particle. Motivation for this relies into the fact that a free vortex line in a perfect fluid flows with the velocity field without any inertial effect: its trajectory coincide with the path of a material element of the fluid. This is not a prerogative of the quantum nature of the fluid (the same behavior appears in the classical perfect fluid).

The Newton equations for a vortex of this kind are thus just equations for force balance. It is also possible to assign an effective mass to the vortex, as discussed by Baym and Chandler (1983). However the central point here is another: a vortex has an *infinite number of degrees of freedom* that are inevitably frozen if we describe it as a point particle. The next fundamental point is how to perform a meaningful average over a portion of fluid that contains many vortices, in order to obtain the macroscopic form the hydrodynamical equations with mutual friction. Both these points are addressed here in a somewhat trivial way, that is nonetheless the standard way: firstly, the vortex is a point; secondly, the macroscopic average is performed by considering a certain set of non-interacting points (dubbed "bundle of vortices") in a fixed and uniform background flow.

We start by considering the equation of motion for a straight segment of vortex line[1]

---

[1] More rigorously we should say that the treatment is valid for a vortex on a 2D film, where the circulation κ is a scalar (like the magnetic field in 3D spacetime) and the background uniform flow is forced live in the same plane of the vortex's induced flow: in this case the vortex is really a particle. In modelling superfluid neutron stars, the present derivation is sometimes interpreted differently: vortices are extended, but their local dynamics is assumed to be the 2D dynamics on a certain plane identified by

with velocity $\mathbf{v}_L$ and circulation κ: the forces considered here are not localized but are averaged forces acting on a suitably small volume around a straight piece vortex (mesoscopic forces); the Newton equation (with no inertia) reads

$$f_M^i + f_D^i = 0$$

where $f_M^i = m_n n_n \epsilon^{iab} \kappa_a$ and f_D^i are the Magnus and drag force respectively. It is useful to work in the frame of the normal component; the notation v_{xp}^i stands for $v_x^i - v_p^i$. Using the fact that $v_{Ln}^i = v_{Lp}^i - v_{np}^i$, the system to solve is

$$\epsilon_{ijk}\hat{\kappa}^j \left(v_{Lp}^k - v_{np}^k \right) - \mathcal{R}v_{Lp}^i = 0 \tag{D.1}$$

with $\mathcal{R} = \eta/(\kappa\rho_n)$ that is usually referred to as "dimensionless drag parameter". Instead of assuming a specific direction for the vortex line (usually the z-axis), we follow here a different method to solve the equation of motion. We define the matrices $K_{ab} = \epsilon_{ajb}\hat{\kappa}^j$ and $R_{ab} = \delta_{ab}\mathcal{R}$; in vectorial notation the application defined by K is the usual cross product, namely $\hat{\kappa} \times \mathbf{v} = K\mathbf{v}$ and $\hat{\kappa} \times (\hat{\kappa} \times \mathbf{v}) = K^2\mathbf{v}$. The force balance can be rewritten as

$$(K_{ia} - R_{ia}) v_{Lp}^a = K_{ib}v_{np}^b \quad \Rightarrow \quad v_{Lp}^i = (K - R)_{il}^{-1} K_{lm}v_{np}^m. \tag{D.2}$$

By using the fact that $\hat{\kappa}_i\hat{\kappa}_i = 1$, it is possible to show that (the properties $K^2 = -\mathbb{1} + \hat{\kappa}\otimes\hat{\kappa}$ and $K^3 = -K$ have to be used)

$$\det(K - R) = -\mathcal{R}(1 + \mathcal{R}^2)$$
$$(K - R)^{-1} = -\mathbb{1}/\mathcal{R} - K/(1 + \mathcal{R}^2) - K^2/(\mathcal{R} + \mathcal{R}^3).$$

Therefore, the vortex velocity in Eq (D.2) can be written as

$$\mathbf{v}_{Lp} = -\left(\frac{\mathcal{R}}{1 + \mathcal{R}^2} K + \frac{1}{1 + \mathcal{R}^2} K^2 \right) \mathbf{v}_{np}. \tag{D.3}$$

In the limit of very weak drag ($\mathcal{R} \ll 1$) we have $\mathbf{v}_{Lp} \approx -K^2\mathbf{v}_{np}$: if $\hat{\kappa}$ and $\mathbf{v}_{np}$ are orthogonal this implies $\mathbf{v}_{Lp} \approx \mathbf{v}_{np}$, namely the vortex line is comoving with the superfluid component as expected from the Kelvin's theorem. On the other hand, in the limit of extremely strong drag ($\mathcal{R} \gg 1$) we have that $\mathbf{v}_{Lp} \approx \mathcal{R}^{-1} K\mathbf{v}_{np}$: the vortex tends to move in a direction orthogonal to both $\hat{\kappa}$ and $\mathbf{v}_{np}$ but with infinitesimal velocity so that it can be considered to be quasi comoving with the normal component.

Let's define $\mathbf{F}_{MF}$ to be the force exerted by the normal component on the superfluid component (and $-\mathbf{F}_{MF}$ the force exerted by the superfluid on the normal component); therefore hydrodynamical equations have the form

$$\rho_n D_t\mathbf{v}_n + ... = \mathbf{F}_{MF} + \text{``gravity''} \tag{D.4}$$
$$\rho_p D_t\mathbf{v}_p + ... = -\mathbf{F}_{MF} + \text{``gravity, viscosity, Lorentz force...''} \tag{D.5}$$

and are eventually coupled to the Poisson and the induction equations (if there is entrainment the Lorentz force is present also in the equation for the v-component). Since $\mathbf{f}_D$ is the force (per unit length) on a vortex due to the presence of the normal fluid we can conclude that $-\mathbf{F}_{MF} = -n_v\mathbf{f}_D$, where the length per unit volume n_v accounts for the presence

---

$\hat{\kappa}^i$. The straight segment of vortex line is nothing but a point with associated $\hat{\kappa}^i$, a sort of elementary spin that interacts with an external field.

of many vortices in every point of fluid at the macroscopic scale. The mutual friction is thus obtained by inserting our solution for $\mathbf{v}_{Lp}$ into $\mathbf{f}_D$ (or, equivalently, into minus the Magnus force). From the hydrodynamical point of view, the acceleration imprinted onto a superfluid particle is

$$\frac{\mathbf{F}_{MF}}{\rho_n} = \kappa\, n_v \left[\frac{\mathcal{R}^2}{1+\mathcal{R}^2}\, \hat{\kappa} \times \mathbf{v}_{np} + \frac{\mathcal{R}}{1+\mathcal{R}^2}\, \hat{\kappa} \times (\hat{\kappa} \times \mathbf{v}_{np}) \right] . \tag{D.6}$$

This notation is particularly convenient when we have to deal with a straight array of vortices that are homogeneously spaced. In this case $n_v = 2\Omega_v/\kappa$. More generally $n_v^2 = \omega_n^i \omega_n^i$ and the density of vortex lines can be regarded as a measure of the vorticity intensity (i.e. it is the number of vortex lines per unit area of a surface locally orthogonal to the bundle). Given the above interpretation of n_v, the vorticity is sometimes written as

$$\omega_n^i = m_n^{-1}\, \epsilon_{iab}\, \partial_a\, p_n^b = \kappa n_v \hat{\kappa}^i \quad \Rightarrow \quad n_v = 2|\nabla \times \mathbf{p}_n|/h . \tag{D.7}$$

This implies that the mutual friction can also be equivalently written as

$$\mathbf{F}_{MF} = \rho_n\, \mathcal{B}_c\, \boldsymbol{\omega}_n \times \mathbf{v}_{np} + \rho_n\, \mathcal{B}_d\, \hat{\omega}_n \times (\boldsymbol{\omega}_n \times \mathbf{v}_{np}) . \tag{D.8}$$

where $\hat{\omega}_n$ is just an alias for $\hat{\kappa}$, the unit vector that indicates the vorticity direction[2], while the dimensionless coefficients are defined as

$$\mathcal{B}_c = \frac{\mathcal{R}^2}{1+\mathcal{R}^2} \qquad \mathcal{B}_d = \frac{\mathcal{R}}{1+\mathcal{R}^2} . \tag{D.9}$$

This force contains two different parts: the term proportional to $\mathcal{B}_c$ originates from the Coriolis force and is conservative (it is formally not different from the magnetic part of the Lorentz force), whereas the one proportional to $\mathcal{B}_d$ is dissipative.

Let us consider the usual right-handed local cylindrical coordinates with axes $(\hat{\mathbf{e}}_x, \hat{\mathbf{e}}_\varphi, \hat{\mathbf{e}}_x)$ and assume $\hat{\kappa} = \hat{\mathbf{e}}_z$, $\mathbf{v}_{np} = x\Omega_{np}\hat{\mathbf{e}}_\varphi$. In this basic scenario of a straight array of equally-spaced vortices, we have $\kappa n_v = 2\Omega_v$; the mutual friction force and the mutual torque can be written as

$$\mathbf{F}_{MF} = -2x\rho_n\Omega_v\Omega_{np}\left(\mathcal{B}_c\hat{\mathbf{e}}_x + \mathcal{B}_d\hat{\mathbf{e}}_\varphi\right) \tag{D.10}$$

$$\mathbf{x} \times \mathbf{F}_{MF} = 2\rho_n\Omega_v\Omega_{np}\left[\mathcal{B}_d\left(xz\hat{\mathbf{e}}_x - x^2\hat{\mathbf{e}}_z\right) - \mathcal{B}_c xz\hat{\mathbf{e}}_\varphi\right] . \tag{D.11}$$

The different possibilities in the regimes of strong and weak drag are summarized in Table (D.1).

---

[2] It is important to note that the present derivation ha simple analytics thanks to the fact that we can identify the macroscopic unit vector $\hat{\omega}$ (i.e. the local direction of a vortex bundle comprised of nearly parallel vortices) with the direction of the microscopic direction $\hat{\kappa}$.

	$\mathcal{R} \ll 1$	$\mathcal{R} \gg 1$
Regime:	dissipative	quasi-conservative
$\mathcal{B}_c$	$\ll \mathcal{R}$	≈ 1
$\mathcal{B}_d$	$\approx \mathcal{R}$	$\approx \mathcal{R}^{-1}$
$\mathbf{v}_{Lp}$	$\approx x\Omega_{np}\hat{\mathbf{e}}_\varphi$	$\approx \mathcal{R}^{-1}x\Omega_{np}\hat{\mathbf{e}}_x$
$\mathbf{F}_{MF}$	$\approx -2x\rho_n\Omega_v\Omega_{np}\mathcal{R}\hat{\mathbf{e}}_\varphi$	$\approx -2x\rho_n\Omega_v\Omega_{np}\hat{\mathbf{e}}_x$

Table D.1: Summary of the various possibilities in the limits of strong and weak drag, assuming $\hat{\kappa} = \hat{\mathbf{e}}_z$, $n_v = 2\Omega_v/\kappa$ and $\mathbf{v}_{np} = x\Omega_{np}\hat{\mathbf{e}}_\varphi$. Perfect pinning corresponds to the extreme regime where a neutron current $\rho_n\mathbf{v}_{np}$ can be sustained without any dissipation. In this case vortices comove with the normal component, $\mathbf{v}_{Lp} = 0$, and the force density exerted on the normal component is directed radially outward: $-\mathbf{F}_{MF} = 2x\rho_n\Omega_v\Omega_{np}\hat{\mathbf{e}}_x$.

Bent vortex lines

The first consistent model of pulsar dynamics with non rigid-body rotation of the superfluid that accounts for the stratified structure, entrainment and pinning has been described in chapter (2), under the hypothesis of rigid and straight vortex lines. The corresponding maximum glitch amplitude is entrainment independent and vortex length independent (if vortices are longer than the vertical section in which pinning is possible), namely the integration along the z-axis is unimportant: the deep reason for this is that the cylindrical surfaces that contain vortex lines coincide with the surfaces of constant x.

This model is built on two working assumptions: the background stellar structure is that of non-rotating hydrostatic equilibrium and the configuration space of the vorticity lines is very limited, namely it consists of a foliation of straight curves γ_x in the superfluid domain (that can be a generic spherical shell). The motivation behind such a construction is the possibility that an array of quantized lines behaves like a bundle which tension is proportional to the square of the number of vortices, providing a realization of the Taylor-Proudman theorem (Ruderman and Sutherland, 1974): single vortices could therefore oscillate, bend and reconnect but the macroscopic vorticity mediated over many lines is still columnar. Identification of these curves γ_x with the microscopic vorticity is very problematic due to the argument given in Sec (2.5): vortices should have an infinite collective rigidity to resist bending induced by the non-homogeneity of the forces applied along its length.

As it stands, while the argument for the turbulent core seems robust and coherent with the accepted formulation of the HVBK equations, it is less clear whether or not vortices can remain collectively straight in the crust, where pinning could help a collective organization of the vortex array.

Since the situation is quite unclear and still debated, we saw in chapter (2) that the infinite rigidity assumption is nothing but a prescription used to project the 3D problem into a cylindrical one by accounting for stratification. Depending on the details of the mutual friction and on the extension of vortex lines it can also have something to do with reality; moreover it provides a convenient way to model the superfluid dynamics in the presence of a stratified background: it may be interesting to generalize this idea to the case of non-tangled macroscopic vorticity. Before moving to construct the model with bent lines there is the need for few more remarks.

Moment of inertia density - In the Newtonian model with straight lines we introduced the

moment of inertia density

$$I_v\, g(x) \;=\; \frac{dI_v(x)}{dx} \;=\; 4\pi\, x^3 \int_0^{z(x)} dz\; \rho_n^*\,, \qquad I_v = \int_0^{R_d} dI_v(x)$$

where $\rho_n^*(r) = \rho_n(r)/m^*(r)$ and $dI_v(x)$ it is the moment of inertia of to the thin cylindrical surfaces of constant radius x that foliate the star.

Interpretation of the pinning forces - Just remember the physical interpretation of f_p: it is not a force but a threshold for the lift force on a little segment of vortex line (Seveso et al., 2016). The procedure used to estimate this pinning force is an average over different translations and orientations of the line with respect to the lattice principal axes: this procedure is actually an average over an ensemble of mesoscopic segments of vortex lines (isotropically distributed) more than over a single vortex line that stretches over a macroscopic distance. A natural interpretation is that f_p defines a threshold for the *collective pinning*, namely the maximum strength of the hydrodynamical lift induced by the macroscopic dissipationless current over a large ensemble of pinned vortex lines.

Bent vortices- An axially symmetric and rigid configuration of macroscopic vorticity (where the curvature radius is of the same order of magnitude of the stellar radius, still a non-turbulent scenario) is a one-parameter family of curves $\gamma_x(\lambda)$ that foliate a meridional slice of the star (no toroidal vorticity is considered). Each curve, e.g. $\gamma_{x_0}(\lambda)$, represents the shape of a vortex bundle that intersects the equatorial plane at $x = x_0$. This construction reduces the dynamical problem in a significant manner, since it is now possible to use just the density of vortex lines on the equatorial plane $n_v(x) = n_v(x, z = 0)$. Vortex creep modifies the density of vortices $n_v(x)$, while vortex lines continuously rearrange their shape from γ_x to γ_{x+dx} when moving from x to $x + dx$. In the dynamical model it is useful to define $m_n\, x\, \Omega_v = p_{n\varphi}$, see Eq (2.10): when vortices are perfectly pinned, Ω_v is stationary[1]. Here we are more interested in its relation with the geometry of vortices. We are going to drop the columnar symmetry of the vortex configuration, therefore this quantity is now a function $\Omega_v(x, z)$.

E.0.1   Newtonian model: model with static curved vortices

Consider an axially symmetric velocity field $\mathbf{v}_v = \mathbf{p}_n/m_n$, namely

$$\mathbf{v}_v(\mathbf{x}) \;=\; v_x(x, z)\mathbf{e}_x(\varphi) + v_\varphi(x, z)\mathbf{e}_\varphi(\varphi) + v_z(x, z)\mathbf{e}_z\,.$$

The curl of this field gives

$$\boldsymbol{\omega}_n \;=\; -\partial_z v_\varphi \mathbf{e}_x + (\partial_z v_x - \partial_x v_z)\mathbf{e}_\varphi + \frac{1}{x}\partial_x(x v_\varphi)\mathbf{e}_z\,.$$

If we impose a fixed and spherical density background, the continuity equation (usually written for the velocity $\mathbf{v}_n$) can be written in terms of $\mathbf{v}_v$ and reads

$$\nabla \cdot (\rho_n^* \mathbf{v}_v) = 0 \quad \Rightarrow \quad \partial_x(x\, v_x) + \partial_z(x\, v_z) = -x\, v_r\, \partial_r \ln \rho_n^*\,,$$

---

[1] This is not true for Ω_n because entrainment couples the neutron superfluid to the charged constituents of the p-component that undergo a steady and slow electromagnetic spin-down.

that poses a strong additional constraint on v_x and v_z. This equation, together with the boundary conditions ($v_r = 0$ at the superfluid boundaries) limits the possible motion that involves meridional circulation. For simplicity we consider $v_r = 0$ everywhere in the domain, such that $\omega_n^\varphi = 0$ (no toroidal vorticity, implying no meridional circulation) and the continuity equation is trivially satisfied. In this case $\mathbf{v}_v = v_\varphi(x, z)\, \mathbf{e}_\varphi$ and $x\,\boldsymbol{\omega}_n = (-\mathbf{e}_x \partial_z + \mathbf{e}_z \partial_x)\,(x\,v_\varphi)$. It is convenient to introduce new coordinates: x_o and
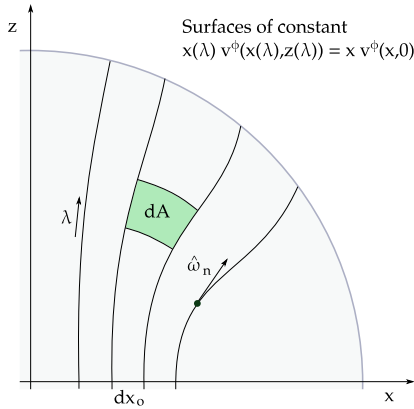
Figure E.1: Sketch of the stellar structure, with the geometrical definitions used and the vorticity surfaces: dA represents the area element in the x-z plane, while vorticity surfaces are parametrized by λ and are labeled by their intersection with the equatorial plane. In principle vorticity lines could also have a component directed along $\hat{\mathbf{e}}_\varphi$ and a non zero winding number around the z-axis. Creeping vortices moves from a vorticity surface to another one. Here vorticity extends trough the core but, as usual, it can be confined into any spherically symmetric domain, namely it is equally possible to label the surfaces using their intersection with a spherical surface rather than with their intersection with the equatorial radius.

the parameter along the vorticity lines λ. We use the notation $x(x_o, \lambda) = x_{\lambda x_o}$ and $z(x_o, \lambda) = z_{\lambda x_o}$: for fixed x_o, λ and φ identify a point on the vorticity surface that intersect the equatorial plane at $x = x_o$. This choice is convenient since the number of intersections of vortex lines with the equatorial plane must be conserved, namely

$$x_o\, \partial_t n_v(x_o, t) + \partial_{x_o}\left[x_o\, n_v(x_o, t)\, v_L^x(x_o, t)\right] = 0\,,$$

where $n_v(x_o) = \omega_z(x_o, 0)/\kappa$. When we use the non-orthogonal set of coordinates (x_o, φ, λ), we must consider that the volume form is $d^3x = dA\, d\varphi$, where

$$dA = dx\, dz\, x = dx_o\, d\lambda\, x_{\lambda x_o}\, |\partial_{x_0} x\, \partial_\lambda z - \partial_{x_0} z\, \partial_\lambda x|\,.$$

The differential $2\pi\, dA$ represents the volume of a thin torus identified by the coordinates λ and x_o, as shown in Fig (E.1). Clearly $x(\lambda, x_o)\, d\varphi$ and $d\gamma = \sqrt{(\partial_\lambda x)^2 + (\partial_\lambda z)^2}\, d\lambda$ are the azimuthal line element and the arc length along a vortex respectively. Therefore the volume element can equivalently be written as $dx^3 = d\gamma\, d\Sigma_\perp$, where the infinitesimal area element $d\Sigma_\perp$ normal to the vorticity is given by

$$d\Sigma_\perp = \frac{|\partial_{x_0} x\, \partial_\lambda z - \partial_{x_0} z\, \partial_\lambda x|}{\sqrt{(\partial_\lambda x)^2 + (\partial_\lambda z)^2}}\, x_{\lambda x_o}\, dx_o\, d\varphi\,.$$

Conservation of the number of vortex lines can be written in terms of the density of vortices on the equatorial plane $n_v(x_o)$ as

$$n_v(x_o)\, x_o\, dx_o\, d\varphi = n_v(x_{\lambda x_o}, z_{\lambda x_o})\, d\Sigma_\perp\,.$$

The macroscopic Feynman relation, Eq (2.8), is written as

$$2\pi\, x\, v_\varphi|_{(\lambda, x_o)} = \int_{\Sigma_\perp} \omega_n\, d\Sigma_\perp = 2\pi \int_0^{x_o} \omega_n(x_{\lambda y}, z_{\lambda y})\, \frac{|x_{,x_o} z_{,\lambda} - z_{,x_o} x_{,\lambda}|}{\sqrt{x_{,\lambda}^2 + z_{,\lambda}^2}}\, x_{\lambda y}\, dy$$

and turns out to be independent on λ by construction. The volume of a bundle of vortex lines that is enclosed in between of the two surfaces labeled by x_o and $x_o + dx_o$ is

$$db = d\varphi\, dx_o \int_{\gamma_{x_o}} d\lambda\, |x_{,x_o}z_{,\lambda} - z_{,x_o}x_{,\lambda}|\, x_{\lambda x_o}\,.$$

We now generalize the prescription of Pizzochero (2011) and (Haskell et al., 2013) that was used to find the critical lag profile of Eq (2.24). Instead of integrating along a single vortex line we consider a bundle of vortex lines, namely

$$db[\,n_v\,(f_p - |\mathbf{f}_M|)\,] = 0 \quad \Rightarrow \quad \int_{\gamma_{x_o}} d\lambda\, x\, |x_{,x_o}z_{,\lambda} - z_{,x_o}x_{,\lambda}|\, (f_p - |\mathbf{f}_M|)\, n_v = 0\,.$$

Note that the factor $n_v\, d\Sigma_\perp$ is the number of vortices that pass through the area element $d\Sigma_\perp$: in this way f_p is the average (local) unpinning threshold for the ensemble of vortices in the bundle, coherently with the new interpretation of the pinning force given before. We use the fact that the number of vortices is constant for every section of the bundle (namely we can replace n_v with the module of the vorticity on the equatorial plane rescaled by the opportune bundle section) and obtain

$$\int_{\gamma_{x_o}} d\lambda\, x_o\, n_v(x_o)\, \sqrt{x_{,\lambda}{}^2 + z_{,\lambda}{}^2}\, (f_p - \kappa\, \rho_n^*\, v_{vp}^\varphi) = 0 \quad \Rightarrow \quad \int_{\gamma_{x_o}} d\gamma\, (f_p - \kappa\, \rho_n^*\, v_{vp}^\varphi) = 0\,.$$

Note that we finally obtained the integrations along the single vortex line, thanks to the inclusion of the n_v factor inside the bundle integrations. It is now straightforward to obtain[2]

$$\Omega_{vp}^{cr}(x_o) = \frac{\int_{\gamma_{x_0}} d\gamma\, f_p}{x_o^2\, \kappa \int_{\gamma_{x_0}} d\gamma\, \rho_n^*\, x^{-1}} + \Omega_p \left[\frac{\int_{\gamma_{x_0}} d\gamma\, \rho_n^*\, x}{x_o^2 \int_{\gamma_{x_0}} d\gamma\, \rho_n^* x^{-1}} - \frac{x^2}{x_o^2} \right]. \tag{E.1}$$

When vortices are straight the vorticity surfaces are defined by $x_{\lambda x_o} = x_o$ and the above equation reduces to Eq (3.13). In complete generality the angular momentum reservoir can be written as

$$\Delta L[\Omega_{vp}] = \int d\Sigma_\perp d\gamma\, x^2\, \Omega_{vp}\, \rho_n^* = \int_0^{R_d} dx_o\, \Omega_{vp}(x_o)\, \frac{dI_v(x_o)}{dx_o}\,,$$

where

$$\frac{dI_v(x_o)}{dx_o} = 2\pi\, x_o^2 \int_{\gamma_{x_0}} d\lambda\, \rho_n^*\, x\, |x_{,x_o}z_{,\lambda} - z_{,x_o}x_{,\lambda}|\,, \qquad I_v = \int_0^{R_d} dI_v(x_o)\,.$$

Finally the maximum glitch amplitude turns out to be

$$\Delta\Omega_{\max} = \frac{2\pi}{I} \int_0^{R_d} dx_o\, x_o^2\, \Omega_{vp}^{cr}(x_o) \int_{\gamma_{x_o}} d\lambda\, \rho_n^*\, x\, |x_{,x_o}z_{,\lambda} - z_{,x_o}x_{,\lambda}|\,. \tag{E.2}$$

---

[2] The specific angular momentum can exit the integrals along γ_{x_o}: just remember that $x_o\, v_v^\varphi(\lambda, x_o) = x_o\, v_v^\varphi(0, x_o)$, namely (for every x_o) the specific angular momentum is constant along the vorticity surface that is parallel to γ_{x_o}. Equivalently, $x_{\lambda x_o}\, v_v^\varphi(x_{\lambda x_o}, z_{\lambda x_o}) = x_{0x_o}\, v_v^\varphi(x_{0x_o}, z_{0x_o})$ or $x_o\, \Omega_{vp}^{cr}(x_o) = x_{\lambda x_o}\, \Omega_{vp}^{cr}(x_{\lambda x_o}, z_{\lambda x_o})\,.$

Bibliography

Aguilera D.N., Pons J.A., Miralles J.A. "2D Cooling of magnetized neutron stars". *Astronomy and Astrophysics* **486**: 255 (2008).

Akbal O., Alpar M.A., Buchner S., Pines D. "Nonlinear interglitch dynamics, the braking index of the Vela pulsar and the time to the next glitch". *MNRAS* **469**: 4183 (2017).

Alpar M.A. "Pinning and Threading of Quantized Vortices in the Pulsar Crust Superfluid". *Astrophys. J.* **213**: 527 (1977).

Alpar M.A., Anderson P.W., Pines D., Shaham J. "Vortex creep and the internal temperature of neutron stars. I. General theory". *Astrophys. J.* **276** (1984).

Alpar M.A., Anderson P.W., Pines D., Shaham J. "Vortex creep and the internal temperature of neutron stars. ii - vela pulsar". *ApJ* **278**: 791 (1984).

Alpar M.A., Baykal A. "Pulsar braking indices, glitches and energy dissipation in neutron stars". *MNRAS* **372**: 489 (2006).

Alpar M.A., Çalışkan Ş., Ertan Ü. "Fallback Disks, Magnetars and Other Neutron Stars". In C.M. Zhang, T. Belloni, M. Méndez, S.N. Zhang, editors, "Feeding Compact Objects: Accretion on All Scales", volume 290 of *IAU Symposium* pages 93–100. (2013).

Alpar M.A., Chau H.F., Cheng K.S., Pines D. "Postglitch relaxation of the Crab pulsar: Evidence for crust cracking". *ApJ, Letters* **427**: L29 (1994).

Alpar M.A., Chau H.F., Cheng K.S., Pines D. "Postglitch Relaxation of the Crab Pulsar after Its First Four Major Glitches: The Combined Effects of Crust Cracking, Formation of Vortex Depletion Region and Vortex Creep". *Astrophys. J.* **459**: 706 (1996).

Alpar M.A., Cheng K.S., Pines D. "Vortex creep and the internal temperature of neutron stars - Linear and nonlinear response to a glitch". *ApJ* **346**: 823 (1989).

Alpar M.A., Langer S.A., Sauls J.A. "Rapid postglitch spin-up of the superfluid core in pulsars". *ApJ* **282**: 533 (1984).

Alpar M.A., Sauls J.A. "On the dynamical coupling between the superfluid interior and the crust of a neutron star". *ApJ* **327**: 723 (1988).

Anderson P.W. "Theory of flux creep in hard superconductors". *Phys. Rev. Lett.* **9**: 309 (1962).

Anderson P.W. "Considerations on the Flow of Superfluid Helium". *Reviews of Modern Physics* **38**: 298 (1966).

Anderson P.W., Alpar M.A., Pines D., Shaham J. "The rheology of neutron stars. Vortex-line pinning in the crust superfluid". *Philos. Mag. A* **45**: 227 (1982).

Anderson P.W., Itoh N. "Pulsar glitches and restlessness as a hard superfluidity phenomenon". *Nature* **256**: 25 (1975).

Andersson N., Comer G.L. "On the dynamics of superfluid neutron star cores". *MNRAS* **328**: 1129 (2001).

Andersson N., Comer G.L. "Slowly rotating general relativistic superfluid neutron stars". *Classical and Quantum Gravity* **18**: 969 (2001).

Andersson N., Comer G.L. "A flux-conservative formalism for convective and dissipative multi-fluid systems, with application to Newtonian superfluid neutron stars". *Class. Quantum Gravity* **23**: 5505 (2006).

Andersson N., Comer G.L. "Relativistic fluid dynamics: Physics for many different scales". *Living Reviews in Relativity* **10**: 1 (2007).

Andersson N., Glampedakis K., Ho W.C.G., Espinoza C.M. "Direct observation of the cooling of the cassiopeia a neutron star". *Astrophys. J. Lett.* **719** (2010).

Andersson N., Glampedakis K., Ho W.C.G., Espinoza C.M. "Pulsar glitches: The crust is not enough". *Physical Review Letters* **109**: 241103 (2012).

Andersson N., Sidery T., Comer G.L. "Mutual friction in superfluid neutron stars". *Monthly Notices of the Royal Astronomical Society* **368**: 162 (2006).

Andersson N., Sidery T., Comer G.L. "Superfluid neutron star turbulence". *Monthly Notices of the Royal Astronomical Society* **381**: 747 (2007).

Andersson N., Wells S., Vickers J.A. "Quantised vortices and mutual friction in relativistic superfluids". *Classical and Quantum Gravity* **33**: 245010 (2016).

Andreev A.F., Bashkin E.P. "Three-velocity hydrodynamics of superfluid solutions". *Zh. Eksp. Teor. Fiz* **69**: 319 (1975).

Antonelli M., Montoli A., Pizzochero P.M. "Effects of general relativity on glitch amplitudes and pulsar mass upper bounds". *Submitted to MNRAS* (2017).

Antonelli M., Pizzochero P.M. "Axially symmetric equations for differential pulsar rotation with superfluid entrainment". *Mon. Not. R. Astron. Soc.* **464**: 721 (2017).

Antonelli M., Pizzochero P.M. "Pulsar rotation with superfluid entrainment". *Journal of Physics: Conference Series* **861**: 012024 (2017).

Antoniadis J., Freire P.C.C., Wex N., Tauris T.M., Lynch R.S., van Kerkwijk M.H., Kramer M., Bassa C., Dhillon V.S., Driebe T., Hessels J.W.T., Kaspi V.M., Kondratiev V.I., Langer N., Marsh T.R., McLaughlin M.A., Pennucci T.T., Ransom S.M., Stairs I.H., van Leeuwen J., Verbiest J.P.W., Whelan D.G. "A Massive Pulsar in a Compact Relativistic Binary". *Science* **340**: 448 (2013).

Archibald R.F., Kaspi V.M., Ng C.Y., Gourgouliatos K.N., Tsang D., Scholz P., Beardmore A.P., Gehrels N., Kennea J.A. "An Anti-Glitch in a Magnetar". *Nature* **497**: 591 (2013).

Ashton G., Jones D.I., Prix R. "Comparing models of the periodic variations in spin-down and beamwidth for psr b1828-11". *Monthly Notices of the Royal Astronomical Society* **458**: 881 (2016).

Ashton G., Prix R., Jones D.I. "Statistical characterization of pulsar glitches and their potential impact on searches for continuous gravitational waves". *Physical Review D* **96**: 063004 (2017).

Baade W., Zwicky F. "Cosmic Rays from Super-novae". *Proceedings of the National Academy of Science* **20**: 259 (1934).

Backer D.C., Kulkarni S.R., Heiles C., Davis M.M., Goss W.M. "A millisecond pulsar". *Nature* **300**: 615 (1982).

Baldo M., Burgio G.F., Schulze H.J. "Neutron star structure with hyperons and quarks". In "Superdense QCD matter and compact stars. Proceedings, NATO Advanced Research Workshop, Erevan", pages 113–134. (2003).

Barenghi C.F., Donnelly R.J., Vinen W.F., editors. *Quantized Vortex Dynamics and Superfluid Turbulence* volume 571 of *Lecture Notes in Physics*. Springer Berlin Heidelberg, Berlin, Heidelberg (2001).

Barenghi C.F., Jones C.A. "The stability of the couette flow of helium ii". *Journal of Fluid Mechanics* **197**: 551–569 (1988).

Barenghi C.F., Parker N.G. "A primer on quantum fluids". *ArXiv e-prints* (2016).

Baym G., Chandler E. "The hydrodynamics of rotating superfluids. i. zero-temperature, nondissipative theory". *Journal of Low Temperature Physics* **50**: 57 (1983).

Baym G., Pethick C., Sutherland P. "The Ground State of Matter at High Densities: Equation of State and Stellar Models". *ApJ* **170**: 299 (1971).

Baym G., Pethick C.J., Pines D. "Superfluidity in neutron stars". *Nature* **224**: 673 (1970).

Baym G., Pethick C.J., Pines D., Ruderman M. "Spin Up in Neutron Stars : The Future of the Vela Pulsar". *Nature* **224**: 872 (1969).

Bean C.P. "Magnetization of Hard Superconductors". *Phys. Rev. Lett.* **8**: 250 (1962).

Bekarevich I.L., Khalatnikov I.M. "Phenomenological Derivation of the Equations of Vortex Motion in He II". *Soviet Physics JETP* **13**: 643 (1961).

Beskin V.S., Balogh A., Falanga M., Treumann R.A. *Magnetic Fields at Largest Universal Strengths: Overview* pages 3–14. Springer New York, New York, NY (2016). ISBN 978-1-4939-3550-5.

Bethe H.A., Wilson J.R. "Revival of a stalled supernova shock by neutrino heating". *ApJ* **295**: 14 (1985).

Bildsten L. "Gravitational Radiation and Rotation of Accreting Neutron Stars". *Astrophysical Journal, Letters* **501**: L89 (1998).

Bildsten L., Epstein R. "Superfluid dissipation time scales in neutron star crusts". *Astrophysical Journal* **342**: 951 (1989).

Burgay M., D'Amico N., Possenti A., Manchester R.N., Lyne A.G., Joshi B.C., McLaughlin M.A., Kramer M., Sarkissian J.M., Camilo F., Kalogera V., Kim C., Lorimer D.R. "An increased estimate of the merger rate of double neutron stars from observations of a highly relativistic system". *Nature* **426**: 531 (2003).

Burrows A., Lattimer J.M. "Neutrinos from SN 1987A". *Astrophysical Journal, Letters* **318**: L63 (1987).

Cameron A.G. "Neutron Star Models." *Astrophysical Journal* **130**: 884 (1959).

Cameron A.G., Greenstein G. "Spin down effects in neutron stars". **222** (1969).

Campbell A., Evetts J. "Flux vortices and transport currents in type ii superconductors". *Advances in Physics* **21**: 199 (1972).

Carter B. *Covariant theory of conductivity in ideal fluid or solid media* pages 1–64. Springer Berlin Heidelberg, Berlin, Heidelberg (1989). ISBN 978-3-540-48142-3.

Carter B., Chamel N., Haensel P. "Entrainment coefficient and effective mass for conduction neutrons in neutron star crust: simple microscopic models". *Nuclear Physics A* **748**: 675 (2005).

Carter B., Chamel N., Haensel P. "Entrainment coefficient and effective mass for conduction neutrons in neutron star crust: macroscopic treatment". *Int. J. Mod. Phys. D* **15**: 777 (2006).

Carter B., Langlois D. "Equation of state for cool relativistic two-constituent superfluid dynamics". *Phys. Rev. D* **51**: 5855 (1995).

Chadwick J. "The existence of a neutron". *Proceedings of the Royal Society of London A: Mathematical, Physical and Engineering Sciences* **136**: 692 (1932).

Chadwick J. "Possible Existence of a Neutron". *Nature* **129**: 312 (1932).

Chamel N. "Effective mass of free neutrons in neutron star crust". *Nuclear Physics A* **773**: 263 (2006).

Chamel N. "Neutron conduction in the inner crust of a neutron star in the framework of the band theory of solids". *Physical Review C - Nuclear Physics* **85**: 035801 (2012).

Chamel N. "Crustal Entrainment and Pulsar Glitches". *Phys. Rev. Lett.* **110**: 011101 (2013).

Chamel N. "Constraint on the internal structure of a neutron star from Vela pulsar glitches". *PoS* **MPCS2015**: 013 (2016).

Chamel N. "Superfluidity and Superconductivity in Neutron Stars". *Journal of Astrophysics and Astronomy* **38**: 43 (2017).

Chamel N., Haensel P. "Entrainment parameters in a cold superfluid neutron star core". *Phys. Rev. C* **73**: 045802 (2006).

Chamel N., Haensel P. "Physics of neutron star crusts". *Living Reviews in Relativity* **11**: 10 (2008).

Chandrasekhar S. "On stars, their evolution and their stability". *Rev. Mod. Phys.* **56**: 137 (1984).

Chatterjee P., Hernquist L., Narayan R. "An Accretion Model for Anomalous X-Ray Pulsars". *ApJ* **534**: 373 (2000).

Chen K., Ruderman M. "Pulsar death lines and death valley". *ApJ* **402**: 264 (1993).

Chiu H.Y., Salpeter E.E. "Surface x-ray emission from neutron stars". *Phys. Rev. Lett.* **12**: 413 (1964).

Coddington I., Engels P., Schweikhard V., Cornell E.A. "Observation of tkachenko oscillations in rapidly rotating bose-einstein condensates". *Phys. Rev. Lett.* **91**: 100402 (2003).

Cognard I., Backer D.C. "A Microglitch in the Millisecond Pulsar PSR B1821-24 in M28". *Astrophys. J.l* **612**: L125 (2004).

Comella J.M., Craft H.D., Lovelace R.V.E., Sutton J.M. "Crab Nebula Pulsar NP 0532". *Nature* **221**: 453 (1969).

Comer G.L., Langlois D. "Hamiltonian formulation for relativistic superfluids". *Classical and Quantum Gravity* **11**: 709 (1994).

Crawford F., Demiański M. "A Comparison of Measured Crab and Vela Glitch Healing Parameters with Predictions of Neutron Star Models". *ApJ* **595**: 1052 (2003).

Cutler C. "Gravitational waves from neutron stars with large toroidal B fields". *Physical Review D* **66**: 084025 (2002).

Datta B., Alpar M.A. "Implications of the Crustal Moment of Inertia for Neutron Star Equations of State". *Astronomy and Astrophysics* **275**: 210 (1993).

Delsate T., Chamel N., Gürlebeck N., Fantina A.F., Pearson J.M., Ducoin C. "Giant pulsar glitches and the inertia of neutron star crusts". *Physical Review D* **94**: 023008 (2016).

Demorest P.B., Pennucci T., Ransom S.M., Roberts M.S.E., Hessels J.W.T. "A two-solar-mass neutron star measured using Shapiro delay." *Nature* **467**: 1081 (2010).

Dodson R., Deshpande A., Lewis D., McCulloch P. "Pulsar glitch substructure and pulsar interiors". (2009).

Dodson R., Lewis D., McCulloch P. "Two decades of pulsar timing of Vela". *Astrophysics and Space Science* **308**: 585 (2007).

Dodson R.G., McCulloch P.M., Lewis D.R. "High Time Resolution Observations of the January 2000 Glitch in the Vela Pulsar". *ApJ, Letters* **564**: L85 (2002).

Donati P., Pizzochero P.M. "Fully consistent semi-classical treatment of vortex-nucleus interaction in rotating neutron stars". *Nuclear Physics A* **742**: 363 (2004).

Donati P., Pizzochero P.M. "Realistic energies for vortex pinning in intermediate-density neutron star matter". *Physics Letters, Section B: Nuclear, Elementary Particle and High-Energy Physics* **640**: 74 (2006).

Douchin F., Haensel P. "A unified equation of state of dense matter and neutron star structure". *Astron. Astrophys.* **380**: 151 (2001).

Dubner G., Castelletti G., Kargaltsev O., Pavlov G.G., Bietenholz M., Talavera A. "Morphological Properties of the Crab Nebula: A Detailed Multiwavelength Study Based on New VLA, HST, Chandra, and XMM-Newton Images". *Astrophysical Journal* **840**: 82 (2017).

Durant M., Kargaltsev O., Pavlov G.G., Kropotina J., Levenfish K. "The Helical Jet of the Vela Pulsar". *Astrophysical Journal* **763**: 72 (2013).

Easson I. "Postglitch behavior of the plasma inside neutron stars". *The Astrophysical Journal* **228**: 257 (1979).

Elshamouty K.G., Heinke C.O., Sivakoff G.R., Ho W.C.G., Shternin P.S., Yakovlev D.G., Patnaude D.J., David L. "Measuring the cooling of the neutron star in Cassiopeia A with all Chandra X-ray observatory detectors". *Astrophys. J.* **777**: 22 (2013).

Epstein R.I., Baym G. "Vortex drag and the spin-up time scale for pulsar glitches". *Astrophys. J.* **387**: 276 (1992).

Espinoza C.M., Antonopoulou D., Stappers B.W., Watts A., Lyne A.G. "Neutron star glitches have a substantial minimum size". *MNRAS* **440**: 2755 (2014).

Espinoza C.M., Lyne A.G., Stappers B.W., Kramer M. "A study of 315 glitches in the rotation of 102 pulsars". *Mon. Not. R. Astron. Soc.* **414**: 1679 (2011).

Fantina A.F., Chamel N., Pearson J.M., Goriely S. "Neutron star properties with unified equations of state of dense matter". *Astron. Astrophys.* **559**: A128 (2013).

Fetter A.L. "Ruderman's Theory of Vortex-Lattice Vibrations in Pulsars". *Nature* **227**: 584 (1970).

Finne A.P., Eltsov V.B., Hänninen R., Kopnin N.B., Kopu J., Krusius M., Tsubota M., Volovik G.E. "Dynamics of vortices and interfaces in superfluid ^{3}He". *Reports on Progress in Physics* **69**: 3157 (2006).

Friedman J.L. "How fast can pulsars spin?" In N. Ashby, D.F. Bartlett, W. Wyss, editors, "General Relativity and Gravitation, 1989", page 21. (1990).

Friedman J.L. "Classical general relativity - rapidly rotating relativistic stars". *Philosophical*

Transactions of the Royal Society of London A **340**: 391 (1992).

Friedman J.L., Stergioulas N. *Rotating Relativistic Stars.* (2013).

Fuentes J.R., Espinoza C.M., Reisenegger A., Stappers B.W., Shaw B., Lyne A.G. "The glitch activity of neutron stars". *ArXiv e-prints* (2017).

Geller M.R., Wexler C., Thouless D.J. "Transverse force on a quantized vortex in a superconductor". *Physical Review B* **57**: R8119 (1998).

Giacconi R., Gursky H., Paolini F.R., Rossi B.B. "Evidence for x rays from sources outside the solar system". *Phys. Rev. Lett.* **9**: 439 (1962).

Glampedakis K., Andersson N. "Hydrodynamical trigger mechanism for pulsar glitches". *Physical Review Letters* **102**: 141101 (2009).

Glampedakis K., Andersson N., Samuelsson L. "Magnetohydrodynamics of superfluid and superconducting neutron star cores". *MNRAS* **410**: 805 (2011).

Glendenning N. *Compact Stars: Nuclear Physics, Particle Physics and General Relativity.* Springer, New York 2nd edition (2000).

Glendenning N.K., Moszkowski S.A. "Reconciliation of neutron-star masses and binding of the in hypernuclei". *Physical Review Letters* **67**: 2414 (1991).

Gold T. "Rotating Neutron Stars as the Origin of the Pulsating Radio Sources". *Nature* **218**: 731 (1968).

Goriely S., Chamel N., Pearson J.M. "Further explorations of Skyrme-Hartree-Fock-Bogoliubov mass formulas. XII. Stiffness and stability of neutron-star matter". *Phys. Rev. C* **82**: 035804 (2010).

Gorter C., Mellink J. "On the irreversible processes in liquid helium ii". *Physica* **15**: 285 (1949).

Gourgoulhon E. "An introduction to relativistic hydrodynamics". In M. Rieutord, B. Dubrulle, editors, "EAS Publications Series", volume 21 of *EAS Publications Series* pages 43–79. (2006).

Gourgoulhon E. "An introduction to the theory of rotating relativistic stars". *ArXiv e-prints* (2010).

Greenstein G. "Superfluid Turbulence in Neutron Stars". *nat* **227**: 791 (1970).

Greenstein G. "Superfluidity in neutron stars. I - Steady-state hydrodynamics and frictional

heating". *Astrophysical Journal* **200**: 281 (1975).

Greenstein G. "Thermal-timing instability in neutron stars". *Nature* **277**: 521 (1979).

Greenstein G. "Glitches, timing noise, and pulsar thermometry". In W. Sieber, R. Wielebinski, editors, "Pulsars: 13 Years of Research on Neutron Stars", volume 95 of *IAU Symposium* pages 291–297. (1981).

Gügercinoglu E., Alpar M.A. "Vortex creep against toroidal flux lines, crustal entrainment, and pulsar glitches". *Astrophys. J.* **788**: L11 (2014).

Haensel P., Potekhin A.Y., Yakovlev D.G. *Neutron stars 1: Equation of state and structure* volume 326. Springer, New York, USA (2007).

Hall H.E., Vinen W.F. "The Rotation of Liquid Helium II. I. Experiments on the Propagation of Second Sound in Uniformly Rotating Helium II". *Proceedings of the Royal Society A: Mathematical, Physical and Engineering Sciences* **238**: 204 (1956).

Harding A.K. "The neutron star zoo". *Frontiers of Physics* **8**: 679 (2013).

Hartle J., Sharp D. "Variational principle for the equilibrium of a relativistic, rotating star". *Astrophys. J.* **147**: 317 (1967).

Hartle J.B. "Slowly Rotating Relativistic Stars. I. Equations of Structure". *Astrophys. J.* **150**: 1005 (1967).

Haskell B. "Tkachenko modes in rotating neutron stars: The effect of compressibility and implications for pulsar timing noise". *Phys. Rev. D* **83**: 043006 (2011).

Haskell B. "The effect of superfluid hydrodynamics on pulsar glitch sizes and waiting times". *MNRAS, Letters* **461**: L77 (2016).

Haskell B., Antonopoulou D. "Glitch recoveries in radio-pulsars and magnetars". *MNRAS* **438**: L16 (2014).

Haskell B., Melatos A. "Models of pulsar glitches". *International Journal of Modern Physics D* **24**: 1530008 (2015).

Haskell B., Melatos A. "Pinned vortex hopping in a neutron star crust". *Mon. Not. Roy. Astron. Soc.* **461**: 2200 (2016).

Haskell B., Pizzochero P.M., Seveso S. "Investigating Superconductivity in Neutron Star Interiors With Glitch Models". *The Astrophysical Journal* **764**: L25 (2013).

Haskell B., Sedrakian A. "Superfluidity and Superconductivity in Neutron Stars". *ArXiv*

e-prints (2017).

Heinke C.O., Ho W.C.G. "Direct Observation of the Cooling of the Cassiopeia A Neutron Star". *ApJ, Letters* **719**: L167 (2010).

Hessels J.W.T., Ransom S.M., Stairs I.H., Freire P.C.C., Kaspi V.M., Camilo F. "A Radio Pulsar Spinning at 716 Hz". *Science* **311**: 1901 (2006).

Hewish A., Bell S.J., Pilkington J.D.H., Scott P.F., Collins R.A. "Observation of a Rapidly Pulsating Radio Source". *Nature* **217**: 709 (1968).

Ho W.C.G. "Magnetic field growth in young glitching pulsars with a braking index". *Mon. Not. Roy. Astron. Soc.* **452**: 845 (2015).

Ho W.C.G., Espinoza C.M., Antonopoulou D., Andersson N. "Pinning down the superfluid and measuring masses using pulsar glitches." *Science advances* **1**: e1500578 (2015).

Hobbs G., Coles W., Manchester R.N., Keith M.J., Shannon R.M., Chen D., Bailes M., Bhat N.D.R., Burke-Spolaor S., Champion D., Chaudhary A., Hotan A., Khoo J., Kocz J., Levin Y., Oslowski S., Preisig B., Ravi V., Reynolds J.E., Sarkissian J., van Straten W., Verbiest J.P.W., Yardley D., You X.P. "Development of a pulsar-based time-scale". *Monthly Notices of the Royal Astronomical Society* **427**: 2780 (2012).

Hobbs G., Lyne A.G., Kramer M. "An analysis of the timing irregularities for 366 pulsars". *Monthly Notices of the Royal Astronomical Society* **402**: 1027 (2010).

Hollerbach R. "Instabilities of Taylor columns in a rotating stratified fluid". *Physics Letters A* **373**: 3775 (2009).

Horowitz C.J., Berry D.K., Briggs C.M., Caplan M.E., Cumming A., Schneider A.S. "Disordered nuclear pasta, magnetic field decay, and crust cooling in neutron stars". *Phys. Rev. Lett.* **114**: 031102 (2015).

Howitt G., Haskell B., Melatos A. "Hydrodynamic simulations of pulsar glitch recovery". *Monthly Notices of the Royal Astronomical Society* **460**: 1201 (2016).

Hulse R.A., Taylor J.H. "Discovery of a pulsar in a binary system". *apjl* **195**: L51 (1975).

Huse D.A., Fisher M.P.A., Fisher D.S. "Are superconductors really superconducting?" *Nature* **358**: 553 (1992).

Itoh N. "Hydrostatic equilibrium of hypothetical quark stars". *Progress of Theoretical Physics* **44**: 291 (1970).

Jackson J.D. *Classical Electrodynamics.* John Wiley & Sons, Inc., New Jersey, USA 3

edition (1991).

Jahan-Miri M. "The Spin-down Rate of a Pinned Superfluid". *ApJ* **650**: 326 (2006).

Jones P.B. "Rotation of the neutron-drip superfluid in pulsars: the resistive force". *Mon. Not. R. Astron. Soc.* **243**: 257 (1990).

Jones P.B. "Rotation of the neutron-drip superfluid in pulsars: the Kelvin phonon contribution to dissipation". *Mon. Not. R. Astron. Soc.* **257**: 501 (1992).

Kantor E.M., Gusakov M.E. "Anti-glitches within the standard scenario of pulsar glitches". *Astrophys. J.* **797**: L4 (2014).

Kiziltan B., Kottas A., De Yoreo M., Thorsett S.E. "The Neutron Star Mass Distribution". *Astrophys. J.* **778**: 66 (2013).

Kobyakov D., Pethick C.J. "Towards a Metallurgy of Neutron Star Crusts". *Physical Review Letters* **112**: 112504 (2014).

Kramer M., Stairs I.H., Manchester R.N., McLaughlin M.A., Lyne A.G., Ferdman R.D., Burgay M., Lorimer D.R., Possenti A., D'Amico N., Sarkissian J.M., Hobbs G.B., Reynolds J.E., Freire P.C.C., Camilo F. "Tests of General Relativity from Timing the Double Pulsar". *Science* **314**: 97 (2006).

Lai D. *Physics in Very Strong Magnetic Fields* pages 15–27. Springer New York, New York, NY (2016). ISBN 978-1-4939-3550-5.

Landau L.D., Lifshitz E.M. *The classical theory of fields.* (1975).

Landau (1932). "On the theory of stars". In D. ter Haar, editor, "Collected Papers of L.D. Landau", pages 60 – 62. Pergamon (1965). ISBN 978-0-08-010586-4.

Langlois D., Sedrakian D.M., Carter B. "Differential rotation of relativistic superfluid in neutron stars". *Mon. Not. R. Astron. Soc.* **297**: 1189 (1998).

Large M.I., Vaughan A.E., Mills B.Y. "A Pulsar Supernova Association?" *Nature* **220**: 340 (1968).

Lattimer J.M., Prakash M. "Neutron star observations: Prognosis for equation of state constraints". *Physics Reports* **442**: 109 (2007). The Hans Bethe Centennial Volume 1906-2006.

Lattimer J.M., Steiner A.W. "Neutron Star Masses and Radii from Quiescent Low-mass X-Ray Binaries". *ApJ* **784**: 123 (2014).

Lieb E.H., Yau H.T. "A rigorous examination of the Chandrasekhar theory of stellar collapse". *The Astrophysical Journal* **323**: 140 (1987).

Link B. "Dynamics of Quantum Vorticity in a Random Potential". *Phys. Rev. Lett.* **102**: 131101 (2009).

Link B. "Thermally Activated Post-glitch Response of the Neutron Star Inner Crust and Core. I. Theory". *The Astrophysical Journal* **789**: 141 (2014).

Link B., Epstein R.I. "Thermally Driven Neutron Star Glitches". *ApJ* **457**: 844 (1996).

Link B., Epstein R.I., Baym G. "Superfluid vortex creep and rotational dynamics of neutron stars". *ApJ* **403**: 285 (1993).

Link B., Epstein R.I., Lattimer J.M. "Pulsar Constraints on Neutron Star Structure and Equation of State". *Physical Review Letters* **83**: 5 (1999).

Link B.K., Epstein R.I. "Mechanics and energetics of vortex unpinning in neutron stars". *Astrophys. J.* **373**: 592 (1991).

Lorimer D.R., Kramer M. *Handbook of Pulsar Astronomy.* (2004).

Lyne A., Hobbs G., Kramer M., Stairs I., Stappers B. "Switched Magnetospheric Regulation of Pulsar Spin-Down". *Science* **329**: 408 (2010).

Lyne A.G., Shemar S.L., Smith F.G. "Statistical studies of pulsar glitches". *MNRAS* **315**: 534 (2000).

Manchester R.N. "Pulsars and gravity". *International Journal of Modern Physics D* **24**: 1530018 (2015).

McCulloch P.M., Hamilton P.A., McConnell D., King E.A. "The VELA glitch of Christmas 1988". *Nature* **346**: 822 (1990).

McKee J.W., Janssen G.H., Stappers B.W., Lyne A.G., Caballero R.N., Lentati L., Desvignes G., Jessner A., Jordan C.A., Karuppusamy R., Kramer M., Cognard I., Champion D.J., Graikou E., Lazarus P., Osłowski S., Perrodin D., Shaifullah G., Tiburzi C., Verbiest J.P.W. "A glitch in the millisecond pulsar J0613-0200". *Mon. Not. R. Astron. Soc.* **461**: 2809 (2016).

Meierovic A.E. "Dynamics of superfluid ^{3}He in ^{3}He-^{4}He solutions". *Zh. Eksp. Teor. Fiz* **87**: 1293 (1984).

Melatos A., Link B. "Pulsar timing noise from superfluid turbulence". *MNRAS* **437**: 21 (2014).

Melatos A., Peralta C. "Superfluid Turbulence and Pulsar Glitch Statistics". *Astrophysical Journal, Letters* **662**: L99 (2007).

Melatos A., Peralta C., Wyithe J.S.B. "Avalanche Dynamics of Radio Pulsar Glitches". **5**: 1103 (2008).

Mendell G. "Superfluid hydrodynamics in rotating neutron stars. I - Nondissipative equations. II - Dissipative effects". *Astrophys. J.* **380**: 515 (1991).

Mereghetti S. "The strongest cosmic magnets: soft gamma-ray repeaters and anomalous X-ray pulsars". *Astronomy and Astrophysics Reviews* **15**: 225 (2008).

Mestel L. "On the theory of white dwarf stars: I. the energy sources of white dwarfs". *Monthly Notices of the Royal Astronomical Society* **112**: 583 (1952).

Migdal A. "Superfluidity and the moments of inertia of nuclei". *Nucl. Phys.* **13**: 655 (1959).

Mignani R.P., Testa V., González Caniulef D., Taverna R., Turolla R., Zane S., Wu K. "Evidence for vacuum birefringence from the first optical-polarimetry measurement of the isolated neutron star RX J1856.5-3754". *MNRAS* **465**: 492 (2017).

Mints R.G., Papiashvili I. "Flux creep in type-II superconductors: The self-organized criticality approach". *Phys. Rev. B* **71**: 174509 (2005).

Misner C.W., Thorne K.S., Wheeler J.A. *Gravitation.* (1973).

Müller B. "The Core-Collapse Supernova Explosion Mechanism". In J.J. Eldridge, J.C. Bray, L.A.S. McClelland, L. Xiao, editors, "The Lives and Death-Throes of Massive Stars", volume 329 of *IAU Symposium* pages 17–24. (2017).

Newton W.G. "Neutron stars: A taste of pasta?" *Nature Physics* **9**: 396 (2013).

Newton W.G., Berger S., Haskell B. "Observational constraints on neutron star crust-core coupling during glitches". *Mon. Not. R. Astron. Soc.* **454**: 4400 (2015).

Noronha J., Sedrakian A. "Tkachenko modes as sources of quasiperiodic pulsar spin variations". *Physical Review D* **77**: 023008 (2008).

Nozières P., Vinen W.F. "The motion of flux lines in type II superconductors". *Philosophical Magazine* **14**: 667 (1966).

O'Connor E., Ott C.D. "Black Hole Formation in Failing Core-Collapse Supernovae". *ApJ* **730**: 70 (2011).

Oppenheimer J.R., Volkoff G.M. "On massive neutron cores". *Phys. Rev.* **55**: 374 (1939).

Özel F., Freire P. "Masses, Radii, and the Equation of State of Neutron Stars". *Annual Reviews of Astronomy and Astrophysics* **54**: 401 (2016).

Pacini F. "Energy emission from a neutron star". *Nature* **216**: 567 (1967).

Page D., Geppert U., Weber F. "The cooling of compact stars". *Nuclear Physics A* **777**: 497 (2006).

Page D., Lattimer J.M., Prakash M., Steiner A.W. "Stellar Superfluids". (2013).

Papitto A., Torres D.F., Rea N., Tauris T.M. "Spin frequency distributions of binary millisecond pulsars". *A&A* **566**: A64 (2014).

Peralta C., Melatos A., Giacobello M., Ooi A. "Transitions between Turbulent and Laminar Superfluid Vorticity States in the Outer Core of a Neutron Star". *Astrophys. J.* **651**: 1079 (2006).

Piekarewicz J., Fattoyev F.J., Horowitz C.J. "Pulsar glitches: The crust may be enough". *Physical Review C* **90**: 015803 (2014).

Piran T., Shaviv N.J. "Origin of the binary pulsar j0737-3039b". *Phys. Rev. Lett.* **94**: 051102 (2005).

Pizzochero P.M. "Angular Momentum Transfer in Vela-Like Pulsar Glitches". *Astrophys. J.* **743**: L20 (2011).

Pizzochero P.M., Antonelli M., Haskell B., Seveso S. "Constraints on pulsar masses from the maximum observed glitch". *Nature Astronomy* **1**: 0134 (2017).

Pons J.A., Viganò D., Rea N. "A highly resistive layer within the crust of X-ray pulsars limits their spin periods". *Nature Physics* **9**: 431 (2013).

Posselt B., Pavlov G.G., Suleimanov V., Kargaltsev O. "New Constraints on the Cooling of the Central Compact Object in Cas A". *ApJ* **779**: 186 (2013).

Prix R. "Covariant vortex in superconducting-superfluid-normal fluid mixtures with a stiff equation of state". *Phys. Rev, D* **62**: 103005 (2000).

Prix R. "Variational description of multifluid hydrodynamics: Uncharged fluids". *Phys. Rev. D* **69** (2004).

Prix R., Comer G.L., Andersson N. "Slowly rotating superfluid Newtonian neutron star model with entrainment". *Astronomy and Astrophysics* **381**: 178 (2002).

Ravenhall D.G., Pethick C.J. "Neutron star moments of inertia". *Astrophys. J.* **424**: 846

(1994).

Rezzolla L., Zanotti O. *Relativistic Hydrodynamics*. (2013).

Ruderman M. "Neutron Starquakes and Pulsar Periods". *Nature* **223**: 597 (1969).

Ruderman M. "Long Period Oscillations in Rotating Neutron Stars". *Nature* **225**: 619 (1970).

Ruderman M., Zhu T., Chen K. "Neutron Star Magnetic Field Evolution, Crust Movement, and Glitches". *Astrophys. J.* **492**: 267 (1998).

Ruderman M.A. "Crust-breaking by neutron superfluids and the VELA pulsar glitches". *The Astrophysical Journal* **203**: 213 (1976).

Ruderman M.A., Sutherland P.G. "Rotating superfluid in neutron stars". *The Astrophysical Journal* **190**: 137 (1974).

Schwarz K.W. "Three-dimensional vortex dynamics in superfluid ^{4}He: Homogeneous superfluid turbulence". *Phys. Rev. B* **38**: 2398 (1988).

Serim M.M., Şahiner Ş., ćerri-Serim D., Inam S.ć., Baykal A. "Discovery of a glitch in the accretion-powered pulsar SXP 1062". *MNRAS* **471**: 4982 (2017).

Seveso S. *Advances in models of Pulsar Glitches*. Ph.d. thesis Università degli studi di Milano (2015).

Seveso S., Pizzochero P.M., Grill F., Haskell B. "Mesoscopic pinning forces in neutron star crusts". *Mon. Not. R. Astron. Soc.* **455**: 3952 (2016).

Seveso S., Pizzochero P.M., Haskell B. "The effect of realistic equations of state and general relativity on the "snowplough" model for pulsar glitches". *Monthly Notices of the Royal Astronomical Society* **427**: 1089 (2012).

Shaham J. "Free precession of neutron stars - Role of possible vortex pinning". *ApJ* **214**: 251 (1977).

Shapiro S.L., Teukolsky S.A. *Black holes, white dwarfs, and neutron stars: The physics of compact objects.* (1983).

Shemar S.L., Lyne A.G. "Observations of pulsar glitches". *MNRAS* **282**: 677 (1996).

Shklovsky I.S. "On the Nature of the Source of X-Ray Emission of Sco XR-1." (1967).

Sidery T., Alpar M.A. "The effect of quantized magnetic flux lines on the dynamics of superfluid neutron star cores". *Mon. Not. R. Astron. Soc.* **400**: 1859 (2009).

Sidery T., Passamonti A., Andersson N. "The dynamics of pulsar glitches: contrasting phenomenology with numerical evolutions". *Monthly Notices of the Royal Astronomical Society* **405**: 1061 (2010).

Smartt S.J. "Progenitors of Core-Collapse Supernovae". *Annual Review of Astronomy & Astrophysics* **47**: 63 (2009).

Smoluchowski R. "Frequency of Pulsar Starquakes". *Phys. Rev. Lett.* **24**: 923 (1970).

Sonin E.B. "Vortex oscillations and hydrodynamics of rotating superfluids". *Rev. Mod. Phys.* **59**: 87 (1987).

Sonin E.B. "Tkachenko waves". *JETP Letters* **98**: 758 (2014).

Sourie A., Chamel N., Novak J., Oertel M. "Global numerical simulations of the rise of vortex-mediated pulsar glitches in full general relativity". *MNRAS* **18**: 1 (2016).

Sourie A., Oertel M., Novak J. "Numerical models for stationary superfluid neutron stars in general relativity with realistic equations of state". *Phys. Rev. D* **93**: 083004 (2016).

Spitkovsky A. "Time-dependent Force-free Pulsar Magnetospheres: Axisymmetric and Oblique Rotators". *Astrophysical Journal, Letters* **648**: L51 (2006).

Stephanov M.A. "QCD phase diagram and the critical point". *Prog. Theor. Phys. Suppl.* **153**: 139 (2004). [Int. J. Mod. Phys.A20,4387(2005)].

Stoner E.c. "The equilibrium of dense stars". *The London, Edinburgh, and Dublin Philosophical Magazine and Journal of Science* **9**: 944 (1930).

Sukhbold T., Ertl T., Woosley S.E., Brown J.M., Janka H.T. "Core-collapse Supernovae from 9 to 120 Solar Masses Based on Neutrino-powered Explosions". *ApJ* **821**: 38 (2016).

Taranto G., Burgio G.F., Schulze H.J. "Cassiopeia A and direct Urca cooling". *MNRAS* **456**: 1451 (2016).

Taylor J.H., Weisberg J.M. "A new test of general relativity - Gravitational radiation and the binary pulsar PSR 1913+16". *apj* **253**: 908 (1982).

Thomann A.U., Geshkenbein V.B., Blatter G. "Vortex dynamics in type-ii superconductors under strong pinning conditions". *Phys. Rev. B* **96**: 144516 (2017).

Thompson C., Duncan R.C. "The soft gamma repeaters as very strongly magnetized neutron stars - I. Radiative mechanism for outbursts". *Mon. Not. R. Astron. Soc.* **275**: 255 (1995).

Thompson C., Duncan R.C. "The Soft Gamma Repeaters as Very Strongly Magnetized Neutron Stars. II. Quiescent Neutrino, X-Ray, and Alfven Wave Emission". *ApJ* **473**: 322 (1996).

Tolman R.C. "Static solutions of einstein's field equations for spheres of fluid". *Phys. Rev.* **55**: 364 (1939).

Tsubota M., Kobayashi M., Takeuchi H. "Quantum hydrodynamics". *Physics Reports* **522**: 191 (2013). Quantum hydrodynamics.

Turolla R., Zane S., Watts A.L. "Magnetars: the physics behind observations. a review". *Reports on Progress in Physics* **78**: 116901 (2015).

Ushomirsky G., Cutler C., Bildsten L. "Deformations of accreting neutron star crusts and gravitational wave emission". *MNRAS* **319**: 902 (2000).

Van Eysden C.A., Melatos A. "Spin-up of a two-component superfluid: analytic theory in arbitrary geometry". *Journal of Fluid Mechanics* **729**: 180 (2013).

Vardanyan G., Sedrakyan D. "Magnetohydrodynamics of superfluid solutions". **54:5** (1981).

Varoquaux E. "Anderson's considerations on the flow of superfluid helium: Some offshoots". *Rev. Mod. Phys.* **87**: 803 (2015).

Viganò D., Rea N., Pons J.A., Perna R., Aguilera D.N., Miralles J.A. "Unifying the observational diversity of isolated neutron stars via magneto-thermal evolution models". *Monthly Notices of the Royal Astronomical Society* **434**: 123 (2013).

Warszawski L., Melatos A. "A cellular automaton model of pulsar glitches". *Mon. Not. R. Astron. Soc.* **390**: 175 (2008).

Warszawski L., Melatos A. "Knock-on processes in superfluid vortex avalanches and pulsar glitch statistics". *Mon. Not. R. Astron. Soc.* **428**: 1911 (2012).

Watanabe G., Maruyama T. "Nuclear pasta in supernovae and neutron stars". (2011).

Watanabe G., Pethick C.J. "Superfluid density of neutrons in the inner crust of neutron stars: New life for pulsar glitch models". *Phys. Rev. Lett.* **119**: 062701 (2017).

Weber F., Negreiros R., Rosenfield P. "Neutron Star Interiors and the Equation of State

of Superdense Matter". (2007).

Wheeler J.A. "Superdense Stars". *Annual Review of Astronomy and Astrophysics* **4**: 393 (1966).

Williams M.R., Fetter A.L. "Continuum model of vortex oscillations in rotating superfluids". *Physical Review B* **16**: 4846 (1977).

Witten E. "Cosmic Separation of Phases". *Phys. Rev. D* **30**: 272 (1984).

Wlazlowski G., Sekizawa K., Magierski P., Bulgac A., Forbes M.M.N. "Vortex Pinning and Dynamics in the Neutron Star Crust". *Physical Review Letters* **117** (2016).

Wolszczan A., Frail D.A. "A planetary system around the millisecond pulsar PSR1257 + 12". *Nature* **355**: 145 (1992).

Woosley S., Janka T. "The physics of core-collapse supernovae". *Nature Physics* **1**: 147 (2005).

Yakovlev D.G., Gnedin O.Y., Gusakov M.E., Kaminker A.D., Levenfish K.P., Potekhin A.Y. "Neutron star cooling". *Nuclear Physics A* **752**: 590 (2005).

Yakovlev D.G., Haensel P., Baym G., Pethick C. "Lev Landau and the concept of neutron stars". *Physics Uspekhi* **56**: 289-295 (2013).

Yakovlev D.G., Levenfish K.P. "Modified URCA process in neutron star cores." *A&A* **297**: 717 (1995).

Yuan J.P., Manchester R.N., Wang N., Zhou X., Liu Z.Y., Gao Z.F. "A very large glitch in psr b2334+61". *The Astrophysical Journal Letters* **719**: L111 (2010).

Zhou X.R., Schulze H.J., Zhao E.G., Pan F., Draayer J. "Pairing gaps in neutron stars". *Phys. Rev. C* **70**: 2 (2004).

Acknowledgments